# STUDIES ON THE EFFECT OF MODULATORY NANOAGENTS IN PROTEIN AMYLOIDOGENEIS

*Thesis submitted for the partial fulfillment of the requirements for the degree of*

**Doctor of Philosophy**

by

**Srijeeb Karmakar**
Reg. No. 176106011


Department of Biosciences & Bioengineering,

Indian Institute of Technology Guwahati,

Guwahati-781039, Assam, India

*This thesis is dedicated to my Lord,*

*Parampremamoy Sree Sree Thakur Anukulchandra,*

*&*

*His living embodiment,*

*Parampujyapada Sree Sree Acharyadev*

*~Srijeeb Karmakar*

Department of Biosciences and Bioengineering
Indian Institute of Technology Guwahati

## CERTIFICATE

This is to certify that the research work in the thesis entitled "**Studies on the effect of modulatory nanoagent in protein amyloidogenesis**", is carried out by me at the Department of Biosciences and Bioengineering, Indian Institute of Technology Guwahati, as partial fulfillment for the award of Doctor of Philosophy under the joint-supervision of Dr. Lalit Mohan Pandey, Associate Professor at the Department of Biosciences and Bioengineering, and Dr. Vimal Katiyar, Professor at Department of Chemical Engineering, Indian Institute of Technology Guwahati, Assam, India. The research outcomes documented in this thesis are accomplished by me and has not been submitted to any other Institute or University for the award of any degree or diploma.

**(Srijeeb Karmakar)**
Roll No: 176106011
Department of Bioscience and Bioengineering
Indian Institute of Technology Guwahati
Guwahati 781039, India

Department of Biosciences and Bioengineering
Indian Institute of Technology Guwahati

## CERTIFICATE

This is to certify that the thesis entitled **"Studies on the effect of modulatory nanoagent in protein amyloidogenesis",** being submitted by **Mr. Srijeeb Karmakar (Roll No: 176106011),** a student of Department of Biosciences and Bioengineering, Indian Institute of Technology Guwahati as partial fulfillment for the award of Ph.D. under my guidance and supervision. The research work documented in this thesis has not been submitted to any other University or Institute for the award of any degree or diploma.

**Prof. Vimal Katiyar**
Department of Chemical Engineering
Indian Institute of Technology Guwahati
Guwahati - 781039, Assam

**Dr. Lalit Mohan Pandey**
Department of Biosciences and Bioengineering
Indian Institute of Technology Guwahati
Guwahati - 781039, Assam

## *Acknowledgement*

The urge of all beings is to exist and grow to the fullest of their potential and possibilities. Also, one cannot exist without the ecosystem where one lives, and that invokes the desire to contribute, however small in magnitude, to the betterment of others. This is a fundamental desire of every scientific work undertaken. The work accomplished for the fulfilment of my doctorate degree is also intended to be a small step towards exploring the ways to create useful materials for the environment. I must, in that regard, express my most sincere gratitude towards Professor Vimal Katiyar, my doctoral advisor, who with his kindness, generosity, and valuable advices guided me all along this journey. I would also like to acknowledge the learning and knowledge I have gained from Dr. Lalit Mohan Pandey, my Joint doctoral advisor. Further, I am sincerely grateful to the members of my Doctoral Committee, Prof. A. B. Kunnumakkara, Prof. P. Iyer and Dr. Amit Kumar for their insights and critical appreciation of my research work, which indeed helped in shaping and improving the scientific quality of the study. Alongside, I must acknowledge the facilities provided to me by the Centre of Excellence-Sustainable Polymers (CoE-SusPol), Department of Biosciences and Bioengineering and Central Instruments Facility (CIF). I am also indebted to the operating members of the Field-Emission Transmission Electron Microscope (FETEM), especially Mr. Sujit Deb for holding his confidence in my operatorship. The help provided by my labmates at CoE-SusPol laboratory and their integral role in this accomplishment is ever irreplaceable. Therefore, I must take this opportunity to thank Dr. Balendu Sekher Giri, Dr. Riddhi Mahansaria, Dr. Tabli Ghosh, Dr. Narendaren S., Dr. Surendra Singh Gaur, Dr. Gourhari Chakroborty, Dr. Siddarth Mohan Bhasney, Dr. Naba Kumar Kalita, Ms. Kona Mondal, Mr. Sayan Bhattacharjee, Ms. Debleena Bose, Ms. Bhanupriya Das, Ms. Munmi Das, Ms. Doli Hazarika and

all others for their constant support. Further, I fondly acknowledge the intangible contribution of my closest people, especially Mr. Satadru Chakraborty, Mr. Sumit Chaudhuri, Mr. Pranjal Sonowal, and Mrs. Bhargabi Saha, for always keeping my morale high.

Everything that one achieves, acquires and accomplishes, rather one's whole existence is dependent and nurtured by his or her parents. My Late father, Sri Jiban Karmakar, was the first person to inspire and encourage me to achieve goals that never occurred to me I could, and My mother, Smt. Bina Karmakar, has been the driving force to my life and every good that has ever come out of it. I have been greatly fortunate to have my sister, Smt. Jayita Karmakar, and brother-in-law Mr. Amitabha Das, as constant support in everything. My nieces and nephew have been always a reason for my happiness.

My final and absolute gratitude is towards the divine light of my God, my Lord, Sri Sri Thakur Anukulchandra, whose blessings never forsook me, and delivered me from every crises of human life. Let every good that I strive for becomes a devotional offering at His Holy feet. I was most fortunate to experience the embodiment of love and divinity in Sri Sri Dada (Rev. Ashok Chakravarty), who had constantly elevated me with His sublime effulgence. My Acharyadev (Rev. Arkadyuti Chakravarty) is my deliverer and savior who has constantly bestowed strength to my will with His grace and compassion. Lastly, I must express, I am ever grateful to Rev. Abinendranath Chakravarty, without whom every aspect of my life is empty and incomplete.

# Abstract

Amyloidogenesis is associated with several proteinopathies (e.g. Alzheimer's disease) and synaptopathies (e.g. bipolar disorder), and also carry out specialized functions like storage of evolutionary informations and hormones. Intriguingly, the material properties of amyloids can also be exploited for designing smart materials like hydrogels, scaffolds, nanoparticle capped amyloid network, etc. Detailed in this report are the studies of modulation of amyloidogenesis of two model proteins (Insulin and Cytochrome C) by physicochemical factors. Upon a prolonged thermal and pH stress applied to Cytochrome C, heme was found to abruptly dissociate from the holo protein, resulting in complete collapse of Three-dimensional functional structure. Heme dissociation was found to engender self-oxidation of the protein, resulting in the conversion of Ferroprotoporphyrin to ferriprotoporphyrin. Binding of $Cl^-$ ions results in the formation of Chloro- ferriprotoporphyrin, and subsequently leads to the formation of fluorescent Quantum Dots through the re-organization of the porphyrin ring of heme. The ultrasmall Quantum Dots of heme (FeQDs) were found to re-adhere to the surface of the macromolecular network of apo-cytochrome C. FeQDs-decorated Cytochrome Camyloid network was found to accelerate BHK-21 fibroblast growth in a biocompatible way. The next study reports the formation of a unique biomolecular condensate-state of insulin molecules in elevated $Zn^{2+}$ and thermal stress, which was found to be cross-linked, viscoelastic and structurally reversible by pH modulation. The unique state was formed by the generation of elastic-like conformational variants (CVs) of insulin molecules through helix unwinding, relaxation of random coil, and subsequently conforming to an aggregate-like β-sheet rich structure. However, the aggregate-like state completely dissolved upon lowering pH, releasing monomeric insulin from the condensed organization. Next, the effect of co-incubation of

modulatory nanoagents, namely, pristine cellulose nanofibers (CNF) and magnetic cellulose nanocrystals (MagCNC) on the condensation of insulin molecules was investigated. It was found that the insulin condensation converts long-fiber semi-crystalline CNF to highly crystalline nanorods, whereas, rod-shaped MagCNC is converted to ultrafine nano-threads, followed by nucleation and microsphere formation. All the three condensate types were found to be biocompatible and accelerated the growth of Baby Hamster Kidney-21 (BHK-21) fibroblasts. In the next study, Insulin was found to be adsorbed on citrate-capped AuNPs with residues of the amyloidogenic stretch, where the helical components are protected from elongation and aggregation. $Zn^{2+}$ ions form protein-protein linkages and causes self-assembly of native-like insulin molecules, exhibiting a structural metaporphosis from a nucleating dendritic species to a condensed assembly with AuNPs presented on the surface. AuNP-decorated [$Zn^{2+}$]:[Insulin] condensed assemblies dissolve upon pH alteration and was found to promote BHK-21 fibroblasts without cytotoxicity. The effect was found to be completely different with IONPs where IONP incubated with [$Zn^{2+}$]:[Insulin] results in the formation of two-dimensional nanosheets. The nanosheets were found to stack with each other and form ordered arrays of surface channels. The IONPs, on the other hand, were found to undergo extensive re-organization into ultrasmall nanoparticles (2-3 nm) and adhere on the surface of the nanosheet. The two-dimensional IONP-decorated insulin nanosheet was found to penetrate inside the BHK-21 cells, thus exhibiting cellular uptake potential.

# *Contents*

# *List of Figures*

c'c", d'd" e'e", f'f" and g'g"; (G) HRTEM image of the CNR with marked areas denoted by 1,2, and 3; (H) and (I) represents the FFT (mask applied) and inverse FFT of the local area 1, respectively. The inset at (G) for local area 1 displays the unmasked FFT image obtained from imageJ (Inset 1); (J) and (K) represents the FFT (mask applied) and inverse FFT of the local area 2 showing the arrangement and direction of the planes. The inset at (G) for local area 2 displays the unmasked FFT image obtained from imageJ; (L) and (M) represents the FFT (mask applied) and inverse FFT of the local area 3 showing the atomic arrangement detected from Moiré pattern. The inset at G for local area 3 displays the unmasked FFT image obtained from imageJ.

# *List of Tables*

# Nomenclature

| | |
|---|---|
| ANS | 8-Anilinonaphthalene-1-sulfonic acid |
| AuNP | Gold nanoparticle |
| BHK-21 | Baby Hamster Kidney-21 |
| CNF | Cellulose nanofiber |
| CNR | Cellulose nanorod |
| CV | Conformation Variant |
| DMEM | Dulbecco's Modified Eagle Medium |
| ESI-MS | Electrospray Ionization Mass Spectrometry |
| EDS | Energy Dispersive Spectroscopy |
| FASTA | Fast-all |
| FTIR | Fourier Transform Infrared |
| FFT | Fast Fourier Transform |
| FeQD | Fe-containing quantum dot |
| FETEM | Field Emission Transmission Electron Microscopy |
| FESEM | Field Emission Scanning Electron microscopy |
| HO | Higher-Order |
| HRTEM | High Resolution Transmission Electron Microscopy |
| IONP | Iron oxide nanoparticle |
| IFFT | Inverse- Fast Fourier Transform |
| INCA | Integrated Calibration and Application Tool |
| MALDI-TOF/MS | Matrix Assisted Laser Desorption/Ionization-Time of Flight Mass spectroscopy |
| MTT | 3-(4,5-dimethylthiazol-2-yl)-2,5-diphenyl tetrazolium bromide |

| | |
|---|---|
| MagCNC | Magnetic cellulose nanocrystal |
| OD | Optical Density |
| PBS | Polybutylene succinate |
| PDI | Polydispersity index |
| RFFT | Reduced- Fast Fourier Transform |
| STEM | Scanning Transmission Electron Microscopy |
| SAED | Selected Area Electron Diffraction |
| SDS-PAGE | Sodium dodecyl-sulfate polyacrylamide gel electrophoresis |
| ThT | Thioflavin T |
| UV | Ultraviolet |
| VSM | Vibrating-sample magnetometer |

***Notations***

| | |
|---|---|
| $(\varepsilon)_{ThT}$ | Fluorescence emission of ThT at a given time |
| $(\varepsilon_0)_{ThT}$ | Fluorescence emission of ThT at 0 hour |
| R1 | Rate of fluorescence emission of ThT |
| $(\varepsilon)_{ANS}$ | Fluorescence emission of ANS at a given time |
| $(\varepsilon_0)_{ANS}$ | Fluorescence emission of ANS at 0 hour |
| $K(fast)_{ThT}$ | Rate constants expressed as a reciprocal of time |
| $K(slow)_{ThT}$ | Rate constants expressed as a reciprocal of time |
| $K(fast)_{ANS}$ | Rate constants expressed as a reciprocal of time |
| $K(slow)_{ANS}$ | Rate constants expressed as a reciprocal of time |
| $(\varepsilon)_{Trp59}$ | Fluorescence emission of Trp59 at a given time |
| $(\varepsilon_0)_{Trp59}$ | Fluorescence emission of Trp59 at 0 hour |
| A | Absorbance |

| | |
|---|---|
| ε | Extinction coefficient |
| G’ | Storage modulus |
| G” | Loss modulus |
| Ɛ | Extrinsic emission of fluorescence at a given time |
| $t_c$ | The mathematical value of t at Ɛ=0 |
| $d_H$ | Hydrodynamic size |

# CHAPTER 1

## Introduction and Literature Review


### Abstract

This chapter presents the fundamental concepts of Amyloids which are a special class of self-assembling supramolecular organizations exhibiting distinct geometric morphologies, 'Cross β' diffraction pattern and a spectrum of nanosized organizational variations. Further, it discusses that albeit the vicious involvement of amyloid fibrils in dreadful neurodegenerative diseases, their salient physico-chemical properties like mechanical strength, elasticity and the ability to interact with other biological molecules endow them the possibility of being employed in designing bionanomaterials. Then, some of the latest reports are presented which show the ability of amyloid fibrils in mimicking the surface topography of Extra Cellular Matrix (ECM) mediating cell adhesion, hybridization with other modulatory nanoagents like Carbon NanoTubes (CNTs), self-assembling into biocompatible sheet tapes, ribbons, fibers, etc. These potentialities offer a wide range application of amyloidl-based nanomaterial from electronics, sensors and actuators to implants, drug delivery vehicles and biomedicine. Therefore, the chapter attempts to present amyloid fibrils as an excellent ingredient to construct various forms of nanomaterials such as nanocomposites, encapsulating envelopes, hydrogels, liquid crystals, biofilms etc. Thereafter, the objectives of the thesis are laid forward as a closure for the chapter.


This chapter is 'under preparation' as a review article, with the title:

**"Amyloid fibrils: A versatile supramolecular organization for Bionanomaterial synthesis"**

## 1.1 Introduction

Amyloid fibrils are β-sheet rich fibrillar structures which are formed when the native structure of a protein gets disoriented and a transition towards 'cross β-sheet'-rich structure takes place [1–3]. These aforesaid fibrils are the major hallmarks of neurodegenerative diseases like Alzheimer's Disease (AD), Parkinson's Diseae (PD), Huntington Disease (HD), etc [4–7]. Very recently, amyloid fibrils have been found to be strongly associated with the most unresolved synaptopathies like Schizophrenia (SCZ), Bipolar Disorder (BD), Autism Spectrum Disorder (ASD) [8–11]. In that light, the association of proteopathies and synaptopathies has been comprehensively reviewed by Karmakar et al [12]. Amyloid fibrils tend to accumulate in the neuronal cells leading to the disruption of cellular functions [13–15]. The pathogenesis of the amyloid-related diseases and the exact mechanism of the transition of even a largely helical protein to a β-sheet rich structure requires comprehensive elucidation [1,16,17]. Strikingly, It has been suggested that the oligomeric aggregates or proto-fibrils are more toxic in nature than their mature counterparts [18].

Besides the involvement of amyloid fibrils in the pathogenesis of dreadful diseases, they have been found to display several coveted properties like high mechanical strength and elasticity which make them potential biomaterials for designing advanced therapeutic and diagnostic tools. In this direction, polypeptides with amphiphilic or repeating amino acid sequences have been successfully used to fabricate fibre-like nanostructures endowed with the ability to promote stem cell differentiation [19]. Self-assemblies of misfolded proteins further present a route for the synthesis of protein-based nano-fibres [20] and conductive nanowires [21].

Furthermore, nanomaterials which are based upon amyloid fibrils have been found to be efficient scaffolds for enzyme activity, tuneable nanowires for electronic systems like diagnostic tools, and also hydrogels for drug delivery [22–24]. Various studies have demonstrated that surface

functionalization of amyloid fibrils displaying ligands on the surface modulates their surface nanochemistry and enhances the scope of engineering advanced materials [3].

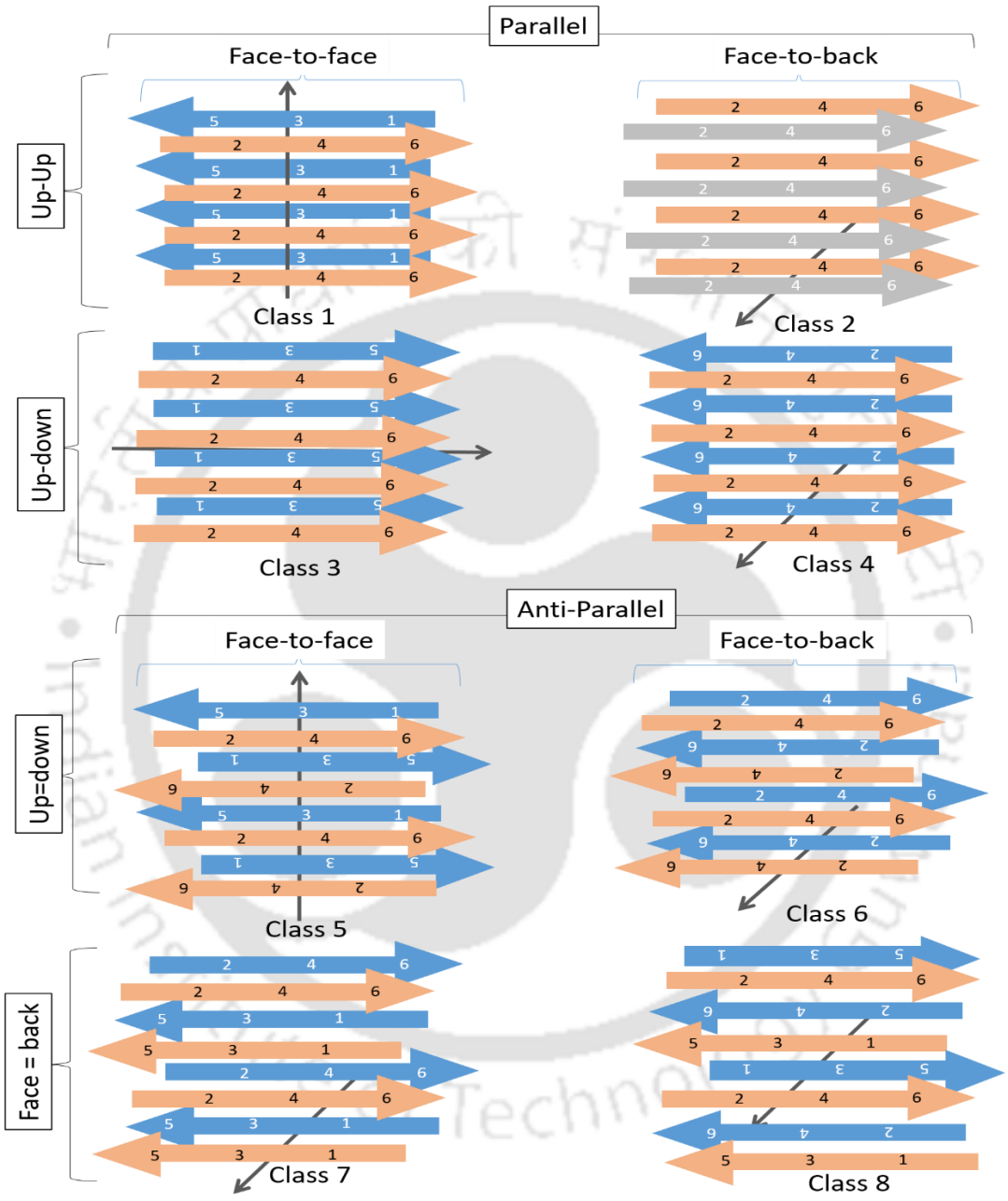


**Figure 1.1:** The eight stacking geometries of amyloid fibrils known as steric zippers. Adapted and modified with permission from Sawaya et al.[25].

**Table 1.1**. List of the eight steric zippers with structural information.

| Steric Zipper Class | Parallel/Antiparallel | Packing of Surfaces | Sheet orientation | Examples |
|---|---|---|---|---|
| Class 1 | Parallel | Face-to-face | Up-up | VQVYK (Tau)<br>NNQQNY (Sup35) |
| Class 2 | Parallel | Face-to-back | Up-up | SNQNNF (Prion) |
| Class 3 | Parallel | Face-to-face | Up-down | Not observed yet |
| Class 4 | Parallel | Face-to-back | Up-down | GGVVIA (Aβ) |
| Class 5 | Antiparallel | Face-to-face | Up-up | Not observed yet |
| Class 6 | Antiparallel | Face-to-back | Up-up | Not observed yet |
| Class 7 | Antiparallel | Face-to-face | Up-down | LYQLEN (Insulin) |
| Class 8 | Antiparallel | Face-to-back | Up-down | MVGGVV (Aβ) |

'Parallel/Antiparallel' refers to whether the strands in the sheets are parallel or antiparallel. 'Face-to-face' refers to the packing of sheets with the same surfaces adjacent to one another. 'Face-to-back' refers to the packing of sheets with different surfaces adjacent to one another. 'Up-up' and 'Up-down' refers to the parallel and antiparallel orientation of the sheets with respect to one another, respectively.

Amyloid fibrils have been functionalized with a spectrum of molecules like biotin [26], graphene (fabricated as biodegradable nanocomposite) [27], various fluorophores [28,29] and functional enzymes [30]. Intriguingly, a particular protein exposed to different in vitro amyloidogenic conditions have been found to exhibit diverse fibril morphology, branching pattern, geometric stacking, length, width etc. which is called amyloid polymorphism [31–33]. Figure 1.1 demonstrates the eight different types of stacking geometries of fibrils which can be formed by the amyloidogenic regions of fibrillation prone proteins. Table 1.1 enlists the eight steric zippers

detailing the presence of parallel and antiparallel strands, surface packing and sheet orientation. The formation of such intricate assemblies can be used to engineer advanced materials by tuning desired properties required for a specific application. For e.g., amyloid fibrils have been found to support and influence the morphology and differentiation of a wide array of cell types [34,35]. Another interesting aspect is the structural similarities found between amyloid fibrils and naturally occurring β-sheet rich assemblies like silk which provokes the notion of their diverse applicability [36,37]. This chapter outlines the mechanisms involved in protein folding/misfolding in brief, salient features of the amyloids compared with other materials, and their application, particularly, in the field of medicine and therapeutics.

**1.2 Protein folding/misfolding**

The process by which a protein folds to its three dimensional native structure has been found to be co-translational, i.e., the polypeptide chain enters the folding cascade while it is being synthesized in the ribosomal complex [38–40]. Anfinsen's experiments demonstrated that the folding pattern of a polypeptide/protein is dictated by its intrinsic amino acid sequence [41]. However, if a polypeptide chain stochastically or randomly searches for its native conformation, then, the estimated time required for the formation of native structure has been calculated to be of astronomical magnitude [42]. According to the Levinthal's paradox, such a stochastic search is impossible as the entire protein assembly is formed within a matter of a few milliseconds or even microseconds [43]. Therefore, it has been understood that a protein enters a specific folding pathway which is driven by the systems thermodynamics [44].

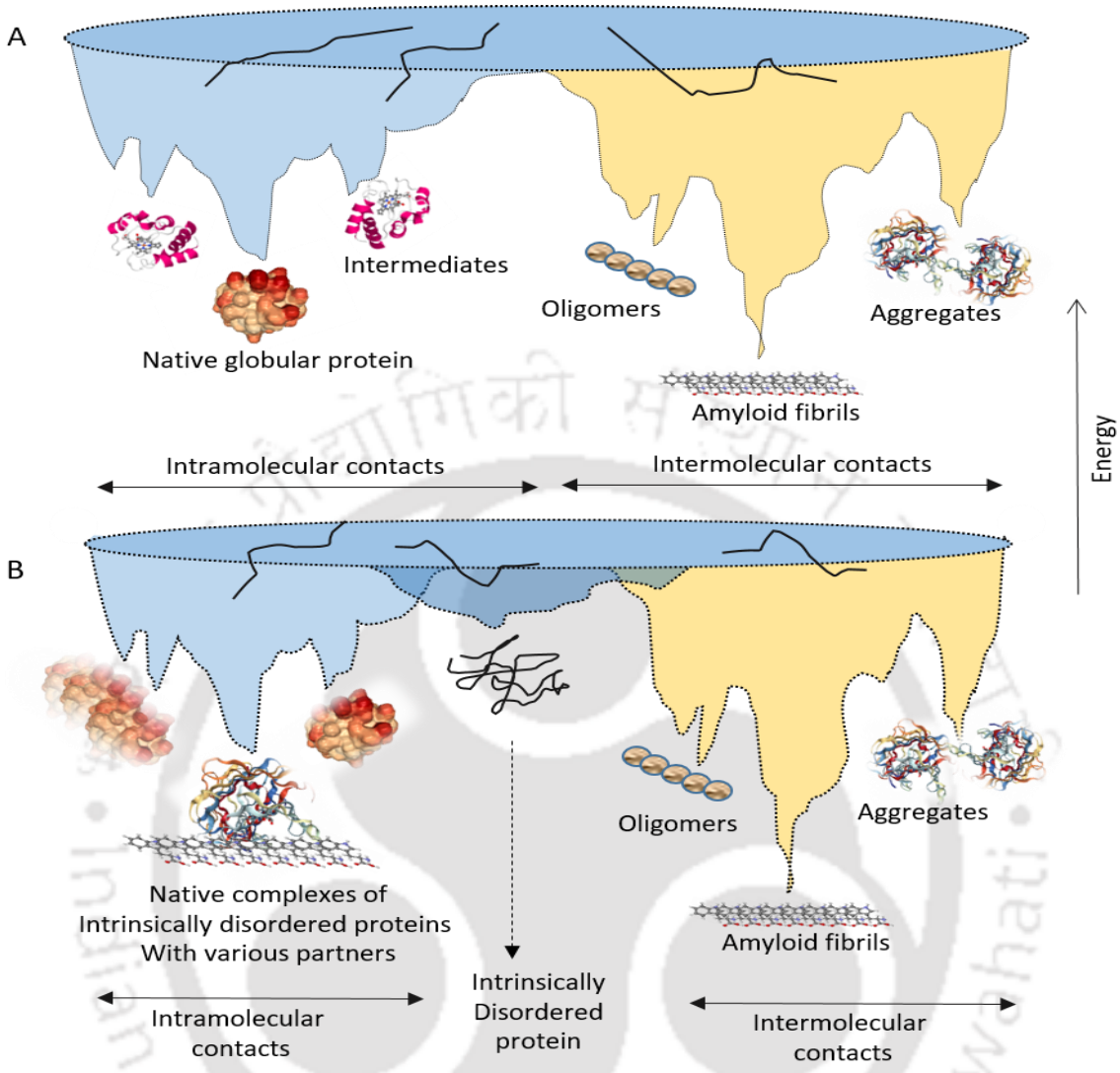


**Figure 1.2:** (A) Formation of native structure of globular proteins (like Bovine Serum Albumin) at a higher free energy level than the free energy of amyloid fibrils. (B) The energy landscape of intrinsically disordered protein. Adapted and modified with permission from Turoverov etal. [45].

"Energy landscape" or "Folding Funnel" represents the distribution of free energy corresponding to different conformers of a protein in the folding process. The funnel-top represents the intermediates with higher conformational entropy and the bottom represents monomeric native structures corresponding to minimum entropy. However, the entropic stabilization of amyloid

fibrils takes place at much lower energies than the native protein which makes the amyloid fibrils extremely stable to degradation [46–48]. Figure 1.2 (A) illustrates the energy landscape of a globular protein, wherein, the native structure has been shown to be formed at higher free energy than its respective amyloid structures. On similar lines, Figure 1.2 (B) illustrates the energy landscape of an intrinsically disordered protein, wherein, the free energy of amyloid fibril formation has been shown to be much lower than the free energy required to form complexes with other interacting partners and thereby, attain a functional conform.

Even though, the understanding of the amyloid fibril formation is in its nascent form, it has been well established that self-assembly of smaller aggregates to fibrillar mature structures is the fundamental amyloidogenic pathway [49–51]. Figure 1.3 illustrates a schematic representation of the self-assembly of smaller order aggregates of a protein to higher order geometric fibrils. In the figure, a monomer of protein (shown as A) gets involved in a series of reversible monomer-monomer associations (orange arrows) resulting in the formation of transient oligomers (shown as B). The transient oligomer B undergoes internal conformational re-organisation which serves as the nucleation point (blue arrows). This marks the structural transition of the protein to cross-β-like structures (shown as $C_1$ and $C_2$ , red arrows) resulting in the formation of fibrillar polymorphs (shown as $D_1$ and $D_2$). The amyloidogenic conditions responsible for the growth of amyloid fibrils influences either fibril fragmentation or a secondary nucleation, which selects a more thermodynamically favourable polymorph over the other. In addition, 'off-pathway' aggregation polymorphic intermediates are also formed (green arrows), such as a metastable oligomer (shown as E) and a protofibril (shown as G). These polymorphs arise from the same cross-β-like nuclei (shown as F). The prefibrillar conformers, $D_1$, $D_2$, E, and G, remain in dynamic equilibrium with

the monomeric and smaller order oligomeric forms, allowing the net transition from less stable forms to more stable forms.

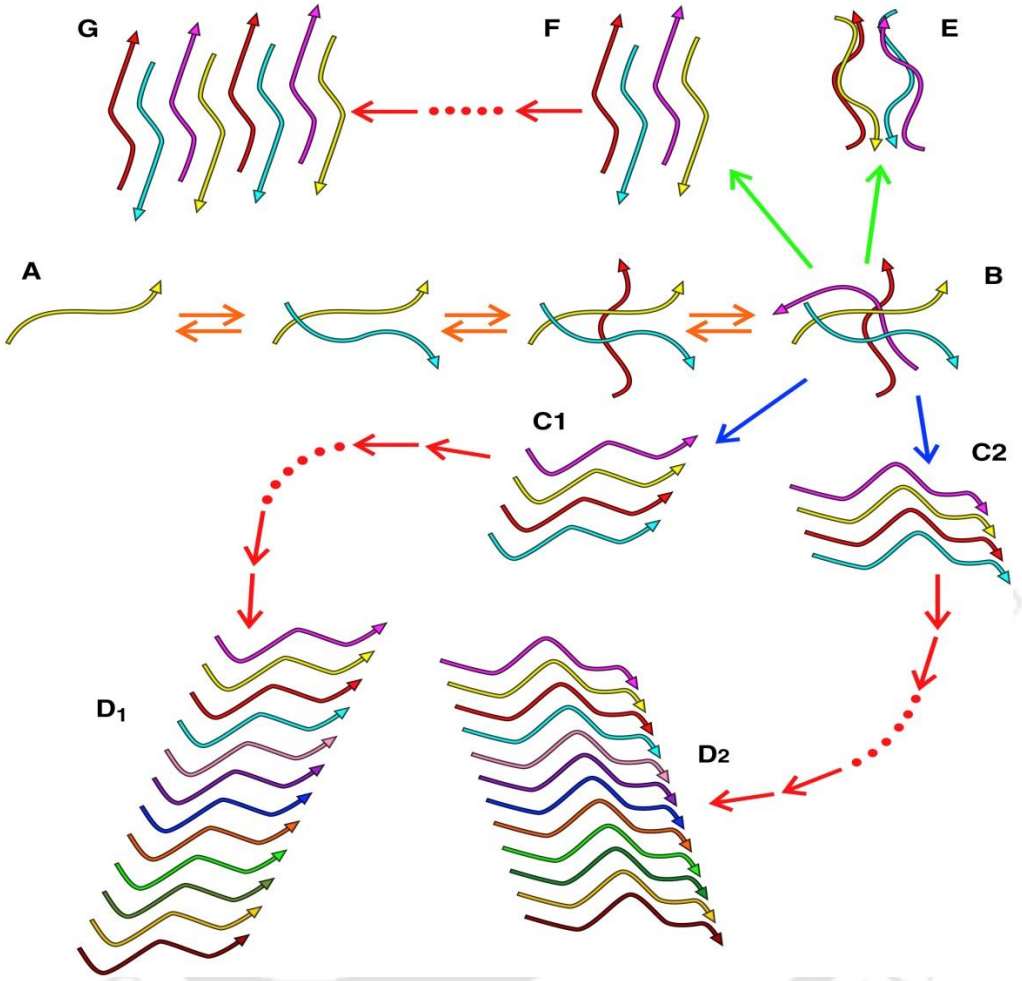


**Figure 1.3.** Schematic Representation of the molecular mechanisms involved in the formation of amyloid fibrils. Here, A refers to a peptide or protein monomer undergoing a series of reversible monomer addition resulting in the formation of a transient oligomer B, which is further capable of internal structural re-arrangement. After nucleation (blue arrows), $C_1$ and $C_2$ are formed which are cross-β like structures. Subsequent monomer addition in $C_1$ and $C_2$ results in the fibril polymorphs $D_1$ and $D_2$. Off-pathways from B (green arrows) might also result in intermediate aggregates like such as metastable oligomer E, cross-β-like nucleus like F, and subsequently a protofibril G. Adapted with permission from Tycko et al. [31].

### 1.3 Physiological implication of amyloids

#### 1.3.1 Pathogenesis of proteopathies

Amyloid fibrils, as already mentioned, accumulate in the neuronal cells and forms recalcitrant aggregates which block the intercellular communications [52–54]. Amyloid fibrils have been highlighted as the pathological hallmark in several proteopathies like AD (amyloid protein: tau, $A\beta_{40}$ and $A\beta_{42}$), PD (α-synuclein), HD (Huntington) etc. Interestingly, it appears that the inherent propensity of all polypeptide chains to aggregate influences a larger spectrum of pathologies, with recent reports highlighting the involvement of protein aggregates in synaptopathies like Bipolar Disorder (BD), Schizophrenia(SCZ), Autism Spectrum Disorder (ASD), and Amylotrophic Lateral Sclerosis (ALS) (amyloid proteins: SNAP25, syntaxin, synaptobrevin, synaptotagmin etc) [8,12,55] Table 1.1 enlists few of the common proteopathies and synaptopathies which are associated with fibrillation of amyloidogenic proteins.

#### 1.3.2 Functional amyloid fibrils

Apart from the involvement of amyloid fibrils in the pathogenesis of a number of diseases, proteins also undergo amyloid transition for performing certain physiological functions. Under chemical or thermal stress, it has been recently found that α-crystallin (the lens protein with two subunits, αA and αB) undergoes a structural change to amorphous aggregates or fibrils to retain their chaperoning activity [56].

Interestingly, the peptides or the proteins of the secretary granules of the endocrine system, for e.g., the pituitary gland, are retained in functional amyloids within the system [57]. Pigment Cell-specific Melanocyte Protein (PMEL) plays a crucial role in melanogenesis through its amyloidogenic cascade. Melanin is deposited on the PMEL fibrils after being synthesized in melanosomes [58].

In the microscopic world, fungal hydrophobins are important proteins which play crucial role in their growth. Among them, class I hydrophobins have been found to exert their function by self-assembling into amyloid fibrils known as rodlets to contribute to the formation of amphiphillic films [59]. Such functional amyloids have also been found to be exhibited by a bacterial protein, chaplin, in the soil-dwelling *Streptomyces coelicolor*. Chaplin fibrils have been reported to contribute to the coating of aerial mycelium and spores by rendering them hydrophobic [60].

**Table 1.2**: Amyloidosis (amyloid related diseases) and their associated proteins

| Amyloidosis | Amyloidogenic protein | Reference |
|---|---|---|
| Alzheimer's Disease | Amyloid β peptide (Aβ);<br>Tau protein | [28,61] |
| Prion Diseases | Prion Protein (PrP) | [62,63] |
| Parkinson's Disease | α- Synuclein | [64,65] |
| Amyotrophic Lateral Sclerosis (ALS) | Superoxide Dismutase,<br>TDP-43,<br>FUS | [66–68] |
| Huntington's Disease | Huntingtin | [69,70] |
| Type II Diabetes | Islet Amyloid Polypeptide (IAPP ; amylin) | [71–73] |
| Peripheral neuropathy | Transthyretin | [73] |
| **Synaptopathies**: | | |
| Schizophrenia,<br>Bipolar Disorder,<br>Amylotrophic Lateral Sclerosis | SNAP25 | [8,12] |

### 1.4 Salient characteristics of amyloids

Amyloid fibrils are characteristically very different from their source protein and exhibits common motifs all across. They are self-assembled structures of highly ordered filaments comprising of β-strand ladders running perpendicularly to the fibril axis [74,75]. Fibrillation of proteins, similar to the crystallization process, begins with a nucleation point from a hydrophobic stretch of the protein called the amyloidogenic region [76,77]. Many amyloidogenic regions are capable of preserving their self-assembling properties even after amino acid deletion or substitutions, extensions, or other modifications. The most amyloidogenic region of the polypeptide $A\beta_{42}$ has been experimentally verified to be $A\beta_{16-21}$ or KLVFFA (lysine-leucine-valine-phenylalanine- phenylalanine-alanine) which can independently form amyloid fibrils [25,78]. Herein, the mechanism of fibrillation is driven by hydrophobicity of the system [79]. A study highlighted that a mutant variant of $A\beta_{42}$ with an additional stretch of phenylalanines at the C terminus resulted in the acceleration of fibrillogenesis. By a combination of biophysical methods like X-Ray and NMR solid-state analyses, the primary contribution of the aromatic amino acids was established [80,81]. Furthermore, the dipeptide phe-phe ($A\beta_{19-20}$) has also been found to demonstrate similar amyloid fibrils [82] which can self-assemble spontaneously to form long and stable nanotubes [83]. Structural analysis has revealed that most amyloid fibrils exhibit a diameter ranging from 7-10 nm to even few micrometers [84]. The cross-sectional structural view of the amyloid fibrils has been found to be hollow, cylindrical or ribbon-like [85,86]. As already mentioned, amyloid fibrils are extremely stable due to their formation in the lowest energy zones of the folding funnel. The stability of the amyloid fibrils is attributed to the non-covalent bonds, primarily hydrophobic interaction and hydrogen bonding, and π-π stacking between main chains and side chains [49]. Further studies on mechanical strength and rigidity of the amyloid fibrils revealed that they are

similar to steel in mechanical strength and silk in rigidity [87]. Table 1.2 enlists some of the broad spectrum properties of amyloid fibrils.

**Table 1.3:** Physical properties of various amyloid fibrils.

| **Physical properties** | **Amyloid fibrils** | **Source protein** | **Reference** |
|---|---|---|---|
| Strength [GPa] | 0.6 ± 0.4 | Insulin | [88,89] |
| Bending modulus [GPa] | 1.0 – 3.9 | Type 1 Collagen | [89,90] |
| Bending rigidity [N $m^2$] | $9.1\pm1\times 10^{-26}$ | Insulin | [91] |
| Shear modulus [MPa] | 2.9 – 33 (depending on conditions) | Type 1 Collagen | [90] |
| Toughness [$kcal.mol^{-1}.nm^{-3}$] | 3.9 – 26.2 | hIAPP | [92] |
| Thermal stability [8C] | ≥ 130 | Prion rods | [89] |
| Torsional rigidity [Pa] | $(1.6\pm1.1) \times 10^{-26}$ | Insulin | [89,91] |
| Elastic modulas [GPa] | 1.0 – 10 | hIAPP (depending on steric zipper pattern) | [92] |
| Young's modulus [GPa] | 1.79 – 3.2 | Aβ40 | [93] |

Studies have pointed out that the toxicity of amyloid fibrils is lesser than that of the oligomeric species of the protein [94–96]. Therefore, lesser toxicity and biocompatibility of the mature fibrils has been highlighted as a lucrative feature for biomaterial synthesis [97,98]. It has also been demonstrated that polypeptide chains, irrespective of their involvement in amyloid-related diseases have inherent tendencies to assemble into nanofibrils *in vitro* [99]. Recently, it has been

also demonstrated that smaller peptides or even a single amino acid is capable of forming amyloid fibrils which opens enormous possibilities for rational designs [82,100]. In addition to the various lucrative properties, amyloid fibrils have been shown to exhibit strong interaction with other biological macromolecules such as polypeptides, nucleic acids (DNA/RNA), small molecules and biomembranes. This is attributed to the surface chemistry of the amyloid fibrils exhibiting strong hydrophobic interaction with other hydrophobic systems (like amphiphilic membrane), and a wide array of alternating charged patches allowing interaction with diverse charged groups [101,102].

**1.5 Modulation of amyloidogenesis for material design**

A decade earlier, the possibility of employing amyloid fibrils in designing bionanomaterial which supports cell-adhesion, migration and differentiation was demonstrated. It involved the incorporation of RGD-sequence (which is associated with cell adhesion in the biological system) and a control sequence (RAD) to the C-terminus of a peptide sequence corresponding to the amyloidogenic protein, transthyretin (residue 105-115). It was reported that the designed peptides self-assembled into fibrillar structures which were morphologically similar to the parent peptide. The RGD group made the fibrils bioactive and interactive with the cell surface [35]. Recent advancement in this direction involved the synthesis of hybrid nanoscaffold of Human Serum Albumin (HSA) fibrils and Gold Nano Rods (GNRs). The strategy was based upon the interaction between GNRs and HSA fibrils which assembled into conductive nanoscaffolds. It was confirmed by the analysis of Surface Plasmon Resonance (SPR) that the plasmonic component of the hybrid system remained unperturbed by the interaction of fibrils and GNRs [103]. Another interesting strategy was developed by Zhang et al. for the synthesis of peptide-nanofibril (PNF) decorated with gold nanoparticles (AuNPs). Figure 1.4 (A) shows the schematic representation of the strategic design of the conjugation of peptide and AuNPs. At first, an amyloidogenic peptide was

synthesized endowed with cysteine and tyrosine residues. The cysteine residues were able to capture the $AuCl^-_4$ (chloroaurate) ions from the solution. Tyrosine, being an efficient reducing agent, reduced the $AuCl^-_4$ to Au. Further, the amyloidogenic peptide underwent a nucleation which resulted in a cascade of self-assembling events, culminating into AuNP decorated PNF. The Au-decorated PNF has been found to display potential electrochemical and calorimetric sensing properties [104,105]

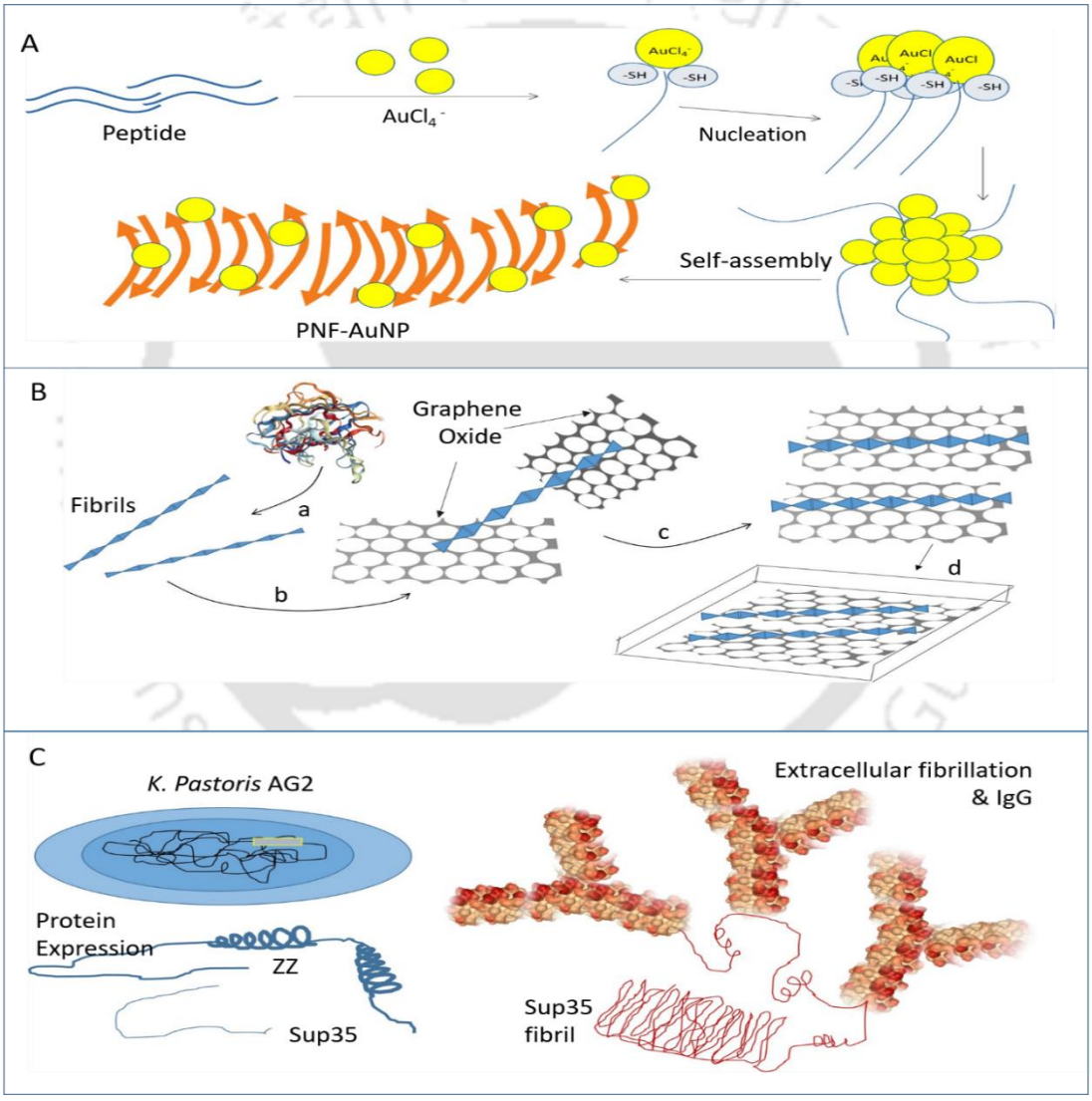


**Figure 1.4.** (A) Schematic of synthesis and self-assembly procedure of PNF-AuNPs. The green arrows of PNF-AuNP refer to the β-sheet structure of self-assembled PNF-AuNPs. Adapted with

permission from Zhang et al. [105]; (B) a. Supramolecular self-organization of β-lactoglobulin into fibrillar structure at amyloidogenic conditions, pH 2, vigorous stirring, and 90 °C. b, Aggregation of β-lactoglobulin fibrils and GO through electrostatic interaction. c, Preferential binding of fragmented amyloid fibrils on the graphene surface throughout the reduction of GO at 80 °C d, Layer-to-layer self-organization of graphene nanosheets and amyloid fibrils into hybridized nanocomposites employing vacuum filtration Adapted with permission from Li et al. [27]; (c) A strategy for the large scale production of amyloid fibrils using genetic engineering. Adapted with permission from Schmuck et al.[106].

A recent study demonstrated the fabrication of an ice-templated and cross-linked aerogel scaffold based upon β-lactoglobulin fibrils with attractive properties like softness, elasticity and water stability. β-lactoglobulin fibrils were freeze-dried and cross-linked using butane tetracarboxylic acid which resulted in the formation of an aerogel. Physical properties such as pore size and elastic modulus of the aerogel were controlled by modulating the fibril concentration and freezing gradient [98]. The rationale behind the choice of source protein is that β-lactoglobulin amyloid fibrils have been found to possess positive surface charge at lower pH. This presents a large surface for the hydrolysis and condensation of other structures, for e.g., silica precursors. Exploiting this property, a recent study demonstrated the fabrication of silica nanotubes which can be further used to prepare superhydrophobic surfaces mimicking lotus leaves [107].These studies highlighted the extent to which the morphology and physicochemical properties of amyloids can be tuned, giving insights for more rationale designs.

The extremely high stability profile of amyloid fibrils which is a desired property of any biomaterial, poses a problem towards biodegradability of amyloid-based biomaterials. A study by

Li et al. addressed the biodegradability problem by fabricating nanocomposites of graphene and amyloid fibrils endowed with enzyme sensing and shape-memory properties alongside good biodegradation [27]. Exfoliated graphene oxide (GO) was used as a source of graphene monolayer in the amyloid-graphene nanocomposite, which was found to be completely degraded by water-pepsin solution at an amyloid-graphene ratio of 1:8. Moreover, the nanocomposite featured conductivity, shape-changing properties in response to humidity, and fine-tuneable morphology which was attained by varying the amyloid fibril/graphene ratio. Figure 1.4 (B) represents a scheme of the strategy involved in the fabrication of graphene/amyloid nanocomposite. Herein, it has been shown that the strategy involved, at first, the fibrillation of β-lactoglobulin to generate amyloid fibrils at low pH (≤2), low ionic strength ($I \leq 20$ mM) and high temperature ($T \geq 80$ °C) [108]. Then, exfoliated graphene oxide (GO) was used as a source of graphene which has the property of reducing into aqueous dispersion of stable graphene monolayers [109]. The charges of the fibrils and graphene nanosheets were opposite at the working pH which bound the materials with electrostatic attractive forces [27].

Yet another study concerned about the real-world large-scale production of amyloid fibrils as an ingredient for biomaterial design was conducted by Schmuck et al. It involved the expression of functionalized nanofibrils from eukaryotic organism, *Komagataella pastoriswas*. At first, Sup35(1-61) nanofibrils decorated with Z-domain dimer were assembled from *Saccharomyces cerevisiae*. Then, *K. pastoriswas* was genetically engineered to incorporate copies of the Sup35(1-61) gene and the chimeric form, Sup35(1-61)-ZZ in its genome. The engineered organism was found to secrete the amyloidogenic proteins in the ECM where they were able to form functionalized mature fibrils (production yield 35 mg/l). Schematic of the strategy which was used to engineer the nanofibrils has been shown in Figure 1.2 (C).

Therefore, it can be comprehended that the dynamic nature of the formation of amyloid fibrils can be effectively engineered to acquire desired structural, biological and physicochemical properties.

### 1.6 Application of Amyloids

Amyloid fibrils, from synthetic peptides and natural sources (both pathological and functional forms), have shown promising potential in the fabrication of nanomaterials [110,111]. Such nanomaterials have been employed to create several therapeutic and diagnostic tools finding application as anticancer therapeutics [112], as antimicrobial agent [113,114], drug delivery vehicles [23] etc. The following two subsections outline the broad spectrum application of amyloid fibril-based nanomaterials in medicine and diagnosis.

#### 1.6.1 Amyloids in medicine

The self-assembling property of the recognition motif of α-synuclein has been exploited to develop a series of hydrogels with potential application in the differentiation of neuronal cells. The recognition peptide sequences were found to assemble into nanofibrous meshwork which mimicked neuronal ECM. These hydrogels were experimentally demonstrated to adhere to the mesenchymal stem cells (MSCs) and induce their differentiation towards neuronal cells. The fibril-based hydrogels were presented as an alternative cell replacement therapy for proteopathies and neuropathies [115]. This is of prime importance as the therapies for neurological conditions are in their nascent form and development of advanced therapeutics is the need of the hour. Figure 1.5 (A) shows the image of component amyloid fibrils which was the structural basis of the amyloid hydrogel. MSCs cultured with the hydrogel resulted in neuronal differentiation. Figure 1.5 (B) and (C) shows the microscopic images which confirmed neuronal morphology. Intriguingly, the amyloid hydrogel was also found to aid the delivery and

engrafting of the MSCs in the caudate putamen and substantia nigra in a parkinsonian mouse model. On similar lines, a graphene-amyloid composite film was developed which was able to self-assemble periodically to troughs and crests. The resultant film was endowed with specific topography for the modulation of contact and guidance to neuronal precursor cells. The film was shown to enable cell differentiation and polarization. This provided the insights that amyloid fibrils can be used to generate micropatterned, cell-adhesive conductive substrates for cellular differentiation and alignment [116].

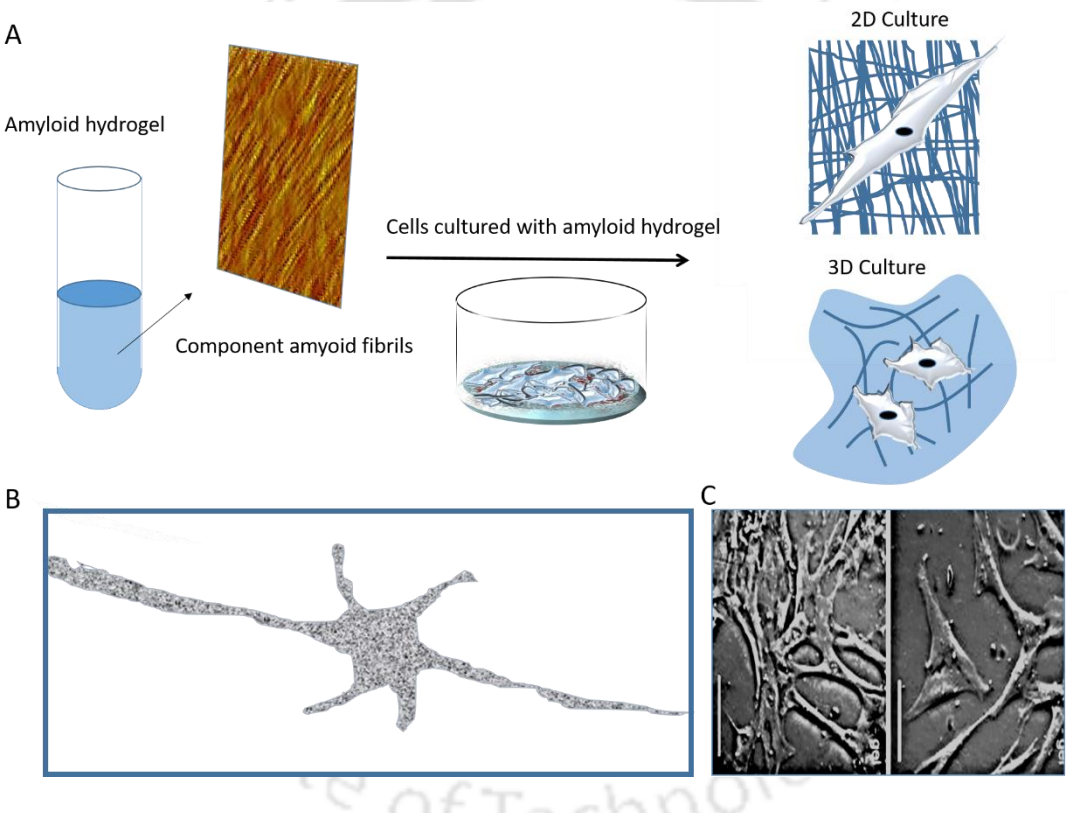


**Figure 1.5.** (A) Schematic representation of the amyloid hydrogel upon which 2D and 3D culture of SH-SY5Y neuroblastoma cells were found which showed neuronal differentiation, cell recognition and adhesion (without recognition sequences like RGD), and enhanced cell viability; (B) SH-SY5Y cells were cultured on the hydrogel which differentiated into elongated

and branched morphology similar to neurons; (c) Morphology of MSCs cultured on the hydrogel and glass surface. Adapted with permission from Das et al. [115].

Amyloid fibrils have also been investigated for their capacity to be used in therapeutic delivery systems. Kirti et al. demonstrated the fabrication of scaffolds from α-synuclein nanofibrils with potential application as targeted gene delivery systems. It was demonstrated that α-synuclein nanofibrils formed in the presence and absence of chitosan and poly-L-lysine amyloids were able to interact with lentiviral particles. A 4-fold increase in transduction efficiency was also observed with the involvement of the amyloid fibrils [117].

As regenerative medicine and implants, functional amyloids of *Escherichia Coli* such as curli fibers have been found to form excellent nanoassemblies with metal nanoparticles. In the natural world, the curli fibers are formed by the polymerization of native monomers and are secreted at the extracellular space to contribute to the formation of bacterial biofilms. These nano-assemblies have been demonstrated to nucleate the formation of AuNPs and gold nanowires (AuNWs). A lucrative property of the nanoassemblies included tuneable electrical conductivity which has been envisioned to create functional living materials from cell-synthesized amyloid fibrils by interfacing biotic and abiotic systems [118]**.** Such biologically active nanomaterials might contribute in the development of regenerative medicine and biocompatible implants.

β-lactoglobulin amyloid fibrils have been shown to act as templates for synthesizing palladium and gold NPs from their salt precursors. The hybrid was found to catalyse the reduction of 4-nitrophenol into 4-aminophenol with a larger rate than the unattached particles. Furthermore, the filter membranes were fabricated from the amyloid fibrils using the metal NP- amyloid fibril hybrid employing vacuum filtration. These membranes were shown to exhibit efficient flow

catalysts with complete substrate conversion to product [119]. This potentiates the possibility of designing large-scale production strategies for therapeutic molecules.

A recent report has presented the multifunctionality of amyloid fibrils attributed to their tuneable properties. Colloidal gels were formed by the amyloid fibrils of β-lactoglobulin and $CaCO_3$ NPs. The salient feature of the hydrogel included the incorporation of $Ca^{2+}$ as the charge screening ion whereas CaNPs served as the cross-linking agent to stabilize the gel network. The resultant gel was found to exhibit enhanced gel strength by two folds and responded to changes in pH displaying self-healing properties. This opens up the possibility of the particular hydrogel to be used in wound healing, drug delivery and as complementing scaffolds for tissue engineering [120].

In yet another study, κ-casein fibrils were employed to for the preparation of hollow microcapsules with potential applications in drug delivery systems. The study featured the layer-by-layer growth of amyloid fibrils which increased linearly with the favour of the electrostatic interactions between cationic κ -casein fibrils with poly(sodium 4-styrenesulfonate) and anionic κ -casein fibrils with poly(acrylic acid) [121]. Amyloid fibrils from Hen Egg White Lysozyme (HEWL) have shown to mimic the ECM in terms of its nano-topography and chemical composition. The amyloid fibrils networks were found to support the growth of Retinal Pigmented Epithelium (RPE) cells providing long term survival and proliferation with minimum production of reactive oxygen species. The proteinaceous base has been highlighted as a multipurpose material for the development of cell culture platforms with immense possibilities in retinal tissue engineering [122]. Amyloid fibrils have been employed to develop therapeutics for a wide range of diseases. Another major global health problem is Iron-Deficiency Anaemia or IDA where iron fortification of foods is a potential strategy to reduce the severity of the disease. Biodegradable amyloid fibrils of β-lactoglobulin have been applied in developing efficient carriers for iron in the fortification of food. The fibrils

were found to be anti-oxidizing nanocarrier and stabilizer for colloidal iron NPs. The ability of the amyloid fibrils to interact with NPs resulted in the synthesis of a hybrid material of stable iron-protein colloidal dispersion which underwent rapid dissolution and released iron ions during enzymatic and acidic digestion. The hybrid material did not cause abnormal accumulation of iron in any organ and did not change the glutathione concentration of whole blood, pointing to safe administration. Such metal-amyloid conjugates can emerge as highly effective drug delivery systems featuring both liquid and solid matrices [123].

In a study by Reynolds et al., TTR-1 based fibrils were decorated with a spectrum of cell adhesive peptides, like RGD and cyclo RGDfk, for creating surfaces which could retain the nanoscale fibrous topography but lacked in the fibrillar surface chemistry. The resultant surface topography was observed to influence the spreading and toxicity of the cells whereas the surface chemistry was found to influence cell attachment. Such network of nanoscale fibrous coatings created through self-assembly of peptides has been found to act as a potential biomaterial to promote mammalian cell growth. These biomaterials have promising utilization in the development of stem cell based regenerative medicine [124]. Owing to the diverse array of physiochemical properties, amyloid fibrils formed through higher order self-assembly have been hypothesized to promote synthesis of hydrogels with desirable properties. The amyloidogenic C-terminus of Aβ42 was investigated to self-assemble into β-sheet rich nanofibrillar hydrogels with properties like thermo-reversibility, non-toxicity and thixotropy [125]. The mechanistic analysis indicated that hydrogen bonding, π-π stacking and hydrophobic interactions served as the driving forces for amyloid network formation. The resultant supramolecular gel structure was found to present a supporting surface for cell attachment and proliferation for a wide range of cell types. By modulating the gel

properties with optimum peptide and salt concentration, scaffolds were drawn which promoted the differentiation of MSCs [125].

### 1.6.2 Amyloids in sensing systems

Amyloid fibrils are being extensively investigated for use in the development of diagnostic tools for several pathologies. Li et al., recently developed a GO-amyloid hybrid nanocomposite of two-dimensional GO nanosheets and one-dimensional lysozyme nanofibrils which were hybridized by electrostatic interaction. The hybrid composite served as a biocompatible platform for the immobilization of enzymes and Au nanocatalysts. The immobilized Au nanocatalysts or enzymes displayed high electrochemical behaviour with potential application in the development of glucose sensing systems. Furthermore, Horse Radish Peroxidase (HRP) was also immobilized on the GO-amyloid matrix as a model enzyme which displayed a platform for sensitive and selective detection of glucose.The nanocomposite based on lysozyme amyloid fibrils and GO displayed an excellent platform for HRP immobilization which also retained its catalytic activity specific to glucose [126]. In another study, self-organized assemblies of BSA amyloid-like nanofibrils were used for the synthesis of fibril-stabilized Au nanosclusters (Fib-Au NC). The resultant AuNC demonstrated significant augmentation in fluorescence with a large red shift of 25 nm in its emission maxima. The conjugation resulted in conformational changes of BSA displaying slightly higher helical content as a result of tyrosine-tyrosine complexes formed due to the reduction of $Au^{3+}$ by tyrosine. The Fib-Au NC was subsequently used for the label-free, sensitive detection of cysteine which is an amino acid essential for retention of cellular antioxidants, cellular metabolism, and detoxification [127]. Therefore, the hybrid material showed potential application in the detection of cysteine whose deficiency implicates in psoriasis, haematopoiesis, hair depigmentation, and leucocyte loss. Amyloid fibrils have been shown to control the molecular and optical properties of

small molecules like organic dyes, for eg., lysozyme and insulin fibrils were found to modulate the optical signature of rhodamine 6G aggregates. The structural variety of the fibrils led to a characteristic molecular arrangement of the rhodamine 6G dye molecules on a stimulated surface. As a result, the light amplification threshold and stimulated emission profiles were greatly enhanced. It can be envisioned that amyloid fibrils can be employed in the construction of broadband emission biolasers with possible diagnostic application [128].

The use of nanomaterial in the construction of instruments and electronic devices is based on the notion that miniaturization of the instrumental components increases the containment of number of functional units in a specific volume. Especially, it is requisite for the purification or the detection of monoclonal antibodies that the entrapment matrix is in the order of the nanoscale analyte. Amyloids being highly networked systems provide a higher surface/volume ratio which can be manipulated according to need. In a report, the cross-β structured protein nanofibrils were manipulated by expressing the chimeric proteins, Sup35-ZZ and ZZ-Ure2, in *Saccharomyces cerevisae*. The expressed proteins were amyloidogenic in nature which offered ZZ-domain and an intricate matrix for antibody binding and entrapment, respectively. The matrix was found to be 20 fold higher in binding efficiency (1.8 mg antibody per mg fibril) than the commercially used medium gold standard, protein A sepharose [129].

In a recent work by Amini et al., a nanosensor specific for the detection of hydrogen peroxide was designed using BSA nanofibrils, wherein, fibrillation was induced by glycation of BSA with fructose. The nanofibril and poly (alizarin yellow R) were immobilized on the glassy carbon electrode (PAYR/AMLNFibs/GCE). The conductivity of poly(alizarin yellow R) and the high surface to volume ratio of BSA nanofibrils allowed the electrode to exhibit excellent catalytic activity for reducing hydrogen peroxide. The nanosensor was specific for the detection of

hydrogen peroxide in the concentration range of 1 μM to 2.2 mM and a sensivity of 290 nM and 0.024 μA/μM. The BSA fibril based sensor displayed high sensitivity, excellent catalytic rate and detection of analyte at very low concentration [130].

**1.7 Amyloids for cell culture platforms**

Although amyloid fibrils have been found to be endowed with coveted physicochemical and biological properties required for designing functional materials, their limited biodegradability is a major problem. Several strategies are being developed for overcoming the problem while designing scaffolds and hydrogel for cell attachment, proliferation and differentiation of stem cells. Das et al, described the used of amyloid fibrils with graphene which is a well-known 2D polymer to develop composites for stem cell differentiation. The composite film of graphene and amyloid film can self-organize and form periodic troughs and crests saving the employment of lithographic techniques and etching. The generated topography of the film provides robust modulators of contact and regulation to neural precursor cells, thereby, enabling well-organized cellular polarization and differentiation [116]. Li et al showed biocompatible amyloid-PNiPAM hybrid hydrogel and amyloid-hydroxyapatite bone biomimetic composites [131].

Electrospun nanofibers are emerging as lucrative materials in replicating elements of the natural extracellular matrix (ECM). However, electrospun scaffolds have been found to be either non-degradable or degradable hydrolytically, whereas in contrast natural ECM degrades proteolytically, mostly through matrix metalloproteinases. Kabay et al developed nanofibers with electrospinning by modulating different ratios of ampicillin and BSA with a large range of diameters for controlled drug hydrophilic drug release [132]. Axpe et al, developed amyloid curli fibers-alginate nanocomposite hydrogel, wherein, the amyloid fibril and alginate were found to complement the limitations of each other [133]. Alginate, which is hydrophilic, has been found to

efficiently form hybrid by electrospinning with polycaprolactone, a hydrophobic polymer. The cross-linked structure also incorporated cellulose nanocrystals and the resultant hybrid of alginate/polycaprolactone/cellulose nanocrystal formed efficient platform for cell growth [134]. Thus, combining the functionalities of amyloid fibrils which have been reported to guide neuronal differentiation by providing elasticity and specific topography, and the softness provided by alginate matrix which would be physically optimized, shall provide a good platform for stem cells and neuronal cells to attach, proliferate and differentiate (in case of stem cells). Recent advances in developing platform for support of cell adhesion, proliferation and differentiation to neuronal lineages has revealed that softer matrices support the differentiation of stem cells to neurons whereas harder matrices support glial cells [135].

### 1.8 Recent Advances in the development of amyloid-based biomaterials

The amyloid fibrils are excellent material which presents a number of desirable properties, however, there are few limitations that comes along. In order to overcome these inadequacies, other biomaterials have been amalgamated to the amyloid fibrils to enhance or modify their properties. For instance, polysaccharides like low-acetylated gellan gum and κ-carrageenan have been diffused in the mesh of β-Lactoglobulin amyloid fibrils, to enhance resistance upon compression with no loss of the intrinsic reactivity of the amyloid fibrils. The hybrid material has been suggested to pave the way for the design of highly functional and environment friendly composites for multifaceted applications [136]. A recent study reported the construction of nanofibrils which were formed by the self-assembly of biohybrid prion-forming domain of the fungal protein named HET-s. The nanofibril provided a platform for the immobilization of [NiFeSe] hydrogenase inside water swollen conductive nanofiber network by a non-covalent cross-linkages. The resultant redox hydrogels were capable of electrolytic oxidation of $H_2$ that

could afford catalytic current densities up to 270 μA $cm^{-2}$, with overpotential of 0.33 V, at 45 °C [137]. In therapeutics, amyloid fibril based smart materials are emerging as a recognized template-platform for designing drug delivery vehicles. Hu et al. fabricated functional soft matter through the self-assembly of molecular building blocks (proteins, nucleic acids, and polyphenols) at a range of length scales [138]. The team demonstrated the ability of the self-assembled fibrils to support the self-assembly and deposition of polyphenols into hybrid nanofilaments and functional macroscopic-hydrogel. The loading capacity of polyphenols significantly increased by 4.0 wt % and improved stability was realized. Upon oral administration the hydrogels were found to transported from stomach to the small intestine, and subsequently to the gut (cecum, colon, rectum), with increased retention time in the colon. In the mice model, oral administration of the hydrogels significantly ameliorated the condition of colitis, and also promoted intestinal barrier function, suppression of pro-inflammatory mRNA expression, and regulated gut microbial dysbiosis.

### 1.9 Research Scope

Amyloid fibrils display certain attractive biophysical features which encourage the notion of fabricating smart nanomaterials by employing them. Several studies have reported that amyloid fibrils can be used to develop nanowires with strong mechanical and conductive properties which are potentially applicable in the development of electrochemical sensors. The ability of the amyloid fibrils to interact with other biological materials endow them with the possibility to be used in a wide array of biological applications. For instance, there have been successful reports regarding the potential of amyloid fibrils to mimic the ECM and provide a supporting platform for the proliferation and differentiation of the stem cells. Intriguingly, the amyloid fibrils have been found to interact strongly with nanoparticles (like AuNPs) which further their potential use in

nanotheranostics. Amyloid fibrils are also biocompatible causing no immune response in the physiological system. However, the degradation of the fibrils is extremely tough owing to their narrower energy landscapes which decrease their usability in biological system. It is a threat to the cellular mechanisms that stable fibrils might accumulate and further lead to cell death. Nonetheless, the recent fabrication of biocompatible and biodegradable nanocomposites of amyloid fibrils with other carbonaceous ingredients like graphite attempts to resolve this problem. In conclusion, extensive research is essential for exploring several applicable aspects of amyloid fibrils along with developing strategies for large scale production and cost-effectiveness, as *in vitro* fibrillation of proteins is a costly process.

Several strategies are being developed for overcoming the problem while designing scaffolds and hydrogel for cell attachment, proliferation and differentiation of stem cells. Therefore, in the studies of this thesis, the modulation of protein amyloidogenesis by nanoagents has been investigated.

The studies were performed on two model proteins, cytochrome c and human recombinant insulin which were exposed to amyloidogenesis-inducing environments through thermal or pH stress, and destabilization of the ionic microenvironment, respectively. Cytochrome C, in particular was not co-incubated with extrinsic nanoagents, rather the protein was destabilized through thermal and pH stress, which is known to dissociate its prosthetic group, heme. The dissociated heme thereby acted as an intrinsic modulatory agent.

Secondly, insulin was exposed to thermal stress and high ionic $Zn^{2+}$ concentration which is known to create aggregates of the protein. In the same experimental set up, organic and metallic nanoparticles were co-incubated and the behavior of the aggregation was investigated. Table 1.4 lists out the modulatory nanoagents used in the study.

**Table 1.4**: List of modulatory nanoagents investigated towards influencing amyloidogensis of model proteins

| Nanoagent | Reason | Reference |
|---|---|---|
| Heme (Intrinsic) | Dissociated from cytochrome C under stress condition. Composed of porphyrin ring. Porphyrins are known to re-organize into ultra-small nanoparticles | [99] [139] |
| Cellulose nanofiber (CNF) | Biocompatible and Interactive to other macromolecules | [140] |
| Iron functionalized CNC (MagCNC) | Biocompatible and Interactive to other macromolecules | [141] |
| Gold nanoparticle (AuNP) | Known to influence the amyloidogenesis of proteins | [141] |
| Fe (II, III) oxide nanoparticles (IONP) | Known to influence the amyloidogenesis of proteins and interactive to protein self-assembly | [142] |

## 1.10 OBJECTIVES

- Modulation of amyloidogenic behaviour and events of cytochrome C under thermal and pH stress
- Modulation of insulin amyloidogenesis by $Zn^{2+}$ ions and cellulosic nanomaterials
- Modulation of amyloidogenesis through sorption of Insulin molecules on citrate-capped Gold nanoparticle surface
- Modulation of insulin amyloidogenesis through dissolution of hydrophobic-hydrophillic phase in IONP-layered $Zn^{2+}$-insulin reaction mixture

### 1.11 Outline of the thesis

**Chapter 1: Introduction and Literature Review**

This chapter discusses the fundamentals of protein structure, protein folding and misfolding pathways, and the supramolecular assembly of proteins into higher-order organizations, i.e., multimers, aggregates, fibrils etc. The concepts of inter and intra interactions of proteins with other biological macromolecules has been deliberated, with latest advancement in the field of modulation of amyloids for construction of useful bionanomaterials.

**Chapter 2: Experimental Details**

This chapter discusses the materials and methodologies used in the study with elaborate description of the induction of protein amyloidogenesis of cytochrome c and insulin, modulation of the amyloidogenesis process by co-incubation of other nanoagents, both intrinsic and extrinsic. Also, the instrumentation and characterization techniques has been mentioned, with elaborate step-by-step details with mathematical process involved. The computational studies for the interaction of proteins with other molecules has also been discoursed.

**Chapter 3: Modulation of amyloidogenic behaviour and events of cytochrome C under under thermal and pH stress**

This chapter presents the amyloidogenic events of cytochrome C when exposed under prolonged thermal and pH stress. The sequence of events leading to the dissociation heme from the holo protein, resulting in complete collapse of three-dimensional functional structure has been entailed. The formation of two distinct structures: (i) A macromolecular amyloid-network formed by the

collapsed protein, and (ii) Fe-containing Quantum-Dots (FeQDs) with 2-3 nm diameter, has been discussed in details.

**Chapter 4: Modulation of Insulin amyloidogenesis by $Zn^{2+}$ ions and cellulosic nanomaterials**

This chapter reports the formation of a unique biomolecular condensate-state of insulin molecules in elevated $Zn^{2+}$ and thermal stress**.** The sequence of events leading to the generation of elastic-like conformational variants (CVs) of insulin molecules and subsequently conforming to an aggregate-like β-sheet rich structure, has been elaborated and interpreted. Next, the co-incubation of modulatory agents, namely, (i) pristine cellulose nanofibers (CNF) with long fiber-length, and (ii) magnetic cellulose nanocrystals (MagCNC) with rod-shaped morphology, their interaction and modulation of the insulin condensation process, leading to the formation of specialized nanostructures has been detailed.

**Chapter 5: Modulation of amyloidogenesis through sorption of Insulin molecules on citrate-capped Gold nanoparticle surface**

This chapter reports the construction of AUNP-decorated [$Zn^{2+}$]:[Insulin] condensed assembly. The synthesis of citrate-capped AuNPs sing the Turkevich method, and its co-incubation with [$Zn^{2+}$]:[Insulin] has been discussed. The effect of surface sorption of insulin molecules and the molecular events leading to the formation of a specialized structure with AuNP decorated insulin supramolecular organization has been elaborated and interpreted with a series of evidence.

**Chapter 6: Modulation of insulin amyloidogenesis through dissolution of hydrophobic-hydrophillic phase in IONP-layered $Zn^{2+}$-insulin reaction mixture**

This chapter presents the novel architecture and potential function of a two-dimensional nanosheet assembly formed by [$Zn^{2+}$]:[Insulin] co-incubated at a hydrophobic-hydrophilic phase-difference with iron oxide (II, II) nanoparticles (IONPs). The supramolecular organization of insulin monomers assembling into two-dimensional nanosheets by intermolecular $Zn^{2+}$-bridges, re-organization of IONPs (18-20 nm diameter) into ultra-small nanoparticles of 2-3 nm size, and formation of surface channels has been detailed. Also shown is the formation of a unique nanosheet organization by the adsorption of re-organized IONPs, to create ultra-small IONP-decorated insulin nanosheet.

**Chapter 7: Conclusions and suggestions for future works**

This chapter summarizes the findings of the study and discusses the importance and relevance of the work, emphasizing on the potential application of the experimental findings in biological field.

# CHAPTER 2

Experimental Details

## 2.1 Materials

Cytochrome C from bovine heart (cat. no. C3131), Thioflavin T (ThT) (cat. no. T3516), 8-Anilino-1-naphthelenesulfonic acid (ANS) (cat. no. A1028) were purchased from Sigma Aldrich and Tris-HCl was purchased from Himedia (Cas. No. 1185-53-1). Corning 96 Well Black polystyrene microplate was purchased from Sigma Aldrich (cat. No. CLS3603-48EA). 300 mesh carbon coated copper grids were purchased from Sigma Aldrich (cat. no. G4901). Insulin, human recombinant (cat. no. 91077C), $ZnCl_2$ was purchased from Sisco Research Laboratories Pvt. Ltd (Catalogue no. 2647112). CNF (trade name BiNFi-s cellulose, WMa-10002) obtained from Sugino Machine, Ltd. Gold (III) Chloride hydrate (254169-500MG) was purchased from Sigma Aldrich. Iron Oxide (II, III), magnetic nanoparticles solution (20 nm avg. particle size, 5 mg/ml in toluene) was purchased from Sigma Aldrich (cat. no.700304). Uranyl acetate dehydrate 98% (cat. no. 037212) was purchased from HPLC, India. $FeCl_2$ (extra pure), and $FeCl_3$ (extra pure) are procured from Nacalai Tesque Inc., Kyoto, Japan. Ammonia solution (28-30 %) is procured from Chameleon reagent, Osaka, Japan. Dulbecco's modified eagle's medium (DMEM), penicillin streptomycin, and fetal bovine serum (FBS) are obtained from Gibco™, USA. Tetrazolium dye MTT (3-(4,5-dimethylthyazol-2-yl)-2,5-diphenyltetrazolim bromide), trypan blue stain, and dimethyl sulfoxide (DMSO) are procured from Sigma Aldrich. Acetone, sodium hydroxide, and ethyl alcohol are obtained from SiscoResearch Laboratories Pvt. Ltd., India.

## 2.2 Experimental procedures

### 2.2.1 Amyloidogenesis of proteins

Appropriate amount of bovine heart cytochrome C was dissolved in Tris-HCl buffer maintained at pH 9 to make a final concentration of 90 μM [143]. The protein solution maintained at pH 9 was subjected to a constant incubation temperature of 75ºC for an extended period of 192 hours, i.e., 8 days. Due to the prolonged incubation time of 8 days, no induction of amyloidogenesis was done. Aliquots were collected in regular time intervals for biophysical characterizations.

### 2.2.2 $Zn^{2+}$-triggered amyloidogenesis of insulin and co-incubation with cellulosic materials

Insulin stock solution was prepared by dissolving appropriate amount of the lyophilized insulin powder in 10 mM Tris-HCl buffer (pH2), followed by gradual increase of pH to the physiological value, 7.4. Next, the solution was filtered through 0.2 μm syringe filter and absorbance was measured at 280 nm employing spectrophotometer. Using Beer-Lambert law, $A=\varepsilon Cl$ (where, A denotes Absorbance, ε denotes extinction coefficient, C denotes concentration, and l denotes the length of the path of light), final concentration of the stock was estimated using the extinction coefficient value 5530 $M^{-1}$ $cm^{-1}$. Subsequently, working concentration of insulin was prepared at 90 μM for the experiments. $ZnCl_2$ solutions were prepared at $[Zn^{2+}]$:[Insulin] stoichiometric ratios, 1:1 (System 1), 1:2 (System 2), 1:3 (System 3), 1:4 (System 4) and 1:6 (System 5). Insulin and $[Zn^{2+}]$:[insulin] were co-incubated at 60 ℃ for 6 hours for ion-induced amyloidogenesis of insulin.

### 2.2.3 Fabrication of Magnetic CNC

The MagCNC was synthesized from pristine CNF following a co-precipitation method described by Ghosh et al. [141]. In this process, the MagCNC was developed by adsorbing iron particles on the surface of CNF molecules through a single step process. A dispersion of CNF was created

using ultrasonication (benchtop sonicator) method for 2 min at 30% amplitude. The prepared CNF dispersion was kept at stirring condition under an inert atmosphere using $N_2$, where, to the dispersion, $FeCl_2$ and $FeCl_3$ (molar ratio of 0.0125 and 0.025 M) were added under vigorous stirring (1000 rpm) at 90 °C for a time period of 4 h. Afterwards, to this mixture, ammonia solution was poured dropwise to the above solution, where the temperature was maintained at 85 °C. It was followed by continuous stirring for 4 hours for the formation of MagCNC. Further, using a permanent magnet, the formulated MagCNC was separated from the above solution followed by washing in triplicates using ethanol and distilled water. The obtained washed MagCNC was freeze dried and was ground to break any lump using mortar pestle. MagCNC was stored at -20°C till further use. Figure 2.1 shows the schematic representation of the fabrication of MagCNC from BiNFi-s CNF through co-precipitation method, leading to the formation of iron adsorbed cellulosic nanoparticle.

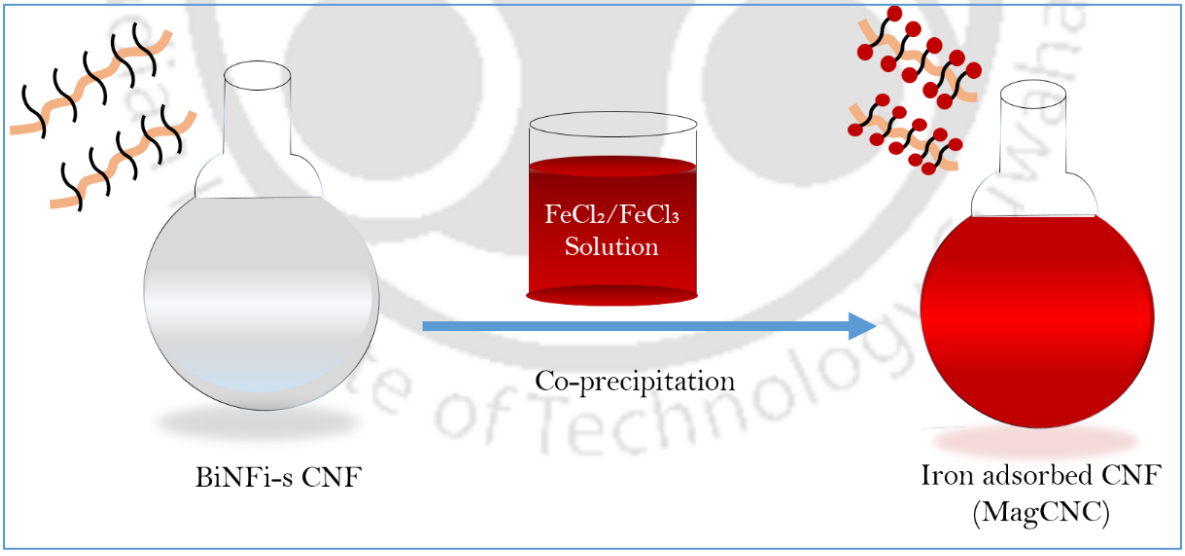


**Figure 2.1**. Fabrication of Iron functionalized Cellulose Nanocrystals (MagCNC) via single step co-precipitation method.

### 2.2.4 Co-incubation of CNF, MagCNC and equimolar [$Zn^{2+}$]:[Insulin]

An appropriate amount of the lyophilized insulin powder was dissolved in 10 mM Tris-HCl buffer (pH 2) to make a concentrated stock solution. The solution pH was adjusted to the physiological value by gradual addition of NaOH. The concentrated solution was then filtered through 0.2 μm syringe filter, followed by estimation of absorbance at 280 nm by employing a spectrophotometer. The final concentration of the insulin stock solution was estimated using Beer-Lambert law, A= εCl ( A denotes Absorbance, ε denotes extinction-coefficient: 5530 $M^{-1}$ $cm^{-1}$ [144], C denotes the concentration and l, the length of path of light). Then, working concentration was prepared at 90 μM through appropriate dilution for experimental purpose. A 5 mM $ZnCl_2$ stock solution was prepared by dissolving appropriate amount of the salt in distilled water. An equimolar reaction mixture of insulin and $ZnCl_2$ was co-incubated with 250 μL of the CNF and MagCNC colloidal solution at 60 °C for 6 hours. Alongside, a control sample was incubated without the modulatory agents. Aliquots were withdrawn with a regular time interval of 60 minutes for characterization

### 2.2.5 Determination of α-helix to β-sheet transition using Thioflavin T (ThT) binding assay

ThT is a benzothiazole dye which emits fluorescence upon specific binding with β-sheets which are one of the prime components of protein secondary structure. It is to be noted that β-sheet content significantly increases when proteins form amyloids. Therefore, increase in the extrinsic fluorescence of ThT upon binding with proteins is directly correlated to the formation of amyloids. For ThT binding assay, appropriate amount of the dye was dissolved in phosphate buffer (pH 6.5) to make a stock concentration of 2.5 mM. Next, appropriate amount of the solution was added to the aliquots of incubated protein samples to make a concentration of 20μM of ThT. Furthermore, samples of ThT in protein at $0^{th}$ hour (Control) and buffer solution alone (blank) were also screened for accurate estimations. The measurements were carried out using 96 well amber plates in a

multiplate reader (Tecan infinite 200 pro) at an excitation-emission of 450 nm/482 nm and slit width of 5 nm. The ThT added samples were incubated at 30 minutes in dark prior to the measurements for proper binding [1].

**2.2.6 Determination of exposure of hydrophobic residues using ANS dye binding assay**

ANS dye binds to the hydrophobic regions of proteins which are generally embedded at the core of the protein structure. To be noted, the process of amyloidogenesis has been found to significantly expose the hydrophobic patches onto the surface of the protein. Therefore, increase in the extrinsic fluorescence of ANS upon binding with proteins is directly correlated to the formation of amyloids. For the ANS binding assay, appropriate amount of the dye was at first dissolved in 50 µl methanol followed by addition of 950 µl of distilled water to make final stock concentration of 2.5 mM. For measurements, the stock concentration of ANS was appropriately diluted and added to the blank, control and test samples in a manner so that ANS concentration is in 100-fold molar excess than the protein concentration. The measurements were carried out using 96-well amber plates in a multiplate reader (Tecan infinite 200 pro) at an excitation-emission of 377 nm/470 nm and slit width of 5 nm. The ANS added samples were incubated at 30minutes in dark prior to the measurements for proper binding [1].

**2.2.7 Determination of intrinsic fluorescence using Tryptophan fluorescence assay**

The aromatic amino acids in protein have been reported to be packed inside the core of the protein structure owing to their hydrophobic nature. Moreover, the tryptophan residues which prominently absorb ultraviolet light at 295 nm and emit fluorescence, are exposed outwardly upon increase in β-sheets and their increased stacking. Therefore, the elevation of intrinsic fluorescence of tryptophan upon aggregation reveals the placement of tryptophan residues at the surface. The intrinsic fluorescence measurements of the samples were carried out using 96 well amber plates in

a multiplate reader (Tecan infinite 200 pro) at an excitation-emission of 295 nm/350 nm (as reported by [145]) and slit width of 5 nm [146,147].

### 2.2.8 Determination of change of Secondary structure using CD spectroscopy

The amyloidogenesis process has been known to exhibit structural transition of α-helix to β-sheets. Therefore, the structural transition of the proteins was rationalized to be understood from CD spectroscopy that probes into the secondary structure of proteins [148]. The measurements of aliquot drawn after the incubation time of the proteins and the protein at its native solution state were carried out in Jasco J1500 spectropolarimeter with a constant temperature cell-holder. Concentration of the samples were maintained at 5 μM and the spectroscopic analysis was done at far UV region (190 -250 nm) in a cuvette with path length of 1mm. The percentage of β-sheets and α-helices was predicted using the integrated software named 'Secondary structure predictor'.

### 2.2.9 Determination of change of Secondary structure using FTIR

FTIR spectroscopy was conducted using the instrument, Shimadzu IR Affinity S1, which autocorrects moisture and $CO_2$ while the recording the FTIR spectra. 2 μL of the co-incubated [$Zn^{2+}$]:[Insulin] were placed on the ZnSe crystal of the FTIR instrument with preset parameters (64 scans, 4 $cm^{-1}$ resolution) and the spectra was recorded in 400–4000 $cm^{-1}$. Subsequently, spectra between 1600–1700 $cm^{-1}$ (amide-I region) was deconvulated and data fitting was done using Gaussian curves at Origin 8.5 Software.

### 2.2.10 Determination of structural reversibility

After confirmation of all aggregation characteristics, the fully formed [$Zn^{2+}$]:[Insulin] aggregate solution formed at pH 7.4 was subjected to rapid reduction of pH to extreme low levels (pH 1-2) by drop-wise addition of 1N HCl, maintained at uniform stirring. Aliquots of the acid-treated

[$Zn^{2+}$]:[Insulin] aggregates were taken for ThT fluorescence assay to determine the event of dissolution, thereby, confirmation of the formation of condensate state. MALDI-TOF/MS measurement of the dissolved HOs was also carried out to realize the monomeric or multimeric forms in the dissolved HOs. Furthermore, non-reducing SDS-PAGE analysis (15% gel) was carried out to determine the molecular sizes of Insulin HOs, dissolved insulin HOs, dissolved MagCNC-insulin HOs, and dissolved CNR-insulin HOs.

### 2.2.11 Synthesis of citrate-capped gold nanoparticles (AuNPs) using Turkevich method

In 25 ml magnetically stirred boiling distilled water (100ºC), 0.1 ml of 1% Gold (III) chloride solution was added, followed by addition of 0.5 ml of 0.05 M sodium citrate. The solution was constantly boiled for ~ 15 minutes until the color of the solution turned completely ruby red [149].

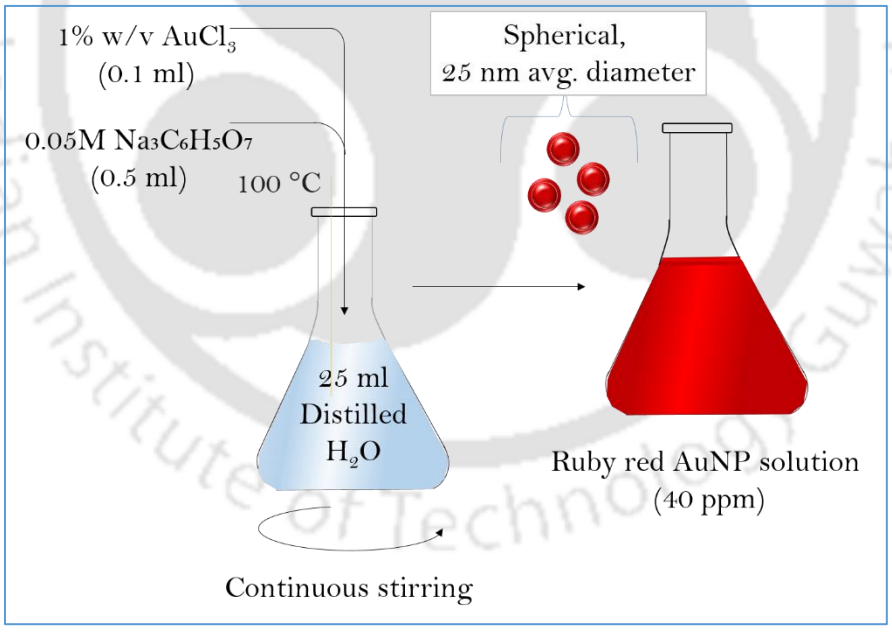


**Figure 2.2.** Schematic representation of the synthesis of citrate-capped AuNPs by using Turkevich method.

The AuNPs thus formed were characterized using visible range spectroscopy and electron microscopy. Figure 2.2 shows the schematic representation of the synthesis of citrate-capped AuNPs by using Turkevich method, leading to the formation of spherical AuNPs with avg. diameter of 25 nm.

### 2.2.12 Co-incubation of citrate-capped AuNPs and equimolar [$Zn^{2+}$]:[Insulin]

An appropriate amount of the lyophilized insulin powder was dissolved in 10 mM Tris-HCl buffer (pH 2) to make a concentrated stock solution. The solution pH was adjusted to the physiological value by gradual addition of NaOH. The concentrated solution was then filtered through 0.2 μm syringe filter, followed by estimation of absorbance at 280 nm by employing a spectrophotometer. The final concentration of the insulin stock solution was estimated using Beer-Lamberts law, $A=\varepsilon Cl$ ( A denotes Absorbance, ε denotes extinction-coefficient: 5530 $M^{-1}$ $cm^{-1}$ [144], C denotes the concentration and l, the length of path of light). Then, working concentration was prepared at 90μM through appropriate dilution for experimental purpose. A 5mM $ZnCl_2$ stock solutions was prepared by dissolving appropriate amount of the salt in distilled water. An equimolar reaction mixture of insulin and $ZnCl_2$ was co-incubated with 100 μL of the citrate-capped AuNP colloidal solution at 60 °C for 6 hours. Alongside, a control sample was incubated without AuNP solution. Aliquots were withdrawn with a regular time interval of 60 minutes for characterization.

### 2.2.13 Co-incubation of Insulin, $Zn^{2+}$ and Iron (II, II) Oxide Nanoparticles (IONPs)

The stock solution of human recombinant Insulin was prepared by dissolving an appropriate amount of the lyophilized in 10 mM Tris-HCl buffer, maintained at pH 2. It was followed by gradual addition of NaOH to increase the pH to the physiological value, 7.4. Subsequently, the insulin solution was filtered through a 0.2 μm syringe filter, followed by estimation of absorbance

at 280 nm by employing a spectrophotometer. The final concentration of the stock solution was estimated using Beer-Lambert Law. Subsequently, a working concentration of insulin was prepared at 90 μM by appropriate dilution. The [$Zn^{2+}$]:[Insulin] reaction mixture (control sample) was maintained at equimolar stoichiometric ratio (screened from a range of stoichiometric ratios) [150]. The [$Zn^{2+}$]:[Insulin] reaction mixture was incubated at 60°C at pH 7.4 for a duration of 6 hour. The test sample was prepared by adding 100μL of IONP (suspended in toluene) to the [$Zn^{2+}$]:[Insulin] reaction mixture which immediately formed an immiscible hydrophobic layer to the hydrophilic protein solution. After 6 hour incubation at 60°C, similar to the control sample, the two-phase IONP-[$Zn^{2+}$]:[Insulin] was kept at 4°C for 24 hour for aging, so that the hydrophobic layer of IONPs interact with the protein solution which transitioned from hydrophilic to hydrophobic nature upon aggregation.

### 2.3 Instrumentation and characterization techniques

#### 2.3.1 UV-Visible spectroscopy

Cytochrome C has a characteristic red color owing to the presence of Fe-containing heme prosthetic group. The said group plays a quintessential role in the formation of the global structure of the protein. Therefore, it was rationale to predict that any structural change of the protein should reflect in the localization of the heme group. Therefore, the aliquots of the incubated cytochrome C were scanned for their absorbance intensity in the soret band and beta band regions. We attempted to observe the relation between changes occurring at the central heme group (soret band) and the reduced/oxidized state at the beta band, if any. The measurements were carried out in a 96 well-plate in Multiscan Go microplate spectrophotometer (Thermo Scientific) from 300-700 nm and 5 nm slit width.

The optical density (OD) measurements for estimating the turbidity of insulin samples which were co-incubated with varying concentration of $Zn^{2+}$ ions at definite stoichiometric ratios, and also the disaggregation of the insulin- $Zn^{2+}$ supramolecular organizations were carried out at 600 nm in a multiplate UV-visible spectrophotometer.

### 2.3.2 Rheological characterization

Viscoelastic property of the cytochrome C amyloid network in comparison to the native form of the protein was characterized employing strain sweep in an Anton Paar MCR 102 rheometer with a 20mm parallel-plate. A 0.3mm zero gap of the parallel-plate and a temperature of 25°C of the measuring system was maintained. Appropriate amounts of the native form of cytochrome C, i.e., control sample (0 hour) and the amyloid form of cytochrome C, i.e. test sample (192 hour) were subjected to strain sweep within the range 0.1–1000 strain%. However, the storage modulus *G′* and the loss modulus *G″* were resolved and plotted within 10 –1000 strain% for better clarity as the effect was prominent from therein.

The native insulin solution maintained at 90 μM (pH 7.4) and the HOs formed at equimolar [$Zn^{2+}$]: [Insulin] (System 1) were subjected to strain sweep within the range of 0.1 to 1 strain (X100 for %values) in an Anton Paar MCR102 rheometer maintained at 25°C. Cone-and-plate (CP) geometry was used for assessment of the storage modulus (G') and loss modulus (G") in order to determine the viscoelastic property of native insulin solution and equimolar [$Zn^{2+}$]: [Insulin] Hos. The aim of the rheology experiment was to determine sol-gel transition which is an important characteristic of the protein condensates. Furthermore, the complex viscosity (in mPa.s) of native insulin solution and equimolar [$Zn^{2+}$]: [Insulin] HOs were determined against a range of angular frequency within the range 0.1 to 10 rad/s in CP geometry.

### 2.3.3 Determination of hydrodynamic radius using Dynamic Light Scattering (DLS)

The hydrodynamic diameter ($d_H$) of the aggregate/condensate of [$Zn^{2+}$]:[Insulin] was analysed employing a Zetasizer-nano-ZS (Malvern instrument, Malvern, UK) at the room temperature. The time-dependent fluctuations in the light-intensity scattered by the [$Zn^{2+}$]:[Insulin] aggregate/condensate in solution was estimated by the aforesaid instrument at a fixed angle of 175°. The $d_H$ of the [$Zn^{2+}$]:[Insulin] aggregate/condensate was determined by using Stokes-Einstein equation, $d_H$=KT/3πηD. Herein, *K* represents the Boltzmann constant, *T* denotes absolute temperature (in K), $\eta$ is viscosity and *D* represents the diffusion coefficient. The aliquots of the samples were diluted to ~1 mg/ml using filtered Milli-Q water.

### 2.3.4 Determination of structural units through Matrix Assisted Laser Desorption/Ionization- Time Of Flight (MALDI-TOF) Mass Spectrometry (MS)

The determination of the molecular weight (Da) of the insulin HOs, and dissolved HOs was done through MALDI-TOF/MS deploying the instrument, Bruker Daltonics-autoflex$^{TM}$ speed MALDI-TOF instrument. The matrix used was 2,5-dihydroxybenzoic acid solution in acetonitrile-water (50/50) in 0.1% TFA. The samples were mixed with the matrix in 1:1 ratio.

### 2.3.5 Analyses of the morphology of amyloid structures using Electron Microscopy

The morphology of the protein supramolecular organizations formed was observed in the bright-field microscopic technique of Field-Emission Transmission Electron Microscopy (FETEM) (instrument type: Jeol, Model: 2100F). A volume of 10 µL of the samples were drop-casted on 300-mesh copper grids and negatively stained with 10 µL of 2% uranyl acetate [151]. The sample grids were completely dried by prolong dessication, and then, observed under high-magnification at 200 KV and 175 µA. Further, the images were analysed in Gatan Digital Micrograph 3 [152]

and ImageJ [153] softwares. 10 μL of AuNPs and IONPs suspension were likewise drop-casted in the cupper grids and dessicated until complete drying. Further, the images were analysed in Gatan Micrograph 3 and ImageJ softwares. The High-Resolution Transmission Electron Microscopy (HRTEM) was performed at 800 K magnification and subsequently processed with Fast Fourier Transform (FFT), and Inverse-FFT (IFFT) for analysing the lattice fringes. Scanning Transmission Electron Microscopy (STEM) was employed for elemental mapping using SightX and INCA softwares [154]. The elemental analysis of sample was performed in bright-field STEM mode in FETEM (instrument type: Jeol, Model: 2100F). The element maps were generated in INCA software , by ETAS, which uses Cliff Lorimer thin ratio section method for analysis [155].

**2.4 Computational studies**

FoldAmyloid, an online web server (http://bioinfo.protres.ru/fold-amyloid/), was employed to find the amyloidogenic regions of cytochrome C based upon its intrinsic amino acid sequence [156]. The FASTA sequence of the protein (NCBI Reference Sequence: NP_001039526.1) was fed as the input and the specific parameters were set (Scale: 'Expected number of contacts 8A°; Averaging frame: 5, and Threshold: 21.4). Based upon the mentioned parameters, the amyloidogenic regions or the amyloidogenic amino acid stretches were identified and estimated. Next, the prediction of folded and unfolded regions of cytochrome C based upon the intrinsic amino acid sequence was done using Foldunfold online server (http://bioinfo.protres.ru/ogu/) [156,157]. The default parameters (Scale: 'Expected number of contacts 8A'; Averaging frame:11; Threshold: 20.4) were used for the estimation. Next, the residues which are protected or unprotected from hydrogen-deuterium exchange in protein chain were estimated using H-protection web server (http://bioinfo.protres.ru/ogp/) [158]. For the mentioned estimation the default parameters were used (Scale: 'Probability of hydrogen bond formation'; Averaging frame:

3; Threshold: 0.695; pH7). IsUnstruct was used to predict the residues in the ordered and disordered regions of the protein [159]. Next, the interactions of the heme group with the cytochrome C residues were predicted using LIGPLOT+ V.2.2 [160] by entering the crystal structure of cytochrome C (PDB code: 2B4Z) [161] as input.

The PDB file of human recombinant insulin (PDB ID: 3I40) was taken from RCSB Protein Data Bank for molecular docking [162]. The three-dimensional structure of citrate was obtained from PUBCHEM database in .sdf format and then converted to .pdb format using ONLINE SMILES TRANSLATOR (https://cactus.nci.nih.gov/translate/). To identify the binding sites of citrate, molecular docking was performed with human recombinant insulin using Patchdock server [163]. Next, the analysis of the nature of interaction and recognition of the interacting residues were done in LIGPLOT software, wherein, a 2-D schematic representation of the Protein-ligand complex is automatically generated [164]

**2.5 Cell culture studies**

BHK-21 fibroblast cells were seeded in fresh 96-well plates, 24 hours prior to the addition of FeQD-decorated cytochrome C amyloid (test) sample to the cells. The working solution of the test sample at 5% (v/v) concentration was prepared in serum-free DMEM. The working solution (test) and serum-free DMEM (control) were added to the plate wells in four replicates (100 µl each). Subsequently, the plates were incubated at 37°C in a humidified atmosphere with 5% CO2. To observe the growth and condition of BHK-21 cells in the presence of FeQD-decorated cytochrome C amyloid and control, Evos XL Core cell imaging system (Invitrogen) was used. MTT assays were performed in a time-dependent manner for regular time intervals of 8, 16, 24 and 48 hours to assess density of live cells. A Multiscan GO UV-visible spectrophotometer was used to carry out optical density measurements at 570 nm. The experiment was conducted in multiplicates.

[$Zn^{2+}$]:[Insulin] (control) and AuNP-[$Zn^{2+}$]:[Insulin] (test) samples were added to BHK-21 fibroblasts cells which were seeded in fresh 96-well plates 24 hours prior to the addition of samples to the cells. The working solution of added sample was kept at 5% (v/v) which was prepared in serum-free DMEM. The working solution (test) and serum-free DMEM (control) were added to the plate-wells in replicates of four (100 µl each). Afterward, the culture plates were incubated at 37°C within a humidified atmosphere with 5% $CO_2$. The growth and condition of BHK-21 cells in the presence the test and control samples was observed periodically. A time-dependent MTT assay for both the test and control sample was performed for regular time intervals of 8, 16, 24 and 48 hours to assess cell density, followed by spectrophotometric analysis. [$Zn^{2+}$]:[Insulin] (control sample) and IONP-[$Zn^{2+}$]:[Insulin] (test sample) were added to BHK-21 fibroblasts in fresh 96-well plates which were seeded 24 hours before the addition of samples. The working solution of the samples, prepared in serum-free DMEM, was maintained at 5% (v/v). The working solution (test) and the serum-free DMEM (control) were added to plate wells in four replicates (100µl each). Then, the BHK-21 cell culture plates were incubated at 37°C within a humidified atmosphere (5% $CO_2$). The condition and growth of the BHK-21 cells in the presence the control and test samples were observed cell imaging system mentioned earlier. A time-dependent MTT assay for both experimental systems were performed at time intervals of 8, 16, 24 and 48 hours to estimate the cell density, followed by OD measurements at 570 nm.

# CHAPTER 3

## Modulation of amyloidogenic behaviour and events of cytochrome C under thermal and pH stress

---

***Motivation***

*There is an on-going interest to utilize the lucrative properties of amyloids derived from diverse proteins to design biomaterials for wide-ranging applications, from cell-proliferating platforms to bioelectronic devices. Cytochrome C is a unique protein that has intrinsic magnetic and electrical properties, has a strong propensity to form amyloid network, and is an integral part of the natural world as a part of both aerobic and anaerobic respiration. Amyloid from cytochrome C might act as an electron-transfer network that can be explored for electro-induction of cell differentiation.*

---

This chapter has been published in the 'International Journal of Biological Macromolecules' as following:

*'Karmakar, Srijeeb, Arjun Sankhla, and Vimal Katiyar. "**Supramolecular organization of Cytochrome-C into quantum-dot decorated macromolecular network under pH and thermal stress**." International Journal of Biological Macromolecules 193 (2021): 1623-1634.'*

**Abstract**

This chapter presents the amyloidogenic events of cytochrome C when exposed under prolonged thermal and pH stress. The holo form of cytochrome-C which is involved in the electron transfer chain of aerobic and anaerobic respiration remains structurally intact by its complex with heme. However, when a prolonged thermal and pH stress was applied, heme was found to abruptly dissociate from the holo protein, resulting in complete collapse of Three-dimensional functional structure. Interestingly, two distinct structures were formed as the consequence of the dissociation event: (i) A macromolecular amyloid-network formed by the collapsed protein, and (ii) Fe-containing Quantum-Dots (FeQDs) with 2-3 nm diameter. Further adding to intrigue, the FeQDs were re-integrated on the surface of the amyloid network leading to FeQD-decorated macromolecular amyloid matrix. The heme interacting Met80 which lies in the amyloidogenic region possibly initiates the amylogenic cascade, and gradual exposure of Trp59 synergistically emits intrinsic fluorescence alongside FeQDs. The development of the aforementioned events were probed through a multitude of biophysical, chemical and computational analyses like ThT/ANS/intrinsic fluorescence assays, CD-spectroscopy, FETEM/STEM/elemental mapping, Foldamyloid/Foldunfold/Isunstruct/H-protection/LIGplot analyses, etc. The resultant FeQD-decorated amyloid-network was found to be gel-like, which supported the growth of BHK-21 fibroblast without cytotoxicity. Further studies on FeQD-decorated cytochrome C amyloid network might open possibilities to design advanced biomaterial for diverse biological applications.

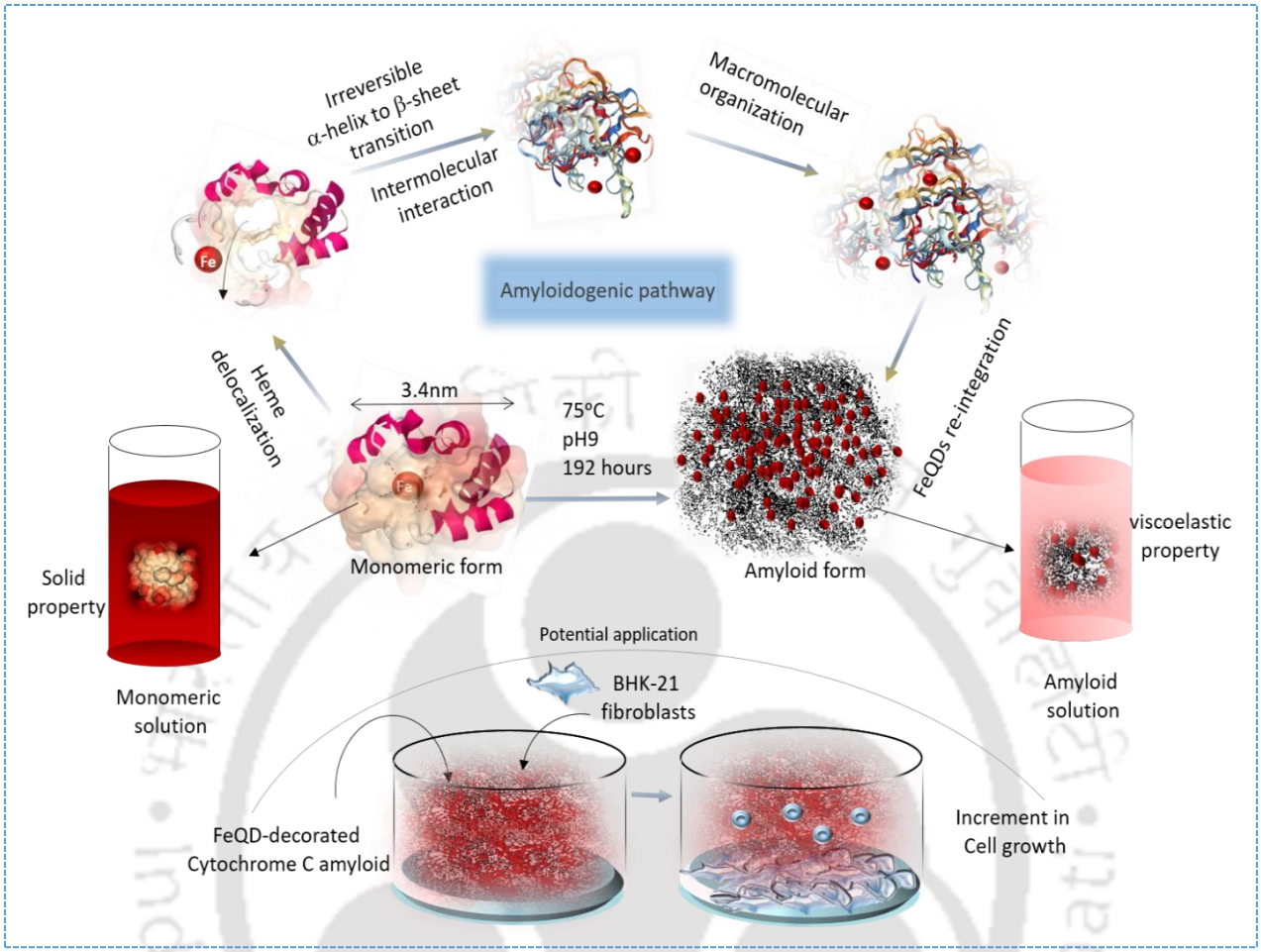


**Scheme of chapter 3**

## 3.1 Introduction

Amyloids (aggregates/fibrils) are a special class of self-assembling supramolecular organization which arise from native proteins and peptides due to a number of factors such as changes in physiological microenvironment, defects in folding/degradation pathways, genetic mutations, etc [14]**.** Thermodynamically, amyloid assemblies navigate lower in the energy funnel than the native protein structures whilst formation, which make them highly stable and recalcitrant to degradation [13]**.** Amyloids formed at diverse conditions exhibit distinct geometric morphologies, 'Cross β' diffraction pattern and a spectrum of nanosized organizational variations, from protofiber beads to

mature fibrils [165,166]**.** Albeit their vicious involvement in dreadful neurodegenerative diseases like Alzheimer's Disease (AD) and Parkinson's Disease (PD), their salient physico-chemical properties like mechanical strength, elasticity and the ability to interact with other physicochemical and biological molecules endow them the possibility to be used in designing bionanomaterials [167–170]. Furthermore, amyloid polymorphism, which is the ability of the same protein to transform into different amyloid structures, offers a beneficial feature to design tuneable nanomaterials of different types [170]**.** Amyloids of synthetic or de novo origin have shown promising potential in mimicking the surface topography of Extra Cellular Matrix (ECM) mediating cell adhesion [171]**,** hybridization with other nanofibers like carbon nanotubes (CNTs) [172]**,** self-assembling into biocompatible sheet tapes, ribbons, fibers etc. These potentialities offer a wide range application of amyloid -based nanomaterial from electronics, sensors and actuators to implants, drug delivery vehicles and biomedicine. Therefore, investigations into the nature of supramolecular organization of different classes of proteins become verily relevant.

The hemoprotein called cytochrome C represents a highly studied model owing to its quintessential involvement in the electron transfer chain of both aerobic and anaerobic respiration [173]**.** Nevertheless, it has been studied primarily for its functional structure and biological function, but there appears to be a lacuna in the investigation of supramolecular assembly of cytochrome C upon exposure to extreme conditions and subsequent formation of amyloid structures. Decades ago, Pertinhez et al. had reported the aggregation of a highly helical cytochrome into β-sheet rich fibrillar structure, but the experimental design proceeded with substituting cysteines with alanines which destabilized the heme group [99]. Therefore, the localization of the heme group was presented as the prime requirement for the maintenance of the helical structure of cytochrome C. Later, Alakoskela et al. reported amyloid fibers formed by cytochrome C induced by anionic

phospholipids. There, the researchers described the formation of variable fibers where some of the region exhibited native-like conformation and some consisted of strong β-sheet enriched amyloid characteristics [174].The unfolding events of apocytochrome C was investigated several years ago by Rankin et al., where it was reported that Trp59 emits enhanced fluorescence upon the unfolding event [145]. Kim et al., while studying the aggregation behaviour of cytochrome C-conjugated Silver nanoparticles observed that the protein shows decreasing trend of the characteristic heme absorption band, while the beta band (500-600 nm) indicates the oxidized form of the protein [175]. More recently, Nucara et al. reported that the morphology of cytochrome C aggregate/fibril is highly modulable. They described three distinct morphologies of cytochrome C: fiber, prefibrillar beads and macroplatelets. The effect of pH was discussed, and it was reported that if the concentration of protein was less than 100μM (limit concentration), then cytochrome C forms unordered aggregates rather than mature fibrils at high pH [176].

Indeed, supramolecular organization of cytochrome C represents a specialized study owing to the unique status of the hemoprotein and its intrinsically magnetic and electrical properties. Firstly, the highly helical structure of cytochrome C maintains its stability through retaining the coordination complexes of His18 and Met80 to the heme group [177]. Furthermore, the intrinsically fluorescent Trp59 remains attached to the heme group through hydrogen bonding. Indisputably, the locality and stability of heme group is essential for cytochrome C, which provokes the questions: (a) What might be the consequence of destabilization of heme group? (b) What might be the nature of the resultant structure formed by cytochrome C after heme delocalization?

Several forms of porphyrins, of which heme is constituted, have been observed to self-organize into nanoparticles [139,178,179].Therefore, one of the prime objective of the study was to track

the delocalization of heme and any reorganization of the porphyrins to form a specialized structure. Also, there is a lacuna of understanding in heme dissociation from cytochrome C albeit a coordination bond present between Met80-heme, and thioether bonds with Cys14 and Cys17 in the bovine heart cytochrome C (model protein under investigation) [180]. Also, the Trp59 residue interacts with heme in cytochrome C and its fluorescence quenches due to the close vicinity of heme complex. Trp59 fluorescence enhances upon unfolding of apocytochrome C as reported earlier [145]. However, there is a gap of explanation of the interactions and placement of Trp59 after a prolonged amyloidogenic process of cytochrome C. In order to investigate the aforementioned primary objectives, a number of biophysical techniques like fluorometry, spectroscopy, rheometry, electron microscopy, etc. have been deployed in the present study. The findings and their interpretation have been elaborately discussed in the subsequent sections of the chapter.

## 3.2 Results

### 3.2.1 Time-dependent extrinsic fluorescence of ThT revealed exponential rise of β-sheets

As mentioned earlier, ThT binds specifically to β-sheets whose significant increase is an indication of amyloidogenesis. A final concentration of 20 μM of ThT was added to the aliquots drawn at regular time intervals (0-192 hours) from cytochrome C solution incubated at 75ºC and pH 9. The extrinsic fluorescence emitted by ThT was found to exponentially rise as time duration of the incubation increased. Figure 3.1 A shows the plot of normalized values of extrinsic fluorescence emitted by ThT-cytochrome C *versus* Time in incubation in hours. The emitted ThT fluorescence trend fitted with the Mononuclear growth model with the following equation:

$$\varepsilon_{ThT} = A_1 - A_2 e^{-k \cdot t} \quad (3.1)$$

Where, $\mathcal{E}_{ThT}$ denotes fluorescence emission of ThT at given time *t*. $A_1$ and $A_2$ are amplitudes which were estimated to be 1.97 ± 0.57 and 1.68 ± 0.56, whereas the rate *k* was estimated to be 0.003 ± 0.001 $hour^{-1}$.

### 3.2.2 Time-dependent extrinsic fluorescence of ANS revealed exposure of inner hydrophobic patches

It has been explained earlier that the hydrophobic residues are embedded at the inner core of a protein while folding. On the contrary, the hydrophobic residues have been found to get exposed on the surface while amyloidogenesis takes place. ANS dye binds specifically to the hydrophobic patches of a protein and emits enhanced fluorescence.

In the present study, ANS dye was added to the aliquots drawn at regular time interval from the incubated cytochrome C solution. The extrinsic fluorescence emitted by ANS upon binding with incubated aliquots of cytochrome C was found to increase exponentially as time of incubation progressed. Figure 3.1 B shows the plot of normalized values of extrinsic fluorescence emitted by ANS-cytochrome C *versus* Time of incubation in hours. The emitted ANS fluorescence trend fitted with the Two-Phase Exponential Association Model with the following equation:

$$\varepsilon_{ANS} = \varepsilon_{0ANS} + A_1(1- e^{-k(fast)_{ANS}\cdot t}) + A_2(1- e^{-k(slow)_{ANS}\cdot t}) \quad (3.2)$$

Where, $(\varepsilon)_{ANS}$ denotes normalized fluorescence emission of ANS, $(\varepsilon_0)_{ANS}$ denotes the fluorescence emitted at t=0, where t is the time. $(\varepsilon_0)_{ANS}$ was estimated to be 0.23±0.018. $k(fast)_{ANS}$ and $k(slow)_{ANS}$ are the two rate constants expressed as a reciprocal of time, and were calculated to be ~0.56 $h^{-1}$ and ~0.025 $hour^{-1}$, which indicated that the hydrophobic residues were fully exposed, tending to reach the saturation. $A_1$ and $A_2$ were estimated to be 0.24 ±0.1 and 4.7±0.3, respectively.

### 3.2.3 Time-dependent intrinsic fluorescence of Trp59 revealed that cytochrome C amyloids are intrinsically fluorescent

Cytochrome C contains five aromatic amino acid residues (Tyr48, Tyr67, Tyr74, Tyr97 and Trp) which are also hydrophobic. Therefore, it was rational to assume that the residues are embedded at the core of the protein. Of the aromatic residues, the most prominent Trp59 residue absorbs UV light at wavelength 295 nm and fluoresces thereby. We conducted a time-dependent estimation of fluorescence emitted by the Trp59 residue in order to understand the localization of the same in the cytochrome C amyloids.

Figure 3.1 C shows the normalized value of intrinsic fluorescence of the Trp59 residue measured at 295 nm *versus* time of incubation in hours. There was a gradual increment of the intrinsic fluorescence of Trp59 which indicated that the residue had moved away from heme and was exposed on the surface upon unfolding, which is otherwise quenched in the vicinity of heme. The trend reached a plateau stage within 48 hour and remained saturated. This indicated that the Trp59 residues changed its configuration rapidly and were occupied the surface regions of the amyloids. The emitted Trp59 fluorescence trend fitted with the Mononuclear growth model with the following equation:

$$\varepsilon_{\mathrm{Trp59}} = \mathrm{A}_1 - \mathrm{A}_2 \mathrm{e}^{-\mathrm{k}\cdot\mathrm{t}} \qquad (3.3)$$

Where, $\varepsilon_{Trp59}$ denotes normalized fluorescence emission of Trp59 at any given time, *t*. $A_1$ and $A_2$ are amplitudes which were estimated to be 0.99 ± 0.004 and 0.26 ± 0.007, whereas the rate *k* was estimated to be 0.043 ± 0.003 $hour^{-1}$.

### 3.2.4 Comparative analysis of CD spectra confirmed collapse of helical structure and α-helix to β-sheet transition

Firstly, the native structure of cytochrome C is known to be largely helical. Secondly, the prime footprint of amyloidogenesis is structural transition of α-helix to β-sheets. Therefore, CD spectroscopy was conducted for cytochrome C control sample (0 hour) and final test sample (192 hour) to evaluate the change of the secondary structures.

Figure 3.1 D and E shows the far UV-CD spectra of cytochrome C control sample and the test sample drawn from the final aliquot, respectively. It was observed that the profile of CD spectra at 0 hour was drastically different than the 192 hour, implying significant structural transition. It was predicted using K2D3 software that at 0 hour, the percentage of α-helix was 93.96 % and that of β-strand was 0.32%. The signature peaks for the helical conformation, 208 nm and 222 nm, were clearly observed at the 0 hour sample.

After incubation of the cytochrome C solution at the aforementioned conditions, the α-helix content reduced to 3.09% (Figure 3.1 E). A prominent negative peak at 200 nm was observed which is indicative of random coil conformation The CD spectra pattern of this heat incubated appeared similar to the findings of Groot et al. [143]. The cooperative native structure of the cytochrome C was completely lost due to unfolding, with the backbone attaining a random coil conformation. This presumably exposed the protein monomers to the solvent, allowing intermolecular interactions to predominate, and thereby causing concentration dependent protein aggregation. According to Groot et al., the native structure of cytochrome C is recovered from its unfolded state provided the prosthetic group remains intact. In the absence of the bound prosthetic group, the native structure of the protein is not recovered, and results in the aggregation of the protein. Also, the aggregation of cytochrome C is not dependent on the transition of helical

structure to β-sheet, rather unfolding of the protein and increase in intermolecular interactions. As stated by Groot et al, 'bovine cytochrome C constitutes yet another example in which secondary structure propensity and amyloid fibril formation are not related'.

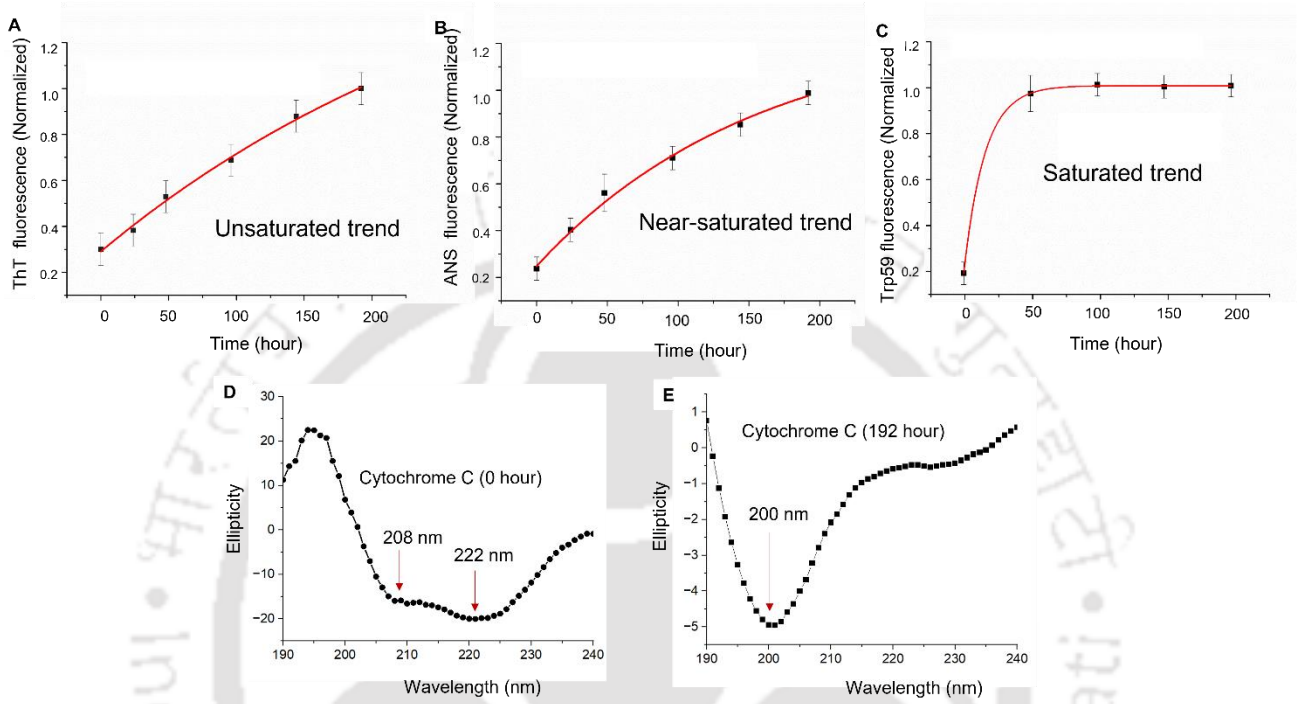


**Figure 3.1.** (A) Normalized extrinsic fluorescence of ThT-cytochrome C *vs.* Time of incubation (hour); (B) Normalized extrinsic fluorescence of ANS-cytochrome C *vs.* Time of incubation (hour); (C) Normalized intrinsic fluorescence of Trp59 residues *vs.* time of incubation (hour); (D) and (E) Far UV-CD spectra of cytochrome C at 0 hourand 192 hour, respectively.

### 3.2.5 Analysis of the dissociation of heme, reduced/oxidized state, and subsequent enhanced heme fluorescence

It has been explained earlier that the Fe-containing prosthetic group 'heme' plays a crucial role in the formation and maintenance of the global structure of cytochrome C. Also, the presence of heme renders the protein a characteristic red color. We observed gradual decolouration of the

cytochrome C solution as incubation progressed. It prompted to investigate the absorbance spectra of the incubated protein in a time-dependent manner. Figure 3.2 A shows the time-dependent absorbance spectra of the characteristic soret band of cytochrome C to assess the optical imprint of the characteristic red color owing to heme. A gradual flattening of the signature peak annotated to the red color of the intact heme group, as time of incubation progressed, was observed. This indicated that the complex of the apo form and the heme group was completely destabilized which resulted in the dissociation of heme and complete collapse of the native 3D-structure of the protein. Cytochrome C also leaves an optical imprint at 500-600 nm which shows the reduced/oxidized state of the protein. The event of dissociation of heme group from the apo-form/heme complex triggers the structural collapse of the protein resulting in the exposure of internally packed residues. Figure 3.2 B shows that the native cytochrome C at 0 hour exhibited two peaks at 520 nm and 550 nm which is characteristically shown by the reduced form of the protein [181], i.e., $Fe^{2+}$ form [182]. However, cytochrome C at 192 hour showed an oxidized pattern, i.e, $Fe^{3+}$ form [182]. Presumably, the attainment of $Fe^{3+}$ form attracted the $Cl^-$ ions of the environment and resulted in the ferroprotoporphyrin conversion to chloro-ferriprotoporphyrin. The porphyrin ring emits fluorescence through excitation-emission at 400 nm/662 nm [183], with a specific indication of presence of chloro-ferriprotoporphyrin with enhanced fluorescence at 662 nm [184]. Figure 3.2 C shows time-dependent fluorescence recorded at 662 nm which showed gradual increment of porphyrin fluorescence which confirmed the aforementioned speculation. Figure 3.2 D shows an illustration of the possible events where gradual dissociation of heme and exposure of aromatic residues (Figure 3.1 C) on the surface took place, as the supramolecular assembly of the network progresses.

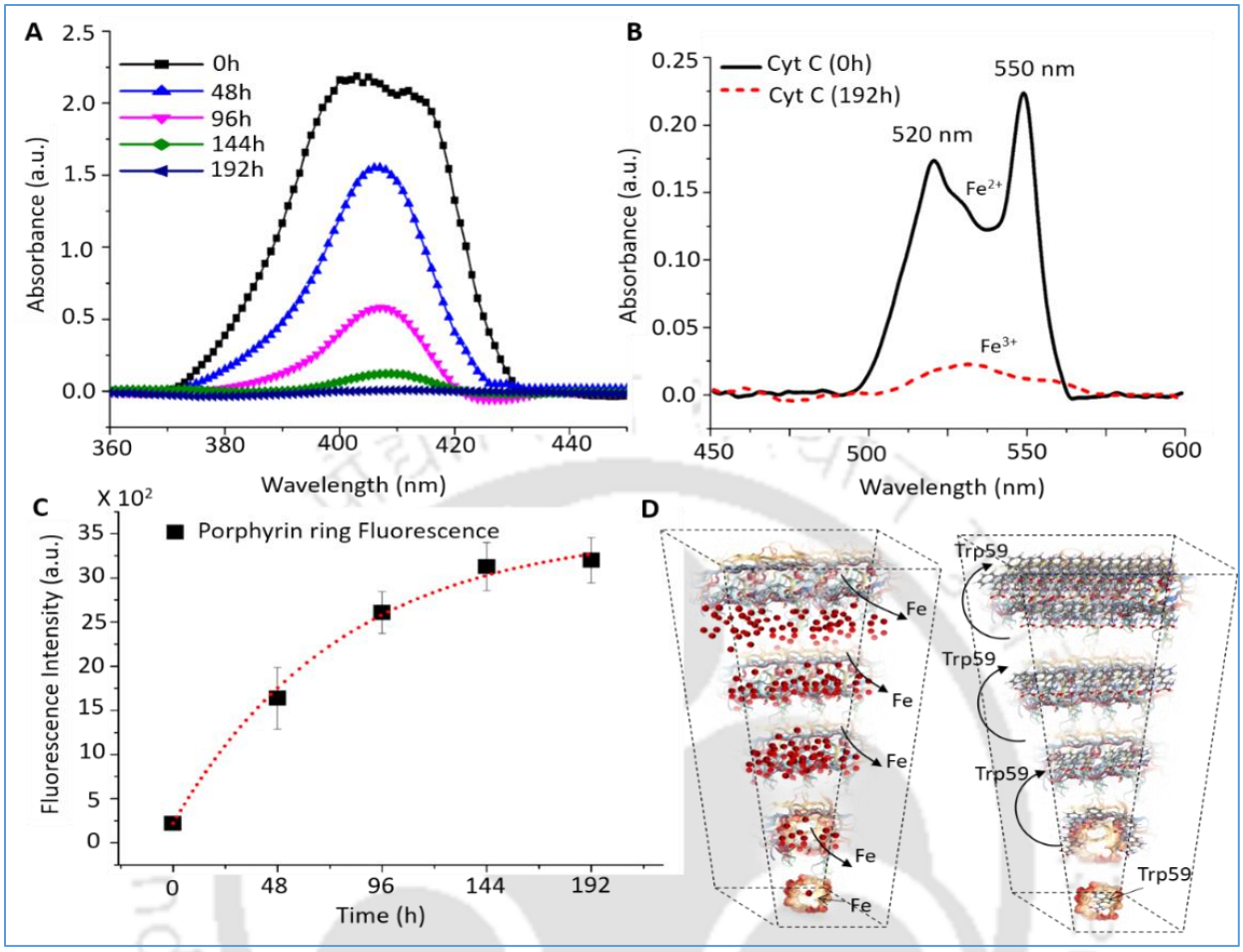


**Figure 3.2.** (A) Time dependent absorbance spectra of cytochrome C incubated at 75ºC , pH 9 for 192 hours, displaying the characteristic soret band; (B) Absorbance spectra of cytochrome C suggesting the conversion of $Fe^{2+}$ to $Fe^{3+}$ form with increase in incubation time; (C) Time-dependent fluorescence increment of porphyrin ring at 400 nm/662 nm, which is indicative of the exposure of the porphyrin ring; (D) Illustration showing the gradual events of heme dissociation and aromatic residue exposure at the surface.

### 3.2.6 Computational studies predicted the nature of structural transitions

At first, the amyloidogenic regions of cytochrome C were predicted using Foldamyloid online server which is used to predict the residues that play an active role in the nucleation stage of amyloidogenesis. For cytochrome C, the software predicted that the residue stretch, 80-MIFAG-

84, was most prone to amyloidogenesis. Figure 3.3 A shows the profile values for the residue numbers which are set according to the threshold value (residues in blue are above the threshold levels indicative of individual amyloidogenic propensity, however, the amyloidogenic regions were evaluated according to clusters). Next, the folded and unfolded regions of cytochrome C were analysed using Foldunfold server which predicted that the aromatic amino acids, namely typtophan and tyrosine, are embedded in the folded structure of the protein. The above analysis has been shown in Figure 3.3 B where the blue dots represent the unfolded regions and the green dots represent the folded region. To be noted, Trp59 was predicted to be strongly embedded in the folded region whereas the tyrosine residues at positions 48, 67, 74 and 97 were either loosely folded or were predicted to be part of the unfolded portion of the protein. This implied that the increment in intrinsic fluorescence as amyloidogenesis progressed was predominantly given out by the tryptophan residue upon unfolding. In par with this interpretation, the H-protection analysis (Figure 3.3 C) predicted that the Trp59 residue is most likely an unprotected residue prone to hydrogen-deuterium exchange in the protein chain (the residues shown in blue are protected, and residues in green are unprotected). However, most of the tyrosine residues were predicted to be protected residues. Therefore, it could be speculated that tyrosine residue played an insignificant role in amyloidogenesis of the protein, and further suggested the prime role of Trp59 residue as mentioned in earlier sections. Next, the IsUnstruct server predicted residues (Figure 3.3 D) involved in the structured and unstructured regions of cytochrome C (residues in blue represent unstructured regions and residues in green represent structured region). The IsUnstruct analysis revealed that the Trp59 residue is strongly involved in the structured region. Therefore, it could be speculated that Trp59 residue played an important role in the destabilization or collapse of the

cytochrome C structure. To be noted, it has been mentioned in section 3.4 that presumably there was a link between the collapse of heme region and increment in the intrinsic fluorescence.

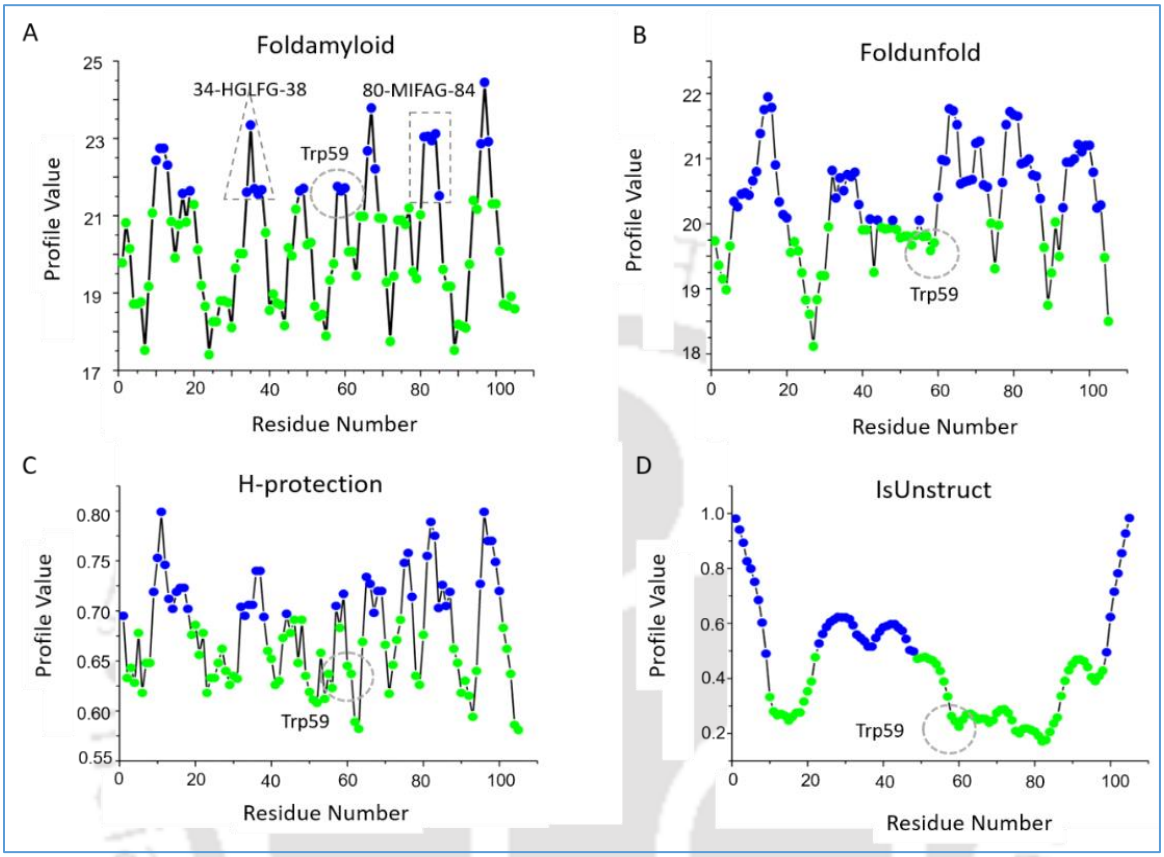


**Figure 3.3.** (A) Foldamyloid prediction of amyloidogenic regions of cytochrome C ((residues in blue are above the threshold levels indicative of individual amyloidogenic propensity, however, the amyloidogenic regions were evaluated according to clusters); (B) Foldunfold analysis of the folded and unfolded regions of cytochrome C (the blue dots represent the unfolded regions and the green dots represent the folded region); (C) H-protection analysis where residues shown in blue are protected, and residues in green are unprotected; (D) IsUnstruct analysis showing the structured and unstructured regions of the protein (residues in blue represent unstructured regions and residues in green represent structured region).

This observation prompted to probe into the organization of the heme in the cytochrome C structure. LIGPLOT + V.2.2 was employed to predict the physicochemical interactions of heme with cytochrome C residues. Figure 3.4 shows the LIGPLOT analysis that predicted that the Trp59 residue binds to the heme region with H-bonding. Furthermore, residues 80,81 and 82 that were predicted as amyloidogenic in Figure 3.3 A, were also predicted to be in interaction with the heme group. Therefore, it could be speculated that the collapse of the heme group results in the destablization of the interactions of heme-Trp59 resulting in simultaneous exposure of Trp59. This is in agreement with the observation detailed in section 3.4.

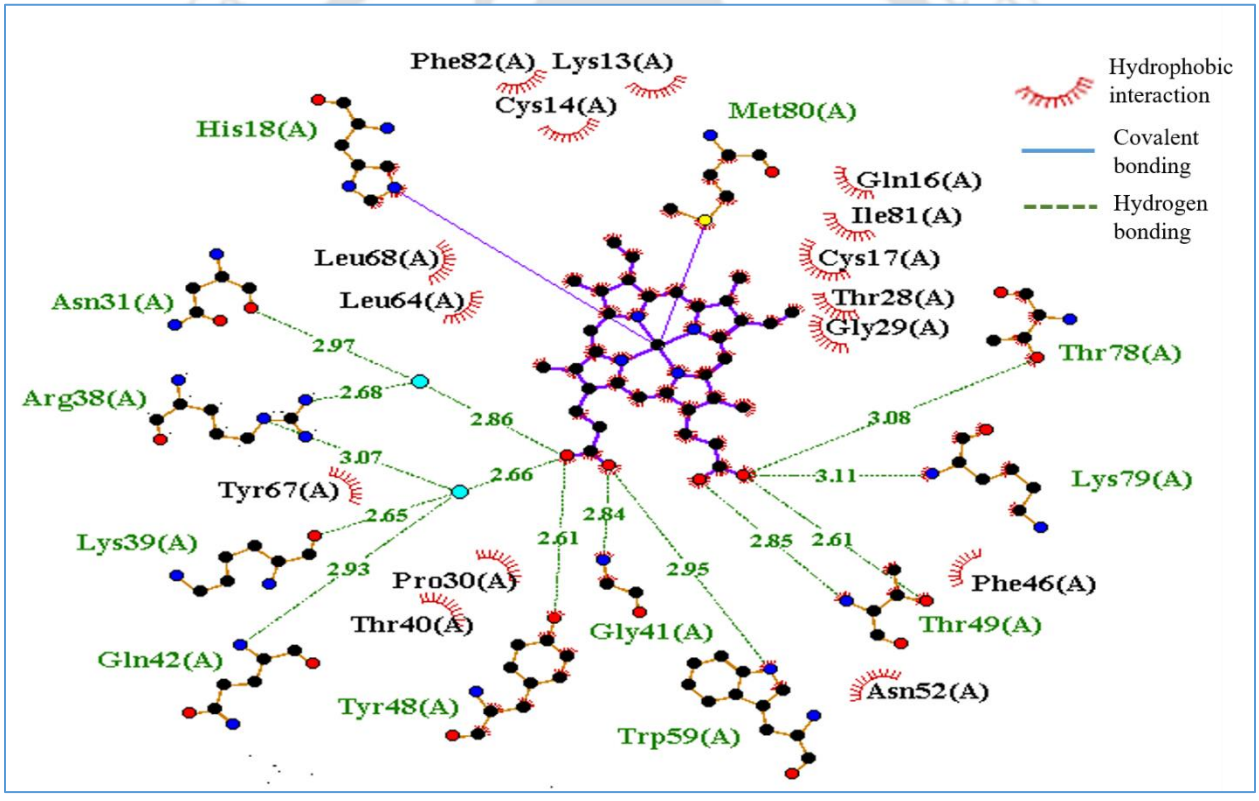


**Figure 3.4**. LIGPLOT analysis of heme in complex with the amino acids of the cytochrome C native structure. His18 and Met80 was predicted to establish covalent bonds with heme, whereas, the Trp59 residue was predicted to form a hydrogen bond of 2.95 Å. Also, amyloidogenic residues like Ile81 and Phe82 were predicted to establish hydrophobic interaction with heme.

### 3.2.7 Electron microscopy revealed macromolecular amyoid network formation and ultra-small nanoparticles integrated in the network

The morphology of the self-assembled cytochrome C amyloids was observed through FETEM imaging which revealed the formation of an intricate cross-linked network with size extending to several micrometres.

The representative images of the intricate macromolecular network taken at 10,000X magnification has been displayed in figure 3.5 A, 3.5 B and 3.5 C. The FETEM images exhibited that the amyloids formed by cytochrome C are highly branched, highly intercalated or cross-linked, and randomly oriented. Also, the existence of extensively distributed pores was detected across the network that appeared like white dots in the aforementioned images. The porous morphology has been found to be a desired property in designing amyloid hydrogel. This morphology of cytochrome C was found to be unlike the long fibrillar species reported earlier [174], rather the morphology was similar to the highly intercalated organizations reported by Nucara et al.[176].

Furthermore, the cytochrome C amyloid network was observed under higher magnification of 50,000X in High-Contrast mode which revealed that there were nanosized dense bodies were integrated within the amyloid network (Figure 3.5 D and 3.5 E). The dense bodies were not found in the background but appeared to be solely presented within the amyloid network. Observing the dense-regions of the amyloid network at further high-magnification, it was revealed that ultra-small nanoparticles were extensively distributed and adhered on the surface of the amyloid network (Figure 3.5 F).

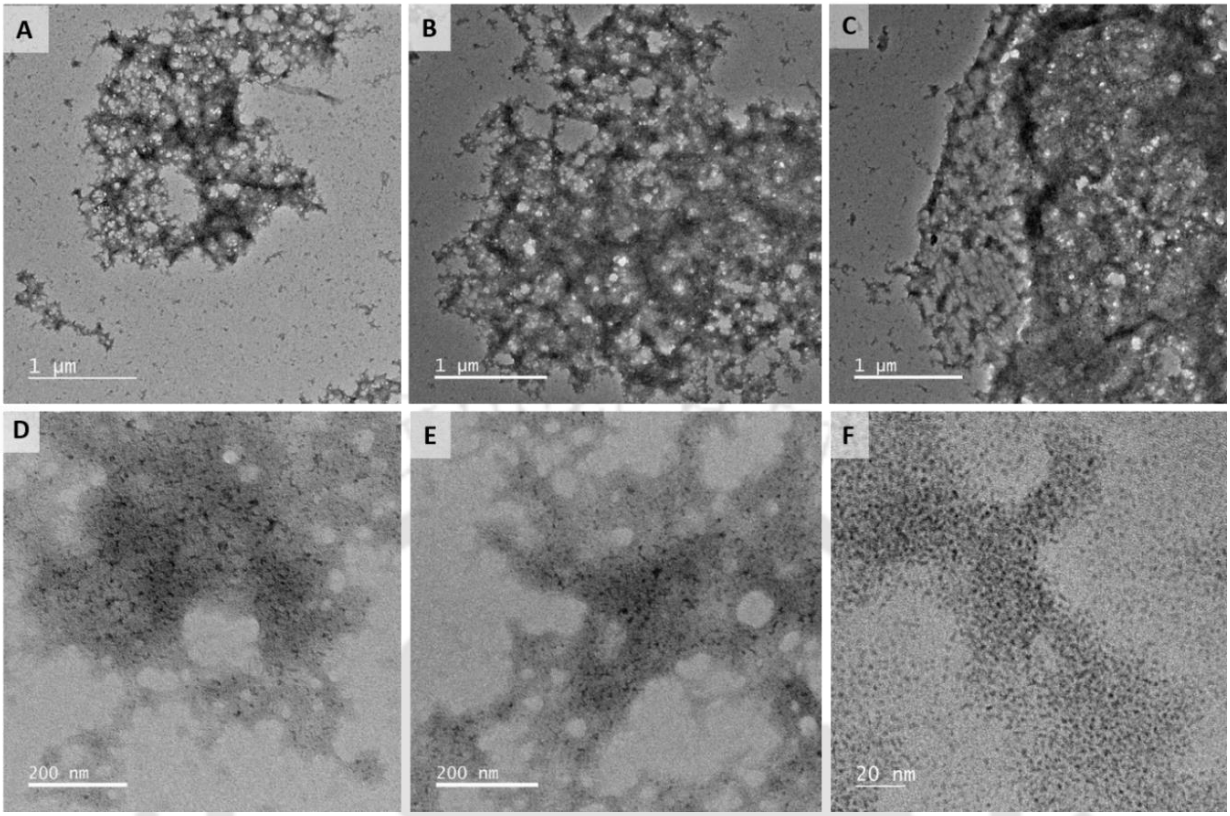


**Figure 3.5.** (A), (B) and (C) Representative FETEM images (10,000X) of intricate amyloid network formed by cytochrome C at 75ºC, pH 9 for 192 hours; (C) and (D) Representative images of nanosized dense bodies integrated into the amyloid network captured at 50,000X magnification in high Contrast mode; (F) Representative image of the ultra-small nanoparticles adhered on the amyloid network.

### 3.2.8 High-Resolution Transmission Electron Microscopy (HRTEM) analyses of the ultra-small nanoparticles

HRTEM analysis of the ultra-small nanoparticles was performed under 800 K magnification, and the representative image is displayed as Figure 3.6. The HRTEM image shows the lattice fringes and also displays the size of the individual ultra-small nanoparticles, ranging from 1.91 to 2.95 nm. Inset 1 shows the FFT image of the selected area (shown within yellow dotted rectangle) with diameter of 5.43 $nm^{-1}$, which corresponds to a d-spacing value of 0.36 nm [$(5.43/2)^{-1}$]. Inset 2

shows the IFFT image of the lattice showing the direction of the plane. Inset 3 shows the SAED pattern of the ultra-small nanoparticles showing polycrystalline nature with d-spacing values, 0.36 nm, 0.22 nm, and 0.18 nm, corresponding to the planes (012), (113), (024) and (300) of $Fe_2O_3$, respectively, and 0.30 nm and 0.14 nm corresponding to the (220) and (440) planes of $Fe_3O_4$, respectively [185]. Interestingly, a d-spacing of 0.34 nm was also detected in some of the nanoparticles which is typical of carbon shells [186], indicating the carbon content of heme.

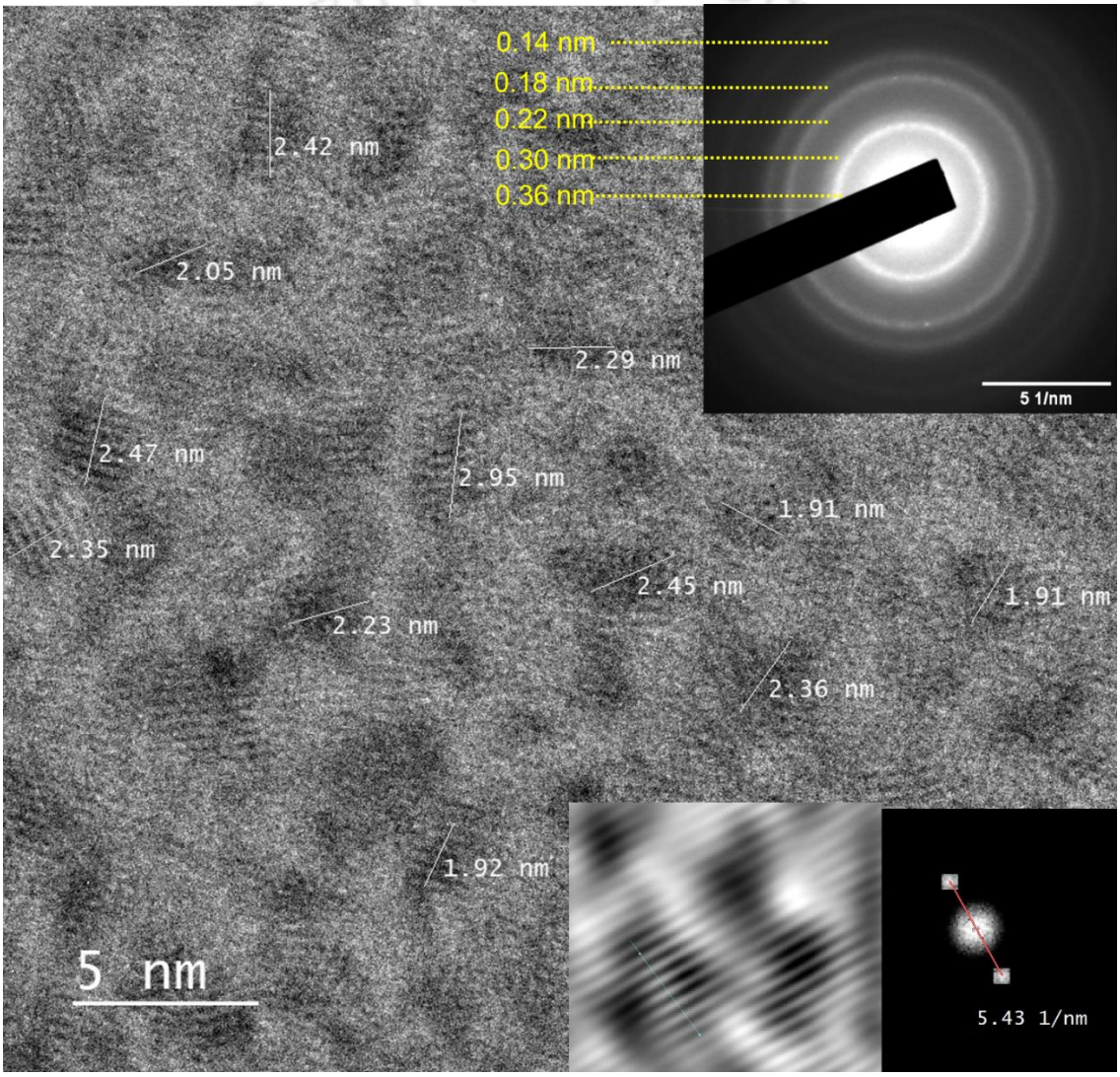


**Figure 3.6.** HRTEM image taken at 800 k magnification showing the lattice fringes and the size of the individual ultra-small nanoparticles, ranging from 1.91 to 2.95 nm. Inset 1 shows the FFT

image of the selected area (shown within yellow dotted rectangle) with diameter of 5.43 $nm^{-1}$, which corresponds to a d-spacing value of 0.36 nm. Inset 2 shows the IFFT image of the lattice showing the direction of the plane. Inset 3 shows the SAED pattern of the ultra-small nanoparticles showing polycrystalline nature with d-spacing values, 0.36 nm, 0.22 nm, and 0.18 nm, corresponding to the planes (012), (113), (024) and (300) of $Fe_2O_3$, respectively, and 0.30 nm and 0.14 nm corresponding to the (220) and (440) planes of $Fe_3O_4$.

### 3.2.9 Elemental Mapping of the cytochrome C amyloid network by Scanning Transmission Electron Microscopy (STEM)

The cytochrome C amyloid network with its intricately adhered ultra-small nanoparticles were subjected to STEM analyses to probe into the probable elements present. Exclusively for the cytochrome C amyloid, the anticipated elements were carbon, oxygen, nitrogen and sulfur, as constituents of the amyloid network must be amino acids of the protein. The presence of iron or Fe from heme could not have constituted the amyloid due to the dissociation of heme from the protein. However, Fe could be detected from the ultra-small nanoparticles under the speculation that dissociated heme resulted in the formation of the ultra-small nanoparticles, and because they remained bound to the amyloid network, the Fe map should superimpose with the edges of the amyloid. In short, detection of Fe in the amyloid network could be considered as evidence that the bound ultra-small nanoparticles were formed of Fe from the dissociated hemes.

Figure 3.7 A represents a portion of the amyloid network which was scanned in STEM mode for mapping the aforementioned elements. To be noted, the elements were expected to lie within the matrix of the shown amyloid network. Figure 3.7 B shows the placement of nitrogen (presented by blue dots) which specifically lies within the boundaries of the structure shown in 3.7 A, thus confirming the network to be proteinaceous amyloid. Next, sulphur (represented by yellow dots)

was identified and mapped, which was found to be localized within the proteinaceous boundaries (3.7 C). The regions showing sulphur could be considered as the regions where cysteine residues were packed in the amyloid network. Next, chlorine Map (3.7 D) confirmed that the $Cl^-$ ions of the buffer solution were bonded to ferriprotoporphyrins, and placed in the amyloid. Next, the Fe atoms (represented by red dots), whose fate after destabilization was the prime question, was scanned and mapped (3.7 E). Herein, it was observed that the Fe Map coincided with the edges of the cytochrome C amyloid which suggested that the Fe still remained as an integral part of the amyloid network. The percentage of the elements are listed in Table 3.1.

**Table 3.1.** Elemental composition of cytochrome C amyloid network through EDS.

| Element | Weight % | Atomic % |
|---|---|---|
| C | 74.54 | 77.37 |
| N | 6.29 | 5.83 |
| O | 14.25 | 15.62 |
| S | 2.25 | 0.22 |
| Cl | 2.55 | 0.93 |
| Fe | 0.12 | 0.03 |

As Fe could not be attributed by the apo form of the protein which formed the amyloid, the presence could be possibly attributed to the ultra-small nanoparticles which were observed to be intricately linked to the amyloid surface. The conglomeration of chlorine and Fe in the amyloid reaffirmed the formation of chloro-ferriprotoporphyrin, which was the only candidate to have

possibly formed the ultra-small nanoparticles. Similar self-organized nanoparticles composed of porphyrins of size 2-3 nm has been previously reported [178].

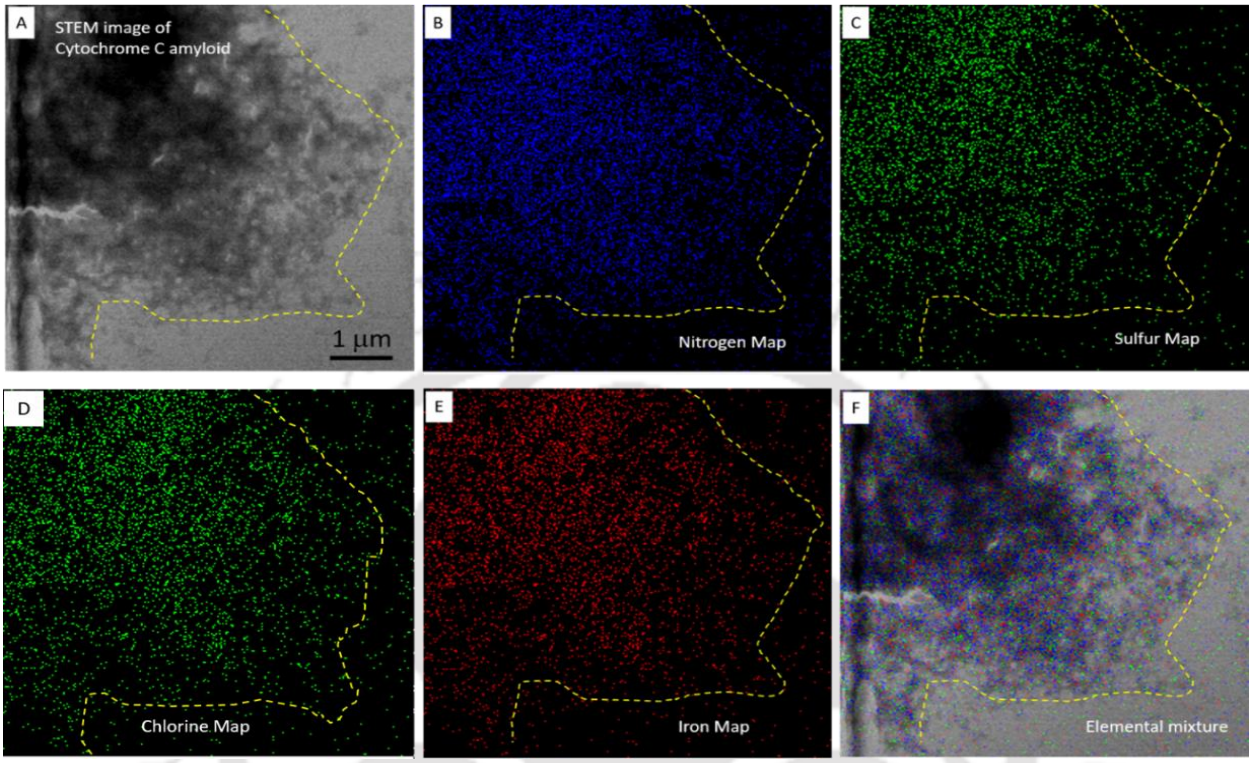


**Figure 3.7.** (A) Representative bright-field image of cytochrome C amyloid network scanned for elemental mapping; (B) The detected presence of nitrogen (N) (blue dots) within the map of the amyloid network; (C) The detected presence of sulphur (S) (yellow dots) within the map of the amyloid network; (D) Chlorine Map; (E) The detected presence of iron (Fe) (red dots) within the map of the amyloid network; (F) The superimposition the elemental maps on the bright-field image of the cytochrome C amyloid network.

Also, it has been previously mentioned that the intrinsic fluorescence (Figure 3.1C) emitted by the cytochrome C amyloid did not corroborate with trend of ThT and ANS fluorescence emissions which are suggestive of the exposure of aromatic hydrophobic residues. The intrinsic fluorescence

was found to have saturated about 1/4$^{th}$ of the total experimental time, unlike ThT and ANS fluorescence. This saturation of the intrinsic fluorescence presumably occurred due to a fluorescent nature of the ultra-small nanoparticles. Therefore, the ultra-small particles were named as Fe-containing Quantum Dots (FeQDs).

### 3.2.10 MALDI-TOF/MS analysis of the amyloidogenic events of bovine heart cytochrome C

It has been shown in the previous sections that under the amyloidogenic conditions of the present study, cytochrome C underwent a high degree of self-oxidation which resulted in the cleavage of the Met80-heme bond, unfolding, and binding of $Cl^-$. This resulted in the conversion of ferroprotoporphyrin to chloro-ferriprotoporphyrin, which organized into FeQDs. However, it wasn't conclusive whether the FeQDs formed with the completely dissociated heme, or formed through onsite reorganization with heme loosely bound through the thioether bonds at Cys14 and Cys17. The said thioether bonds are highly stable in cytochrome C, but cleavage of the thioether bonds is required for the release of apoprotein and subsequent amyloidogenic events.

It has been established that protein oxidation results in the fragmentation of proteins and formation of protein-protein linkages [187]. As cytochrome C was found to undergo oxidation as time of incubation progressed, MALDI-TOF/MS analysis was done to probe into the speculation whether fragmentation occurred, which is also an evidence for the cleavage of thioether bonds [188].

Figure 3.8 A shows the MALDI-TOF/MS plot of cytochrome C after 12 hour incubation, where a single prominent peak at ~12363 Da was observed which corresponds to the cytochrome C monomer. However, at 48 hour with the progress of oxidation events, the protein was found to undergo fragmentation, showing additional peaks at ~6150 Da and ~5456 Da (Figure 3.8 B).

The possible fragments that could most presumably generate the aforementioned masses are as follows:

*1-MGDVEKGKKIFVQK**(C14)**AQ**(C17)**HTVEKGGKHKTGPNLHGLFGRKTGQAPGFSYTD-51 (~5519 Da)*

*52-ANKNKGITWGEETLMEYLENPKKYIPGTK**(M80)**IFAGIKKKGEREDLIAYLKKATNE-105 (~6203Da)*

Certainly, there are other possibilities too other than the aforementioned fragments, but however might the fragments be arranged, the Cys14/Cys17 residues and Met80 residue would always lie on different fragments. This is only possible when the complete split of heme from the protein had taken place, resulting in one completely free fragment containing the cysteine residues, and another containing the methionine residues.

At 48 hour, there was also a large fraction of monomeric cytochrome C, which indicated that the fragmentation of the protein had initiated around 48 hour . Next, the MALDI-TOF/MS plot of cytochrome C after 192 hour revealed that the monomeric fraction had significantly declined and an extensive population of smaller fragments grew with m/z values of ~1686 Da, ~3103 Da, ~3887 Da, ~5212 Da, and ~6488 Da (Figure 3.8 C). This indicated that the oxidation events occurring in the present study resulted in extensive fragmentation of the protein, causing the different stretches containing cysteine residues and methionine residues to split. Subsequently, the aggregation of the protein was triggered by the interaction of the fragments. Thus, the oxidation of the protein and extensive fragmentation of were the prime events of the aggregation pathway.

This also suggested a complex interplay at work, of Met80-heme bond cleavage, formation of chloro-ferriprotoporphyrin, fragmentation of the protein, cleavage of thioether bonds, and subsequently formation of cytochrome C aggregates and reorganization of heme to FeQDs.

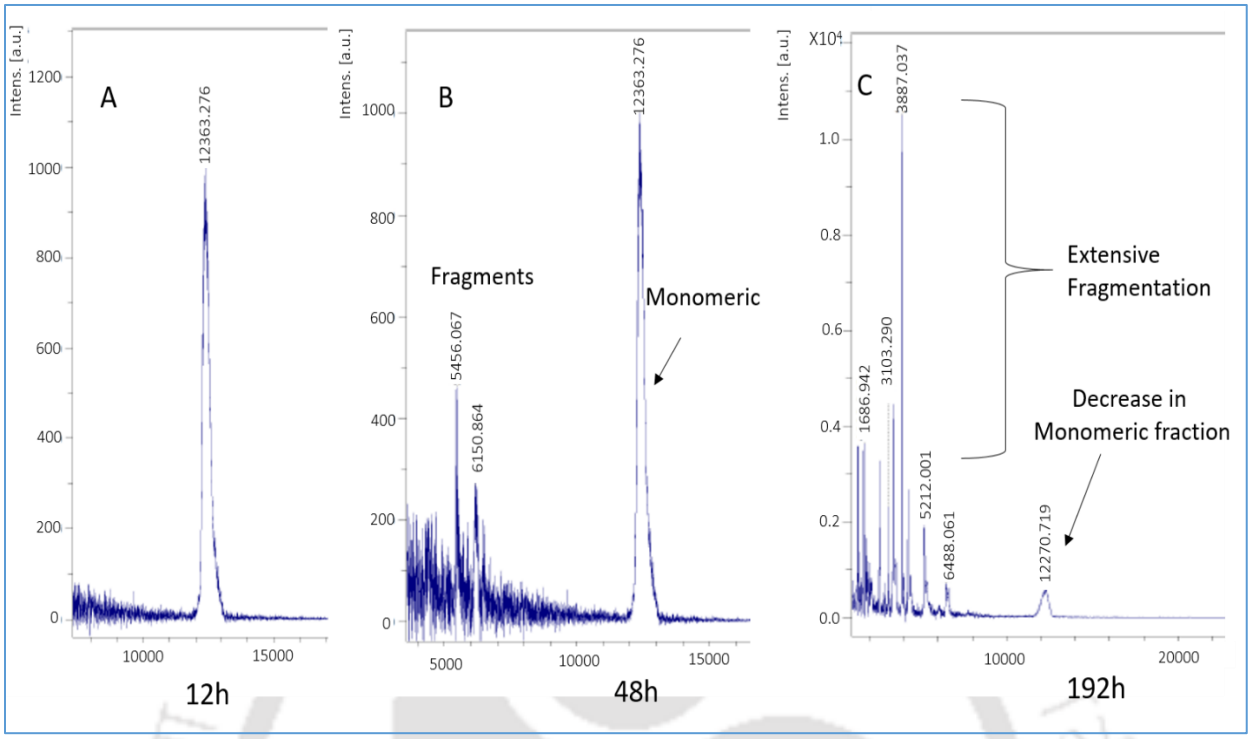


**Figure 3.8**. (A) MALDI-TOF/MS plot of bovine heart cytochrome C after 12 hour incubation; (B) 48 hour incubation; (C) 192 hour incubation.

However, the molecular weight of monomeric bovine heart cytochrome C in phosphate buffer (pH 9, without $Cl^-$) was found to be ~12326.43 Da (Figure 3.9 A) which is close to the reported molecular weight 12327 Da). This meant that there was a ~36 Da extra mass in the 12 hour sample. Also, cytochrome C incubated in phosphate buffer (pH 9, without $Cl^-$) showed negligible change of molecular mass around 12329.78 Da upon incubating at the experimental conditions of the study for 12 hour (Figure 3.9 B).

Furthermore, the binding of a $Cl^-$ to form the chloro-ferriprotoporphyrin which contributed ~35 Da to this extra mass was confirmed by a slight blueshift of the $\lambda_{max}$ in the absorbance spectra of the cytochrome C treated for 12 hour than the untreated protein (Figure 3.10 A). The blue-shift was presumably due to the binding of $Cl^-$. Speculatively, it is possible that the cleavage of the

Met80-heme bond made the porphyrin core more accessible to the $Cl^-$ attack, which might have been an additional trigger for the cleavage of C-S thioether bonds, as reported [189].

Also, there was a conformational change at the Trp59 position of the protein at 12 hour which was found to be in the exponential phase of Trp59 fluorescence (Figure 3.1 C), whereas the untreated protein showed negligible change of Trp59 fluorescence at 12 hour (Figure 3.10 B). Nevertheless, no evidence was found for the complete dissociation of heme through the cleavage of thioether bonds at 12 hour.

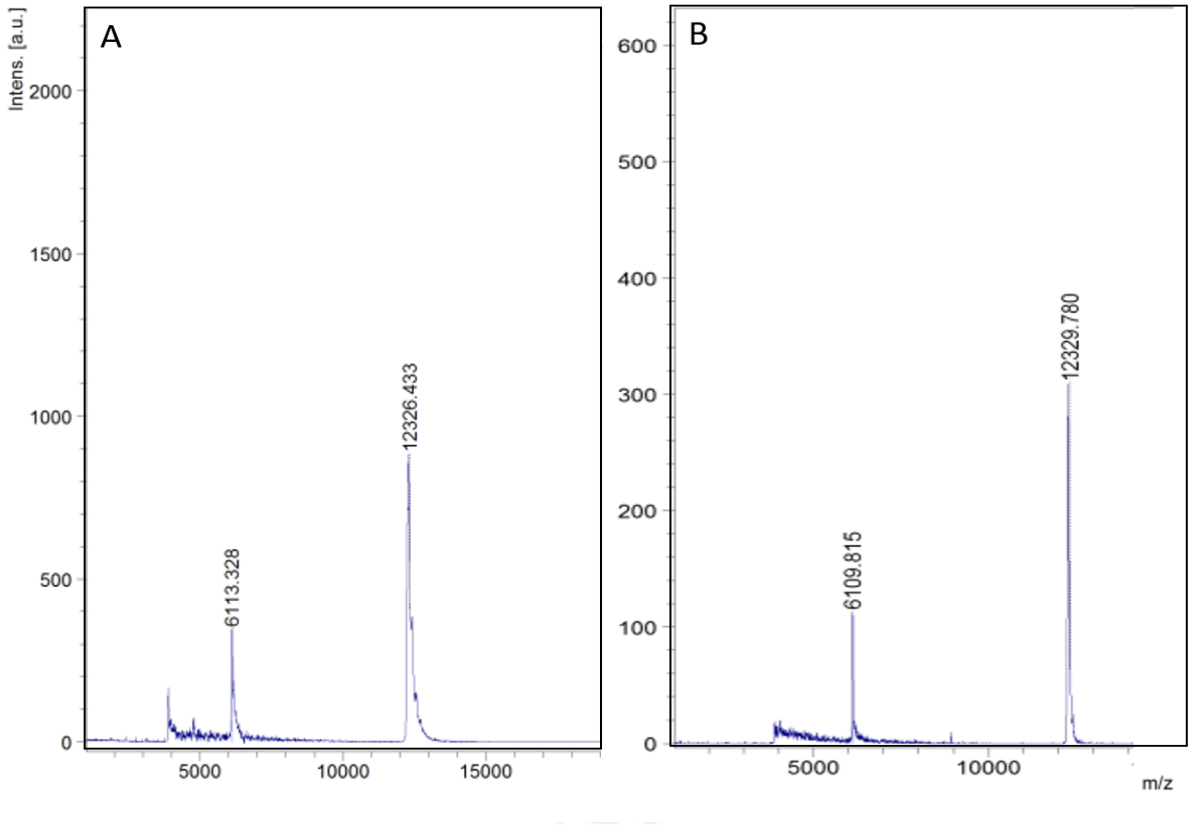


**Figure 3.9:** (A) MALDI-TOF/MS spectra of untreated Bovine Heart cytochrome C in phosphate buffer at pH 9 (without $Cl^-$); (B) MALDI-TOF/MS spectra of Bovine Heart cytochrome C in phosphate buffer (without $Cl^-$) incubated at pH 9 and 75ºC for 12 hour.

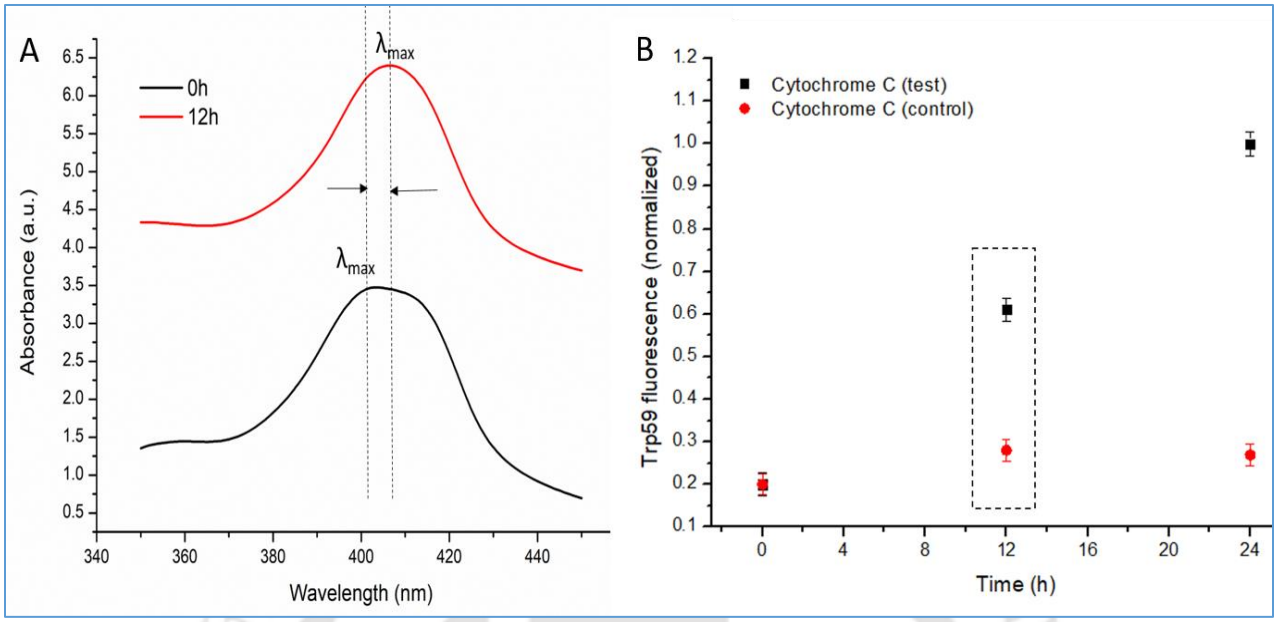


**Figure 3.10:** (A) Absorbance spectra of cytochrome C at 0 hour in comparison with 12 hour. There was a shift of $\lambda_{max}$ ; (B) Trp59 fluorescence for cytochrome C (test sample, i.e., incubated at the experimental condition), and cytochrome C (Control) without any treatment.

### 3.2.11 Rheological characterization of FeQD-decorated cytochrome C amyloid and its potential towards cell adhesion and proliferation platform

Next, strain sweep was conducted for the native protein, i.e. cytochrome C control sample (0 hour) and final test sample (192 hour) or the β-sheet rich amyloid network, in order to determine the change in the rheological characteristics. It was observed that the native protein exhibited consistent viscous nature which was evident from the elevated values of loss modulus (G") over storage modules (G') (Figure 3.11 A). However, the amyloid network of cytochrome C exhibited a deviant nature from the native form of the protein. The values of G' were elevated than G" in the initial stage which implied that the amyloid network was of insoluble and elastic nature, thereby, it exhibited gel nature. However, a crossing over of G'/G" was observed as strain was increased, which implied that upon increased strain the cytochrome C amyloid network underwent a gel to

liquid transition (Figure 3.11 B). Such transition is a lucrative feature which can be further explored to design amyloid hydrogels with FeQD-decorated cytochrome C amyloid network. Nonetheless, the nature of the FeQD-decorated cytochrome C amyloid contained gel-like properties.

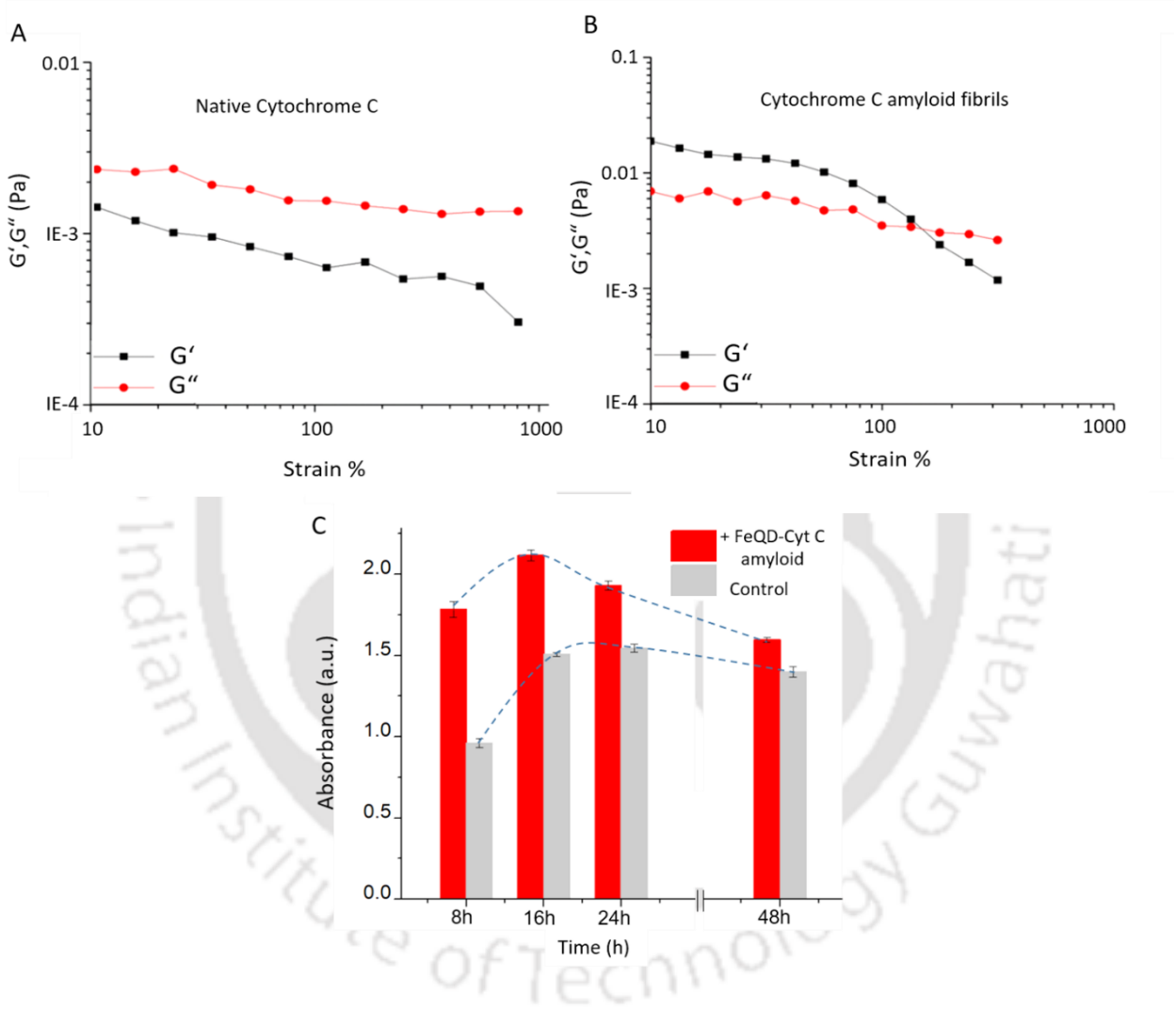


**Figure 3.11. (A)** Viscous nature of native cytochrome C exhibiting G"> G'; (B) Gel-to-liquid transition of cytochrome C amyloid network exhibiting crossing over of G'/ G"; (C) MTT assay of BHK-21 fibroblasts grown in presence of FeQD-decorated cytochrome C amyloid (red bars) and serum-free media which served as the control (Light-gray bars).

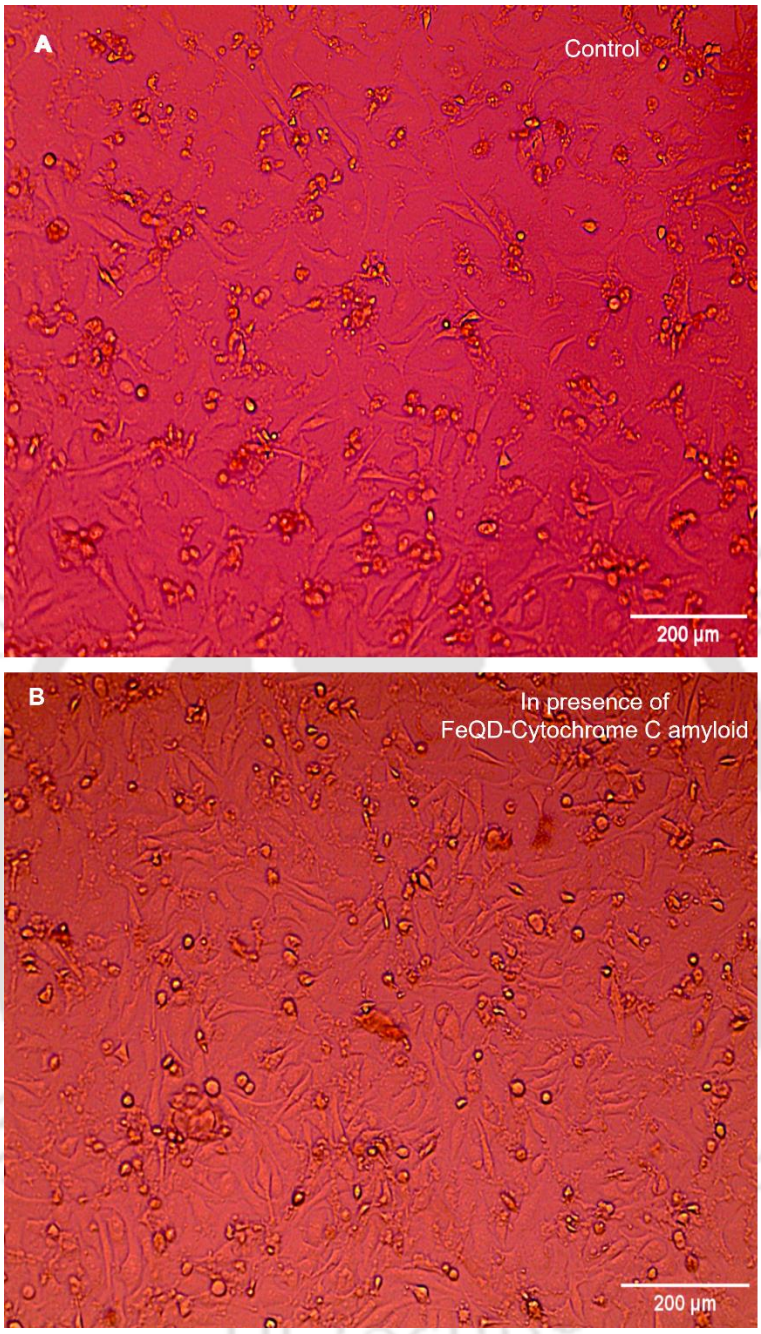


**Figure 3.12.** Microscopic images of BHK-21 fibroblasts; (A) Control; (B) in presence of FeQD-decorated cytochrome C amyloid.

Next, BHK-21 cells that were seeded in serum containing media and grown for 24 hours were treated with, (i) serum free Media as control, and (ii) with 5% (v/v) dilution of FeQD-decorated

cytochrome C amyloid (test) sample. It was observed that the presence of the gel-like cytochrome C amyloid promoted the growth of BHK-21 fibroblasts significantly for the first 16 hours of the total incubation, in comparison to the control (Figure 3.11 C). The MTT assay indicated that there was no trace of cytotoxicity of the amyloid to BHK-21 fibroblasts, rather it presumably served for a rich source of nutrients. The growth pattern of the BHK-21 fibroblasts was found to be augmented in presence of the amyloid, in comparison to the BHK-21 cells grown in serum-free media (control). The microscopic images of the fibroblasts revealed that there was a mixed species of suspended and adherent cells (Figure 3.12 B ), however, showing an augmented growth pattern without any cytotoxicity.

### 3.3 Discussion

The structure and function of cytochrome C, which plays an important role in the electron transfer chain of aerobic and anaerobic respiration, is maintained by the complex between the *apo* protein and the prosthetic group, heme. The prosthetic group retains its integral position through coordination complexes with His18 and Met80, and also through hydrogen bonding with densely packed residues like Trp59. However, in an oxidation event, the cleavage of Met80-heme iron bond has been reported to break [190]. Indeed, the association of the prosthetic group and the *apo* protein is the prime essential factor for maintenance of the structure, and the destabilization of the heme group can presumably cause the unpacking of aforementioned amino acids, consequently loss of structure and function. However, there appears to be a lack of investigation on heme delocalization, amyloid network formation and subsequent fate of heme after dissociation event, in proteins like cytochrome C. Therefore, the present study aimed at understanding the fate of cytochrome C and heme after destabilization of the *holo* protein in amyloidogenic condition.

Firstly, cytochrome C was incubated at 75°C in Tris-HCl buffer maintained at pH 9 for an extended period of 192 hour, i.e., 8 days. The induced amyloidogenesis resulted in the loss of the characteristic red color of cytochrome C solution which is rendered by the integrated Fe-containing heme group. The visible observation resulted in the speculation of structural changes occurring at the sites of heme-protein association [191]. The initial investigation depended on spectroscopic analyses on the characteristic red color of cytochrome C and fluorometric analyses on the intrinsically fluorescent Trp59 residue which remains bound to the Fe-containing prosthetic group by hydrogen bonding. Therefore, it could be contemplated that changes in the heme group would also result in the changes of fluorescence emission by Trp59 as it might also lose its conformational position. Next, heme dissociation was presumed to result in the unfolding of cytochrome C which is responsible for the exposure of hydrophobic residues. Subsequently, hydrophobic exposure and increased intermolecular interactions is known to drive the amyloidogenic formation of protein aggregates. The hydrophobic exposure was monitored through ANS-dye binding assay and increase in β-sheets was monitored by ThT binding assay. It was observed that the amyloid network exhibited increment in β-sheets which was evident through the steep increase of ThT fluorescence (1A). ANS fluorescence corroborated with ThT fluorescence trend showing a gradual exposure of hydrophobic residues (1B). CD spectroscopy further confirmed the drastic structural transition of cytochrome C from a highly helical structure to a completely β-sheet rich structure (1D). This α-helix to β-sheet transition is the hallmark of amyloidogenesis.

Next, through computational studies it was predicted that hemeinteracting Trp59 is an unprotected residue from to hydrogen-deuterium exchange, albeit its position in the strongly folded region of the protein. In relation, Met80 was predicted to lie on the amyloidogenic region of the protein, i.e., the nucleation of amyloidogenesis formation is most likely to begin around Met80. Therefore,

there was a clear correlation between heme, Met80 and Trp59 (3A-3D). In the native protein, heme causes the quenching of fluorescence of Trp59, however, it was found that Trp59 fluorescence gradually incremented with incubation time (1C). This suggested that Trp59 residues had moved away from the heme complex, and were placed on the surface of the amyloid network rendering an intrinsically fluorescent nature (1C).

In bovine heart cytochrome C, the heme group is linked to the apoprotein with His18 and Met80 through covalent bonding, according to the crystal structure of bovine heart cytochrome C reported by Mirkin et al [161]. The heme group exists in a hexacoordinated configuration with His18 and Met80 as two axial ligands. It has also been found in the LIGPLOT analysis shown in Figure 3.4. The Met80 residue according to the foldamyloid analysis falls under the amyloidogenic region of the protein, i.e., the initiation of amyloidogenesis takes place at Met80 residue. Again, Figure 3.2 B showed the oxidized form of cytochrome C during the amyloid formation, which further suggests that Met80-heme bond presumably broke due to oxidation event, as reported by Wang et al. [190]. This meant that the heme either dissociated completely, or remain loosely attached to the protein. Further, the amyloidogenic driving forces triggered the initiation of amyloidogenesis of cytochrome C from 80-MIFAG-84 region. Therefore, after the cleavage of Met80-heme bond, the apoprotein indulged into the forming cytochrome C amyloid network. Now, the next question was the fate of heme which is a porphyrin based molecule. One of the possibilities was pointed by the report of porphyrins self-organizing into nanoparticles [21].The porphyrin ring fluorescence recorded at 400 nm/662 nm was also found to increase significantly with time of incubation (2C). This indicated that porphyrin rings were in free state and presumably self-organized.

Thereafter, FETEM analyses revealed a striking macromolecular amyloid network extending up-to several micrometers (5A-5E) and the surface of the amyloid was decorated by ultra-small

nanoparticles (5F). Herein, it was speculated that the ultra-small nanoparticles could be the organized hemes. The HRTEM analyses of the ultra-small nanoparticles revealed they were well distributed in the macromolecular network with an approximate sizes ranging from 2-3 nm. Lattice fringes, characteristic of crystalline substances were clearly visible in the ultra-small nanoparticles with d-spacings, 0.36 nm, 0.22 nm, and 0.18 nm, corresponding to the planes (012), (113), (024) and (300) of $Fe_2O_3$, respectively, and 0.30 nm and 0.14 nm corresponding to the (220) and (440) planes of $Fe_3O_4$.

Also, elemental mapping deploying STEM analysis confirmed that Fe atoms were still integrated in the amyloid matrix. This was unexpected as heme was determined to be dissociated from the protein and subsequently lie detached from the amyloid network. In that case, it was expected that Fe atoms should have been found randomly distributed in the TEM grid. Also, heme in its singular form should remain invisible to the TEM, unless they are reorganized into structures in visible size range. Also, chlorine Map overlapped the Fe Map which indicated that $Cl^-$ ions also adhered with the amyloid network. This was possibly due to the conversion of ferroprotoporphyrin ($Fe^{2+}$ heme form) to ferriprotoporphyrin ($Fe^{3+}$ heme form) through oxidation (2B), opening avenue for $Cl^-$ ions to bind with the later and form chloro-ferriprotoporphyrin. With Fe atoms showing distinctly adhered to the amyloid matrix, presence of ultra-small nanoparticles with defined size and crystallinity, and enhanced fluorescence emitted by porphyrin rings, it was therefore confirmed that dissociated heme groups reorganized into the ultra-small nanoparticles with a fluorescent nature; hence, the ultra-small nanoparticles were termed as FeQDs. The sequential events are shown schematically in Figure 3.13.

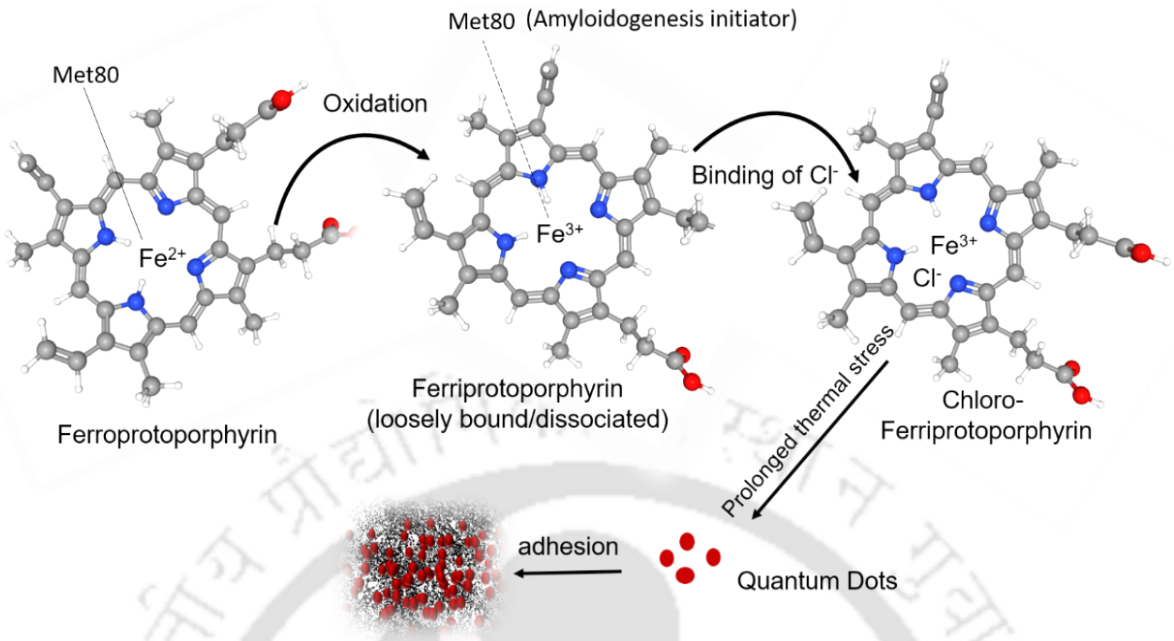


**Figure 3.13.** Schematic representation of the formation of FeQDs. Dissociation of heme resulted in the self-oxidation of cytochrome C, i.e., conversion of ferroprotoporphyrin to ferriprotoporphyrin (also reported by [175]). Self-oxidation results in the cleavage of Met80-heme bond of cytochrome C (also reported by [190]). The $Cl^-$ from the microenvironment binds to the ferriprotoporphyrin to form chloro-ferriprotoporphyrin, followed by reorganization of the porphyrin species to 2-3 nm quantum dots, named FeQD in the present study. The FeQDs then bind to the macromolecular network formed by the apo protein. Thus, FeQD decorated cytochrome C macromolecular network is formed.

The FeQDs were found to adhere to the amyloid matrix, which could be due to surface adsorption or perhaps the heme groups were loosely bound rather than completely dissociated resulting in onsite reorganization. The latter scenario is possible when thioether bonds at Cys14 and Cys17 were not cleaved, but the cleavage of Met80-heme bond propelled the unfolding and aggregation of the protein. However, MALDI-TOF/MS plots of the cytochrome C during the aggregation

process revealed that the protein oxidation resulted in extensive fragmentation of the protein, with the cysteine residues lying in different fragment than the Met80 residue. It is possible only when heme had completely dissociated, as heme is the nexus between the cysteine residues and methionine residue which otherwise occupy different subunits of the protein. There are number of factors which could lead to the cleavage of the thioether bonds: (i) cysteine and methionine are both susceptible to oxidation for the presence of S atoms, and electron transfer has been reported to cleave thioether bonds, which appears to be the most possible and predominant role player [187,192]. Additionally, (ii) chloride ion binding has also been reported to particularly influence the C-S bond cleavage which could also be speculated to play a role in the cleavage [40], (iii) Conformational changes trigger thioether bond cleavage by making them more accessible [188], (iv) Also, the bond lengths of the Cys14 and Cys17 thioether bonds in bovine heart cytochrome C are relatively large compared to other cytochromes (according to the reports elucidating the three-dimensional structure of bovine heart cytochrome C) [161,193]. Therefore, the dissociation of the thioether bonds in bovine heart cytochrome C is comparatively facile. It has been reported in earlier studies that thioether bonds with cysteine is dependent on reducing environment [194]. Presumably, the oxidizing events of the present study had rendered the Cys14 and Cys17 thioether bonds of bovine heart cytochrome C more susceptible to cleavage.

However, as the thioether bonds of cytochromes has been found to be highly variable, evolving and elusive according to the source of the protein [194], further studies are required to illuminate the mechanisms with more clarity. The effect of the experimental conditions of the present study may or may not be the same with other forms of cytochrome C, which needs extensive scrutiny. As for the present study, the apoprotein generated after heme dissociation, and subsequent

fragmentation of the apoprotein appears to be quintessential for the formation and surface sorption of the FeQDs.

Cytochrome C holo form thus created two kinds of material after the rupture of the three-dimensional functional structure: (i) FeQDs though reorganization of heme, and (ii) macromolecular amyloid network from the protein fragments of apocytochrome C. Upon a strain sweep analysis, it was observed that the FeQD-decorated amyloid network exhibited gel-like property (8B). The presence of FeQDs in the amyloid network could be further explored to design potential magnetic amyloid networks through further studies relying on the intrinsic magnetic and electrical properties of cytochrome C [177,195,196]. The ability of the FeQD-decorated cytochrome C amyloid to promote cell growth was investigated with BHK-21 fibroblasts. The presence of FeQD-decorated cytochrome C amyloid solution significantly promoted the growth of BHK-21 fibroblasts in comparison to the control samples and MTT assay showed no trace of cytotoxicity (8C-8D).

### 3.4 Conclusion

Under high temperature and elevated pH, the three-dimensional functional structure of *holo* form of cytochrome C drastically ruptures due to the dissociation of its prosthetic group, heme. The dissociation of heme was engendered by self-oxidation of the thioether bonds at Cys14 and Cys17, and Met80-heme bond, and destabilization of coordination complexes with His18. Also, the self-oxidation resulted in the fragmentation of the released apoprotein, which interacted amongst each other to form a cytochrome C amyloid network. As a result of the aforementioned events, two distinct structural entities were reorganized, (i) a macromolecular cytochrome C amyloid network formed by supramolecular organisation of the protein fragments, and (ii) fluorescent quantum dots (FeQDs) formed by the reorganization of the dissociated heme, and chemical conversion from

ferroprotoporphyrin to chloro-ferriprotoporphyrin. The fluorescent FeQDs were found to be highly crystalline in nature, and were found to be adsorbed on the amyloid network decorating its surface. The resultant FeQD-decorated cytochrome C amyloid network was observed to be porous, intrinsically fluorescent, large sized (micrometre range), highly branched, viscoelastic, biocompatible and capable of promoting BHK-21 fibroblast growth when added in the media. In conclusion, the study presents a highly simplified way to create FeQD-decorated amyloid network with an intrinsic fluorescent nature, that can be further explored to create smart materials for specialized applications.

# CHAPTER 4

## Modulation of Insulin amyloidogenesis by $Zn^{2+}$ ions and cellulosic nanomaterials

---

***Motivation***

*The supramolecular assembly of insulin in presence of $Zn^{2+}$ is a highly sensitive system and has been under investigation for decades for applications such as pharmaceutical formulations and biomaterial design. On the other hand, nanocellulosic materials are being explored for designing multicomponent platforms for their beneficial properties such as interactivity, biodegradability, and structural variation, to name a few. Thus, co-incubation of nanocellulosic material with insulin and $Zn^{2+}$ might open the possibility of developing a hybrid protein-cellulose system that can be used as a cell culture platform.*

---

Parts of this chapter has been published in the 'Journal of Molecular Liquids' as following:

*'Karmakar, Srijeeb, Tabli Ghosh, Arjun Sankhla, Sayan Bhattacharjee, and Vimal Katiyar.* ***"Insulin biomolecular condensate formed in ionic microenvironment modulates the structural properties of pristine and magnetic cellulosic nanomaterials."*** *Journal of Molecular Liquids 363 (2022): 119580.'*

## Abstract

This chapter reports the formation of a unique biomolecular condensate-state of insulin molecules in elevated $Zn^{2+}$ and thermal stress, which was found to be cross-linked, viscoelastic and structurally reversible by pH modulation. The unique state was formed by the generation of elastic-like conformational variants (CVs) of insulin molecules through helix unwinding, relaxation of random coil, and subsequently conforming to an aggregate-like β-sheet rich structure. However, the aggregate-like state completely dissolved upon lowering pH, releasing monomeric insulin from the condensed organization. The ions ($Na^{+}$, $Cl^{-}$ and $Zn^{2+}$) were found to interlink the CVs into a single state through the localized ionic interaction. Next, pristine cellulose nanofibers (CNF) with long fiber-length and magnetic cellulose nanocrystals (MagCNC) with rod-shaped morphology were independently co-incubated with [$Zn^{2+}$]:[Insulin]. The longer CNF semi-crystalline fibers were reduced to highly crystalline cellulose nanorods (CNRs), whereas, MagCNCs were reduced to ultrasmall thread-like fibers which interacted together and formed spherical cellulosic particles within insulin microspheres. The unique insulin condensate, and its hybrid variants with CNF and MagCNC were found to be biocompatible and supported BHK-21 fibroblast growth with 68.4%, 74.5% and 70.32% increase, respectively. The unique insulin state and its specialized hybrid variants might have an enormous impact in material science.

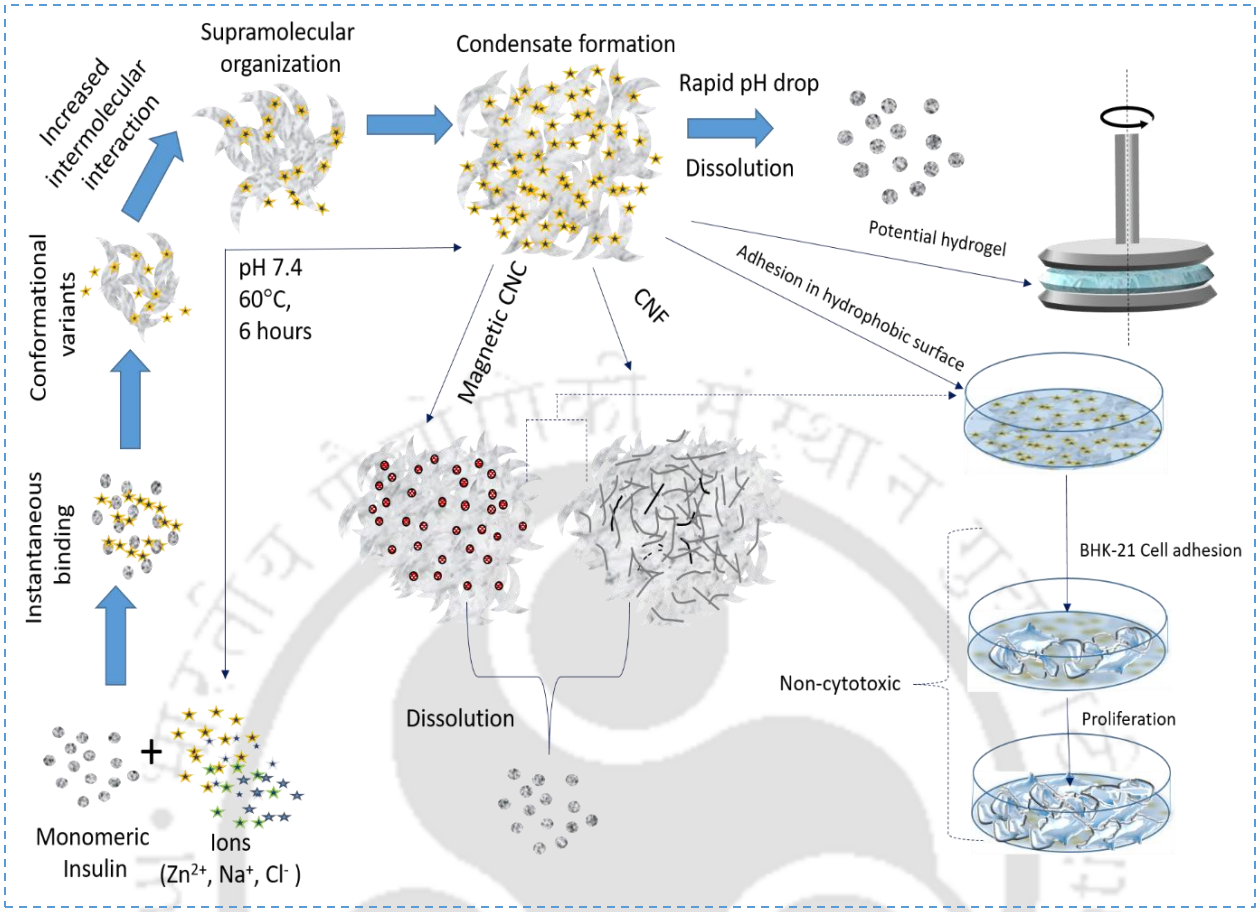


**Scheme of chapter 4**

## 4.1 Introduction

The emergence of the relatively new concept of biomolecular condensate, especially of protein condensate, has forced scientists to rethink about the established models of cellular processes involving the membrane-bound organelles [197]. Biomolecular condensates appear like membrane-less organelles which are formed through liquid-liquid phase separation or sol-gel transition, and they are found abundantly distributed across the cell [198,199]. One of the conclusive information on protein condensates was reported by Brangwynne et al., who found that localization of RNA and protein-rich P granules to the posterior of *Caenorhabditis elegans* embryo

involved rapid condensation and dissolution of P granules. The illusive mechanisms that drove the localization of P granules through condensation and controlled dissolution were termed as the 'P granule Conundrum' [200] . The research team further reported that the shape and size of the nucleolus in *Xenopus laevis* oocyte arise due to the formation of RNA-protein condensate which relies upon phase separation. It was explained that nucleoli behave like liquid-like droplets exhibiting *viscous* fluid dynamics [201]. These reports provoked the scrutiny of the mechanisms through which proteins undergo rapid condensation and dissolution. Subsequently, Li et al. reported that the multivalent signalling proteins that can interact with multiple partners can enable liquid-liquid phase separation and condensation of proteins to form micrometre sized assemblies [202] . The understanding of the protein assemblies deepened with emergence of later reports which linked the self-assembly of proteins to their Intrinsically Disordered Regions (IDRs) [12] . Recently, tau protein which is a key contributor to the Alzheimer's Disease pathology has been found to form protein condensates [203] . Furthermore, protein condensates have been implicated in the activation of innate immune signalling [204], tumorigenesis in cancer [205,206], triggering fibrillation of inclusion bodies in ALS [207], etc. While the pathophysiological importance of protein condensates is clearly apparent, the mechanisms that drive the proteins to rapidly condense and dissolve, and on the contrary trigger fibrillation or aggregation of proteins, are yet not conclusively elucidated.

In this context, the formation of distinct protein condensate is confounded by the processes of protein multimerization [208–210] (as proteins like insulin are known to form higher-order multimers [150,211]) and the irreversible supramolecular organization of proteins into amyloid fibrils, or protein aggregates [212–214]. The latter is implicated in the pathophysiology of neurodegenerative disorders and synaptopathies [12] and is characterized by an irreversible 'α-

helix-to-β-sheet' transition [215]. Protein multimerization, on the other hand, is characteristically different from the formation of amyloid fibrils. For instance, it is well established that the hexameric organization of insulin is driven by a 1:3 stoichiometric ratio between $Zn^{2+}$ ions and insulin molecules at physiological conditions [216]. The hexameric structural organization is formed to maximize the stability of otherwise unstable insulin molecules, thereby acting as a storage unit that allows control release of the hormone [217–219]. The obvious implication is that the functional conformation of insulin remains intact in these stable multimers which are formed by a definite number of monomeric units. Also, it is apparently conclusive that these multimers are in equilibrium with each other [150,220]. The scenario, however, becomes incomprehensible if the higher-order organization (HO) is formed by an indefinite number of insulin molecules,and whether they form dissoluble condensates or irreversible aggregates. This has been raised in the present study through scrutinizing the distinction between protein multimerization, protein condensation and the process of protein aggregation, deploying insulin as the *in vitro* model.

Based on the above discussion, in the current study, we employed a constant and high concentration of insulin at which the protein is known to form clusters due to crowding through increased intermolecular interactions [150]. We performed the experiments at the physiological pH 7.4 because at this condition it is well established that $Zn^{2+}$ ions form coordination complexes with the protonated Histidine residues of Insulin, and forms multimers [221,222]. The rationale of the study was based on the fact that the process of insulin multimerization is highly sensitive to the concentration of $Zn^{2+}$ ions (denoted from herein as [$Zn^{2+}$]) and also, temperature of the system. Now, in order to promote macromolecular organization of insulin, we varied [$Zn^{2+}$] beyond the physiological 1:3 ratio at an elevated temperature of 60°C. Subsequently, the effect of co-incubation of cellulose nanofibers (CNF) and magnetic cellulose nanocrystals (MagCNC) during

the [$Zn^{2+}$]:[Insulin] macromolecular organization was investigated. Nanocellulosic materials have potential applications in the therapeutic and diagnostic fields [223,224]. Further, the cell-adhesion potential, and cytotoxicity was assessed using Baby Hamster Kidney-21 (BHK -21) fibroblasts. The experimental findings of the study, their analyses, interpretations and discussions are entailed in this chapter.

## 4.2 Results

### 4.2.1 Study on Turbidometry, ThT fluorescence, Hydrodynamic Size analyses of [$Zn^{2+}$]:[Insulin] higher-order organization

The studies on turbitometry, ThT and ANS fluorescence, hydrodynamic size analyses of [$Zn^{2+}$]:[Insulin] macromolecular organiation indicated the amyloid properties. A varying range of [$Zn^{2+}$] was deployed keeping concentration of [Insulin] constant in such a way that reaction mixtures of [$Zn^{2+}$]:[Insulin] were obtained with a range of molar stoichiometric ratios, 1:1 (System 1), 1:2 (System 2), 1:3 (System 3), 1:4 (System 4) and 1:6 (System 5), with $Zn^{2+}$-free insulin as control. At first, the time-dependence in attainment of turbidity at various aforementioned systems based upon [$Zn^{2+}$]:[Insulin] systems was evaluated by estimating optical density at 600 nm (OD@600 nm) from $0^{th}$ to $6^{th}$ hour. It was observed that OD values in all the [$Zn^{2+}$]:[Insulin] systems increased exponentially within the first ~60 minutes without any lag phase which was in contrast to the control which showed no significant change (Figure 4.1 A). The degree of saturation, however, was found to be solely dependent on the contribution of [$Zn^{2+}$] in reaction systems, exhibiting a directly proportional relation, i.e., the HO organization was found to follow the following pattern: [$Zn^{2+}$]:[Insulin] :: 1:1 (System 1) > 1:2 (System 2) > 1:3 (System 3) > 1:4 (System 4) >1:6 (System 5) > $Zn^{2+}$-free insulin.

Further, the final OD values representing the end-point of the [$Zn^{2+}$]:[Insulin] reaction from all the systems were plotted against the respective [$Zn^{2+}$] concentrations, in order to determine the relation between turbidity (OD) and [$Zn^{2+}$]. It was observed that the increment of the saturated OD values was directly proportional to the [$Zn^{2+}$] in the reaction mixtures (Figure 4.1 B). The data of OD values *vs.* [$Zn^{2+}$] was found to fit into Boltzmann model with the following equation:

$$OD = OD_2 + (OD_2\text{-}OD_1)/(1+\exp([Zn^{2+}]\text{-}[Zn^{2+}]_0)/d[Zn^{2+}])) \quad (4.1)$$

Where, $OD_2$ and $OD_1$ are quantified turbidity at the final and initial points of the reaction respectively, $[Zn^{2+}]_0$ is the concentration of $Zn^{2+}$ at the initial point of the experiment. $d[Zn^{2+}]$ stands for the difference of concentration of $Zn^{2+}$.

The analysis of the aliquots of [$Zn^{2+}$]:[Insulin] reaction mixtures was done for a time-dependent ThT binding assay after screening out the systems 1,3 and 5, representing the ratios, 1:1 (where maximum OD was observed), 1:3 (physiologically relevant), 1:6 (physiologically relevant), respectively. On a conceptual note, ThT binds specifically to β-sheets which characteristically augment as protein form aggregates, and consequent to binding, the dye emits enhanced fluorescence in the excitation/emission range, 450 nm/482 nm.

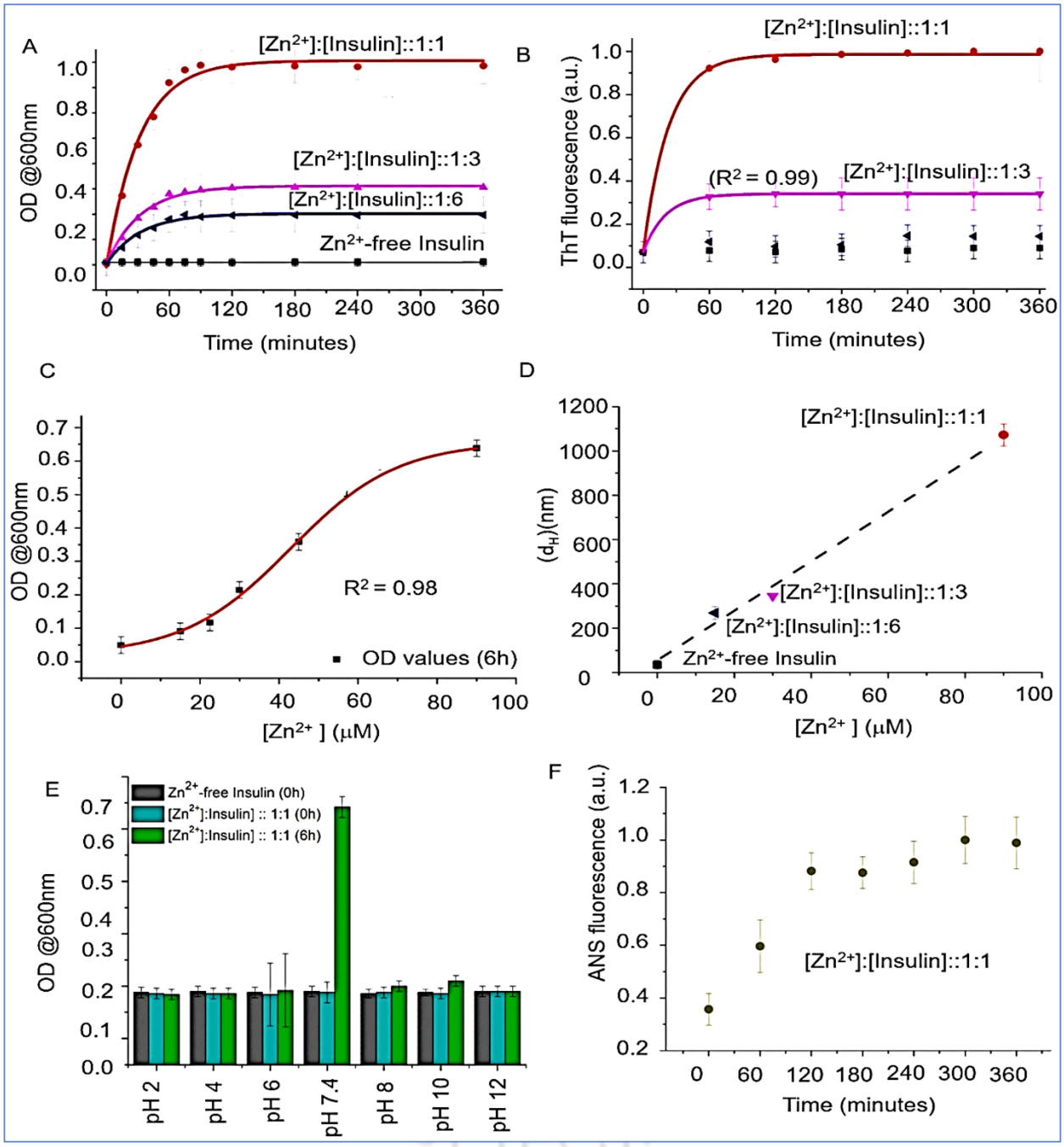


**Figure 4.1**. (A) The time-dependent optical density (OD) or turbidity measurements (at 600 nm) of [$Zn^{2+}$]:[Insulin] reaction mixtures at different ratios of [$Zn^{2+}$]:[Insulin]; (B) The time-dependent normalized ThT fluorescence of [$Zn^{2+}$]:[Insulin] reaction mixtures at ratios, [$Zn^{2+}$]:[Insulin]:1:1; 1:3;1:6; (C) The plot of OD@600 nm values of the individual saturated reaction mixtures vs [$Zn^{2+}$];

(D) The plot of the hydrodynamic size (in nm) of the [$Zn^{2+}$]:[Insulin] organizations vs [$Zn^{2+}$] at [$Zn^{2+}$]:[Insulin]:1:1;1:3;1:6; (E) The turbidity estimation of [$Zn^{2+}$]:[Insulin]:1:1 reaction conducted in a range of pH; (F) The representative graph of the time-dependent fluorescence emitted by aliquots of [$Zn^{2+}$]:[Insulin]::1:1 reaction mixtures upon binding with ANS.

The time-dependence of the β-sheet increment (correlated with extrinsic ThT fluorescence) was plotted and presented in Figure 4.1 C. It was observed that the extrinsic ThT fluorescence increased exponentially without a lag phase, and reached saturation within ~60 minutes of the reaction. Additionally, the saturation points of fluorescence for the various mixtures was found to be dependent on increasing [$Zn^{2+}$], i.e., ThT fluorescence emission ($\varepsilon_{ThT}$) followed [$Zn^{2+}$]:[Insulin]::1:1>1:3>1:6> Control. The $\varepsilon_{ThT}$ data was found to fit into the Mononuclear Exponential Growth Model with the following equation.

$$\varepsilon = A(1 - e^{-k\,(t-tc)}) \qquad (4.2)$$

Wherein, $\varepsilon$ denotes extrinsic emission of fluorescence at a given time, A is the amplitude; t is time and $t_c$ is the mathematical value of t at $\varepsilon$ =0, and K is the rate of emission of fluorescence.

For [$Zn^{2+}$]:[Insulin]::1:1, A was estimated to be ~ 0.99 ± 0.007, $t_c$ was -1.7±0.20 min, K was estimated to be 0.044 ± 0.003 $min^{-1}$. The $R^2$ value for the fitting was 0.99. For [$Zn^{2+}$]:[Insulin]::1:3, A was estimated to be ~ 0.34 ± 0.005, $t_c$ was -4.65 ±0. 13 min, K was estimated to be 0.05 ± 0.001 $min^{-1}$. The $R^2$ value for the fitting was 0.99. The higher rate at 1:3 is due to the faster achievement of saturation point with a lower amplitude value than the 1:1.

Additionally, it can be contemplated that the increase of β-sheets results in increased intermolecular interaction and formation of large-sized HOs. Hence, the hydrodynamic size ($d_H$) of the HOs was evaluated using Zetasizer Nano. It was found that at [$Zn^{2+}$]:[Insulin]::1:1 (System 1) largest aggregates were formed with ~1072 nm diameter (Polydispersity Index (PDI)= 0.307). It was followed by 1:3 (System 3) with ~ 345 nm (PDI=0.059), and 1:6 (System 5) with ~262 nm (PDI=0.049) and the $Zn^{2+}$-free insulin (control) with ~ 35 nm.

Figure 4.1 D represents the plot of the hydrodynamic radius observed for various [$Zn^{2+}$]:[Insulin] ratios vs. concentration of [$Zn^{2+}$]. With the aforementioned observations, we reflected that increasing proportion of [$Zn^{2+}$] in the [$Zn^{2+}$]:[Insulin] reaction mixtures resulted in the insulin structure to undergo structural modification into β-sheet rich structures, and thereby form large-sized organizations due to increased intermolecular interaction.

Next, the effect of various pH (Figure 4.1 E) and assessment of hydrophobic residues-exposure (Figure 4.1 F) was estimated in System 1 only, where the maximum macromolecular organization was observed. Keeping the stoichiometry, temperature and reaction time of the System 1 constant, pH was varied from pH2 to pH12. The macromolecular HO was found to form only at pH 7.4, implying that its formation was entirely pH dependent, thereby, also on the localized charges of the protein surface. The time-dependent ANS fluorescence estimated in System 1 was found to follow a similar pattern like ThT fluorescence profile. This indicated that the hydrophobic regions of insulin gradually exposed on the surface as the reaction proceeded. It is well understood that the hydrophobic residues of proteins are packed into the inner folds of the protein three-dimensional structure. Therefore, the exposure of the hydrophobic residues from inner core to the surface indicated the unwinding of the insulin structure, presumably promoting higher intermolecular interaction.

### 4.2.2 Studies on formation of conformational variants of insulin

The insulin forms conformational variants, which is initiated from the regions of extended structures, $3_{10}$-helix and regular helix. At first, in order to determine the structural reorganization of the secondary structures of insulin molecules in presence of $Zn^{2+}$, the structural information about the $Zn^{2+}$-free insulin was essential, which served as the control of the experiment. Figure 4.2 A shows the second-derivative of the amide I absorption spectra with characteristic peaks of native insulin. The 1610.4 $cm^{-1}$ (Figure 4.2 A) has been reported to be attributed by anti-parallel β-sheets which are insignificantly found in the native structure of insulin. It should be noted that amyloidogenesis or fibrillation of proteins proceed through the rise and stacking of anti-parallel β-sheets. FTIR peak 1622 $cm^{-1}$ (broad peak ~1628 $cm^{-1}$ -1634 $cm^{-1}$), although is attributed to β-sheets during aggregation, has been annotated to the extended chains of native structure of insulin molecule (B3-B6, B24-B28, A20-A21)[225] . The peak, ~1639 $cm^{-1}$ has been annotated to the $3_{10}$-helix of native insulin molecules corresponding to the residues of chain A1-A9 and A13-A19. The broad peak at ~1649 $cm^{-1}$ (Figure 4.2 A) is a unified peak of ~1646 $cm^{-1}$ corresponding to random coil (B1-B2, B29-B30, A10-A12) and ~1651 $cm^{-1}$ which corresponds to the α-helix of native insulin molecule (B9-B19). This shift of the random coil and α-helix peaks presumably indicates a dynamic equilibrium of the structural elements. The peaks, ~1666 $cm^{-1}$ and ~1681/1683 $cm^{-1}$ corresponds to β-turns of the insulin molecule spanning between the residues B7-B8 and B20-B23.

The Gaussian fitting of the spectral data of $Zn^{2+}$-free insulin (Figure 4.2 B) indicated a predominant α-helical nature of the native insulin molecule and was found to contain 33% α-helix and 19% β-sheet-like structure in Tris-HCl Buffer (pH 7.4). The β/α ratio that has been reported to indicate

structural transition [226] was calculated to be 0.57. This ratio for native $Zn^{2+}$-free insulin is nevertheless overstated as structures considered as β-sheets are rather unordered regions. However, this ratio has been calculated for comparative studies with other [$Zn^{2+}$]:[Insulin] HOs found in the study. Additionally, the ratio of absorbance at 1660 $cm^{-1}$/1690 $cm^{-1}$ has been reported to indicate the degree of cross-linking during intermolecular organization [227]. For native structure, although overstated, the ratio was found to be 1.31.

At the physiologically relevant ratio, [$Zn^{2+}$]:[Insulin]::1:3, i.e., System 3 in this work, it was found that after 6 hours of incubation at 60ºC , much of the α-helical structure remained conserved (Figure 4.2 C) exhibiting ~30 % of the total structure. Presumably, the assemblies of the [$Zn^{2+}$]:[Insulin] at this stoichiometric ratio had retained their helical structure, and thereby it could be presumed that the assemblies at this stoichiometry were relatively stable. However, there was also increase of intermolecular β-sheets (1620 $cm^{-1}$) which implied multimer-multimer interaction to form higher order structures. It appeared that the protein intermolecular interactions favored higher order organization by assembling β-sheets but without significantly disrupting the helical structural components. It could be presumed herein that at [$Zn^{2+}$]:[Insulin]::1:3 (60ºC , pH 7.4, 6 hour), insulin molecules attained conformational variation to assemble into a specific biomolecular organizational state with higher degree of helicity that was retained.

The total α-helix and β-sheet contents were estimated to be 30% and 62 %, respectively. The β/α ratio was calculated to be 2.06. The ratio of absorbance at 1660 $cm^{-1}$/1690 $cm^{-1}$ was found to increase to 2.6.

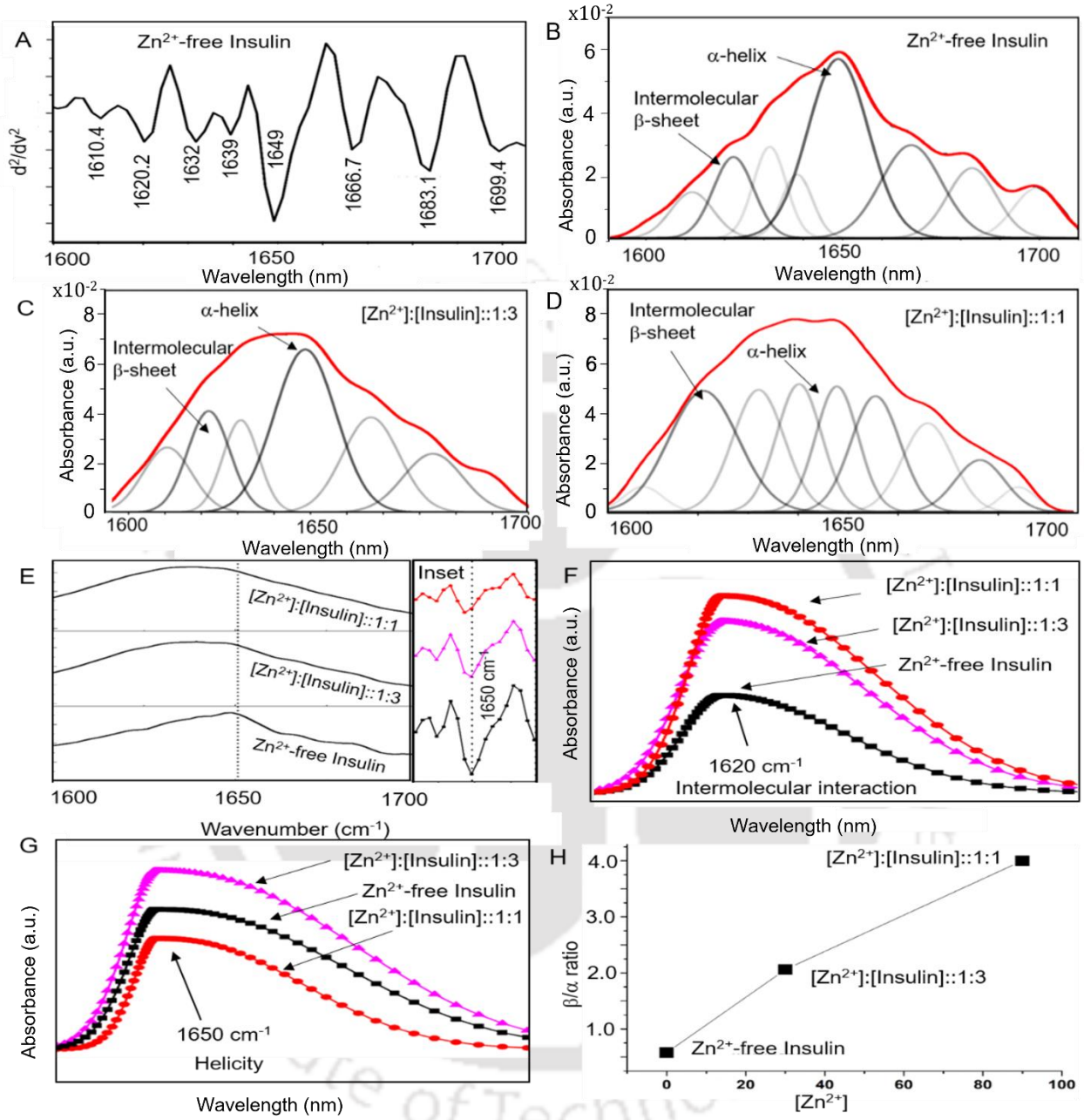


**Figure 4.2**. (A) The second-derivative of the amide I absorption spectra with characteristic peaks of native insulin; (B) The Gaussian fitting of the spectral data of $Zn^{2+}$-free insulin indicating a predominant α-helical nature of native insulin; (C) The Gaussian fitting of the spectral data of the physiologically relevant ratio, [$Zn^{2+}$]:[Insulin]::1:3; (D) The Gaussian fitting of the spectral data

of [$Zn^{2+}$]:[Insulin]::1:1; (E) A comparative analysis of the Gaussian fitted data of the absorbance spectra of $Zn^{2+}$-free insulin, [$Zn^{2+}$]:[Insulin]::1:1, and [$Zn^{2+}$]:[Insulin]::1:3; (F) The stacking of the 1620 $cm^{-1}$ peaks (which indicates intermolecular β-sheets) of $Zn^{2+}$-free insulin, and ratios1:3 and 1:1, resolved from the second derivative of the Gaussian fitted spectra data; (G) The stacking of the 1649 $cm^{-1}$ peaks (which indicates helical component) of $Zn^{2+}$-free insulin, and ratios 1:3 and 1:1, resolved from the second derivative of the Gaussian fitted spectra data; (H) The β/α ratio of the reaction mixtures which correlates to 'α-helix to β-sheet' transition. It was observed that, β/α ratio increased with increase in [$Zn^{2+}$].

The Gaussian fitting of the spectral data of System 1, i.e., [$Zn^{2+}$]:[Insulin]::1:1 (Figure 4.2 D) indicated that there was a significant decrease in the α-helical content (considering the range 1651 $cm^{-1}$ -1654 $cm^{-1}$ ) with increase of intermolecular β-sheets (1620 $cm^{-1}$). This implied that at equimolar ratio, in which $Zn^{2+}$ was in excess (considering the physiological ratio, i.e., 2 $Zn^{2+}$/ 6 Insulin molecules corresponding to 1:3), there was higher intermolecular interaction. The intermolecular β-sheets, as reported previously, are known to cause loss of distinctness or individuality of protein molecules. Total α-helix and β-sheet contents were estimated to be 12% (reduced by 21% as compared to control) and 48.5 %, respectively (increased by 29.5 % compared to the control). The β/α ratio was calculated to be 4.0. The ratio of absorbance at 1660 $cm^{-1}$/1690 $cm^{-1}$ was found to increase to 3.02.

Furthermore, a comparative analysis of the Gaussian fitted data of the absorbance spectra of $Zn^{2+}$-free insulin, [$Zn^{2+}$]:[Insulin]::1:1, and [$Zn^{2+}$]:[Insulin]::1:3 was performed (Figure 4.2 E). It was observed that the unified peak of 1649 $cm^{-1}$ which corresponds to the residues (random coil: B1-B2, B29-B30 and A10-A12; α-helix: B9-B19) gradually shifted towards lower wavenumbers

($Zn^{2+}$-free insulin>1:3>1:1). By looking at the pattern of the Gaussian fitted data, it could be verily comprehended that the variation of the structure was represented by the first half of the range (1600-1650 $cm^{-1}$) which harbors the extended structures, random coil, $3_{10}$-helix, and regular helix. It could be presumably reflected, that in the above conditions of [$Zn^{2+}$]:[Insulin] reactions, the unwinding of the helical elements took place, followed by intermolecular interaction with the random coil, and attainment of a conformational variant to favor HOs organization.

Figure 4.2 F demonstrates the stacked 1620 $cm^{-1}$ graphs of the aforementioned samples which were resolved from the second derivative plot of the Gaussian fitted spectra data. It has been previously mentioned that 1620 $cm^{-1}$ have been reported to represent the intermolecular interactions. The comparative analysis revealed that at 1:1, there was highest enhancement of intermolecular interaction, followed by 1:3 and $Zn^{2+}$-free insulin solution. Therefore, it could be presumed that in the same pattern, [$Zn^{2+}$]:[Insulin] reaction mixtures attained cross-linking which could be assessed through 1660 $cm^{-1}$/1690 $cm^{-1}$ ratio. Accordingly, the ratio of the same in $Zn^{2+}$-free insulin solution was calculated to be 1.31 which could be due to the formation of dimers as insulin monomers are highly unstable. The ratio significantly incremented in equimolar [$Zn^{2+}$]:[Insulin] ::1:3 to 2.6, and equimolar [$Zn^{2+}$]:[Insulin] to 3.02 which indicated that crosslinking had been promoted in presence of $Zn^{2+}$, and the degree of cross-linking depended on the increased [$Zn^{2+}$].

Figure 4.2 G represents the augmentation of the helicity (represented by 1649 $cm^{-1}$) in the 1:3 ratio compared to the $Zn^{2+}$-free insulin solution, whereas the helicity in the 1:1 ratio decremented. This anomaly in pattern could indicate that the higher-order structural organization of [$Zn^{2+}$]:[Insulin] proceeded at 1:3 through the increment in β-sheets but conglomeration of high number of insulin molecules with retained helices also resulted in the amplification of the α-helical elements in the

organized structural units. Therefore, it could be reflected that the structure of insulin could be highly dynamic and elastic in presence of [$Zn^{2+}$].

Figure 4.2 H represents the β/α ratio of the aforementioned reaction mixtures which correlates to 'α-helix to β-sheet' transition. It was observed that, β/α ratio increased with increase in [$Zn^{2+}$]. Therefore, it was evident that at 1:1, highest degree of cross-linking with augmented β-sheet content was achieved. From herein, because the effect of [$Zn^{2+}$] is most prominent in the equimolar ratio 1:1, i.e., System 1, the further investigation focused solely on the reaction products at this of the said system.

### 4.2.3 Electron microscopy analyses

The electron microscopy analyses revealed that [$Zn^{2+}$]:[Insulin] formed cross-linked, micrometer-sized and porous aggregate-like structures at 1:1 stoichiometric ratio. After confirming that insulin molecules in presence of various [$Zn^{2+}$] formed HOs after attaining a β-sheet rich structure, we attempted to investigate the morphology of the organizations at [$Zn^{2+}$]:[Insulin]::1:1 (System 1) only, as the effect was most prominent in this system.

Figure 4.3 A represents the FETEM images of the organization which was observed at 50 K magnification. It was clearly evident that the resultant organizations were highly cross-linked and porous. The size of the [$Zn^{2+}$]:[Insulin]::1:1 organization was found to extend to several micrometers. The disagreement in the size observed at FETEM and hydrodynamic size described in Figure 4.1 D was verily expected because the latter considers the particle size suspended in solvent, whereas the sample preparation for FETEM requires complete dessication.

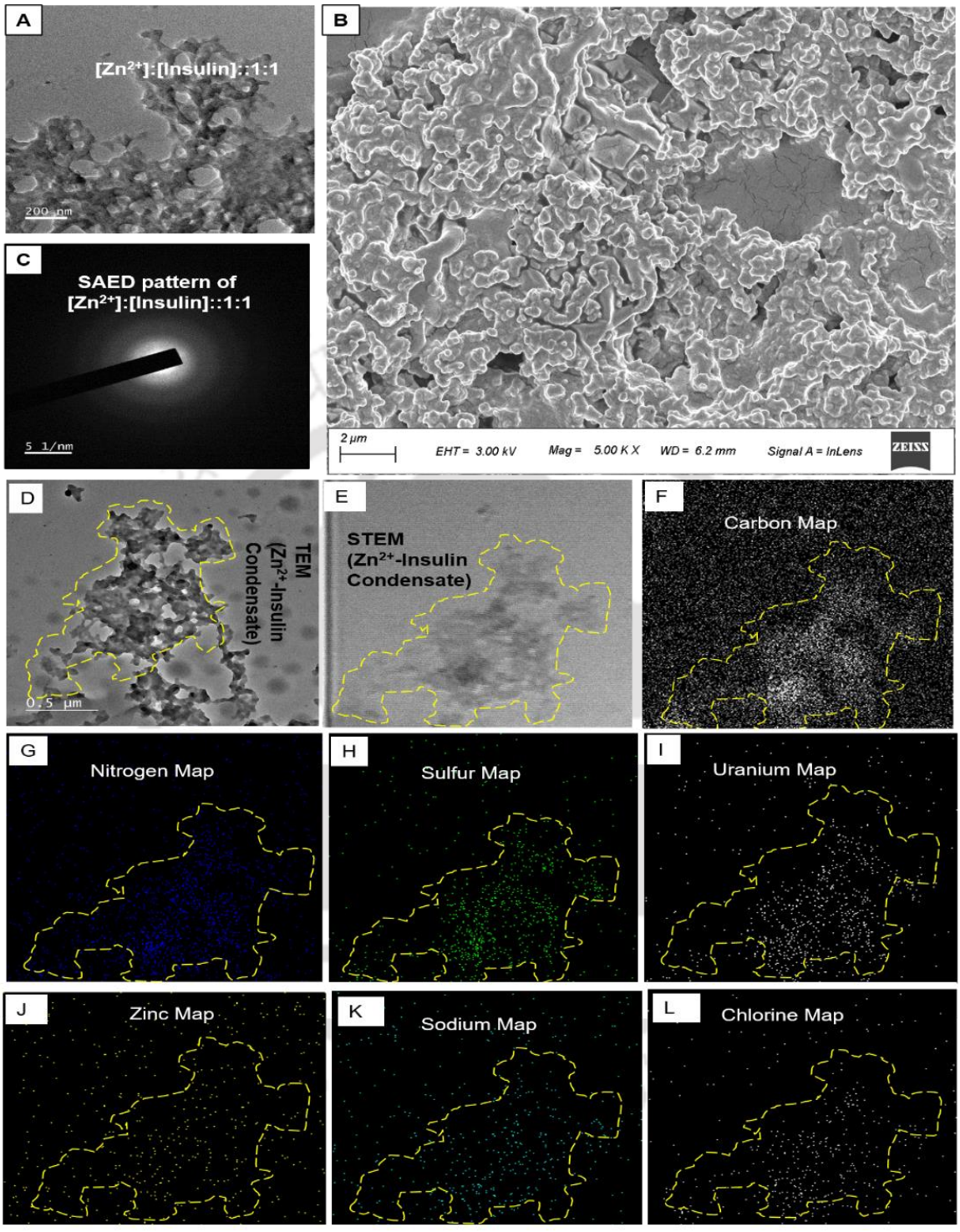


**Figure 4.3**. (A) The FETEM image of the organization formed at [$Zn^{2+}$]:[Insulin]::1:1 observed at 50 K magnification; (B) The lower magnification FETEM image of cross-linked organization of [$Zn^{2+}$]:[Insulin]::1:1; (C) The three dimensional FESEM image of the cross-linked organization of

[$Zn^{2+}$]:[Insulin]::1:1. Inset: The Selected Area Electron Diffraction (SAED) pattern of cross-linked organization of [$Zn^{2+}$]:[Insulin]::1:1 indicating amorphous nature; (D) The FETEM image of the [$Zn^{2+}$]:[Insulin]::1:1 HOs with the selected area for the elemental mapping (shown with yellow outline); (E) The three-dimensional STEM image of the selected region shown in 3D; (F) Carbon map; (G) Nitrogen map representing the imprint of the amino groups; (H) Sulfur map representing the imprint of S-containing amino acids; (I) Uranium map from uranyl acetate stain; (J) Zinc map showing the placement of $Zn^{2+}$ in the structure (white arrows points to the detection of linear patterns); (K) and (L) The elemental maps of $Na^{2+}$ and $Cl^{-}$, respectively, showing the placement of the elements in the selected area of the structure.

Nevertheless, the two sizes obtained explain the nature of organization in motion within solution (hydrodynamic size) and onto the surface of carbon-coated copper grid in complete non-aqueous environment. Furthermore, the three dimensional FESEM image of the higher-order structures (Figure 4.3 B) corroborate with Figure 4.3 A displaying the large size, porosity and crosslinking attained at 1:1. The nature of the cross-linked organization was found to be amorphous which was evident from the SAED pattern which has been displayed in the inset of Figure 4.3 C.

The intriguing question was about the role and fate of $Zn^{2+}$ after the insulin HOs were formed. On a conceptual note, it is known that $Zn^{2+}$ remains bound to the activated histidine residues at pH 7.4 at the dimeric, hexameric and further multimeric forms 18. Therefore, it was rationale to presume that these histidine residues remained activated also in the HOs. Hence, it provoked investigation into the placement of $Zn^{2+}$ in the aforesaid insulin HOs (formed at [$Zn^{2+}$]:[Insulin]::1:1). The presence of $Na^{2+}$ and $Cl^{-}$ introduced during pH adjustment, the latter being also present in the

buffer, was also scrutinized for their respective roles, if any. The elemental mapping offered by the Scanning Transmission Electron Microscopy (STEM) mode was deployed for the purpose. The [$Zn^{2+}$]:[Insulin]::1:1 (System 1) HOs after staining with 2% uranyl acetate was imaged through STEM mode of Jeol FETEM instrument.

The selected area from the representative TEM image has been displayed in Figure 4.3 D. The three-dimensional STEM image of a portion of the selected region of [$Zn^{2+}$]: [Insulin]::1:1 HOs is shown in Figure 4.3 E. The placement of carbon was mapped as the backbone of the HOs is composed of carbon (Figure 4.3 F). Next, the placement of nitrogen (Figure 4.3 G) and sulfur (Figure 4.3 H) was carried out as the elements were the salient features of protein, i.e., insulin only, thereby confirming that the object under view was indeed the protein. Next, further confirmation was done through mapping uranium (Figure 4.3 I) from uranyl acetate which was used to stain insulin HOs. All the aforementioned elemental maps were found to exactly align with the area represented by the STEM image (marked with dotted yellow outline) displayed in Figure 4.3 E.

Therefore, there remained no ambiguity that the structure under visualization was indeed the insulin HOs of [$Zn^{2+}$]:[Insulin]::1:1. Next, the ions originally present in the reaction mixture of System 1, i.e., excess $Zn^{2+}$, $Na^{+}$ and $Cl^{-}$, were mapped. The $Zn^{2+}$ map (Figure 4.3 J) confirmed that the HOs found in System 1 indeed contained the element, and interestingly, linearly arranged elemental patterns of $Zn^{2+}$ were detected. These patterns could presumably suggest the binding role of the element bringing smaller organizations in proximity, and interlinking them. In that light, $Zn^{2+}$ has been reported by other studies to play a binding role in cross-linked structures [228–231]

Next, the placement of $Na^+$ (Figure 4.3 K) and $Cl^-$ (Figure 4.3 L) were mapped, which indicated a possible role of local charges of the protein molecule, binding the aforesaid cation and anion with negatively and positively charged side chains of the amino acids. Both the elements were found to be intricately bound or integrated into the structure which can be observed visually through the yellow outer-line drawn for better understanding. It was, therefore, confirmed that the ions, $Zn^{2+}$, $Na^+$ and $Cl^-$, acted as role-players in the structural organization of the HOs of insulin. Also, the proteinaceous structure could be speculated to be highly interactive owing to a high density of local charges. Next, we investigated the interactive ability of the structure by co-incubating CNF and Magnetic CNC in the experimental conditions of System 1.

### 4.2.4 Co-incubation of [$Zn^{2+}$]:[Insulin] with cellulose nanofibers (CNF)

A volume of 250 µl hydrophobic CNF corresponding to equal concentration (w/v) of insulin fraction in the system 1 was incubated with the [$Zn^{2+}$]:[Insulin] reaction mixture. The resultant mixture separated into two phases as the [$Zn^{2+}$]:[Insulin] solution was hydrophilic initially and CNF hydrophobic. Gradually, as [$Zn^{2+}$]:[Insulin] reaction proceeded with increase in hydrophobic exposure as described in ANS fluorescence plot in Figure 4.1 F , CNF and insulin fractions merged together in a stage-wise manner, until the phase separation completely disappeared. The bare CNF and the resultant CNF-[$Zn^{2+}$]:[Insulin] reaction products were independently analyzed under FETEM in bright-field imaging mode for comparison.

The bare CNF was found to be intricately branched composed of extremely long continuous fibers (Figure 4.4 A) with maximum length recorded as 7.2 µm and diameter ~26 nm (HRTEM image shown in Figure 4.4 B). The CNF fibers did not show lattice fringes and exhibited an amorphous nature as evident from its FFT image (Figure 4.4 C). Whereas, in CNF-[$Zn^{2+}$]:[Insulin] reaction

product the CNF fibers were found to be resolved into CNRs with length ranging from ~46 nm to ~76 nm and diameter of ~7 nm, and dispersed in the macromolecular organization of insulin (Figure 4.4 D). The high resolution imaging mode resolved to 800 K magnification revealed the crystal grains (i.e., the lattice fringes and atomic arrangement) of the CNRs (Figure 4.4 E).

The FFT of the CNR HRTEM revealed multiple planes as shown with the FFT image denoted by a'a'', b'b'', c'c'', d'd'' e'e'', f'f'' and g'g'' (Figure 4.4 F) and the interplanar distances were calculated to be 0.34 nm, 0.34 nm, 0.34 nm, 0.29 nm, 0.34 nm, 0.21 nm, and 0.30 nm, respectively. Further, the planes visible in Figure 4.4 E were analyzed locally in Gatan Micrograph 3 software, using FFT transformation, applying mask, and deploying inverse FFT. Local areas denoted by 1,2, and 3 in the HRTEM image of the CNR was clarified using bandpass filter of imageJ software, and has been displayed in Figure 4.4 G.

The FFT (mask applied) and inverse FFT of the local area 1 has been displayed in Figure 4.4 H and 4.4 I, showing the arrangement and direction of the planes, with interplanar distance of 0.33 nm. The unmasked FFT image obtained from imageJ (Inset 1) revealed two more planes with spacings, 0.41 nm and 0.49 nm. The FFT (mask applied) and inverse FFT of the local area 2 has been displayed in Figure 4.4 J and 4.4 K, showing the arrangement and direction of the planes, with interplanar distance of 0.34 nm.

The unmasked FFT image obtained from imageJ (Inset 2) revealed another plane with a spacing value of 0.30 nm The FFT (mask applied) and inverse FFT of the local area 3 has been displayed in Figure 4.4 L and 4.4 M, showing the atomic arrangement as Moiré pattern with interplanar distance of 0.33 nm and 0.34 nm. The unmasked FFT image obtained from imageJ (Inset 3) revealed another plane with a spacing value of 0.44 nm. The possible Miller indices of the planes

corresponding to the interplanar spacings were (002)(0.34 nm), (210)(0.30 nm), (200)(0.41 nm), (101) (0.49 nm) and (110)(0.44 nm).

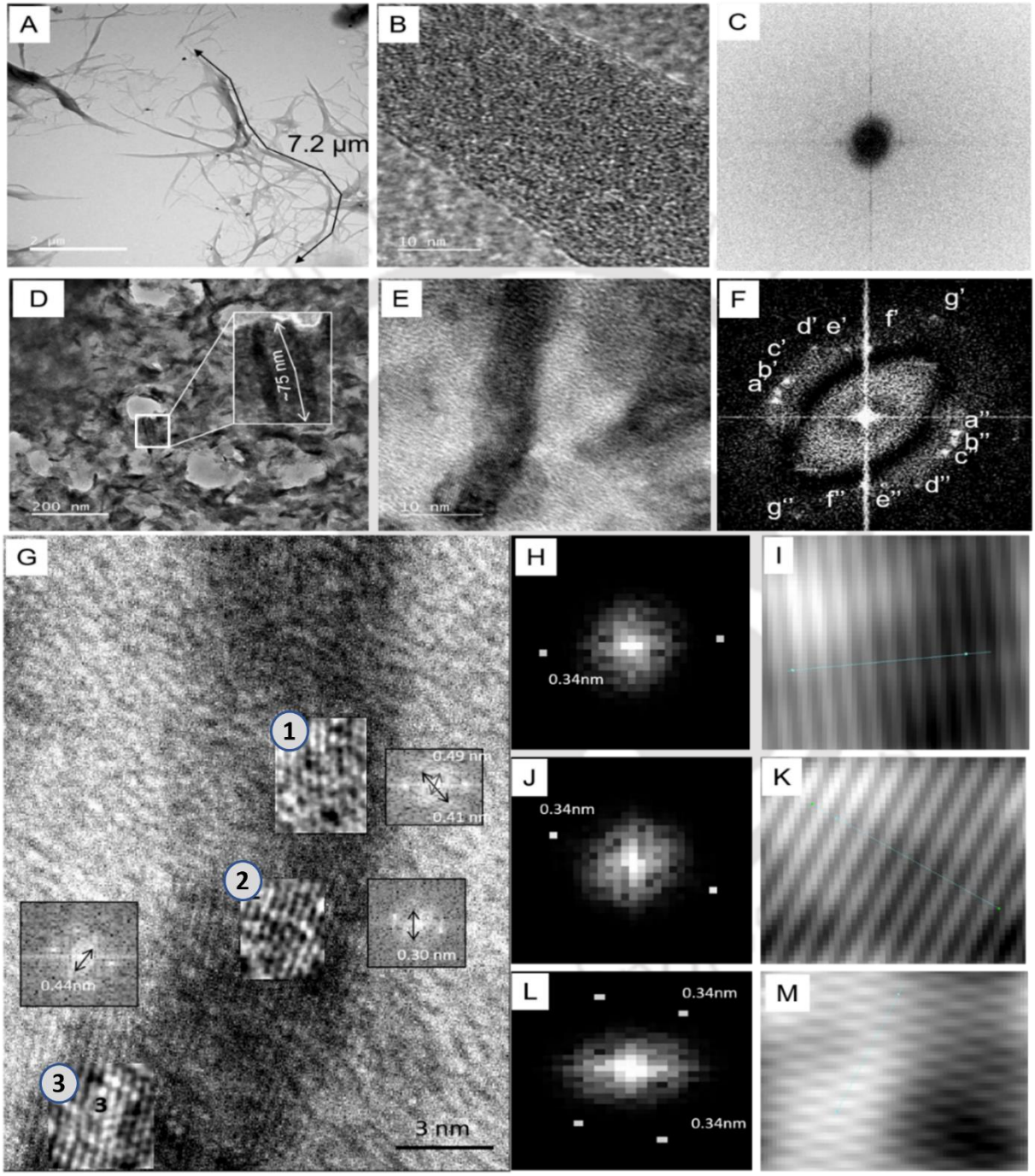


**Figure 4.4**.(A) The pristine CNF exhibiting intricately branched network of extremely long continuous fibers; (B) The HRTEM image of the fiber showing amorphous nature and a diameter

~26 nm; (C) The FFT image of the HRTEM of the fiber; (C) The CNF-[$Zn^{2+}$]:[Insulin] reaction product showing the resolution of the long fibers of CNF fibers into CNRs; (D) The CNR-dispersed macromolecular organization of insulin; (E) HRTEM of a CNR revealing the lattice fringes and atomic arrangement; (F) The FFT of the CNR HRTEM revealing multiple planes denoted by a'a'', b'b'', c'c'', d'd'' e'e'', f'f'' and g'g''; (G) HRTEM image of the CNR with marked areas denoted by 1,2, and 3; (H) and (I) represents the FFT (mask applied) and inverse FFT of the local area 1, respectively. The inset at (G) for local area 1 displays the unmasked FFT image obtained from imageJ (Inset 1); (J) and (K) represents the FFT (mask applied) and inverse FFT of the local area 2 showing the arrangement and direction of the planes. The inset at (G) for local area 2 displays the unmasked FFT image obtained from imageJ; (L) and (M) represents the FFT (mask applied) and inverse FFT of the local area 3 showing the atomic arrangement detected from Moiré pattern. The inset at G for local area 3 displays the unmasked FFT image obtained from imageJ.

The interplanar spacings were consistent with earlier reports, corroborating formation of rod-shaped cellulose nanocrystals [232], which has been named as CNR in this study. Therefore, the CNR functionalized insulin macromoeluclar organization was successfully designed. The CNR-conjugated insulin HO could be of particular utility owing to the lucrative properties of cellulose nanocrystals [233] Thus, the c**o**-incubation of [$Zn^{2+}$]:[Insulin] with CNF resulted in the resolution of the large amorphous CNF fibers to cellulose nanorods (CNRs), well dispersed in the matrix.

### 4.2.5 Co-incubation of [$Zn^{2+}$]:[Insulin] with MagCNC

Magnetic CNC or MagCNC was developed from aforementioned long-fiber pristine CNF by adsorbing iron or Fe particles on the CNF surface (detailed in materials section). The

characterization of morphology, crystallographic planes, elemental analysis and magnetic nature of the MagCNCs has been detailed in Figure 4.5.

Magnetic CNC or MagCNC was developed from aforementioned long-fiber pristine CNF by adsorbing iron or Fe particles on the CNF surface. However, the process (detailed in materials section) resulted in the formation of shorter-fiber rod-shaped CNCs with chemically incorporated iron or adsorbed Fe-containing NPs on the surface. The FETEM image of the MagCNC has been shown in Figure 4.5 A, where it has been revealed that the CNF to MagCNC conversion resulted in the formation of distinct rod-shaped shorter fibers of 150-170 nm length. Figure 4.5 A displays the morphology, shape and size of the fabricated MagCNCs which revealed that the continuously branched morphology of long CNF fibers (shown in Figure 4.4 A) had converted to discreet short-length fibers.

Also, the rod-shaped CNCs were found to have spherical shaped NPs which remained adhered on the surface of the rod-shaped fibers (4.5 B). The cluster of the MagCNCs laid out a polycrystalline profile in the SAED pattern (4.5 C) with interplanar spacings: 0.12 nm, 0.21 nm, 0.26 nm, 0.30 nm, 0.34 nm, 0.49 nm, 0.17 nm, 0.16 nm, 0.15 nm, 0.10 nm, 0.09 nm and 0.086 nm. Amidst the aforementioned, the interplanar spacings of 0.21 nm, 0.34 nm, 0.30 nm and 0.49 nm corresponded with the CNRs mentioned in the previous section. A cluster of the MagCNCs have been shown in Figure 4.5 D, from where, a region was selected for STEM and elemental analysis (shown with white rectangle). The selected area displayed in the STEM image (4.5 E) was analyzed for the presence of oxygen and iron. The oxygen atoms were attributed to the Cellulosic portion of the MagCNC, whose map coincided with the structure of the STEM image, confirming that the material under observation was indeed MagCNC (4.5 F). The iron or Fe Map (4.5 G) laid out a similar pattern of elements corresponding to the MagCNC STEM image, and had distinctly

coincided with the morphology of the MagCNCs (4.5 H). Therefore, it was confirmed that the rod-shaped CNCs and the adhered spherical NPs were composed of iron or Fe atoms. Figure 4.5 I represents the VSM profile of the MagCNCs confirming a paramagnetic nature.

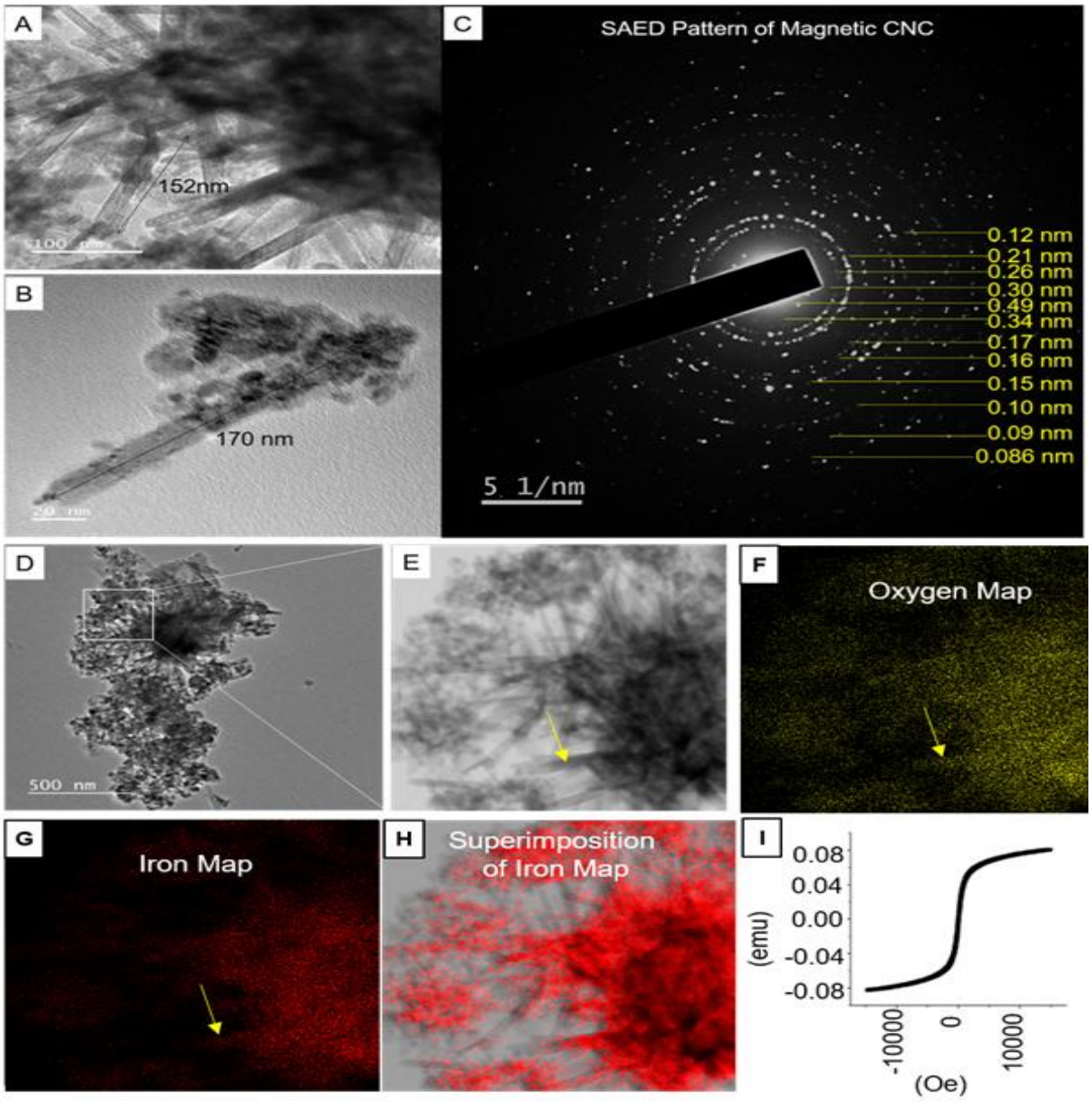


**Figure 4.5**. (A) FETEM image of Mag-CNC which was derived from pristine CNF (displayed in Figure 4A). The fiber length is shortened and uniformity was achieved leading to rod-shaped crystalline CNC fibers. The length of a CNC is displayed as 152 nm; (B) FETEM image of an

isolated MagCNC displaying a rod-shaped morphology with 170 nm length. Spherical Fe-containing NPs were observed to be adhered on the surface of the CNCs. (C) SAED pattern of a cluster of Mag-CNC displaying the polycrystalline nature and the interplanar spacings are displayed; (D) A cluster of Mag-CNC observed at 500 nm scale bar; (E) STEM imaging of a region of the MagCNC Cluster highlighted in 4D; (F) Oxygen Map of MagCNC; (G) Iron or Fe Map of MagCNC; (H) Iron or Fe map superimposed on the STEM image of the selected region of Mag-CNC. It was observed that the Fe atoms are present both in the spherical and rod shaped NPs; (I) VSM profile of the MagCNCs confirming a paramagnetic nature.

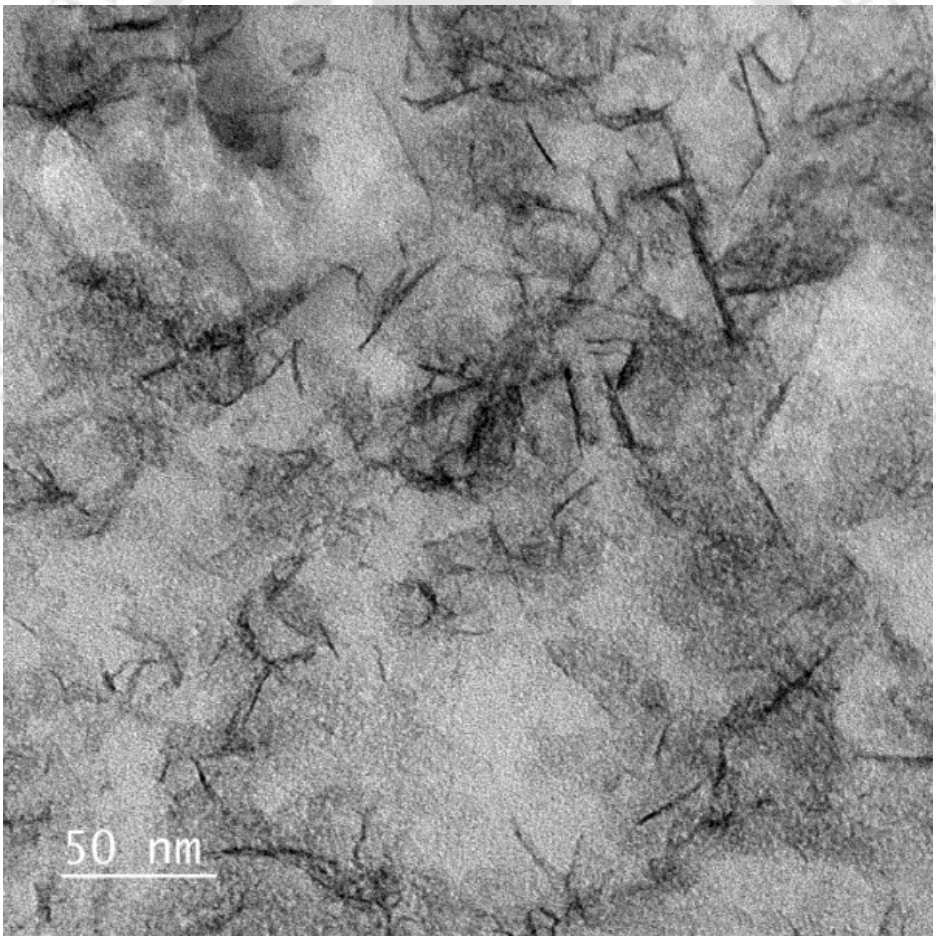


**Figure 4.6.** MagCNC resolved into finer fibers with reduced diameter and found dispersed in the [$Zn^{2+}$]:[Insulin] HOs.

A volume of 250 µl hydrophobic MagCNC corresponding to equal concentration (w/v) of insulin fraction in the system 1 was incubated with the [$Zn^{2+}$]:[Insulin] reaction mixture. The resultant mixture separated into two phases as the [$Zn^{2+}$]:[Insulin] solution was hydrophilic initially and MagCNC was hydrophobic.

However, as the reaction proceeded, the [$Zn^{2+}$]:[Insulin] HOs exhibited hydrophobic surface exposure resulting in the gradual dissolution of the separate phases to a single phase. Analysis of the aliquots drawn from the exponential phase of the reaction revealed that the rod-shaped CNCs were further resolved into finer thread-like fibers. The resolved fibers were found to be scattered and distributed into the insulin condensate matrix (Figure 4.6).

It was followed by the nucleation of the finer fibers within pockets of the [$Zn^{2+}$]:[Insulin] HOs. Figure 4.7 A and 4.7 B shows the finer fibers interacting among each other to form nucleating species within the pockets of the [$Zn^{2+}$]:[Insulin] HOs. The inset in Figure 4.7 A shows an enlarged view of the interacting finer threads to create the nucleating species. Inset at Figure 4.7 B shows the SAED pattern of the MagCNC-[$Zn^{2+}$]:[Insulin] HOs, displaying a crystalline nature of the hybrid complex.

A representative HRTEM image of a fine CNC fiber has been shown in Figure 4.7 C, displaying the typical lattice fringes of CNCs. Insets of the region 1 shows the FFT and inverse FFT analyses displaying an interplanar spacing 0.36 nm, region 2 revealed an interplanar spacing of 0.34 nm, region 3 revealed interplanar spacings of 0.33 nm, 0.36 nm and 0.94 nm, region 4 revealed an interplanar spacing of 0.28 nm. These crystallographic information coincided with MagCNCs displayed in Figure 4.5 C.

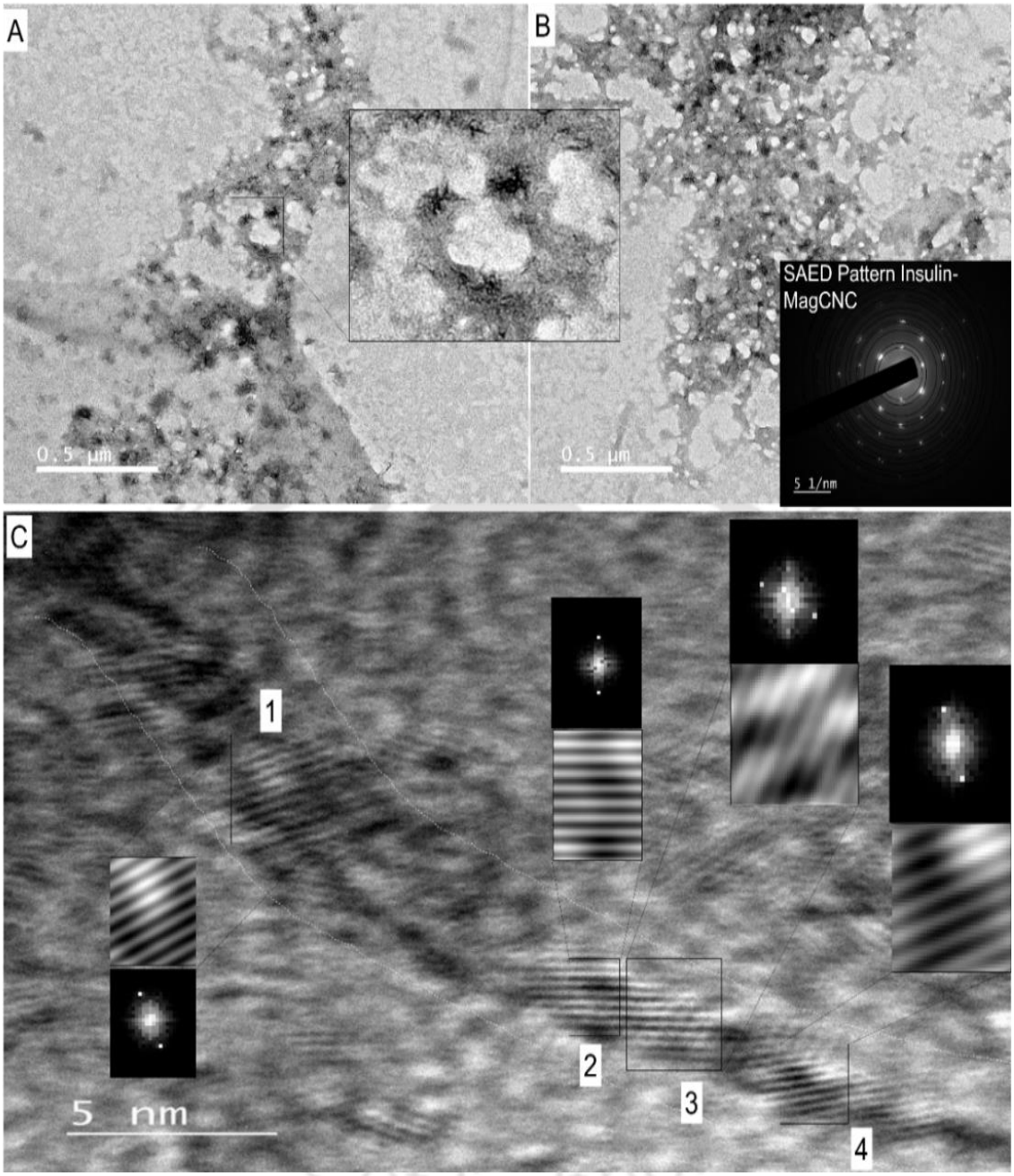


**Figure 4.7**. (A) and (B) FETEM images of finer CNC fibers creating nucleating species in the -[$Zn^{2+}$]:[Insulin] macromolecular complex. The inset shows a cropped and enlarged view of the fine CNC fibers being packaged inside pockets of the matrix. Inset at the (B) shows the SAED pattern of the MagCNC-[$Zn^{2+}$]:[Insulin] macromolecular complex revealing a crystalline nature of the complex in contrast with amorphous nature of only [$Zn^{2+}$]:[Insulin] macromolecular

complex (C) HRTEM analysis of a CNC fiber displaying the lattice fringes. Insets of the region 1 shows the FFT and inverse FFT analysis of interplanar spacing 0.36 nm, region 2 revealed a interplanar spacing of 0.34 nm, region 3 revealed interplanar spacings 0.33 nm, 0.36 nm and 0.94 nm, region 4 revealed interplanar spacing of 0.28 nm.

### 4.2.6 STEM analysis of MagCNC-[$Zn^{2+}$]:[Insulin] complex

The STEM image of a selected region of the MagCNC-[$Zn^{2+}$]:[Insulin] complex has been displayed in Figure 4.8 A. The carbon map (4.8 B), nitrogen map (4.8 C), oxygen map (4.8 D), sulfur map (4.8 E) and uranium map (4.8 F) confirmed the structure was protein, which is the [$Zn^{2+}$]:[Insulin] HO complex.

Next, it was investigated whether the nucleating species embedded in the pockets of the [$Zn^{2+}$]:[Insulin] HOs contained iron or Fe atoms. The elemental map of iron revealed that the positions of the element coincided with the positions of the nucleating species at the HOs (4.8 G), confirming the presence of Fe.

The superimposition of the elemental maps has been displayed in 4.8 H and the quantitative elemental analysis (4.8 I) confirmed the presence of 70.4% oxygen (from CNC and insulin), 17.2% nitrogen (exclusively from insulin), 9.5% sulfur (exclusively from insulin) and 2.8% iron or Fe atoms. By the coincidence of the Fe-Map with the nucleating species confirmed that they contained Fe atoms.

Next, after the completion of the MagCNC-[$Zn^{2+}$]:[Insulin] co-incubation, the predominant species of the HOs were found to resolve into microspheres of similar shape and sizes, with MagCNC NPs packed within the interior. A representative image of the structure is illustrated in Figure 6A. Further images at different resolutions are shown in 4.9 A to 4.9 E.

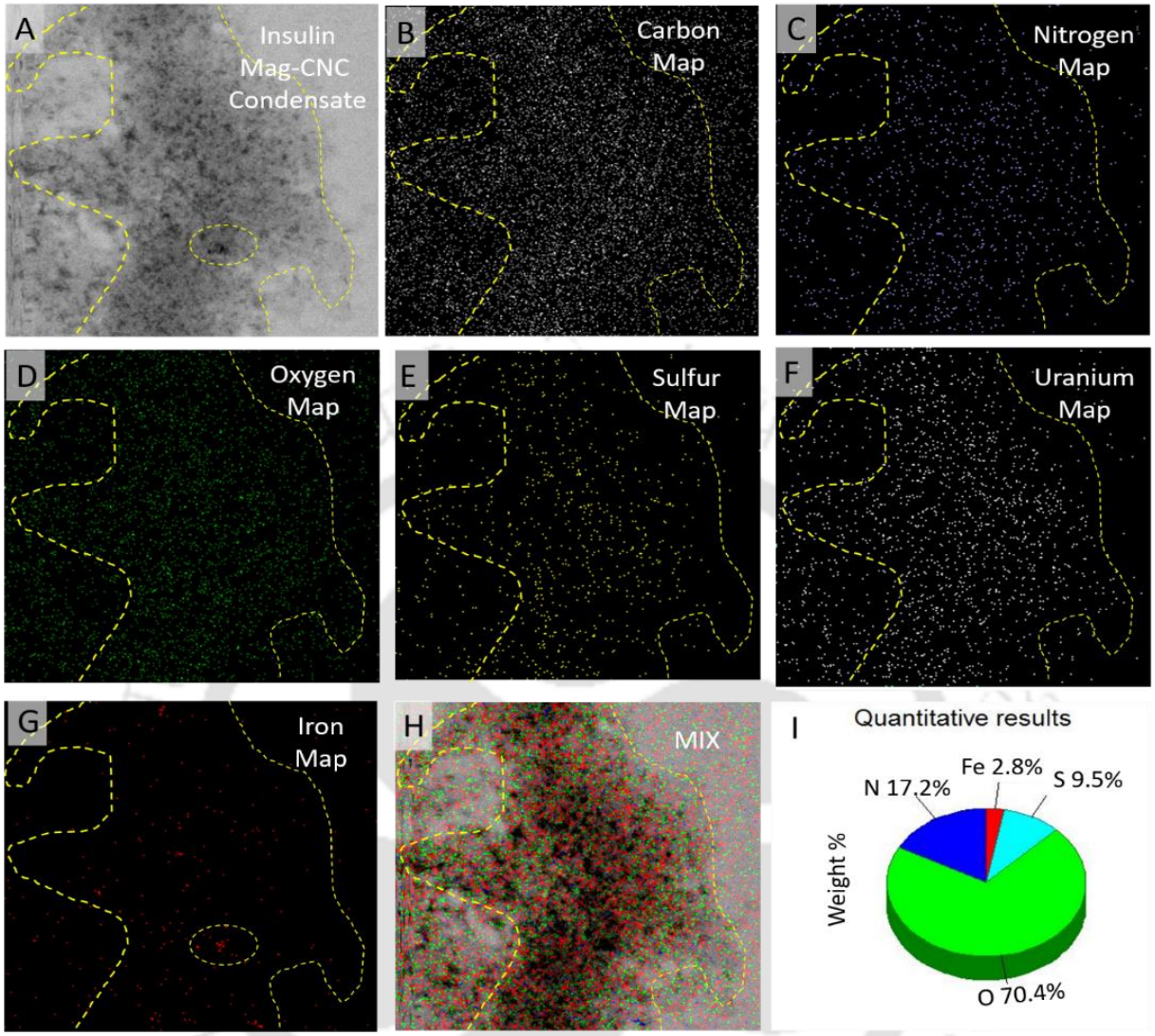


**Figure 4.8.** (A) The STEM image of a selected region of the MagCNC- [$Zn^{2+}$]:[Insulin] complex; (B), (C), (D), (E) and (F) Shows the elemental maps of the selected region as Carbon Map, Nitrogen Map, Oxygen Map, Sulfur Map and Uranium Map, respectively; (G) The Iron or Fe Map of the selected region showing the presence of iron in the nucleating species of the finer CNCs; (H) Shows the superimposition of the elements in the elected region; (I) Quantitative elemental analysis of the selected region revealing 70.4% Oxygen, 17.2% Nitrogen, 9.5% Sulfur and 2.8% iron or Fe atoms.

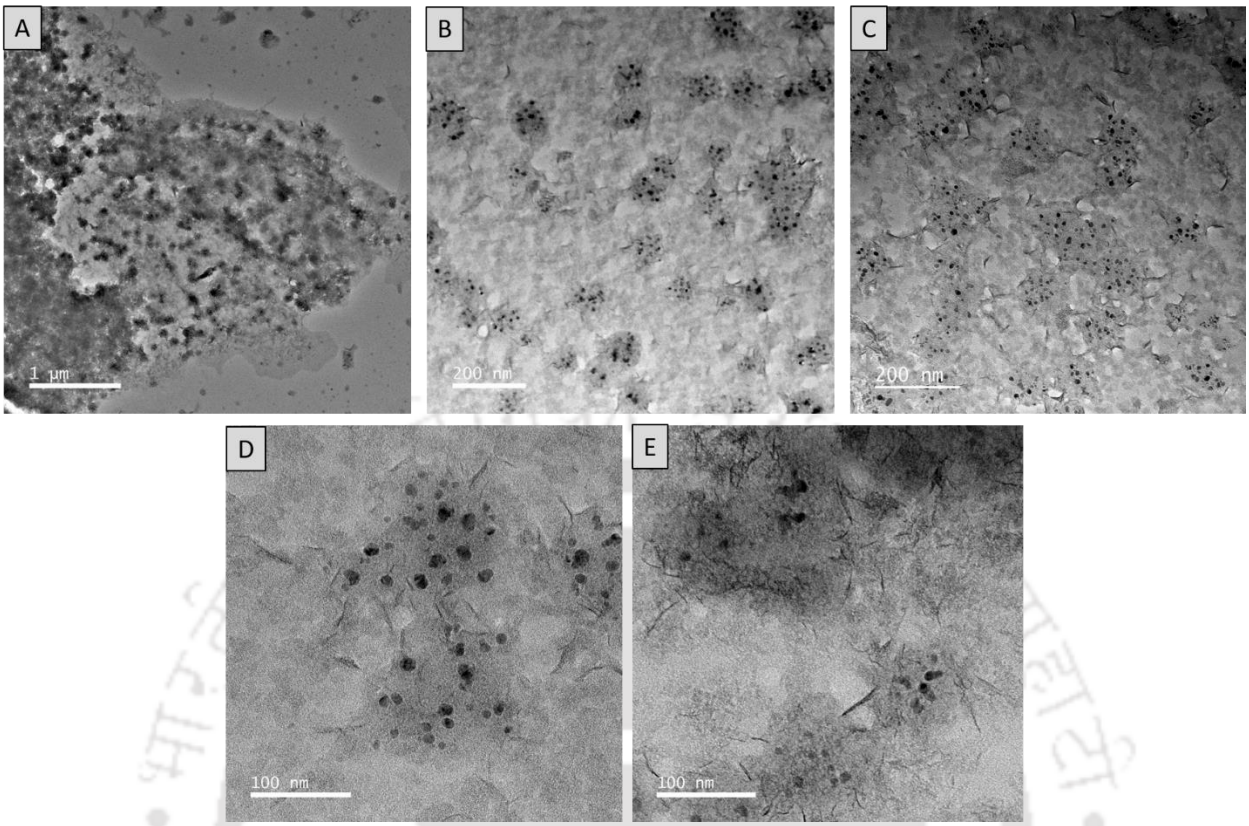


**Figure 4.9.** FETEM images of Insulin- MagCNC microspheres viewed at various magnifications.

Such microparticles of insulin have potential application in delivery systems [234,235]. Further probing into the adjoining surface of NPs of the HOs revealed a mixed pattern of amorphous and crystalline patches (4.10 A). The typical interplanar spacings of CNC were found to be exhibited, which were 0.34 nm, 0.30 nm, 0.47 nm, and 0.18 nm. The mixed pattern of amorphous and crystalline patches is of particular advantage, as crystallinity endows strengths and amorphous allows flexibility. Therefore, the resultant MagCNC-[$Zn^{2+}$]:[Insulin] complex could be further explored in these lines. Extremely small particles of less than 10 nm were also detected and two representative images has been displayed in Figure 4.10 B and 4.10 C. The interplanar spacings were found to be 0.34 nm, 0.16 nm and 0.28 nm predominantly.

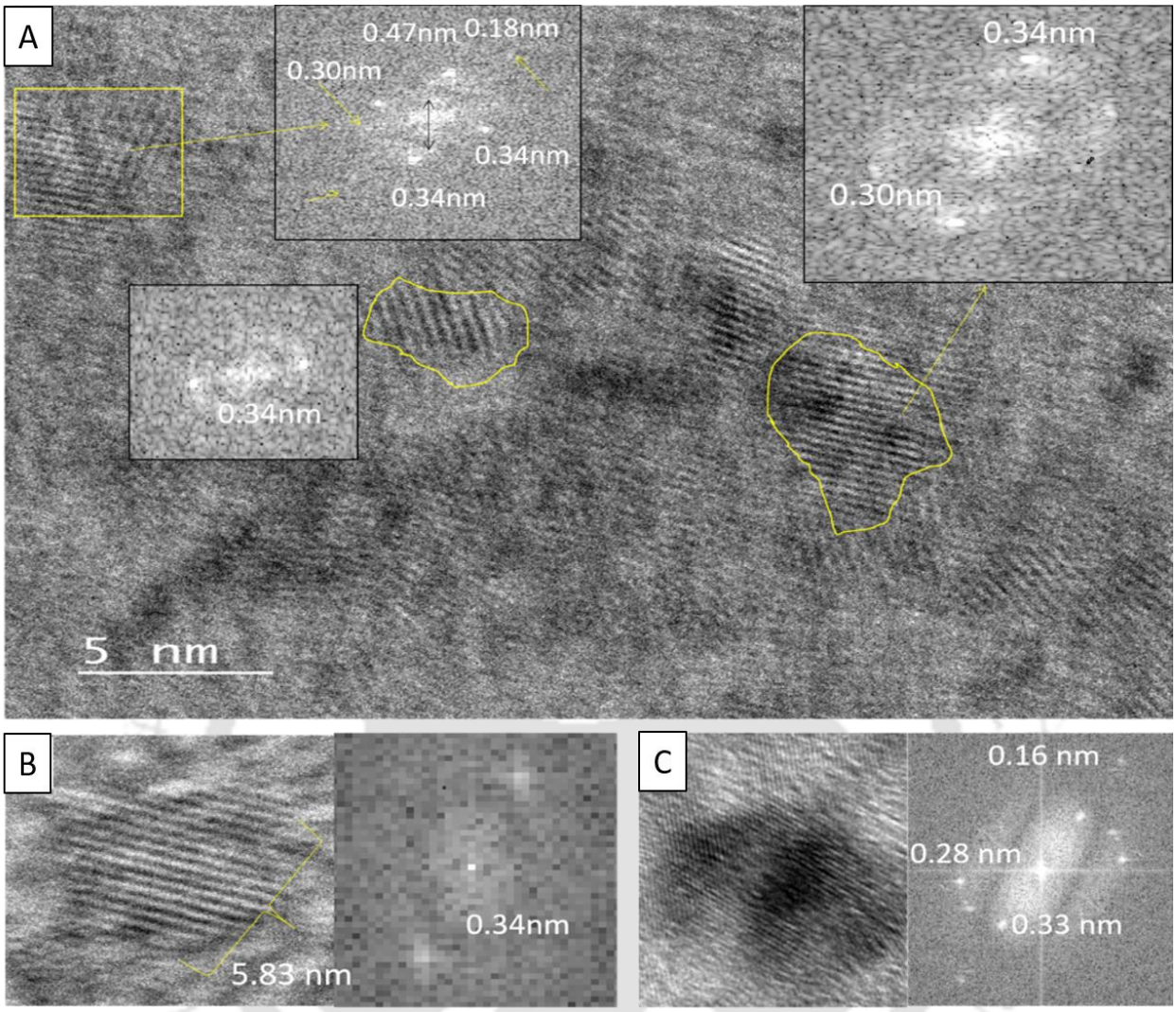


**Figure 4.10.** (A) HRTEM image of the surface of the MagCNC-[$Zn^{2+}$]:[Insulin] macromolecular complex revealing a mixed feature of crystallinity and amorphous nature. The FFT analysis of the crystalline regions revealed characteristic interplanar spacings of CNC; (B) and (C) shows HRTEM images of circular MagCNCs with characteristic 0.34 approx interplanar spacings.

The conversion of long-fiber CNF to CNR, and resolution of rod-shaped MagCNC to finer threads, and subsequent nucleation leading to spherical MagCNCs, seemed to have retained the crystallographic plane (002) corresponding to the interplanar spacing distance of 0.34 nm. A

schematic representation of the Mag-CNC to resolve into finer thread-like fibers, creation of nucleating species, and transformation into circular nanoparticles is shown in Figure 4.11.

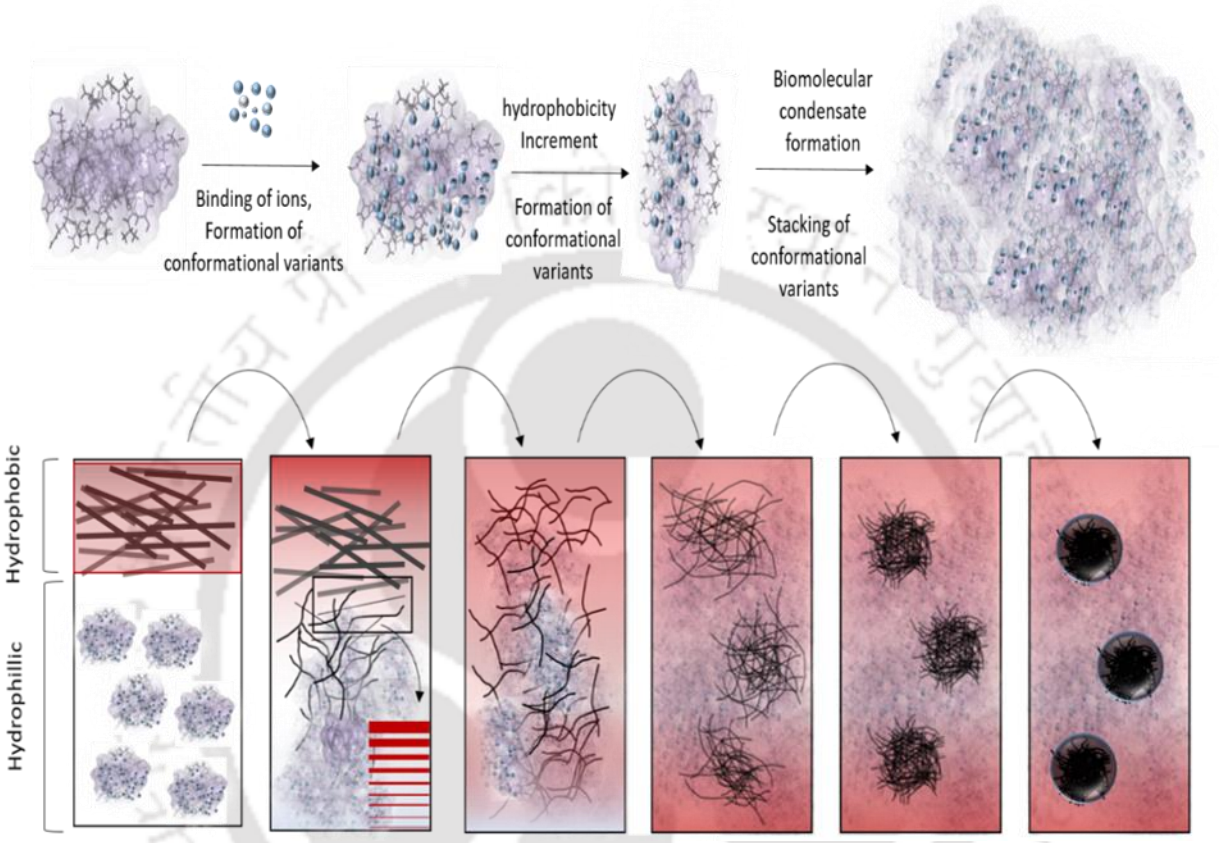


**Figure 4.11:** Schematic interpretation of the condensation of insulin molecules in presence of elevated $Zn^{2+}$, $Na^{+}$ and $Cl^{-}$ resulting in local charge interaction, formation of conformational variants and higher-order organization to form the condensate cluster. Addition of hydrophobic MagCNC creates a phase difference with the hydrophilic fraction of native insulin solution. Increase in the hydrophobicity of insulin molecules results in the gradual dissolution of the phase difference, resolution of the CNC fibers to finer threads, nucleation, and formation of spherical CNC crystals.

### 4.2.7 Studies on the dissolution of [$Zn^{2+}$]:[Insulin] HOs

The [$Zn^{2+}$]:[Insulin] macromolecular organization proceeds through the formation of dissociable higher-order multimers, giving rise to a viscoelastic structure which dissolves into monomeric form upon pH alteration. Next, we probed into quantifying the molecular weights of insulin HOs deploying MALDI-TOF/MS analyses. Till this point, it was not understood whether the insulin HOs were reversible or irreversible, although the understanding from the prominent transition of helical structure to β-sheet rich structure pointed towards the latter possibility. In that case, the monomeric form to be found in MALDI-TOF/MS was expected to be less and multimeric (definite or indefinite) organizations to be in significant higher proportion. Surprisingly, upon MALDI-TOF/MS measurements, it was revealed that it was the monomeric form which formed the most significant fraction, with multitudes of HOs from dimers to dodecamers with decreasing order of intensities (Figure 4.12 A). This possibly indicated that the macromolecular organization of insulin in presence of elevated $Zn^{2+}$, formed through physical stacking of structurally modified insulin monomers and also through local ionic interactions, rather than anti-parallel hydrogen bonding. With the presumption from the above findings that the macromolecular organization was structurally elastic, we probed into the viscoelasticity of the organizations employing rheometry. Figure 4.12 B displays the representative graphs of the storage and loss modulus of the [$Zn^{2+}$]:[Insulin]::1:1 HOs and the native insulin for comparison. The black and the red line denotes the storage and loss modulus of the [$Zn^{2+}$]:[Insulin]::1:1 HOs obtained from shear strain rheometry. It can be observed from the aforementioned figure that the insulin HOs formed at [$Zn^{2+}$]:[Insulin]::1:1 exhibited higher loss modulus (G") than storage modulus (G'), which indicated the viscous nature of the organizations. However, upon strain sweep, there was a crossing over point between G' and G" at 40% strain, followed by elevated G', i.e., the viscous nature of the

organizations converted into elastic nature. This viscoelastic nature of these organizations could be explored for the fabrication of hydrogel.

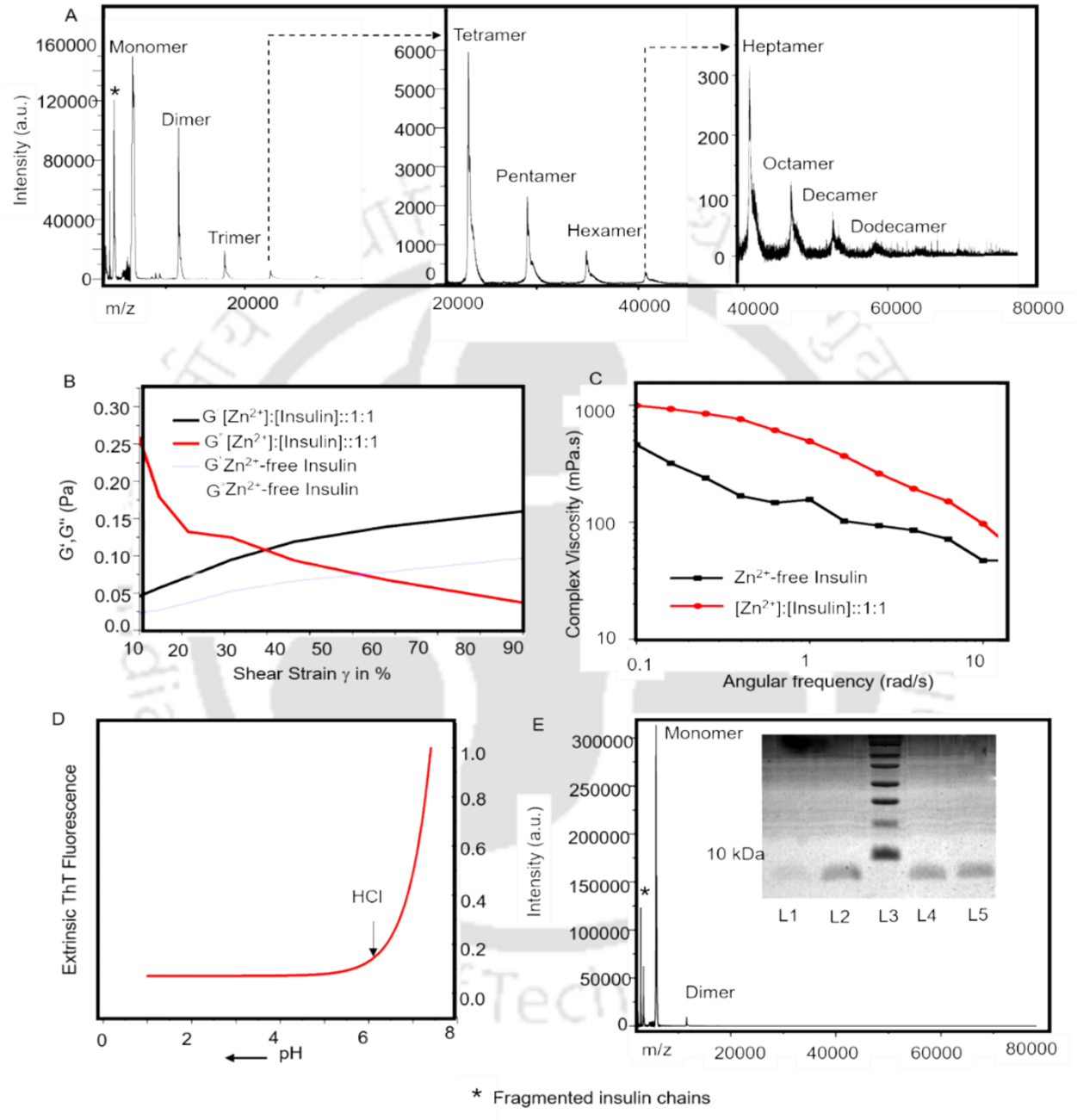


**Figure 4.12.** (A) MALDI-TOF/MS plot of [$Zn^{2+}$]:[Insulin]::1:1 HOs revealing insulin multimerization in the macromolecular structure; (B) The representative graphs of the storage (G$^{'}$)

and loss modulus ($G^{''}$) of the [$Zn^{2+}$]:[Insulin]::1:1 saturated reaction mixture and the native insulin; (C) Complex viscosity profile of [$Zn^{2+}$]-free insulin and [$Zn^{2+}$]:[Insulin]::1:1 revealing viscous fluid dynamics of the macromolecular structure of insulin; (D) The representative graph of the exponential decrement of ThT fluorescence by [$Zn^{2+}$]:[Insulin]::1:1 HOs with reduction of pH; (E) MALDI-TOF/MS plot of the dissolved [$Zn^{2+}$]:[Insulin]::1:1 HOs showing the prominence of the monomeric form of insulin. The inset displays the SDS-PAGE results of the HOs (L1), dissolved HOs (L2), 10k Da ladder (L3), dissolved CNR-Insulin organization (L4), dissolved MagCNC-Insulin organization (L5).

Nevertheless, the $Zn^{2+}$ -free insulin solution or the native insulin solution was also subjected to strain sweep, which also showed the same aforementioned pattern. However, the G'/G" profile is significantly demoted in the absence of [$Zn^{2+}$]. After confirmation of the initial viscous nature of [$Zn^{2+}$]:[Insulin]::1:1 HOs and native insulin, we investigated in to the complex viscosity profiles of the two. The complex viscosity of the [$Zn^{2+}$]:[Insulin] HOs was found to be in elevated state than the native insulin solution (Figure 4.12 C). This corroborated with the viscous fluid dynamics of protein condensates reported by Brangwynne et al.[200,201].

At this point, it could be seen that the HOs exhibited several properties of typical biomolecular condensate state of proteins, especially phase transition and viscous fluid dynamics. This provoked the investigation into the salient feature of protein condensates, i.e., dissolution, of the macromolecular organization appearing like amyloids. The understanding so far was that the formation of HOs was dependent upon specific pH. Therefore, we altered the pH to observe whether the HOs exhibited dissolution. The β-sheet rich HOs formed at [$Zn^{2+}$]:[Insulin]::1:1 was treated with 1N HCl by regularly dropping 10μL of HCl directly to 2 ml of the saturated reaction mixture (at room temperature). Simultaneously, pH of the solution was recorded with each

subsequent drop and aliquots were withdrawn for characterization. It was observed that the turbid solution instantly turned into a transparent solution when pH was dropped to 6 and stirred. However, pH was recorded till extreme low levels (pH 1) and aliquots were drawn for characterization. The aliquots of the 1N HCl treated HOs were treated with ThT dye, followed by incubation for 15 minutes in dark and measurement of fluorescence emission in Tecan infinite pro instrument.

Figure 4.12 D shows the representative graph of the exponential decrement of ThT fluorescence by [$Zn^{2+}$]:[Insulin]::1:1 HOs with reduction of pH. It can be observed that ThT fluorescence decremented steeply till pH 6 and reached the lowest level therein, and subsequently remained approximately constant till pH 1. This presumably indicated that the coordination complexes of $Zn^{2+}$ and Histidine residues were destabilized upon lowering pH, resulting in the structural destabilization of the complex. Also, the decrement of ThT fluorescence indicated reversal of β-sheets and disaggregation of the higher-order macromolecular structure of insulin. Therefore, it was strongly suggested that indeed insulin and $Zn^{2+}$ formed biomolecular condensate state at pH 7.4. The dissolved fraction was then analyzed in MALDI-TOF/MS and SDS-PAGE to investigate into the molecular fate of the HOs. Figure 4.12 E shows the MALDI-TOF/MS results for the dissolved HOs showing prominence of the monomeric form of insulin with the slight presence of dimeric form. Also, the fragmented chains of insulin were also detected which might have arisen due to breakage while ionization event in MALDI-TOF/MS . The inset of the Figure 4.12 E displays the SDS-PAGE results of the HOs (L1), dissolved fraction (L2), 10k Da ladder (L3), dissolved CNR-Insulin organization (L4), dissolved MagCNC-Insulin organization (L5). Interestingly, all of the above resolved into the monomeric form of insulin. This indicated that the insulin HOs in presence of elevated $Zn^{2+}$ was formed through localized ionic interactions between

the structurally modified forms of insulin molecules, which dissociated in presence of SDS. The typical properties of biomolecular condensate state like macromoleuclar organization into micrometre-sized assemblies, viscous fluid dynamics, conformational elasticity, and dissolution, were verily confirmed in the insulin HOs with all the aforementioned experimental findings. Thereby, there remained no ambiguity that the insulin HOs in presence of elevated $Zn^{2+}$ was indeed the biomolecular condensate state of insulin. Furthermore, it was anticipated that the insulin condensate structure could be modulated to design useful materials, owing to its viscoelastic nature, hydrophobicity, and ability to interact with organic and inorganic nanoparticles. Next, we investigated the effect of now-called insulin condensate in BHK-21 fibroblast cell line to investigate its cytotoxicity, and its ability to provide a platform for cell adhesion and proliferation.

### 4.2.8 Insulin condensate, CNR-insulin condensate and MagCNC-insulin condensate promotes cell adhesion, cell proliferation and cell growth of BHK-21 fibroblast cells

Next, the Insulin condensate, CNR-insulin condensate and MagCNC-insulin condensate were found to promote proliferation of BHK-21 fibroblast cells with no trace of cytotoxicity. There was a 68.4% increase of fibroblast growth in presence of insulin condensate, 74.5% increase with CNR-insulin condensate, and 70.32% increase with MagCNC-insulin condensate. CNR-insulin condensate and MagCNC-insulin condensate thin films were also found to support cell adhesion and proliferation. MagCNC in particular was found to adhere to the cell surface or enter the interior regions of the cells, provoking further possibilities to design potential material for cell culture applications.

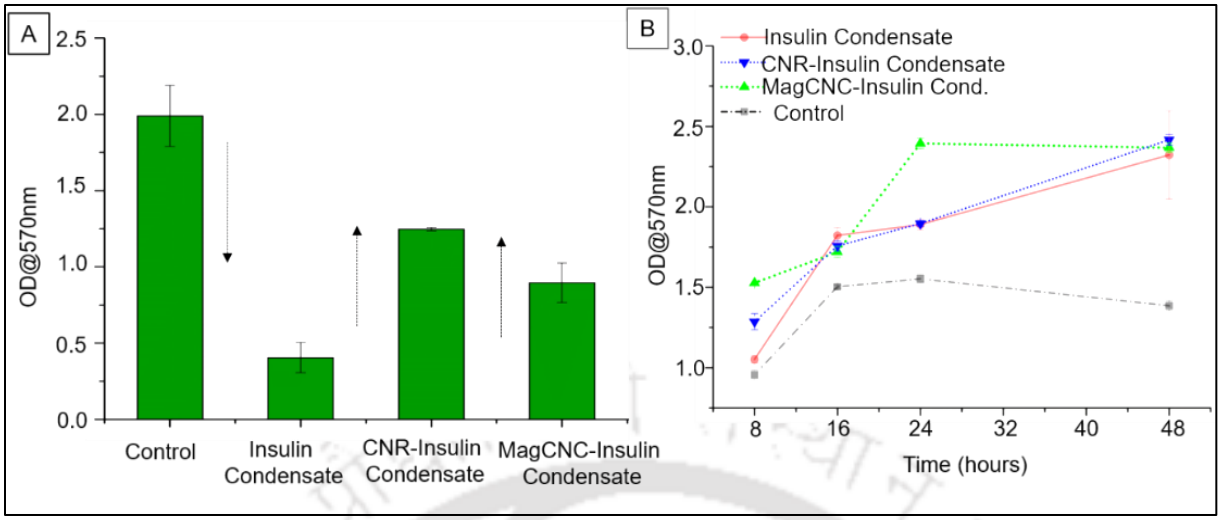


**Figure 4.13.** (A) Bar graph illustrating the growth of BHK-21 fibriblasts cells on different surfaces, i.e., polysterene surface (control), insulin condensate film, CNR-insulin condensate film, and MagCNC-insulin condensate film. The growth of the cells reduced in insulin condensate surface, however, increased in both CNR and MagCNC inuslin condensates; (B) Time dependent growth profile of BHK-21 cells upon addition of 500 µl of insulin condensate, CNR-insulin condensate, and MagCNC-insulin condensate solution to growth media. All the three improved the cell growth till 32 hours of incubation in varying degrees. The MTT assay results confirmed that the condensates were non-cytotoxic.

Figure 4.13 A shows the final growth profile of the BHK-21 cells on different surfaces, i.e., polystyrene surface (control), and different condensate surfaces. The growth of fibroblasts was maximum at the polystyrene surface (control ) with healthy cell morphologies observed after 48 hours of incubation (Figure 4.14 A). However, the insulin condensate surface did not favor the adhesion and growth of BHK-21 cells. The thin film also appeared to have ruptured, in addition with the cells being in suspension rather than adhered (Figuire 4.14 B). In contrast, the CNR-insulin condensate favored the adherence of BHK-21 cells and resulted in the significant

improvement of cell growth with healthy morphology (Figure 4.14 C). The MagCNC-insulin condensate also favored cell growth with better adhesion pattern than insulin-condensate but poorer than CNR-insulin condensate (Figure 4.14 D). Interestingly, the MagCNC-insulin condensate was found to adhere on the surface of the fibroblasts cells grown on the MagCNC-insulin condensate film (Figure 4.14 E), which can be further studied deeply. The observation suggested that MagCNC-insulin condensate could be explored for its cell-targeting potential. Next, 5% (v/v) of insulin condensate, CNR-insulin condensate, and MagCNC-insulin condensate in plain DMEM was added to the culture wells where BHK-21 cells were grown. The time-dependent growth of BHK-21 cells in presence of the condensate variants has been shown in Figure 4.13 B. The cells were found to show significantly higher growth in insulin condensate, CNR-insulin condensate, and MagCNC-insulin condensate in comparison to the control, and without any cytotoxicity as revealed by the MTT assay. The growth of the cells in presence of insulin condensate was found to be slightly higher after 8 hours than control, but significantly improved within 48 hours. Both the CNR-insulin condensate and MagCNC- insulin condensate showed significant improvement of growth after 8 hours in comparison to both the control and insulin condensate. However, CNR-insulin condensate and MagCNC-insulin condensate showed different pattern of cell growth. MagCNC-insulin condensate exhibited a stationary phase after 24 hours, whereas, CNR-insulin condensate showed a gradual increment in growth till 48 hours. Figure 4.14 F, 4.14 G and 4.14 H displays the microscopic images of the morphology and growth of BHK-21 cells on insulin condensate, CNR-insulin condensate and MagCNC-insulin condensate, respectively. Here too, the fibroblasts grown in presence of MagCNC-insulin condensate appeared to take up the material inside the interior of the cells, as well as, adhere on the cell surface. These

preliminary results could be further explored to modulate the properties of insulin condensate for specific requirements.

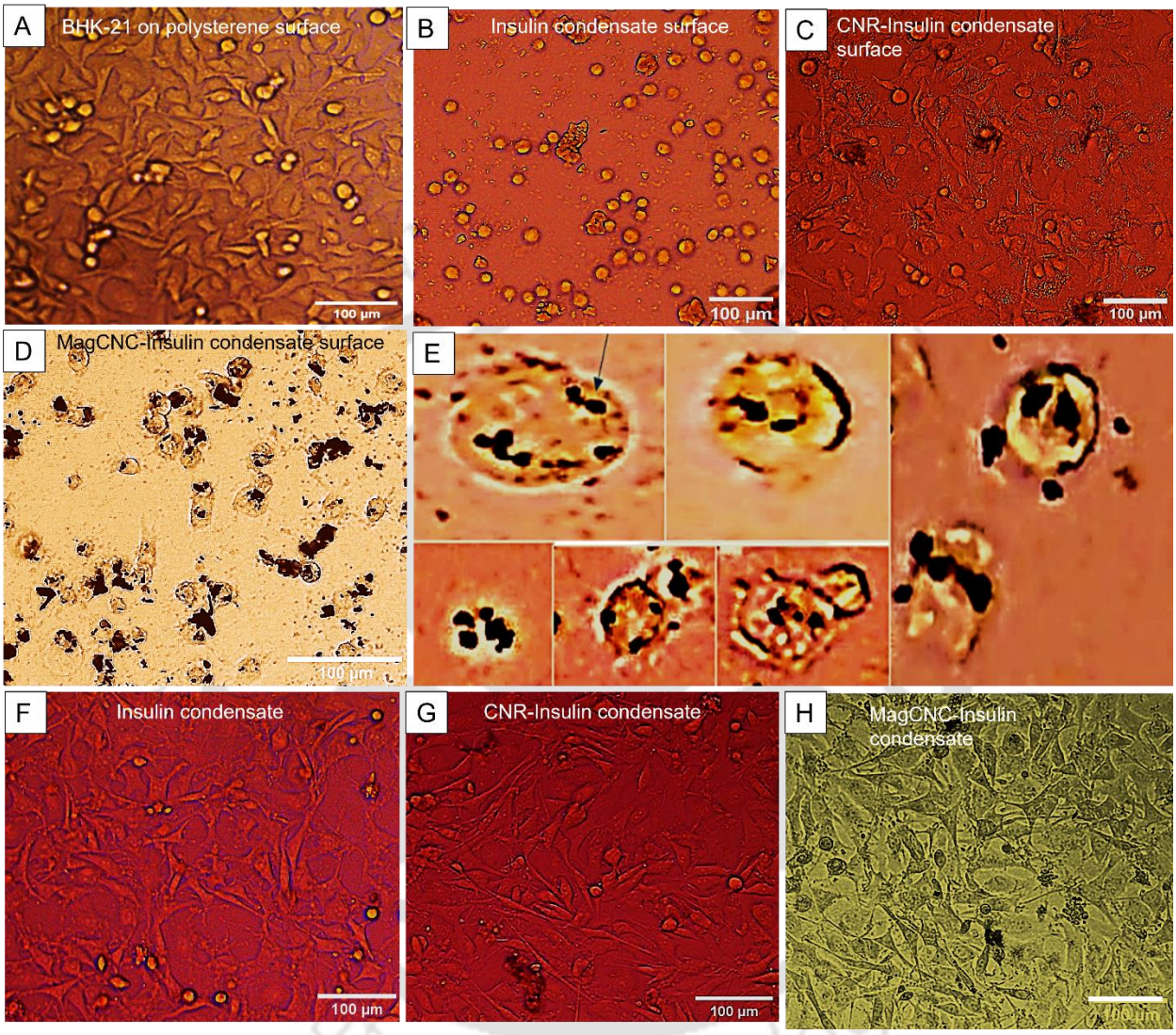


**Figure 4.14**. (A) The microscopic images of BHK-21 cells adhered on the surface of polysterene surface (control); (B) BHK-21 cells adhered on the surface of insulin condensate showing absence of adhesion; (C) BHK-21 cells on the surface of CNR-insulin condensate film showing the presence of adhesion and normal morphologies; (D) BHK-21 cells on the surface of MagCNC-insulin condensate film showing improved adhesion in comparison to insulin condensate film, adhesion of MagCNC- insulin condensate on the surface, and penetration of the material inside

the cells; (E) Cropped and enlarged images of some BHK-21 cells showing the cell adhesion and penetration of MagCNC-insulin condensate on the surface or inside of the cells, respectively; (F), (G) and (H) Microscopic image of the adhesion and growth of BHK-21 cells in presence of Insulin condensate, CNR-Insulin condensate, and MagCNC-Insulin condensate, respectively.

In addition, all the condensate forms were found to be non-cytotoxic through the MTT assay. Presumably, the positive effect of the insulin condensates was due to control release of insulin from the surfaces leading to greater uptake of glucose from the medium, promoting DNA replication and protein synthesis [236–238].

### 4.3 Discussion

The early findings about protein condensates has prompted investigation into their physiological role [239], the mechanisms which leads to the formation of the state [240], the conformational variations of proteins attained during the process, , the implication of it in neurodegenerative disorders [241] and cancer [242], and the potential of it in designing drug delivery vehicles, etc. In the context of the formation of higher-order structures by proteins via supramolecular organization, the state of condensate has been markedly distinguished from aggregate and multimer state. Unlike irreversible aggregate state and the defined multimeric complexes composed of defined numbers of monomeric units, the condensate state follows a salient pattern of organizing indefinite number of monomers into a transient droplet characterized by liquid-liquid phase transition or sol-gel transition.

The current study presents the first report of condensate formation by insulin molecules, which was found to be modulated by the presence of $Zn^{2+}$ at definite stoichiometry. Albeit the well-established understanding of higher-order structures formed by insulin, known through previously

reported studies, we have attempted to understand the macromolecular organization of insulin in a new light towards the ability to form condensate. Firstly, it is understood that that insulin binds to $Zn^{2+}$ following the ratio, [$Zn^{2+}$]:[Insulin]::1:3, in the physiological system (i.e., pH 7.4 and 37°C) to form the stable insulin hexamer. Furthermore, such a multimerization process of insulin has also been reported to be modulated by [$Zn^{2+}$] resulting in the formation of tetramers, octamers, and further higher order multimers [150]. Secondly, such macromolecular organization of insulin molecules is sensitive towards changes in pH and temperature which acts as amyloidogenesis inducer, resulting in the formation of well-defined irreversible aggregates, or fibrils or amyloids. Prompted by the aforesaid points, we found it rationale to investigate condensate forming ability of the protein distinguished from reversible [$Zn^{2+}$]:[Insulin] multimers and irreversible aggregates.

A constant 90 μM concentration of insulin in 10 mM Tris-HCl buffer was maintained at pH 7.4, and the concentration of [$Zn^{2+}$] was varied in different [$Zn^{2+}$]:[Insulin] reaction mixtures to attain a range of stoichiometric ratios ([$Zn^{2+}$]:[Insulin]::1:1,1:3,1:6). The temperature of the reaction systems was maintained at 60°C to make the environment amyloidogenic. It was observed that the elevated presence of [$Zn^{2+}$] and high temperature triggered insulin molecules to undergo conformational transition towards a β-sheet rich structure, and assemble into large sized macromolecular structure through self-assembly. The formation of the macromolcular entities and the shift towards β-sheet rich conformation was confirmed by turbidometry and ThT fluorescence emission, respectively. The process of the said observation was found to be dependent on the concentration of [$Zn^{2+}$] with the effect visibly augmented with increased [$Zn^{2+}$]. The secondary structure variation occurring at various stoichiometric ratios of the [$Zn^{2+}$]:[Insulin] reaction mixture was observed by FTIR spectra. It was noticed that the insulin molecules at [$Zn^{2+}$]:[Insulin] conformed towards a β-sheet rich structure and exhibited higher intermolecular interaction. It was

presumably due to the known stacking effect of β-sheets, the augmented hydrophobicity of the system due to increased exposure of hydrophobic regions, and hydrogen bonding between indefinite number of monomeric units to form a single condensate state.

Insulin molecules could be imagined to lose their individual conformational states to attain a macromolecular organization within a single condensate state. In order to do so, insulin molecules undergo a variant configuration that is fit for higher intermolecular interaction between each other. Also, the resultant structure is modulated by the binding of insulin and [$Zn^{2+}$], the latter role-playing as the binder to the complex. In addition, the presence of $Na^{+}$ and $Cl^{-}$ ions bind to the structure through localized ionic interactions. Dropping the pH of the solution resulted in the instant dissolution of the macromolecular structure to monomeric forms (5808 kDa). This instant dissolution of the β-sheet rich structure, to the best of our knowledge, is first reported here for any organization of [$Zn^{2+}$]:[insulin] till date. This was also the quintessential evidence which affirmed that the β-sheet rich HOs of [$Zn^{2+}$]:[insulin] formed in the experimental conditions of this present study, could not be considered as amyloid fibrils but rather the state of condensate.

Furthermore, both the [$Zn^{2+}$]:[insulin] condensate and the native insulin were found to be capable of undergoing a transition from viscous nature to an elastic nature, with the effect being augmented in the presence of elevated [$Zn^{2+}$]. Further studies could find application of the presented condensate in designing dissoluble [$Zn^{2+}$]:[insulin] hydrogels potent of entrapping and releasing drugs, nanoparticles, etc. More intriguingly, the [$Zn^{2+}$]:[insulin] condensates could be explored for oral delivery by exploring the functional state of the protein after the process of dissolution. Next, the condensate structure was investigated for its interactivity with pristine CNF and MagCNC in order to explore its potential towards designing biomaterials. An interesting phenomenon was thus observed, that insulin condensation in presence of CNF and MagCNC resulted in the resolution of

the fibers to shorter and finer fibers with increased crystallinity. Presence of semi-crystalline CNF during the condensation of insulin molecules resulted in the shortening of the fibers to discreet nanorods with increased crystallinity. Therefore, we called the nanorods thus produced as CNR. The presence of MagCNC further added to the intriguing phenomena of resolution of larger fibers to finer fibers. The rod-shaped MagCNC NPs were resolved into extremely fine threads, a number of which formed nucleating species in the pockets of the condensate surface, followed by formation of spherical CNCs. The causative agent for the aforementioned transformations could be the hydrophobic-hydrophillic phase separation at the initial start of the experiment and gradual dissolution of the phase separation as the experiment proceeded, creating a higher degree of interaction between different chemical groups.

### 4.4 Conclusion

In conclusion, insulin molecules were found to form a reversible biomolecular condensate in elevated [$Zn^{2+}$], physiological pH and high temperature. The process of formation of the condensate proceeded through, (i) Rapid binding of [$Zn^{2+}$]:[insulin] and localized ionic interactions, resulting in instant nucleation, (ii) Formation of insulin conformational variants experiencing rampant intermolecular interaction, (iii) Supramolecular organization of the conformational variants into large sized condensates with $Zn^{2+}$ acting as binder, (iv) Instant dissolution of the condensate upon pH drop. Also, there is a strong indication that insulin exhibits an aggregate-condensate duality in presence of elevated $Zn^{2+}$. Further studies are necessary to elucidate the fine equilibrium between the two states, and the rupture of the equilibrium that drives the proteins from the route of reversible condensation to irreversible aggregation. The insulin condensation in presence of CNF and MagCNC suggested a strong interactive capacity of the insulin condensate, supporting the cell proliferation of fibroblasts cells. Further studies with other

physicochemical agents might open newer avenues to develop smart materials. Although subjected to various limitations presently, the insulin condensates could also be explored in the development of oral delivery strategies as the acidic environment of the stomach presumably might dissolve the condensates into monomeric forms. However, the sudden dissolution of the condensates is a critical limitation and requires extensive research, especially towards strategies in combination with other materials.

# Chapter 5

## Modulation of amyloidogenesis through sorption of Insulin molecules on citrate-capped Gold Nanoparticle surface

---

***Motivation***

*The oral insulin formulations have been faced with several challenges, particularly with the structural intactness of the protein. In that regard, AuNP-insulin conjugation is being explored for maintaining the native-like conformation of the protein. Insulin and $Zn^{2+}$ has been previously shown to exhibit a transient aggregation called condensate at pH 7.4, which dissolves at pH 2, i.e., similar to the acidic environment of the stomach. However, a structural transition was also observed during the process of condensate formation. Therefore, AuNP-insulin conjugation is used in the condensation process to achieve structural intactness, followed by a brief investigation into cellular response.*

---

*The research work presented in this chapter has been accepted for publication as an article in the 'European Journal of Pharmaceutical Sciences' as following:*

***'**Karmakar, Srijeeb, Arjun Sankhla, and Vimal Katiyar. "**Reversible and biocompatible AuNP-decorated [Zn2+]:[Insulin] condensed assembly for potential therapeutic applications**." European Journal of Pharmaceutical Sciences (2022): 106168.)'*

## Abstract

This chapter reports the construction of Gold Nanoparticle (AUNP)-decorated [$Zn^{2+}$]:[Insulin] condensed assembly which was found to be reversible and biocompatible. At first, citrate-capped AuNPs were synthesized using the Turkevich method, and the colloidal solution was co-incubated with [$Zn^{2+}$]:[Insulin] maintaining an equimolar stoichiometry, at physiological pH, 60°C and 6 hours. Accordingly, the effect of excess $Zn^{2+}$ and surface sorption events were investigated. The surface chemistry of protein sorption on AuNPs involved interaction of surface citrate with the amyloidogenic residues of insulin Chain A (L13, E17, N18) and Chain B (V12, Y16, L17), and also C7:A, C7:B, C20:A. The surface sorption involved a number of driving forces which were predicted to be covalent, H-bonding and hydrophobic interactions. Upon the capture of a fraction of insulin molecules, the $Zn^{2+}$ was found to form cross-links between the unbound monomers and insulin bound on AuNP, thus forming nucleating species with dendritic morphology. The dendritic species self-assembled into linear and branched structure, followed by the formation of densely packed AuNP-decorated [$Zn^{2+}$]:[Insulin] condensed assembly. Subsequently, alteration of pH resulted in changes of local charges, thus destabilizing the intermolecular ionic interactions, and subsequently caused the reversal of the condensed assembly back to monomeric forms. Furthermore, the reversible AuNP-decorated [$Zn^{2+}$]:[Insulin] condensate was found to be biocompatible, and promoted the growth of the adherent cell line, BHK-21 fibroblasts. The non-cytotoxic and reversible material thus formed might have enormous applications in bioelectronics, cell culture matrices, and drug-delivery systems.

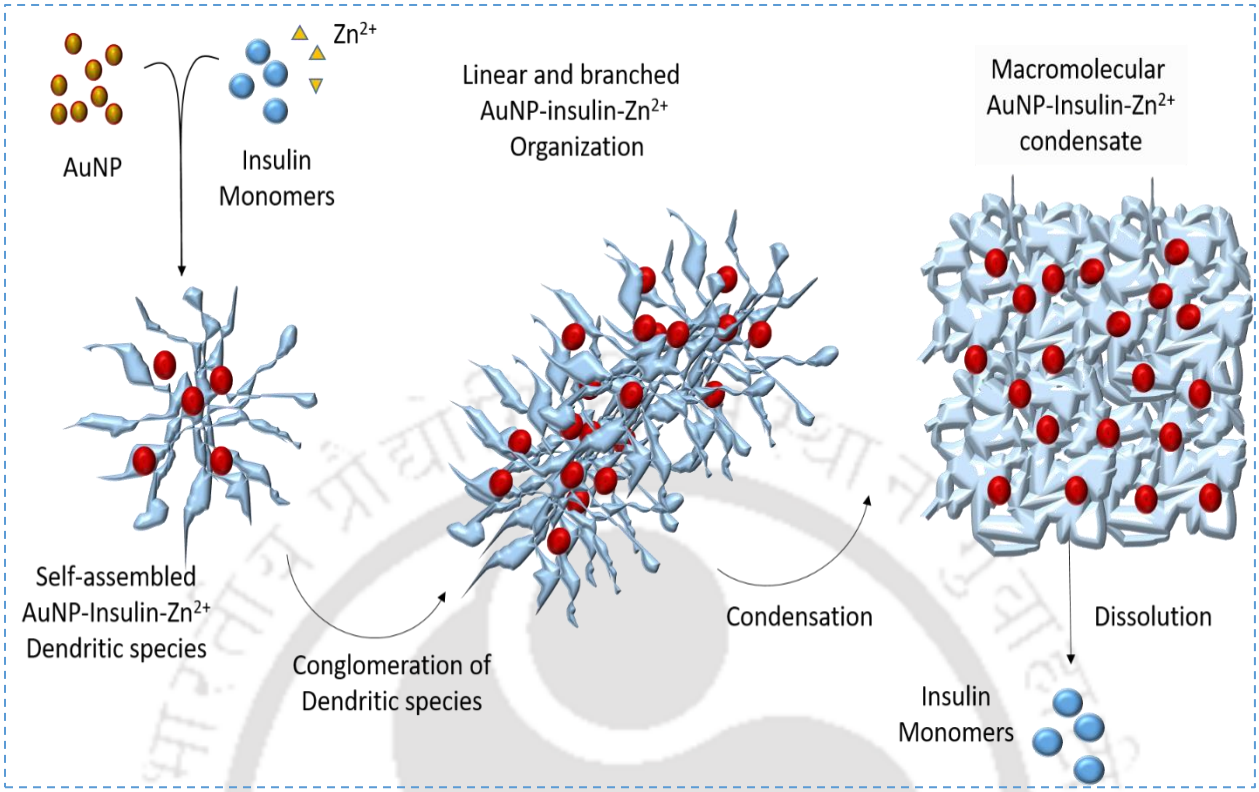


**Scheme of chapter 4**

## 5.1 Introduction

The surface sorption of proteins on metallic nanoparticles has been extensively studied over the recent years for their potential wide-range applications from bioelectronics to therapeutics [243–246]. Recently, insulin has been conjugated to Gold Nanoparticles (AuNPs,) capped with modified apple polysaccharide, for successful oral delivery of insulin in rats [247]. In this line, Cho et al reported the successful oral delivery of insulin with chondroitin-sulfate capped AuNPs [248]. In another recent report, Lee et al demonstrated prolongation of insulin activity with dextran-encapsulated AuNP insulin carriers [249]. Likewise, insulin-AuNP conjugation has been explored in developing sensing systems for the detection of insulin [250–252]. Also, thermostable AuNP coated with osmoprotectants have been investigated for restricting insulin amyloidogenesis during

thermal stress [253]. Therefore, the investigation of the interaction between insulin and AuNPs is significantly relevant and is expected to open newer avenues in theranostics. Monomeric insulin is highly unstable and reactive unless bound to $Zn^{2+}$, i.e., insulin forms stable multimers with $Zn^{2+}$ which is physiologically more relevant [254,255]. Also, multimeric forms of proteins are being investigated for their ability to form ordered assemblies and delivery of active monomers in a time-dependent manner [256]. In particular, insulin is known to form multimers in the physiological system at particular microenvironment and stoichiometry with $Zn^{2+}$, with the most stable form as the hexameric insulin [257]. Due to this reason, the present formulations of subcubcutaneous insulin therapies deliver insulin in its $Zn^{2+}$-bound hexameric form in order to prevent the aggregation of insulin monomers [258]. However, there has been a lacuna to involve higher-order organizations of insulin and considering the insulin- $Zn^{2+}$ interactions while developing AuNP-mediated insulin delivery strategies.

In the current study, we attempted to conglomerate AuNPs, insulin and $Zn^{2+}$, with the latter two in defined stoichiometric ratios. Turkevich method was deployed to synthesize citrate-capped AuNPs which is one of the simplest and reproducible method [149]. Moreover, the Turkevich method is highly adjustable and modifiable to design AuNPs with various size-ranges [259], with ease in capping varied biomolecules [260]. Deploying Turkevich method extends the modulatory scope of the system being developed, in accordance with the desired objective.

Subsequently, [$Zn^{2+}$]:[Insulin] in defined stoichiometry was co-incubated along with AuNPs whose surface sorption properties were under prime investigation. The objective of the study also had the strong consideration that the conjugation of AuNPs and insulin should be reversible. A number of biophysical techniques were deployed to probe into time-dependence of the experiments which included Thioflavin-T (ThT) fluorescence assays, Absorbance spectroscopy,

Field-Emission Transmission Electron Microscopy (FETEM), Scanning-Transmission Electron Microscopy (STEM), Matrix-Assisted Laser Desoption/Ionization (MALDI) spectroscopy, and computational methods like molecular docking using Patchdock server [163]. The prediction of interaction between citrate, which decided the surface chemistry of the AuNPs, and insulin employing LIGPLOT software was conducted [164]. The amyloidogenic propensity of insulin initiating from the regions, 3-LYQLEN-18 (A chain) [261] and 12-VEALYL-17 (B chain) [262], was especially considered as the binding of the amyloidogenic residues prevented their degree of freedom to initiate amyloidogenesis. Accordingly, the findings of the study have presented in the chapter.

## 5.2 Results

### 5.2.1 Characterization of citrate-capped AuNPs

The citrate-capped AuNPs were synthesized according to the established Turkevich method or citrate reduction method. The AuNPs were subsequently characterized for probing into the morphology, shape, size, crystal grain and absorption of light. When viewed under FETEM in the bright-field imaging mode, the citrate-capped AuNPs were found to be of spherical shape and dispersed in clusters (Figure 5.1 A and 5.1 B). The inset at 5.1 B shows the absorbance spectra of citrate-capped AuNPs exhibiting a $\lambda_{max}$ at 526 nm, which corroborates with a recent report [263]. and the SAED pattern (Figure 5.1 C) displayed a polycrystalline nature of the clusters. The SAED analysis revealed the characteristic planes of AuNPs according to JCPDS data [1], which were (111) corresponding to the d-spacing ~ 0.23 nm, (200) for ~ 0.2 nm, (220) for ~ 0.14 nm, and (311) for ~ 0.12 nm [264].

The high resolution imaging mode resolved to 800 K magnification revealed the crystal grains, i.e., the lattice fringes and atomic arrangement. Figure 5.1 D represents the HRTEM image of a citrate-capped AuNP nanocrystal showing a spherical shape, diameter of ~20 nm and the characteristic Moiré pattern revealing the atomic arrangement. The lattice fringes and atomic arrangement were well exhibited confirming high crystallinity of the AuNPs. Upon Inverse Fast Fourier Transform (IFFT) of the highlighted region of 5.1 D, the atomic arrangement of the Au atoms was observed (Figure 5.1 E). Multiple planes were detected as shown with the Reduced-FFT images displayed in Figure 5.1 F. Interplanar distances calculated for Figure 5.1 D for the planes represented by a'a'', b'b'', c'c'', d'd'' and e'e'' were 0.23 nm (111), 0.23 nm (111), 0.23 nm (111), 0.20 nm (200), and 0.20 nm (200), respectively.

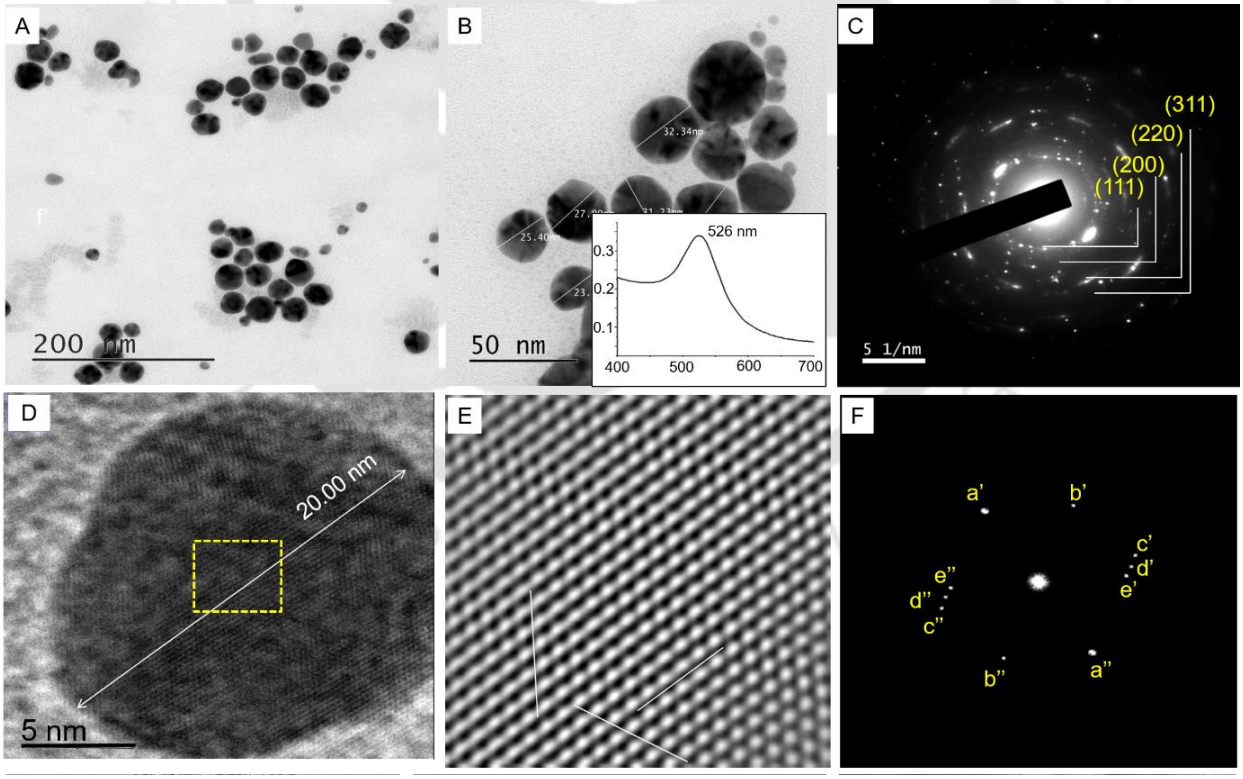


**Figure 5.1.** (A) and (B) Representative bright-field TEM images of citrate-capped AuNPs at 200 nm and 50 nm scale bar, respectively. Inset at B shows the absorbance spectra of citrate-capped

AuNPs exhibiting a $\lambda_{max}$ at 526 nm; (C) SAED pattern of citrate-capped AuNPs showing the characteristic planes (111), (200), (220) and (311); (D) HRTEM image of an AuNP at 800 K magnification; (E) IFFT image of the highlighted region of HRTEM image showing the atomic arrangement of Au atoms; (F) Reduced-FFT image of the highlighted region of HRTEM image showing multiple planes denoted by a'a'', b'b'', c'c'', d'd'' and e'e''.

Figure 5.2 A shows the size distribution profile of the AuNPs which indicated that most number of AuNPs ranged from 22 nm to 27 nm. Also, the AuNPs were found to form clusters as seen in Figure 1A and 1B, therefore inter-particle spacing/distance was analyzed and the distribution of the inter-particle spacing/distance has been shown in Figure 5.2 B. The average spacing between the AuNP particles was found to be 2.23 ± 1.25 nm, which was indicative that the AuNPs were in a clustered form. This is an important observation as it can play a decisive role in the nature of adsorption of protein molecules.

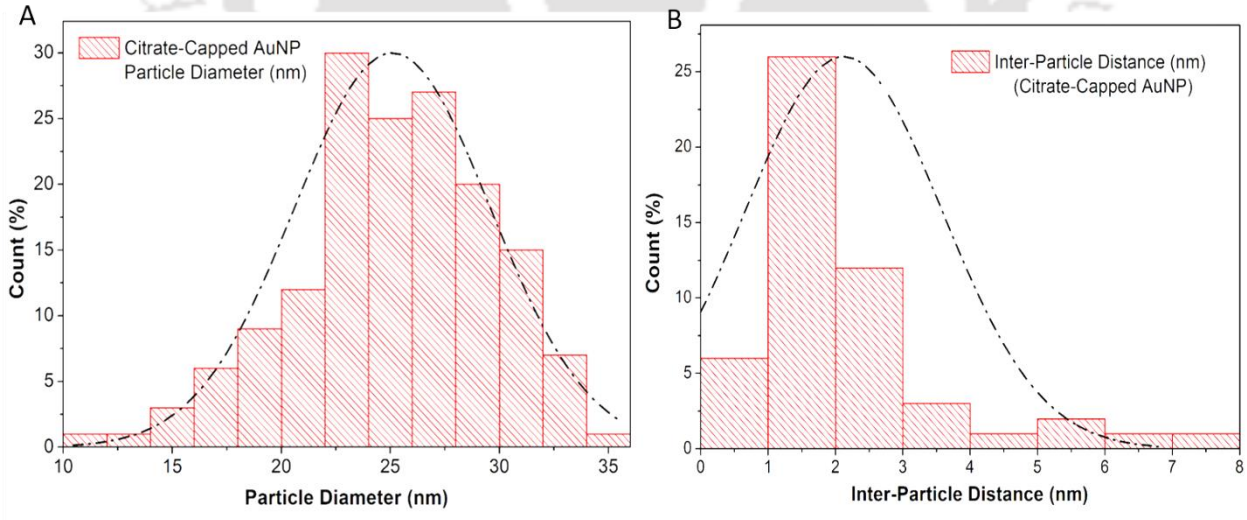


**Figure 5.2.** (A) Size distribution profile of the citrate-capped AuNPs; (B) Profile of the inter-particle spacing/distance in citrate-capped AuNPs.

### 5.2.2 Time dependent analysis of β-sheet increment in [$Zn^{2+}$]:[Insulin] and citrate-capped AuNP-[$Zn^{2+}$]:[Insulin] systems

[$Zn^{2+}$]:[Insulin] (control) and AuNP-[$Zn^{2+}$]:[Insulin] (test) samples were incubated at physiological pH and 60°C for 6 hours, independently. It is well-known that elevated $Zn^{2+}$ triggers the aggregation/multimerization of Insulin and forms a macromolecular organization rich in β-sheets [150,265,266]. ThT fluorescence assay was employed to probe into the β-sheet increment of the test and control samples, as ThT binds specifically to β-sheets and emits enhanced fluorescence [267]. It was observed that the equimolar [$Zn^{2+}$]:[Insulin] reaction mixture showed significantly elevated levels of β-sheets without exhibition of any lag phase (Figure 5.3 A). The β-sheet increment showed exponential increase within the first hour, i.e., 60 minutes of the reaction, thereafter decelerated to a constant plateau phase. Thereby, the aggregation of insulin in the control sample was confirmed. The time-dependent ThT fluorescence trend for [$Zn^{2+}$]:[Insulin] fitted into the Mononuclear Exponential Growth Model with the following equation:

$$\varepsilon = A(1 - e^{-k\,(t-tc)}) \qquad (5.1)$$

Where, ε is the fluorescence emission intensity at a given time, A is the amplitude which was estimated to be ~ 5211 ± 35; t is time and $t_c$ is the mathematical value of t at ε=0 which was found to be -1.77 ± 0.020 min, and k is the rate of emission of fluorescence which was estimated to be 0.042 ± 0.005 $min^{-1}$.

However, the AuNP-[$Zn^{2+}$]:[Insulin] sample showed no increase of β-sheets with insignificant fluctuations, which indicated that the citrate-capped AuNPs had inhibited the $Zn^{2+}$ triggered aggregation of insulin. However, there still remains a possibility of an indefinite multimerization of [$Zn^{2+}$]:[Insulin] taking place owing to the chemical propensity of $Zn^{2+}$ to form self-assembled

organizations through establishing intermolecular $Zn^{2+}$-bridges [268,269], without increment of β-sheet.

Figure 5.3 B shows the absorbance, excitation and emission spectra of AuNP-[$Zn^{2+}$]:[Insulin] reaction mixture which were normalized for comparison. The absorbance maxima was estimated at 412 nm, and the excitation/emission maxima were found to be 450 nm / 482 nm.

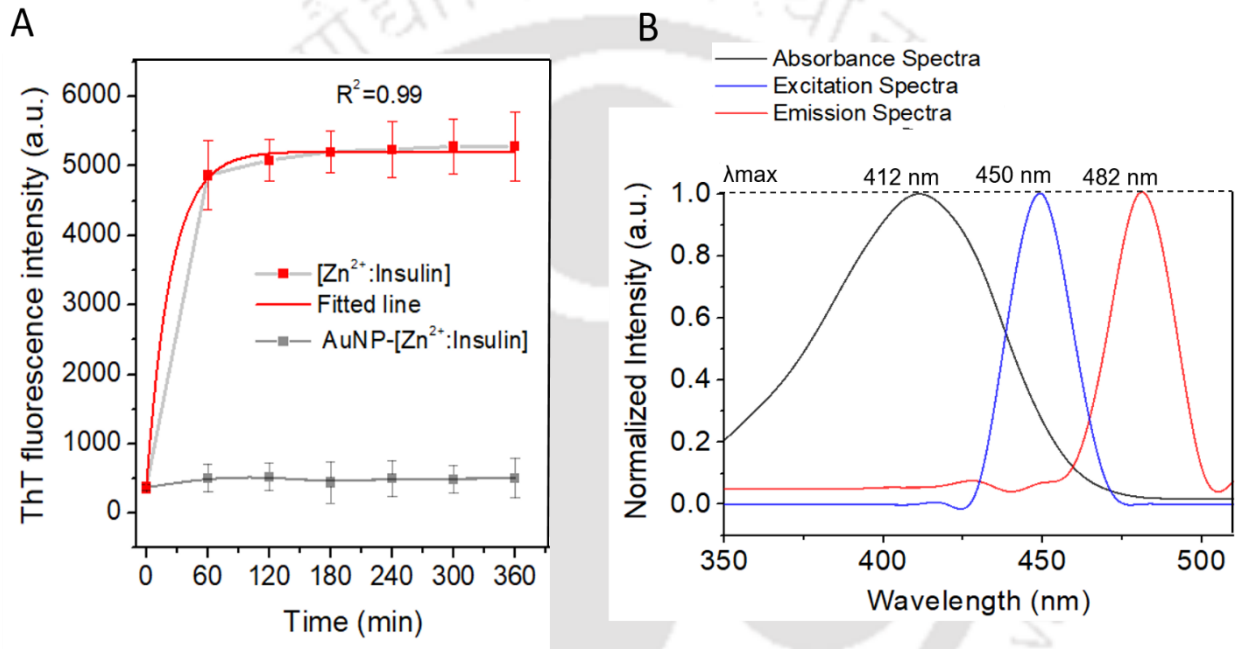


**Figure 5.3.** (A) Time-dependent profile of ThT fluorescence intensity (a.u.) *vs* Time of incubation (minutes) for equimolar [$Zn^{2+}$]:[Insulin] control sample and AuNP-[$Zn^{2+}$]:[Insulin] test sample. Each data point represents the mean ±SD obtained from three sets of experimental runs of different preparations. The red line represents the fitted line of the data sets and the $R^2$ value for the fitting is 0.99; (B) Normalized absorbance, excitation and emission spectra of AuNP-[$Zn^{2+}$]:[Insulin] reaction mixture.

### 5.2.3. Analysis of secondary structural changes using CD spectroscopy

Further secondary structural changes occurring in [$Zn^{2+}$]:[Insulin] and AuNP-[$Zn^{2+}$]:[Insulin] reaction mixtures were analysed by CD spectroscopy. Figure 5.4 A represents the CD spectroscopic profiles of [$Zn^{2+}$]:[Insulin] sample at 0 hour, [$Zn^{2+}$]:[Insulin] aggregated sample at 6 hour and AuNP-[$Zn^{2+}$]:[Insulin] sample at 6 hour.

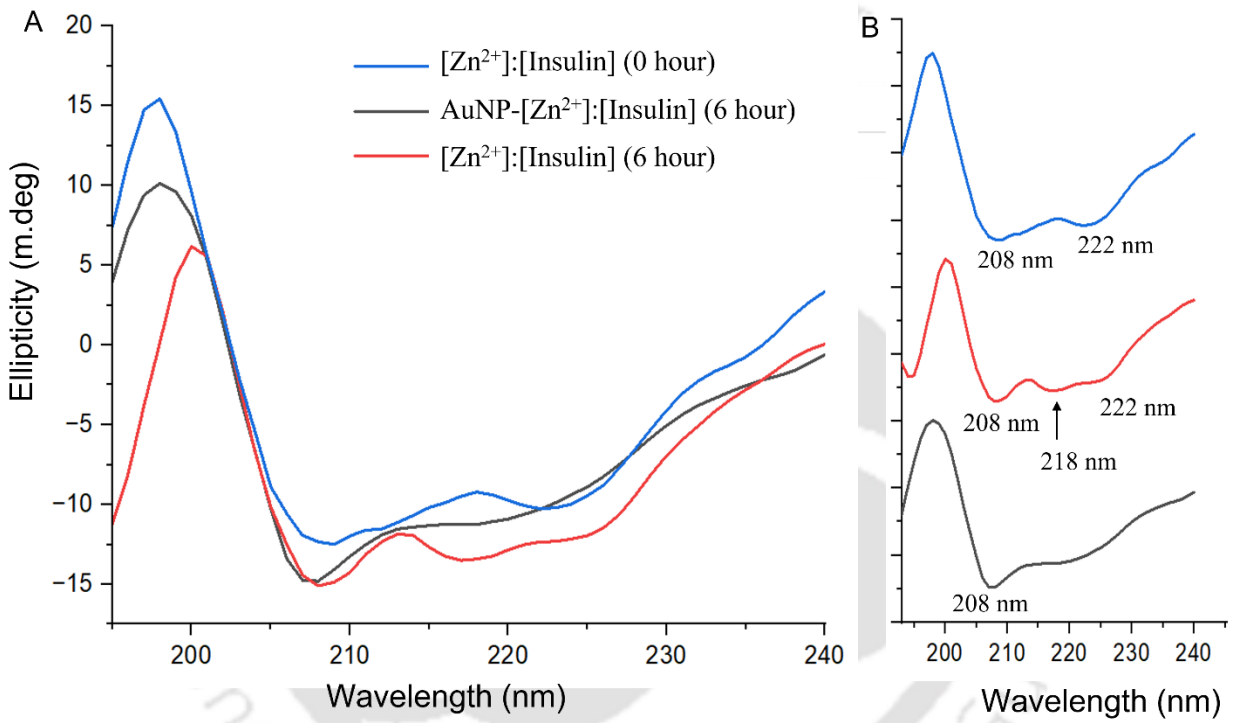


**Figure 5.4**. (A) CD profile of [$Zn^{2+}$]:[Insulin] sample (0 hour and 6 hour) and AuNP-[$Zn^{2+}$]:[Insulin] (6 hour); (B) Stacked CD profile of [$Zn^{2+}$]:[Insulin] sample (0 hour and 6 hour) and AuNP-[$Zn^{2+}$]:[Insulin] (6 hour), showing the peak positions of helix and β-sheets.

It was observed that at the start of the reaction, [$Zn^{2+}$]:[Insulin] exhibited a predominant helical structure, with ~53.96 % α-helix and ~5.99 % β-strands. It is consistent with the fact that insulin is a helical protein ((appearance of negative 208 nm and 222 nm peaks) and contains extended

structures in place of β-sheets. However, after the incubation period, the CD profile of the [$Zn^{2+}$]:[Insulin] was markedly deviant from the sample at 0 hour. The α-helix content decreased to ~15.43 % and the β-strand increased to ~26.43 % (appearance of negative 218 nm peak). Therefore, it was confirmed that the thermal stress and elevated levels of [$Zn^{2+}$] had altered the configuration of helical insulin to β-sheet rich aggregates.

However, after the 6 hour incubation with the AuNPs, the helical and β-strand content of the protein was found to be 44.17 % and 6.29 %, respectively. Clearly, incubation of [$Zn^{2+}$]:[Insulin] in presence of the AuNPs resulted in the partial protection of the helical nature of the protein and prevented formation of β-sheet structure.

To be noted, the CD spectra profile at 0 hour showed distinct negative peaks at 208 nm and 222 nm, which are characteristic peak of the helical conformation (Figure 5.4 B). However, after incubation with the AuNPs, the peak at 208 nm was found more pronounced, whereas the peak at 222 nm almost disappeared. This indicated a conformational change of the protein when bound to AuNPs. Presumably, the citrate-capped AuNPs had interacted and influenced the binding of [$Zn^{2+}$]:[Insulin], and maintained the native-like state of insulin, while its absence resulted in the formation of β-stands as indicated by the appearance of negative 218 nm peak.

### 5.2.4 Analysis of morphology using Electron microscopic studies

The inhibition of the structural change by the presence of AuNPs was suggestive of intricate interaction between the citrate-capped AuNPs and [$Zn^{2+}$]:[Insulin]. Nevertheless, the complex interaction of proteins to the surface chemistry of AuNPs to form conformational variants and thereby, reduce the amyloidogenic propensity has been previously described [244]. The AuNP-[$Zn^{2+}$]:[Insulin] reaction was probed in a time-dependent manner through FETEM imaging.

Samples drawn from the halfway of exponential phase (0 to 60 minutes) revealed that discreet units of higher-order organization of insulin were adhered on the surface of AuNPs which exhibited a dendritic morphology (Figure 5.5 A and 5.5 B).

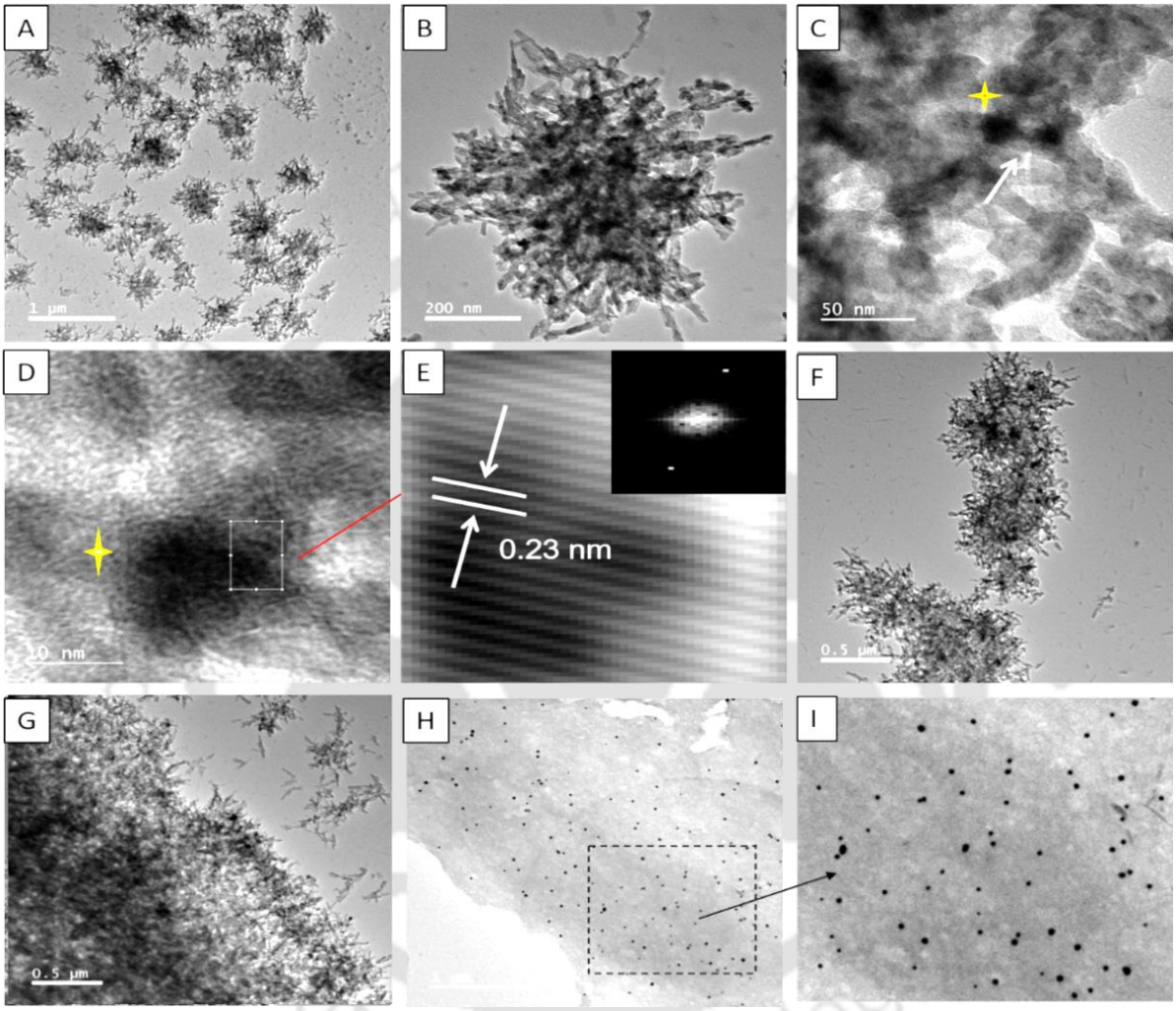


**Figure 5.5.** (A) Dendritic intermediate species formed by surface sorption of [$Zn^{2+}$]:[Insulin] on ccitrate-capped AuNPs, during the exponential phase of reaction; (B) Enlarged view of an intermediate dendritic species; (C) AuNPs embedded into the [$Zn^{2+}$]:[Insulin] assembly; (D) HRTEM image of an AuNP embedded in dendritic intermediate species; yellow crosses at C and D indicate that the AuNP at display is the same particle; (E) IFFT image analysis of the AuNP

shown in 4D, displaying the characteristic (111) plane corresponding to the d-spacing of 0.23 nm. The inset of the image shows the Reduced-FFT image of the plane; (F) and (G) Dendritic units interacting with each other to form larger organizations with linear and branched morphology; (H) The final condensation of the AuNP-[$Zn^{2+}$]:[Insulin] assemblies to form AuNP-decorated [$Zn^{2+}$]:[Insulin] condensed assembly; (I) Enlarged view of the surface of AuNP-decorated [$Zn^{2+}$]:[Insulin] condensed assembly showing well dispersed AuNPs.

The HRTEM analysis of an AuNP embedded in the higher order insulin organization (Figure 5.5 C and 5.5 D) revealed the characteristic lattice fringes of the AuNPs (Figure 5.5 E). The Inverse Fast Fourier Transform (IFFT) image of the AuNP embedded in insulin organization revealed the characteristic (111) plane of AuNPs with d-spacing 0.23 nm. The inset of 4E represents the corresponding Reduced-FFT image of the lattice fringes showing the characteristic dots of the plane under analysis. After 2h, AuNP-[$Zn^{2+}$]:[Insulin] dendritic species were found to interact and form larger organizations (Figure 5.5 F), with dendritic units merging into the larger organization (5.5 G). After the end of the incubation, supramolecular organization of AuNP-decorated [$Zn^{2+}$]:[Insulin] condensed assembly was found, with AuNPs decorating the surface of the condensed assembly (Figure 5.5 H). An enlarged image of a region of the AuNP-decorated [$Zn^{2+}$]:[Insulin] condensed assembly has been shown in Figure 5.5 I.

In order to better understand the morphology of the dendritic species, a representative low-magnification FESEM image of the clusters of dendritic species has been displayed in Figure 5.6 A. The inset at south-west displays a high-magnification image of a single dendrite, taken at 200 nm scale bar. The FESEM images revealed the only endings of the dendritic branches, and AuNPs

were not seen, which indicated that the AuNPs were not present on the surface of the dendritic species, rather embedded within inner regions. Presumably, the insulin molecules were initially adsorbed on the clusters of citrate-capped AuNPs, and as the supramolecular organization proceeded, the AuNPs were displayed on the surface.

Also, an interesting observation was the increase of inter-particle spacing in the final form of the AuNP-[$Zn^{2+}$]:[Insulin] assemblies as seen in Figure 5.5 I, compared to extremely small distances in the initial AuNP clusters (Figure 5.1 A, 5.1 B). A distribution profile of the inter-particle spacing/distance of AuNPs in the final AuNP-[$Zn^{2+}$]:[Insulin] assembly has been displayed in Figure 5.6 B. By the inter-particle spacing/distance profile, it was clear that the AuNPs were significantly more dispersed in the AuNP-[$Zn^{2+}$]:[Insulin] assemblies with an average spacing of 275 ± 116 nm. The significant increase of the inter-particle spacing/distance from an average of 2.23 ± 1.25 nm in the AuNP clusters to 275 ± 116 nm in the AuNP-[$Zn^{2+}$]:[Insulin] assemblies was indicative of the extensive re-organizational events.

Furthermore, the Absorbance spectra of the AuNP-[$Zn^{2+}$]:[Insulin] assemblies underwent a red-shift of the $\lambda_{max}$ from 526 nm to ~534 nm (Figure 5.6 C). As found by the ThT and CD profile, the insulin molecules involved in the formation of this AuNP-decorated [$Zn^{2+}$]:[Insulin] condensed assembly had native-like features rather than amyloidogenic. However, in order to reaffirm that the material around the AuNPs was insulin, elemental analysis was performed. Also, the elemental analysis of AuNP-decorated [$Zn^{2+}$]:[Insulin] condensed assembly was thought to shed light on the nature of the binding involved.

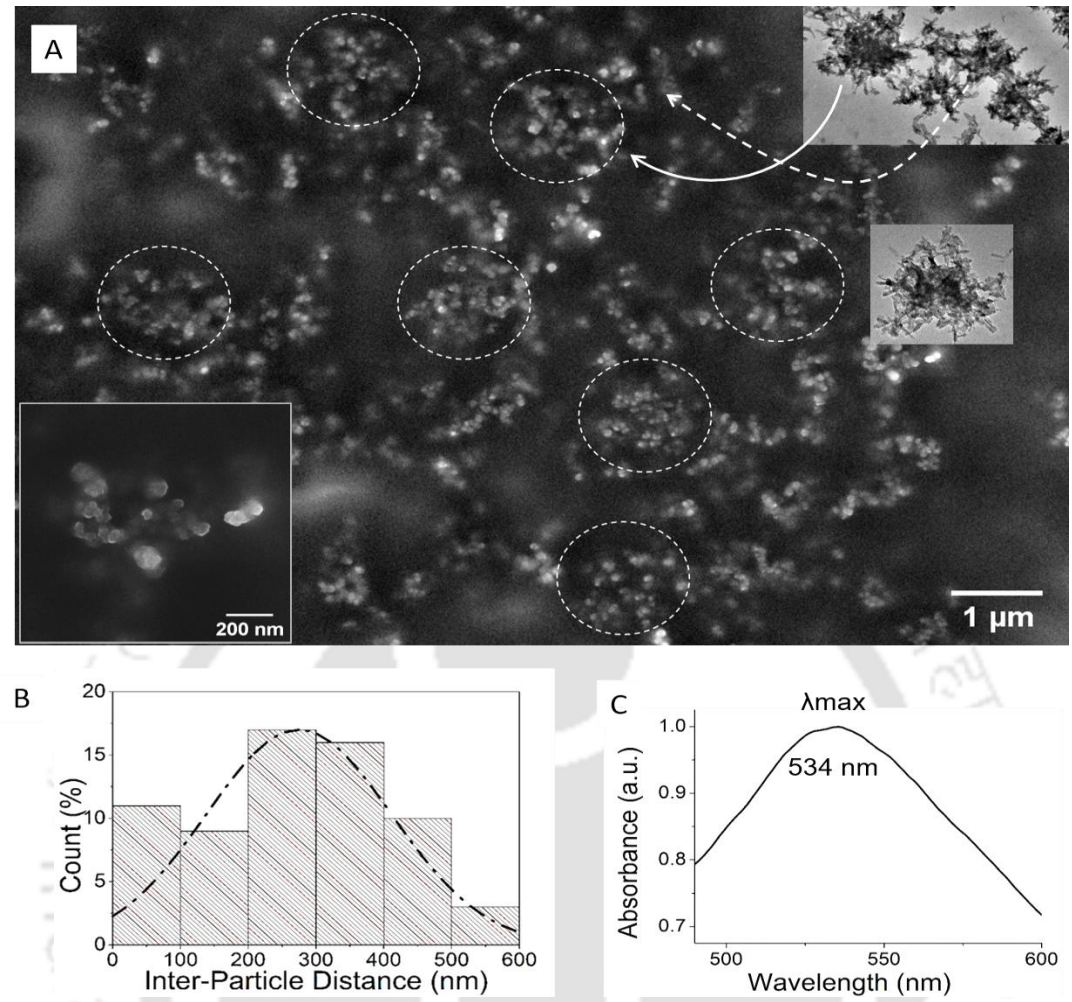


**Figure 5.6**. (A) Representative low-magnification FESEM image of the AuNP-[$Zn^{2+}$]:[Insulin] dendritic species. Inset at south-west displays a high-magnification of a dendritic species; (B) Distribution profile of the inter-particle spacing/distance between AuNPs at the final condensed form of the AuNP-[$Zn^{2+}$]:[Insulin] assembly; (C) UV-Visible Absorbance spectra of AuNP-[$Zn^{2+}$]:[Insulin] showing a $\lambda_{max}$ of ~534 nm.

### 5.2.5 Elemental analysis of the AuNP-decorated [$Zn^{2+}$]:[Insulin] condensed assembly employing STEM

In order to substantiate that the organization formed around citrate-capped AuNPs was indeed [$Zn^{2+}$]:[Insulin], elemental mapping was performed to identify the dense concentration of elements

occupying organization. The rationale was that the salient elements forming the structural units of protein, namely, nitrogen from amino groups and sulfur from the cysteine residues, should lie on the boundaries of the organization around the AuNPs. Also, if the insulin organizations were formed and intercalated by $Zn^{2+}$, the said element should also lie within the boundaries of the organization. Chloride ions of the buffer and $ZnCl_2$ was yet another candidate to have bound with the localized positive charges. Therefore, the mapping was done for N, S, Zn, Cl and Au. Figure 5.7 A shows the high resolution STEM image of a portion of the AuNP-decorated [$Zn^{2+}$]:[Insulin] condensed assembly which displays three AuNPs adhered on the surface of the organization. The Au map confirmed that the spherical particles are composed of Au atoms (5.7 B).

Figure 5.7 C and 5.7 D represents the elemental maps of N and S, respectively, which were found to densely present on the organization formed around the AuNPs, confirming that the condensed assembly was formed by insulin, as N and S could only be exhibited by the protein. Also, the S map revealed a higher concentration of S near the regions occupied by AuNPs (shown with dashed circles), indicating a possible role of cysteine residues in the surface sorption of insulin on AuNP surface.

Next, the Zn map revealed that the element occupied the organizational boundaries (5.7 E), similar to N and S maps, indicating that the insulin molecules were held together by the $Zn^{2+}$ ions. The Cl map (5.7 F) revealed a similar pattern which indicated that the localized charge interactions played an important role in the formation of the organization. The EDS spectra of the AuNP-decorated [$Zn^{2+}$]:[Insulin] condensed assembly has been displayed in Figure 5.8 and the results are listed in table 5.1.

**Table 5.1**. Elemental composition of AuNP-[$Zn^{2+}$]:[Insulin] condensed assembly through EDS.

| Element | Weight % | Atomic % |
|---|---|---|
| N | 29.67 | 40.63 |
| O | 39.11 | 49.09 |
| S | 11.12 | 6.66 |
| Cl | 3.77 | 2.04 |
| Zn | 2.42 | 0.71 |
| Au | 16.33 | 1.59 |

Thus, the surface sorption of the insulin molecules on the surface of the citrate-capped AuNPs was substantiated, with the cysteine residues playing an important role, whereas, $Zn^{2+}$ triggered the intermolecular interaction of insulin molecules to form ionic linkages among each other and form supramolecular organization.

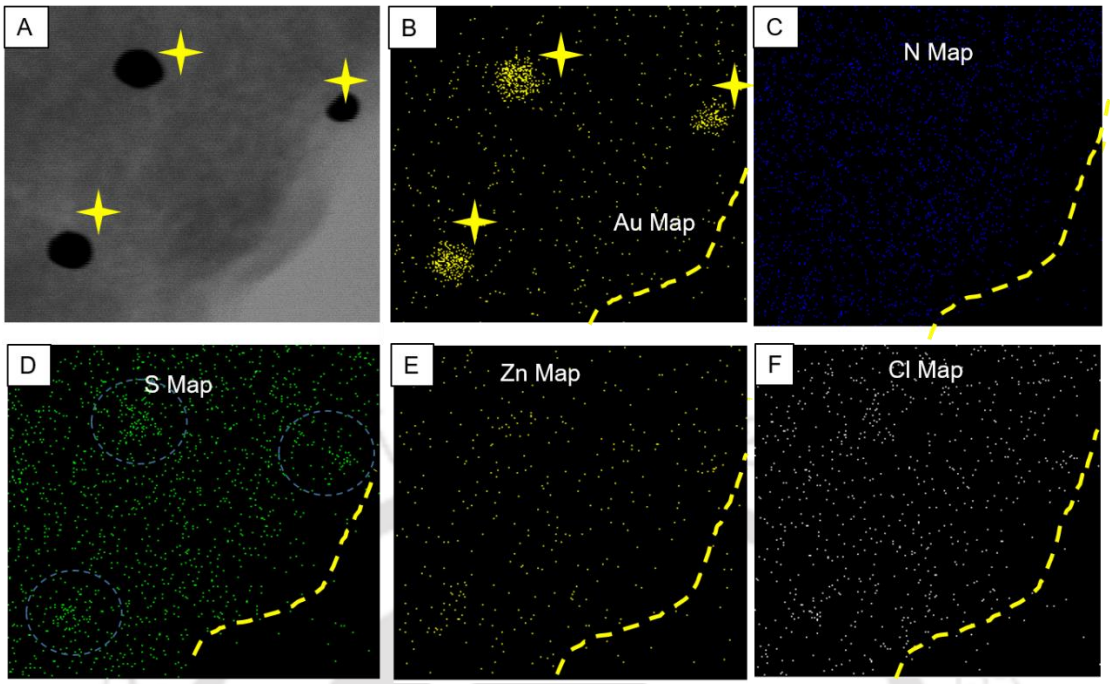


**Figure 5.7.** (A) STEM image of AuNPs embedded in the condensed assembly of [$Zn^{2+}$]:[Insulin]; (B) Au map showing that the particles in 5A are composed of Au atoms; (C) and (D) Represents the N and S map, respectively, showing that the condensed assembly was indeed formed by insulin molecules. The S atoms were found found to be densely distributed near the regions occupied by AuNPs, confirming the role of S-containing amino acids on the surface sorption insulin; (E) and (F) Represents the Zn and Cl map lying within the AuNP-[$Zn^{2+}$]:[Insulin] condensed assembly, indicating a possible role of localized ionic interactions in the formation of the organizations.

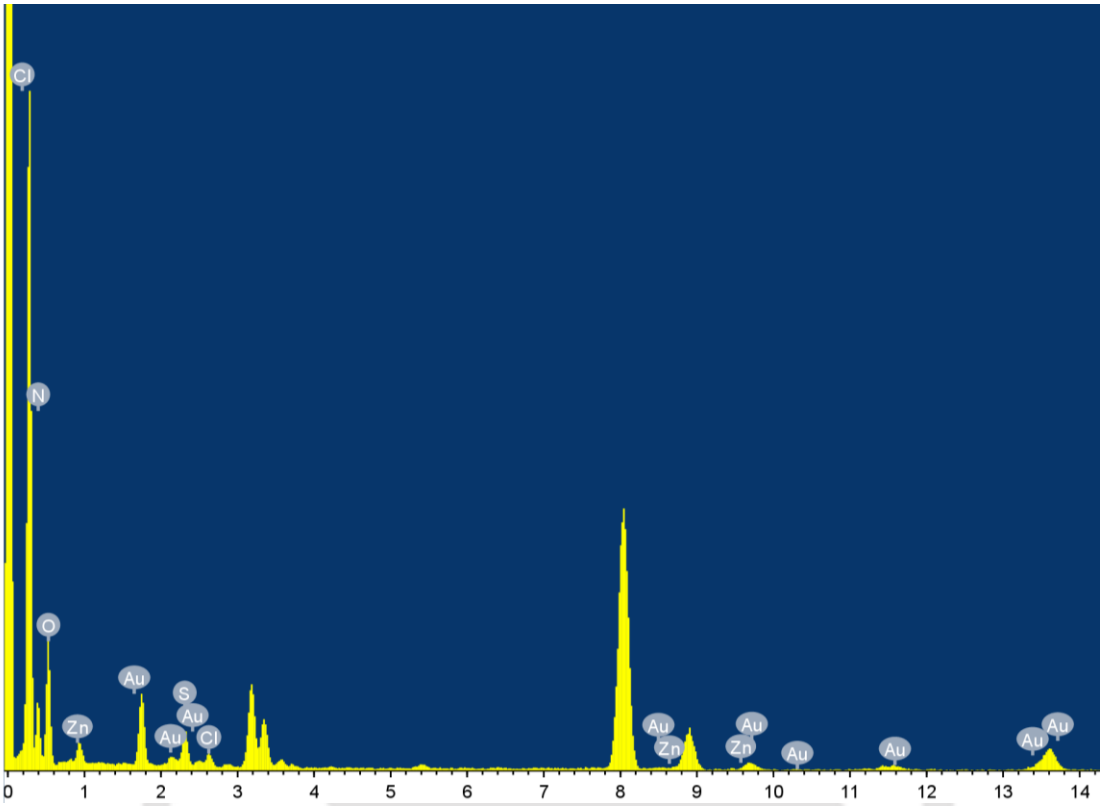


**Figure 5.8.** EDS Spectra of AuNP-decorated [$Zn^{2+}$]:[Insulin] condensed assembly. The elements present in the Cu grid has been screened. For e.g., Cu, Cr, Fe, etc.

### 5.2.6 Computational studies to analyze interaction of citrate and insulin

The nucleation of insulin molecules amyloidogenic event, i.e., structural conversion of α-helix to β-sheet, has been reported to be initiated from the aggregation-prone regions of 13-LYQLEN-18 (Chain A) [261] and 12-VEALYL-17 (Chain B) [262]. In order to investigate whether the AuNP capping agent, citrate, interacted with the amyloidogenic regions of insulin and thereby, prevented their involvement to form β-sheet rich amyloidogenic species, molecular docking and LIGPLOT analysis were employed. Through the aforementioned analyses, it was predicted that a number of these residues comprising the amyloidogenic regions of insulin possibly interacted with citrate through establishing covalent, H-bonding, and hydrophobic interactions. Figure 5.9 A and 5.9 B

shows the LIGPLOT analysis of two such possibilities, where it was predicted that the amyloidogenic residues, L13 (Chain A) and L17 (Chain B), established hydrophobic interactions with citrate. Also, amyloidogenic residue E17 (Chain A) interacted with the capping agent on the surface of AuNP (6B).

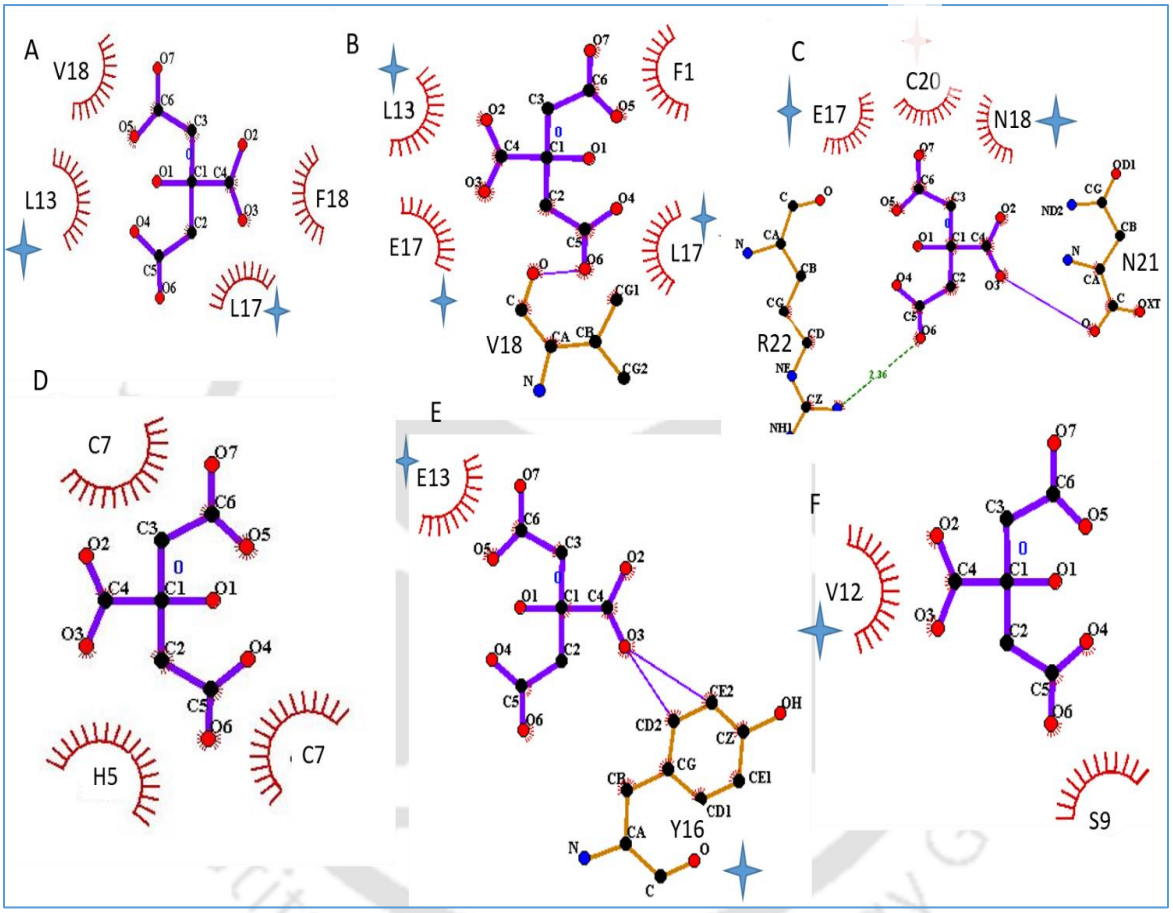


**Figure 5.9.** LIGPLOT analysis of citrate-insulin. The amyloidogenic residues are indicated by blue crosses.

Figure 5.9 C and 5.9 D predicted a possible interaction of C7 (Chain A and Chain B) and C20 (Chain A) with the capping agent of the AuNP surface, thereby, corroborating the S-map (5D) where it was revealed that S atoms were densely concentrated in the regions occupied by the AuNPs.

Also, the LIGPLOTs predicted the possible hydrophobic interaction of E17 (Chain A) and N18 (Chain A) with the capping agent, and the residue R22 to form H-bonding with the capping agent (Figure 5.9 C). Covalent bonding was predicted between the amyloidogenic residue Y16 (Chain B) and citrate (Figure 5.9 E) alongside a hydrophobic interaction with E17 (Chain A). Figure 5.9 F shows the prediction that V12 (Chain B) also possibly interacted with the capping agent of AuNP surface.

It is to be noted, that the amyloidogenic region 13-LYQLEN-18 (A chain) falls under the $3_{10}$-helix of insulin native structure, comprising of residues Chain A (13-19), and C7 is constituted in another $3_{10}$-helix from Chain A (1-9) [270,271]. Similarly, the amyloidogenic region, 12-VEALYL-17 (B chain), falls under the α-helix of the insulin native structure, comprising the residues Chain B (9-19) [270]. In an amyloidogenic event, these helical structures unwind or relaxes to generate extended structures, followed by formation of β-sheets upon maturation [272,273].

On the surface of citrate-capped AuNPs, the sorption of the insulin molecules involving the amyloidogenic residues, alongside nearby residues like C20 and R22, restricted the degrees of freedom of these helical stretches to unwind or elongate under amyloidogenic condition. This explained the possible role of the citrate-capped AuNPs in the prevention of amyloidogenesis. In contrast, the amyloidogenic regions of the control samples remained unprotected from helix unwinding, and thereby, resulted in the aggregation of the insulin molecules.

### 5.2.7 Investigation of reversibility of the AuNP-decorated [$Zn^{2+}$]:[Insulin] condensed assembly

The AuNP-decorated [$Zn^{2+}$]:[Insulin] condensed assembly, according to the findings mentioned in the previous sections, was formed by native-like units linked by the localized ionic interactions,

predominantly by the action of $Zn^{2+}$. The localized charges are strongly dependent on the pH of protein microenvironment [274], therefore, a switch of pH was presumed to dissolve the condensed assembly into monomeric units. Therefore, rapid pH reduction of the assembly was done by drop-wise addition of 1N HCl and dropping the value to pH 2, to engender alteration of the charges on the protein surface making the ionic cross-links susceptible to disintegration. Also, low pH values correspond to the abdominal environment in contrast to the physiological value, 7.4.

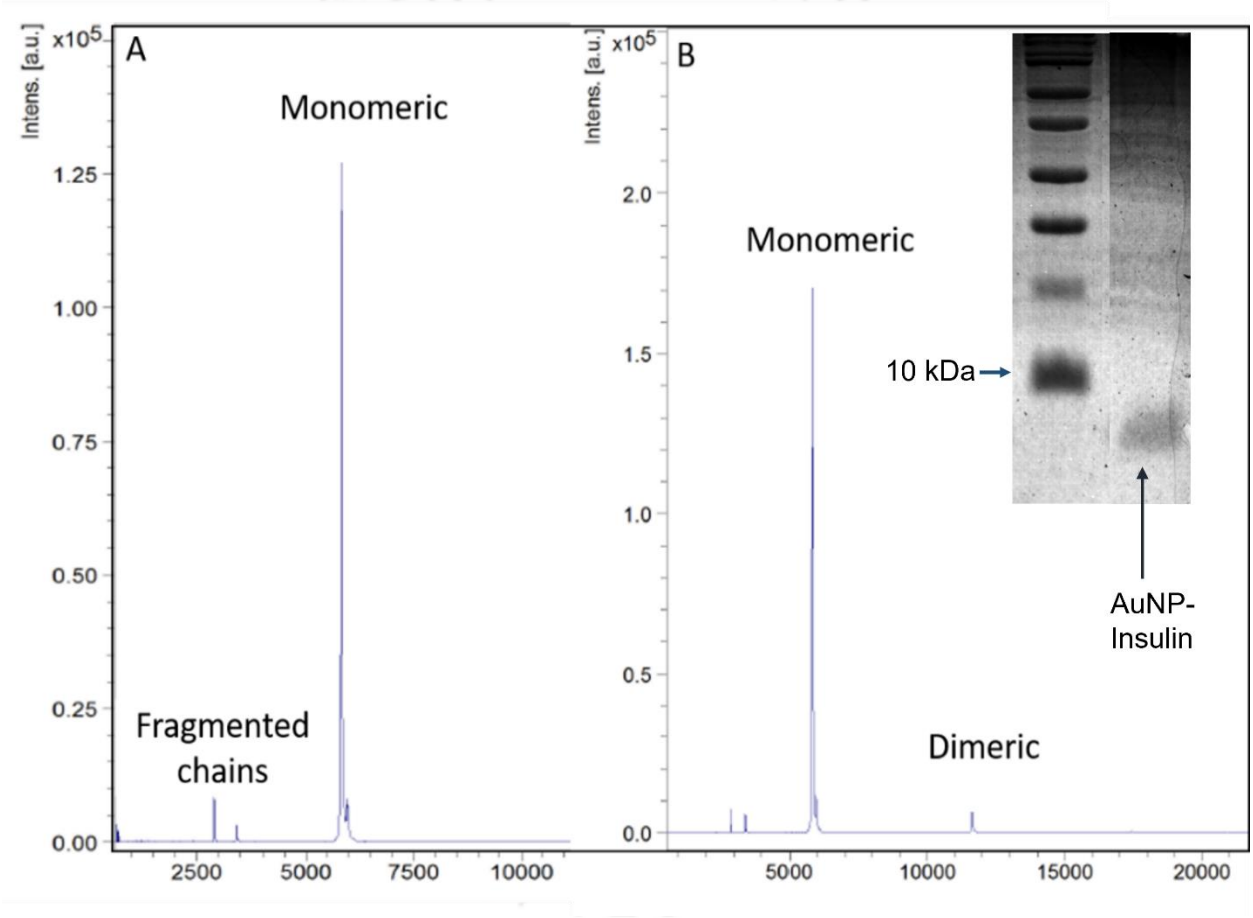


**Figure 5.10.** (A) ESI-MS plot of native solution of insulin showing a strong peak of ~5817 Da indicating monomeric form of the protein; (B) ESI-MS plot of the AuNP-decorated [$Zn^{2+}$]:[Insulin] assembly upon dissolution by rapid pH reduction, exhibiting predominant

monomeric form. Inset shows the non-reducing SDS page of dissolved AuNP-decorated [$Zn^{2+}$]:[Insulin] showing a band at 5.8 kDa, thereby displaying structural intactness.

Accordingly, ESI-MS analysis was conducted to the dissolved AuNP-decorated $Zn^{2+}$]:[Insulin] and compared with the ESI-MS plot of native insulin solution. Figure 5.10 A shows the ESI-MS plot of native insulin solution which exhibited a predominant peak at ~5817 Da, similar to the molecular weight of insulin. Fragmented chains were also detected which might have arisen due to the ionization process of ESI-MS.

Figure 5.10 B shows the ESI-MS plot of the dissolved AuNP-decorated [$Zn^{2+}$]:[Insulin] condensed assembly, wherein, a strong peak was observed at ~5815 Da, corresponding to the monomeric form of insulin. Alongside, fragmented chains and dimeric forms of insulin were also detected. The results indicated that the formation of AuNP-decorated [$Zn^{2+}$]:[Insulin] condensed assembly was primarily dependent on the intermolecular ionic interaction of insulin, and upon reduction of pH, the condensed assembly reversed to monomeric units. In order to assess the structural intactness of insulin after the dissolution event of the condensed assembly, non-reducing SDS-PAGE was performed. The inset at 5.10 B shows that the dissolved assembly formed a band below 10 kDa which is indicative of insulins molecular weight at 5.8 kDa, thereby indicating structural intactness.

Therefore, a reversible AuNP-decorated [$Zn^{2+}$]:[Insulin] condensed assembly was developed which could have a profound impact on the therapeutic delivery of insulin in oral mode.

The fate of the AuNPs after the dissolution of AuNP-decorated [$Zn^{2+}$]:[Insulin] condensed assembly was probed by employing FETEM imaging and Surface Plasmon Resonance (SPR) analysis. The FETEM images of the dissolved fraction revealed that the AuNPs re-organized into

clusters, similar to the initial form of citrate-capped AuNPs (Figure 5.11 A). However, the continuous clustering of AuNPs was not seen in the dissolved fraction, rather 5-20 AuNPs formed the clusters which were found to be scattered.

Also, it was observed that some of the clusters were contained in unidentified structures which gave rise to the doubt whether these were insulin assemblies. Therefore, EDS and STEM elemental mapping was performed. Figure 5.11 C to 5.11 E shows the elemental maps of the selected highlighted area shown in Figure 5.11 A, which were found to be Au, Cl, and Na atoms, respectively. The elemental mapping confirmed that there were no N or S atoms present, which indicated the absence of insulin.

As mentioned earlier, it was observed that the formation of AuNP-decorated [$Zn^{2+}$]:[Insulin] condensed assembly led to a red-shift of the AuNPs from 526 nm to 534 nm. Therefore, we investigated whether the dissolution of the condensed assembly left an imprint on the SPR of the AuNPs. Figure 5.11 B shows a stacked representation of the Absorbance plot of citrate-capped AuNPs, AuNP-decorated [$Zn^{2+}$]:[Insulin] condensed assembly, and dissolved fraction of the assembly. As aforementioned, there was red-shift of the AuNPs when the condensed assembly was formed (shown with red arrow).

After the dissolution, it was observed that the AuNPs absorbance underwent a blue-shift (indicated with a blue arrow), with a $\lambda_{max}$ value of ~528 nm. The slight difference of $\lambda_{max}$ with the initial citrate-capped AuNPs might have arisen due to the association of Cl and Na containing structures as seen in Figure 5.11 D to 5.11 E. Nevertheless, there was no N and S detected which indicated the dissociation of AuNPs from the insulin assemblies.

The corresponding EDS spectra of the region has been shown in Figure 5.12 inset, which revealed a 63.65 % of O atoms which were distributed throughout the region non-specifically (shown in

inset of Figure 5.12 A). Alongside, Au was found to be 18.56 %, Cl was found to be 11.02 % and Na was 6.77 %. Clearly, there were no insulin atoms attached to the AuNPs as there were no N and S atoms found. The distribution profile of the inter-particle spacing/distance has been displayed in Figure 5.12 B, which shows the restoration of the initial spacing, with an average value of 3.14 ± 1.7 nm.

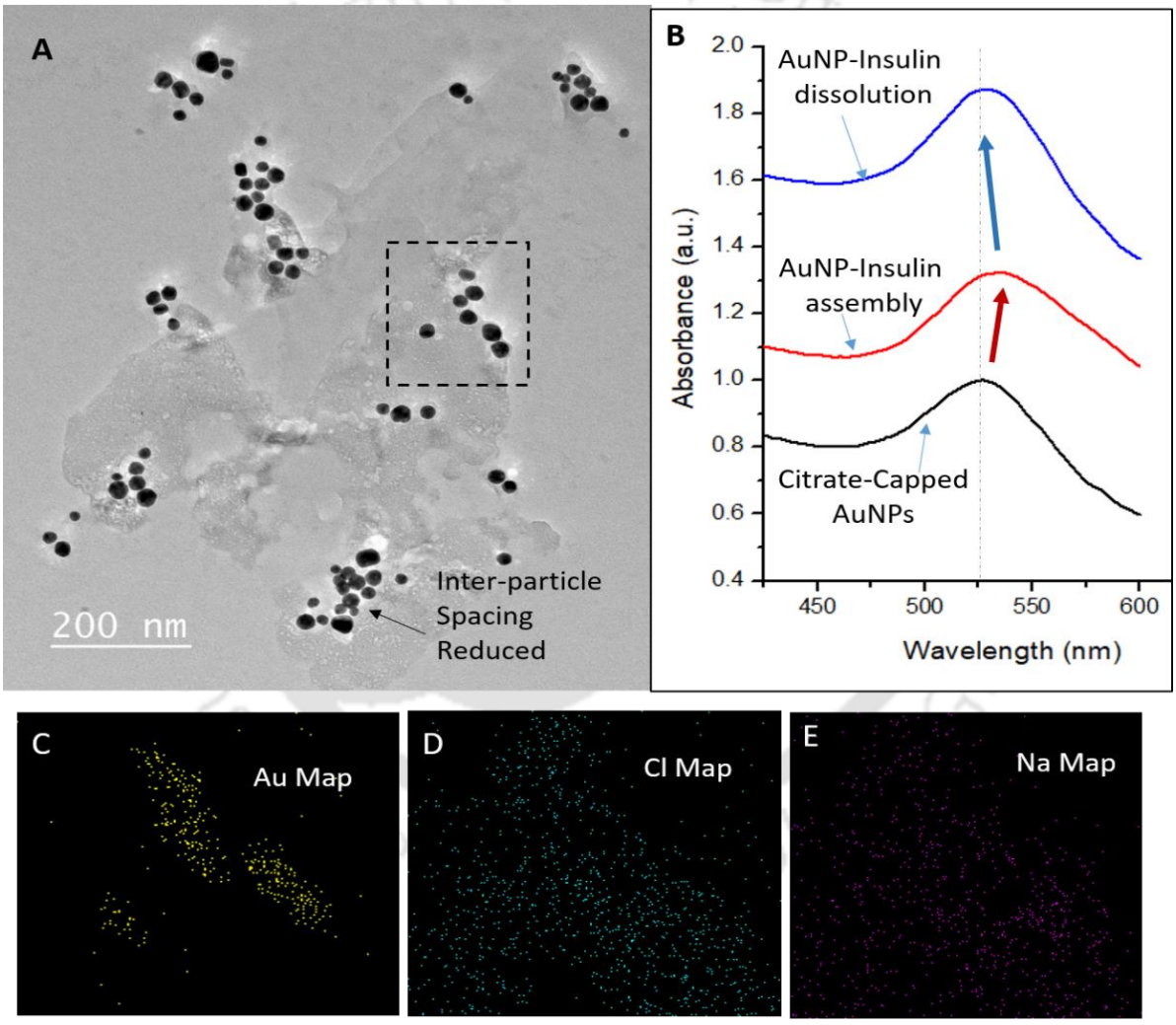


**Figure 5.11**. (A) Representative image of the AuNPs after dissolution of the condensed assembly; (B) Stacked representation of the Absorbance plot of citrate-capped AuNPs, AuNP-decorated

[$Zn^{2+}$]:[Insulin] condensed assembly, and dissolved fraction of the assembly. Red and blue arrows indicate red-shift and blue-shift, respectively; (C) Au Map; (D) Cl Map; (E) Na Map.

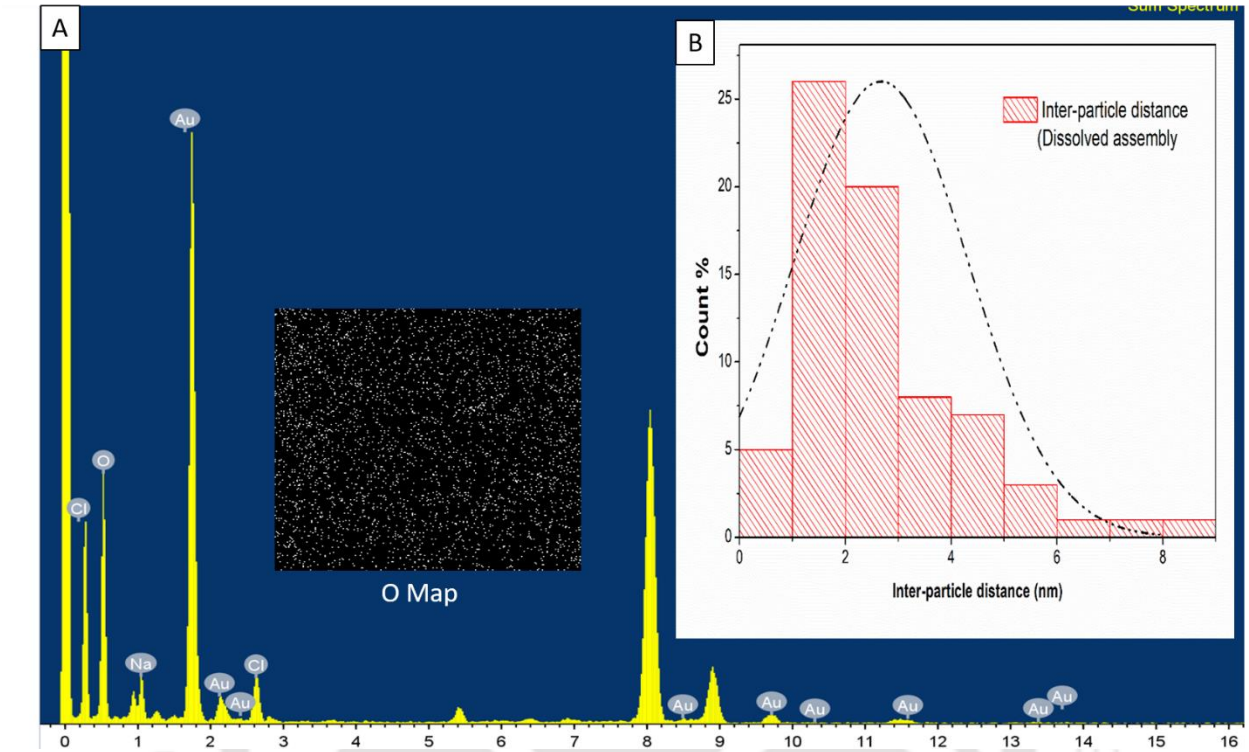


**Figure 5.12. (A)** EDS Spectra of the dissolved fraction of the AuNP-decorated [$Zn^{2+}$]:[Insulin] condensed assembly. The elements present in the Cu grid has been screened. For e.g., Cu, Cr, Fe, etc; (B) Profile of the inter-particle spacing/distance between AuNPs in the dissolved fraction of the AuNP-decorated [$Zn^{2+}$]:[Insulin] condensed assembly.

### 5.2.8 Effect of the AuNP-decorated [$Zn^{2+}$]:[Insulin] condensed assembly on BHK-21 fibroblasts

BHK-21 cells that were already seeded and grown for 24 hour in serum containing media were treated with serum free Media (control) and with 5%(v/v) dilution of AuNP-decorated [$Zn^{2+}$]:[Insulin] condensed assembly (test). A time-dependent OD measurement was done, wherein, it was observed that the fibroblasts showed significant growth enhancement when treated

with the AuNP-decorated [$Zn^{2+}$]:[Insulin] condensed assembly, in comparison to control (Figure 5.13 A).

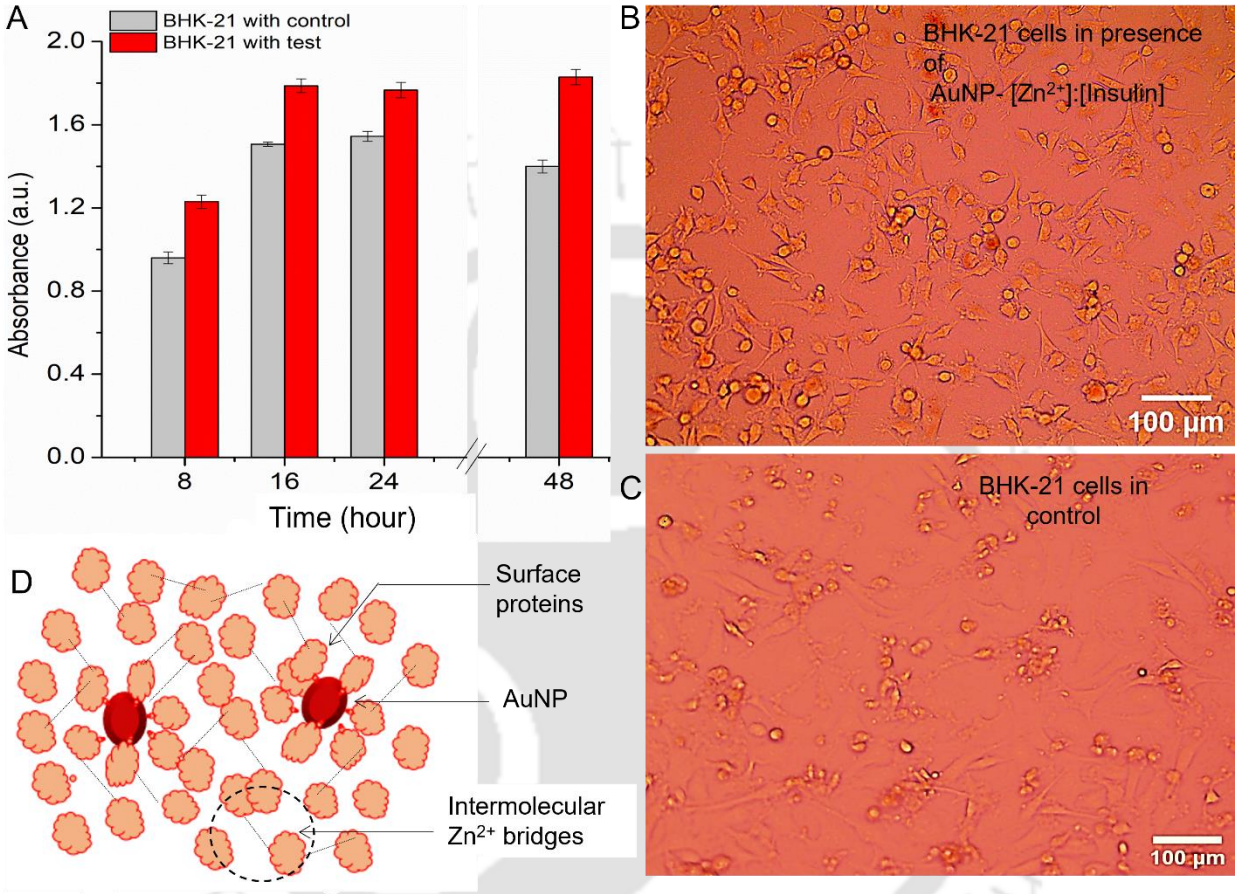


**Figure 5.13.** (A) MTT assay of BHK-21 fibroblasts grown in presence of AuNP-decorated [$Zn^{2+}$]:[Insulin] condensed assembly (red bars) and serum-free media which served as the control (Light-gray bars); (B) Microscopic images of BHK-21 fibroblasts grown in presence of AuNP-decorated [$Zn^{2+}$]:[Insulin] condensed assembly, showing both suspended and adherent cells (48 hours); (C) BHK-21 fibroblasts in control (48 hours); (D) Scheme showing the possible mechanism of the formation of AuNP-decorated [$Zn^{2+}$]:[Insulin] condensed assembly.

The growth of the BHK-21 fibroblasts showed significant increment till the 16 hour of incubation, and then reached a stagnant phase till the 48 hour. However, the control samples showed comparatively less fibroblast growth till the 16 hour, compared to the test samples. There was a slight growth of BHK-21 from 16 hour to 24 hour indicating that the growth had decelerated within the duration. Thereafter, the growth of the cells was found to decline at the 48 hour. Through MTT assay, the time-dependent growth of BHK-21 cells in AuNP-decorated [$Zn^{2+}$]:[Insulin] condensed assembly were found to show no cytotoxicity. Presumably, the AuNP-decorated [$Zn^{2+}$]:[Insulin] condensed assembly acted as growth inducer due to a slow release of monomeric insulin from the condensed assembly. Insulin has been found to favour the growth of BHK-21 fibroblasts in previous studies [275]. Therefore, the reversible AuNP-decorated [$Zn^{2+}$]:[Insulin] condensed assembly was also found to be biocompatible in BHK-21 model system. Figure 5.13 B shows the microscopic images of the fibroblasts grown in presence of AuNP-decorated [$Zn^{2+}$]:[Insulin] condensed assembly, where a mixed species of suspended and adherent cells were observed, however, exhibiting an augmented growth pattern without any cytotoxicity.

**5.2 Discussion**

The present study demonstrated the construction of AUNP-decorated [$Zn^{2+}$]:[Insulin] condensed assembly which was found to be reversible and biocompatible, which might have an immense impact on the oral delivery systems for insulin. The construction of the reversible condensed assembly is mechanistically simple and facile, and has shown promising results for delivery of monomeric insulin from a condensed [$Zn^{2+}$]:[Insulin] complex. The citrate-capped AuNPs were synthesized using a very simplistic and highly reproducible method which is known as the Turkevich method. Next, the AuNPs were co-incubated with [$Zn^{2+}$]:[Insulin] reaction mixture maintained at an equimolar stoichiometry. The assembly proceeded by the surface sorption of

insulin molecules on the citrate-capped AuNPs resulting in the formation of dendritic species. It was followed by the condensation of the dendritic assemblies to highly compact assembly AuNPs-decorated [$Zn^{2+}$]:[Insulin] assembly.

Figure 5.13 D shows a schematic representation of the possible mechanism of the formation of AuNP-decorated [$Zn^{2+}$]:[Insulin] condensed assembly. At first, the insulin molecules interacted with the citrate-capped surface of AuNPs through a number possible interactions ranging from covalent bonding (Y16: citrate, figure 5.9 E), H-bonding (V18: citrate, figure 5.9 B and N21:R22:citrate, figure 5.9 C), and hydrophobic interactions (shown as radiant lines in figure 5.9 A-5.9 F). A number of the residues establishing these interactions constitutes the amyloidogenic regions of insulin, 13-LYQLEN-18 (A chain) and 12-VEALYL-17 (B chain). These amyloidogenic regions have also been reported to lie within the helical components of the native structure. The amyloidogenic residues L13, E17 and N18 of Chain A and amyloidogenic residues of V12, Y16, L17 of Chain B were predicted interact with citrate in a number of modes. Presumably, the surface sorption of the insulin molecules through interaction of AuNP capping agent, citrate, had checked the degrees of freedom of these helical amyloidogenic regions and thereby prevented the aggregation of insulin. This was corroborated by the ThT profile (Figure 5.3) and CD spectroscopy profile (Figure 5.4) where it was confirmed that AuNP-[$Zn^{2+}$]:[Insulin] did not show β-sheet increment.

However, the presence of the elevated levels of $Zn^{2+}$ ions established intermolecular ionic interactions to form an assembly of monomeric insulin condensed to a macromolecular arrangement. A similar effect was also observed by Lin et al. where they reported tightly self-assembled multimeric organization of insulin while adsorbing on the surface of nanodiamonds [276]. This is also corroborated by the Zn map (Figure 5.7 E) where Zn atoms were found to lie

within the condensed assembly. This was possibly due to the formation of cross-linking intermolecular ionic linkages, which has been previously reported in other studies on similar lines [277,278] The S map (figure 5.7 D) showed that the S atoms were densely present near the AuNPs, which indicated an interaction of cysteine residues of insulin in the surface interaction with AuNPs. The LIGPOTs 5.9 C and 5.9 D corroborated with the prediction that C7 (Chain A), C7 (Chain B) and C20 (Chain A) possibly interacted with citrate.

As the local ionic charges of protein are largely dependent on the pH of the environment, a rapid pH reduction resulted in the alteration of these charges, thereby, destabilizing the intermolecular ionic interactions. This resulted in the dissolution of the condensed assembly to monomeric forms as indicated by the ESI-MS plot of dissolved AuNP-decorated [$Zn^{2+}$]:[Insulin] condensed assembly (Figure 5.10 B). However, when BHK-21 cells were grown in presence of AuNP-decorated [$Zn^{2+}$]:[Insulin] condensed assembly, the metabolism presumably resulted in slight changes of local pH of the microenvironment, causing local dissociation of insulin molecules, followed by uptake and metabolism.

Hence, the present study showed the formation of a transient condensed assembly of [$Zn^{2+}$]:[Insulin] with surface decorations of citrate-capped AuNPs, which was found to be reversible and biocompatible.

**5.3 Conclusion**

Reversible and biocompatible AuNP-decorated [$Zn^{2+}$]:[Insulin] condensed assembly has been designed in this study by exploiting the surface sorption properties of insulin on citrate-capped AuNPs. The elevated levels of $Zn^{2+}$ triggered intermolecular ionic interactions among the insulin monomers to form an organized and condensed assembly of native-like insulin molecules, which could be reversed upon alteration of pH. The transient state condensate form of the insulin

molecules, and the surface sorption of insulin molecules with the residues of the amyloidogenic region prevented the structural conversion of insulin to aggregates. The surface chemistry of the insulin molecules on the citrate-capped AuNPs depended on covalent bonding, H-bonding and predominant hydrophobic interactions of surface capping agent with the amyloidogenic stretches. The non-amyloidogenic sorption of insulin on the AuNPs prevented the clustering of other unbound monomers, which formed macromolecular organization with $Zn^{2+}$-linkages. The reversible AuNP-decorated [$Zn^{2+}$]:[Insulin] condensed assembly was found to promote the growth of BHK-21 fibroblast cells without showing any cytotoxic effect. Therefore, the AuNP-decorated [$Zn^{2+}$]:[Insulin] condensed assembly so formed can be of potential therapeutic applications owing to its transient nature, release of monomeric forms due to dissolution, and non-cytotoxic effect.

# Chapter 6

## Modulation of insulin amyloidogenesis through dissolution of hydrophobic-hydrophillic phase in IONP-layered $Zn^{2+}$-insulin reaction mixture

---

***Motivation***

*The supramolecular assembly of insulin and $Zn^{2+}$ is a highly modulable system which can be further tempered to create advanced nanomaterial. IONPs in hydrophobic phase introduces a phase difference with the hydrophilic insulin-$Zn^{2+}$ reaction mixture which itself transitions from hydrophilic to hydrophobic phase during aggregation. At the instant when both the nanoparticle and protein are in the hydrophobic phase, there is possibility of hybridization amongst the IONPs and insulin. Further, the possibility of using the hybrid as a cell culture platform is of desired interest.*

---

*Parts of this chapter haves been published in 'Colloids and Surfaces A' journal with the following title:*

*'Karmakar, Srijeeb, Arjun Sankhla, and Vimal Katiyar. "**A novel IONP-decorated two-dimensional [Zn2+]:[Insulin] nanosheet with ordered array of surface channels and cellular uptake potential.**" Colloids and Surfaces A: Physicochemical and Engineering Aspects 648 (2022): 129148.'*

## Abstract

This chapter presents the novel architecture and potential function of a two-dimensional nanosheet assembly formed by [$Zn^{2+}$]:[Insulin] co-incubated at a hydrophobic-hydrophilic phase-difference with iron oxide (II, II) nanoparticles (IONPs). Under thermal stress (65ºC), the supramolecular organization of [$Zn^{2+}$]:[Insulin] (at stochiometric ratio 1:1) shifted the initial hydrophilic phase of the reaction mixture to hydrophobic, which gradually dissolved with the IONP hydrophobic phase, after 24 hours aging at 4ºC. Consequent to the phase-dissolution, insulin monomers assembled into two-dimensional nanosheets by intermolecular $Zn^{2+}$-bridges, whereas, the IONPs (18-20 nm diameter) underwent extensive re-organization to ultra-small nanoparticles of 2-3 nm size. The re-organized IONPs, thereafter, adsorbed on the nanosheet surface to create ultra-small IONP-decorated insulin nanosheet. Interestingly, the nanosheets were found to interact with each other and form a stacked assembly by giving rise to striking patterns of crystalline surface wrinkles. The angular stacking of the equidimensional wrinkle lattices of stacked nanosheets created geometric arrays of ordered surface channels. This unique nanosheet surface promoted the attachment and proliferation of BHK-21 fibroblasts, and interestingly penetrated inside the cellular compartments as well as adhered on the cell surface. The two-dimensional IONP-[$Zn^{2+}$]:[Insulin] nanosheet might act as a cell-targeting system, and also contribute to the understanding of protein interactions.

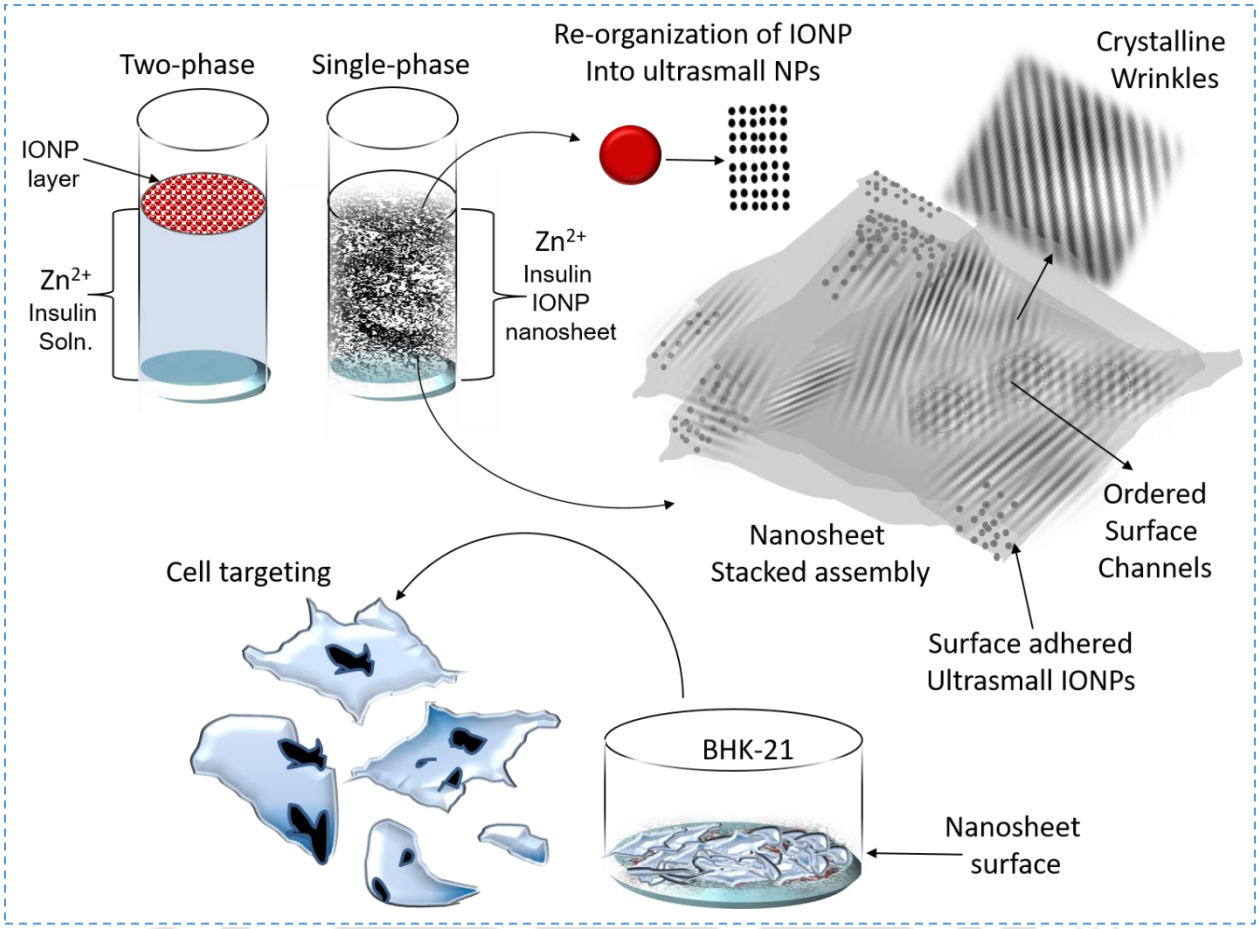


**Scheme of chapter 6**

## 6.1 Introduction

In the recent years, the supramolecular organization of proteins and peptides has been found to have an immense potential for creating several biocompatible material for varied applications, ranging from therapeutics to bioelectronics [279–281]. Proteins and peptides in combination with other metallic nanoparticles have been explored to create advanced nanostructures like enzyme-induced iron-nanostructure [282] and protein/copper nanoclusters [283], with a spectrum of functionalities. In this line, a highly functional biomimetic membrane composed of 2D crystals and nanosheets of highly-packed pore-forming membrane proteins was demonstrated by Tu el al.

which could function as a high-throughput filter [284]. with a similar objective, Zhang et al. reported the construction of an ultrathin two-dimensional nanosheet formed by single-layer assembly of Tobacco Mosaic Virus mutant (TTVm) crosslinked by $Cu^{2+}$-catalysed disulphide bond formation. The resultant protein nanosheet was found to precisely separate substances of ~4 nm order [285]. Nanosheet of fibronectic fibers assembled at a liquid-liquid interface was demonstrated to guide mesenchymal stem cells towards neuronal differentiation [286]. Further, self-assembled ovalbumin was found to form amyloid nanosheet which elicited T-cell 2 based immune response, alongside slow release of native-like ovalbumin. The ovalbumin nanosheet was also found to be capable of loading the anticancer drug doxorubicin, and delivered the same in a controlled and slow manner. The said report by Tufail et al. presented self-assembled protein to amyloid nanosheet as a potential material for immunotherapy and chemotherapy [287]. Interestingly, co-assembly of fluorescent proteins, EBFP2 and EGFP, was explored for the template-free construction of a highly-ordered fluorescent protein nanosheet for harvesting light [288]. Several other reports are being presented lately which display the potential of supramolecular assembly of proteins and peptides to create smart materials. For instance, tunable 'amyloid-like nanosheet' designed from an amyloidogenic segment of Alzheimer's Aβ was found to be efficient in retroviral transduction enhancement, and several more functionalities [289]. Therefore, studying the self-assembly of proteins in conjunction with other functional materials is emerging as highly relevant and important investigation.

In this report, we attempted to investigate the $Zn^{2+}$ triggered self-assembly of insulin in conjugation with Iron (I, II) oxide nanoparticles (IONPs) dissolved in toluene. The motivation was derived from extensive studies on insulin as a potential material for designing advanced structures [258,290], depending on the inherent interaction with $Zn^{2+}$ at physiological pH. The physiological

stoichiometry which is most relevant for [$Zn^{2+}$]:[Insulin] is 1:3, which promotes the formation of the most stable hexameric complex. However, at elevated levels of $Zn^{2+}$, insulin molecules have been found to be triggered to form higher-order organization [150]. Other than the formation of coordination complexes formed between histidine residues and $Zn^{2+}$, the latter has been found to form cross-linking $Zn^{2+}$-bridges between protein higher-order organizations. The said $Zn^{2+}$ bridges have been explored in a number of proteins as a drive for supramolecular organization, designing number of strategies for drug-delivery, sensing systems, cell culture matrices, and many more functionalities [291].

Correspondingly, variable IONPs have been investigated for their tuneable properties to design smart materials for a number of applications [292–294] Amongst the biological applications, IONPs have been recently reported to be potential carriers of bio self-healing concretes [295], to function as multifunctional biomimetic Iron Oxide nanozyme [142], as a constituent of hybrid coatings for biomedical devices owing to antibacterial and antifungal properties [296], etc. The emphasis on IONPs in biological application is based on the property of cytocompatibility and facile delivery. For instance, IONP core-shell microspheres and magnetic IONP-hollow silica spheres have been recently found to efficiently deliver therapeutic drugs [297,298]. Furthermore, ultra-small IONP-encapsulated nanogels have been recently reported to act as glutathione-responsive contrasting agent for tumor targeted magnetic resonance imaging [299]. Therefore, the effect of the IONPs on the supramolecular organization of [$Zn^{2+}$]:[Insulin] was investigated in this study, and the resultants biological response was investigated in this study. Accordingly, the findings of the study have been entailed in this chapter.

## 6.2 Results and Discussion

### 6.2.1 Transmission Electron Microcopy (TEM) studies of IONP[(b)]

TEM was deployed to probe into the morphology, size, shape, atomic arrangement, and electron diffraction pattern of bare IONPs (suspended in toluene). It was found that the IONPs were spherical in shape (Figure 6.1 A) with ~20 nm diameter (Figure 6.1 B). The SAED pattern (Figure 6.1 C) on a cluster of the IONPs revealed a polycrystalline nature with d-spacings, 0.30 nm, 0.25 nm, 0.22 nm, 0.18 nm and 0.16 nm, primarily.

The HRTEM image on a single IONP crystal at 800 K magnification revealed the lattice fringes and the characteristic Moiré pattern (Figure 6.1 D). The Inverse- Fast Fourier Transform (IFFT) of the selected area in 1D showed the atomic arrangement of the IONPs, exhibiting compact arrangement of atoms in definite geometric arrangement (Figure 6.1 E). Figure 6.1 F shows the Reduced-FFT pattern of the selected area of the IONP displayed in 6.1 D. The corresponding planes, their intersection, and interplanar spacing thereby, were analyzed. The characteristic planes of IONPs which were not detected in the SAED pattern, were exhibited by the HRTEM. The Reduced-FFT images revealed the crystallographic planes corresponding to the d-spacings, 0.54 nm, 0.34 nm, 0.30 nm, 0.25 nm, and 0.16 nm, some of which corresponded with the SAED pattern. The d-spacing value 0.22 nm and 0.30 nm with the (222) and (220) plane of face cubic $Fe_3O_4$ crystals, respectively, and 0.18 nm corresponds to $Fe_2O_3$ (024) [300]. Interestingly, the d-spacing 0.54 nm corresponds to the (100) or (010) plane of $FeS_2$ [301].

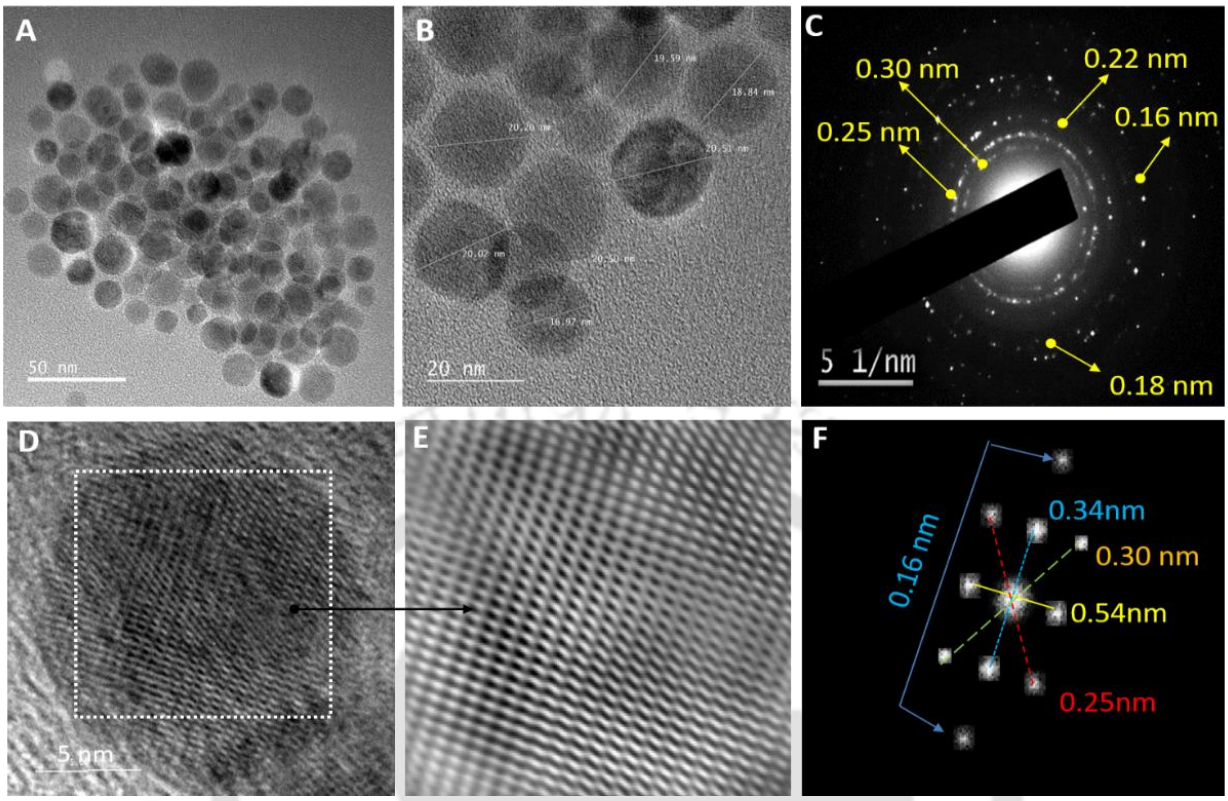


**Figure 6.1.** (A) Representative bright-field FETEM images of bare IONPs at 50 nm scale bar; (B) High magnification FETEM image of bare IONPs displaying a size of ~20 nm; (C) SAED pattern of bare IONPs with characteristic d-spacing values; (D) Representative High Resolution TEM (HRTEM) image of a IONP crystal displaying the characteristic lattice fringes and Moiré pattern; (E) Inverse FFT image of the atomic arrangement of the selected region of the IONP displayed at D; (F) FFT transformation (mask applied) of the HRTEM image displaying the characteristic d-spacing values.

### 6.2.2 Morphology and crystallinity analyses of the IONP-[$Zn^{2+}$]:[Insulin] conjugate

After the dissolution of the hydrophobic layer of the IONPs covering the surface of the [$Zn^{2+}$]:[Insulin] reaction mixture, the resultant single-phase reaction products were viewed under TEM. The IONP-[$Zn^{2+}$]:[Insulin] conjugates were found to form thin-layer nanosheets which

stacked upon each other to form a complex overlapping assembly. Figure 6.2 A and 6.2 D shows the IONP-[$Zn^{2+}$]:[Insulin] nanosheets thus formed in bright-field TEM. In the said figures, the highlighted regions marked as 1 were processed with ImageJ to obtain the enlarged images displayed in Figure 6.2 B and 6.2 E.

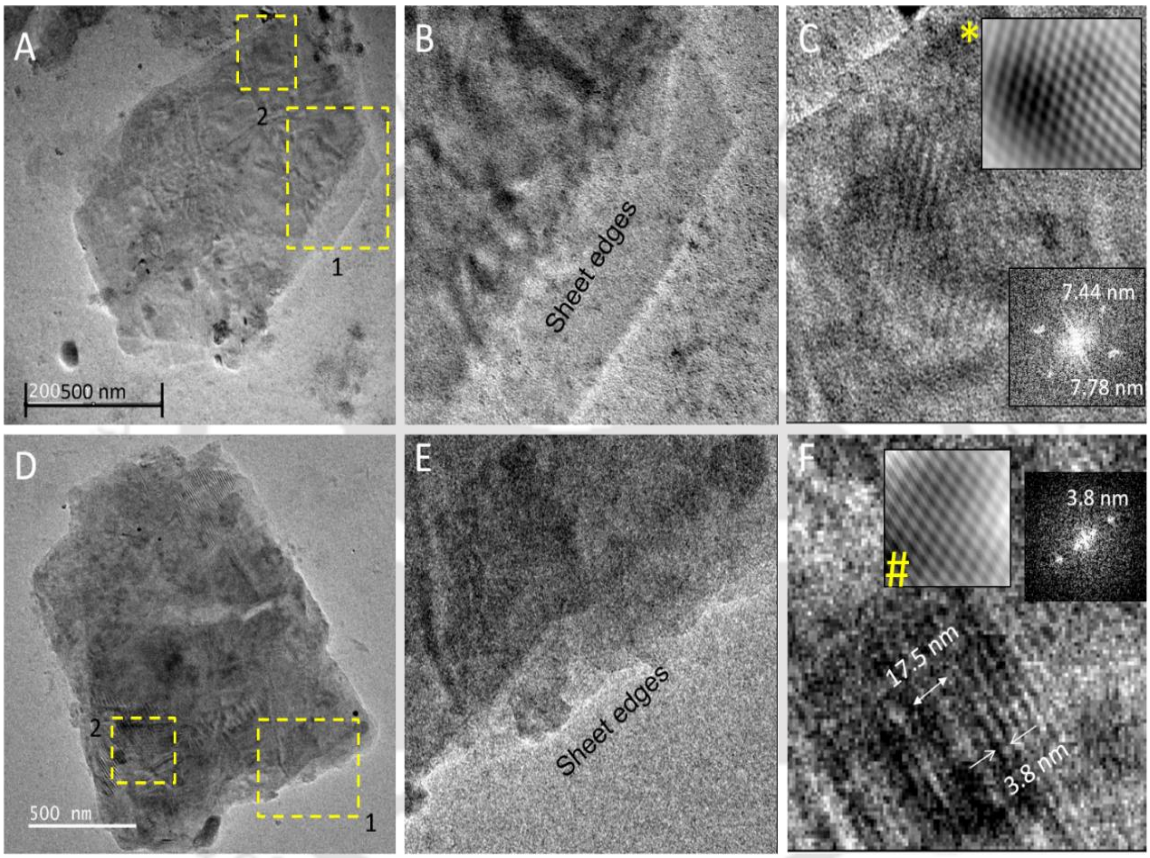


**Figure 6.2.** (A) and (D) Representative FETEM images of IONP-[$Zn^{2+}$]:[Insulin] nanosheet assembly; (B) and (E) Representative FETEM images of nanosheet edges showing the thin-section two-dimensional surface; (C) and (E) FETEM images of the surface corrugations showing crystalline wrinkles with FFT transformation and IFFT atomic arrangements.

The enlarged images of the regions one displays the overlapping edges of the nanosheets. Interestingly, the surface of the nanosheets displayed a heterogenous morphological feature by exhibiting crystalline-like arrangement at patches. Figure 6.2 C shows the enlarged image of the highlighted region 2 of 6.2 A, which was found to exhibit lattice fringes. The inset of the 6.2 C shows the FFT (inset) of this region displaying the 'dots' which appear in crystalline substances.

The inset marked with a (*) shows the IFFT image of the selected region which revealed a crystalline arrangement of particles in that region. Likewise, Figure 6.2 F shows the highlighted region 2 of 6.2 D which displayed lattice fringe-like pattern with a characteristic crystalline FFT (inset). The inset marked with a (#) shows the IFFT image of the selected region which also revealed a crystalline arrangement of particles in that region

The interplanar d-spacings exhibited by the crystallographic regions of the nanosheets were calculated to be 7.44 nm and 7.78 nm (Figure 6.2 C), and 17.5 nm and 3.8 nm (Figure 6.2 F). These elevated values do not correspond to the characteristic interplanar d-spacings reported anywhere for IONPs, which indicated that these were not exhibited by IONP, should in case it was presumed IONPs conjugated herein.

The possible explanation for these lattice fringes to appear in the -[$Zn^{2+}$]:[Insulin] nanosheets was the surface corrugations like wrinkles, ripples and crumples which are exhibited by two-dimensional materials. Such crystallographic orientation of surface corrugations has been under investigation lately [302]. Interestingly, these crystalline nature rendered by surface corrugations has been reported for two-dimensional graphene sheets [303], but such nanosheets formed by insulin with crystallographic orientation of surface corrugations is entirely the novel finding here.

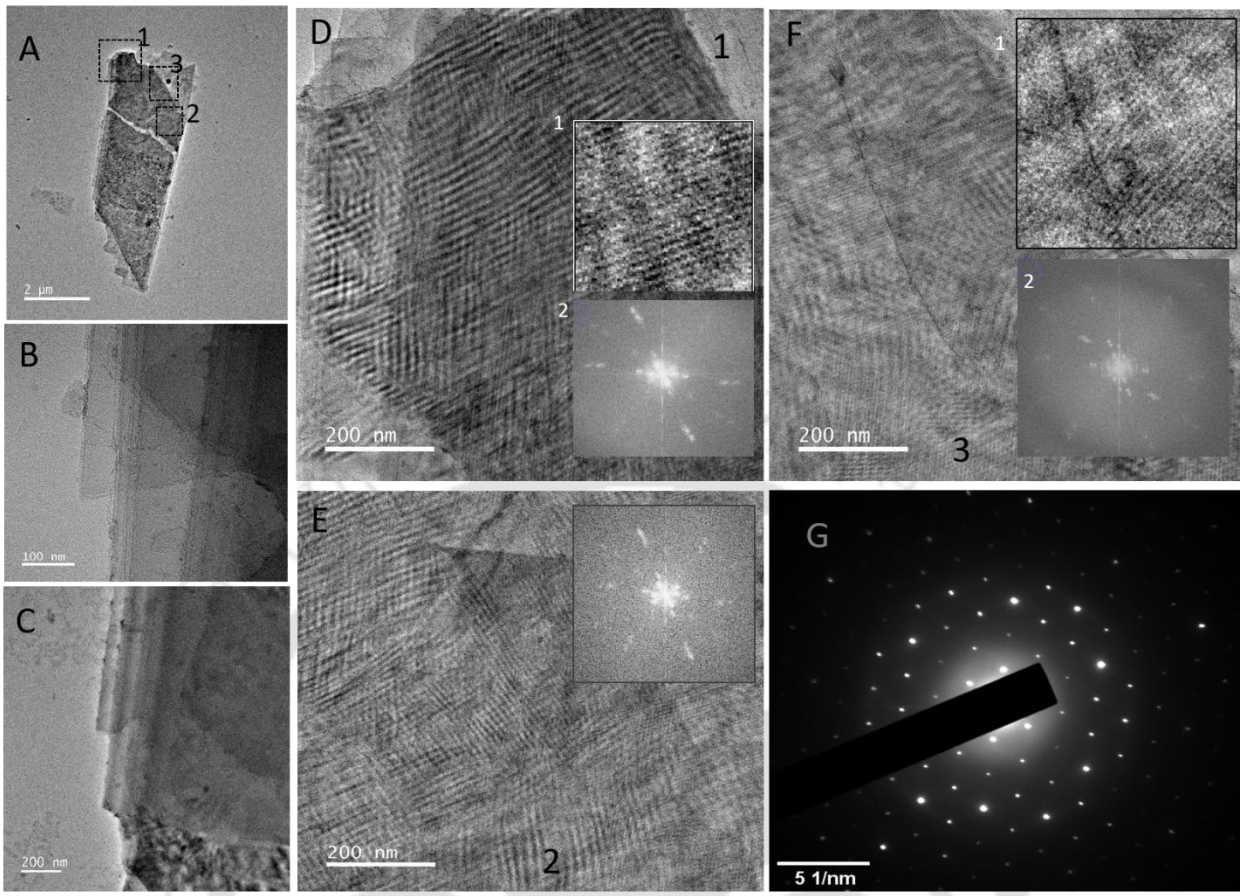


**Figure 6.3.** (A) Low-Magnification image of micrometer-sized IONP-[$Zn^{2+}$]:[Insulin] nanosheet assembly; (B) and (C) Nanosheet side edges; (D) Higher magnification image of region 1 marked in A. Inset 1 shows a magnified image of finer wrinkles. Inset 2 shows the FFT transformation; (E)) Higher magnification image of region 2 marked in A. Inset shows the FFT transformation; (F)) Higher magnification image of region 3 marked in A. Inset 1 shows a magnified image of finer wrinkles. Inset 2 shows the FFT transformation; (G) SAED pattern of the wrinkles exhibiting highly crystalline nature.

Furthermore, it was found that the size of the nanosheet assemblies can extend up to several micrometers, for instance, the larger side of the assembled nanosheets shown in Figure 6.3 A was recorded to be ~6.37 µm. Several thin section nanosheets were found to interact and overlap with

each other which could be distinctively observed at the edges (Figure 6.3 B and 6.3 C), where, no crystalline surface corrugations are observed. This indicated that the surface corrugations were engendered by the interactions of the nanosheets, resulting in crystalline wrinkles.

Figure 6.3 D represents the magnified view of the region marked in 6.3 A, where, extensive surface corrugations could be observed throughout a large area. Two types of wrinkles, large wrinkles and relatively finer wrinkles, were found to be formed irrespective of the orientations, as shown in inset 1. Inset 2 shows the FFT image of the whole region displayed in 6.3 D and the d-spacings calculated are as follows: 4.42 nm, 6.80 nm, 7.31 nm, 7.39 nm, 11.55 nm, 13.47 nm (large wrinkles); 2.11 nm, 2.47 nm, 2.95 nm, 2.32 nm (finer wrinkles). Similarly, Figure 6.3 E represents a separate region of the nanosheet assembly displayed at 6.3 A, which shows extensive surface corrugations predominantly in the form of wrinkles. The inset represents the FFT image of the whole region and the calculated d-spacings are as follows: 6.73 nm, 7.05 nm, 11.96 nm, 12.02 nm (large wrinkles); 1.95 nm, 2.18 nm, 2.25 nm, 2.68 nm (finer wrinkles). The d-spacings from the FFT image of inset 2 at 6.3 F were 4.30 nm, 6.46 nm, 8.16 nm, 14.02 nm (large wrinkles) and 1.34 nm, 1.64 nm, 2.20 nm (finer wrinkles). A snippet of the finer wrinkles has been displayed in inset 1 of 6.3 F. The SAED pattern of the wrinkled region displayed a highly crystalline hexagonal pattern indicating distinct geometric arrangement [304] (6.3 G). Thus, the surface corrugations (wrinkles) of the two dimensional IONP-[$Zn^{2+}$]:[Insulin] nanosheets were found to be highly crystalline, whereas, the regions without the wrinkles were amorphous in nature. Such combination of amorphous and crystalline surface has been known to be flexible in nature.

### 6.2.3 Salient features of the nanosheet surface

The thin-section two dimensional IONP-[$Zn^{2+}$]:[Insulin] nanosheets appeared to have stacked with each other, similar to a bundle of papers. The layer-by-layer formation of the nanosheet assembly indicated that the inter-interactive surface properties of the nanosheets.

While stacking, the surface architecture of corrugations of the individual nanosheets, in the form of wrinkles and ripples, allowed the formation of multidirectional fold-structures. The fringe lengths of these corrugations ranged from extremely fine folds with 1-3 nm to large folds with ~16-18 nm. Another peculiar structure formed at the surface was bead-like projections which were geometrically arranged in variable arrays and patterns, thus creating ordered surface channels.

Figure 6.4 A shows the surface architecture of a multi-layer nanosheet assembly, with multidirectional wrinkle fringes with d-spacings 2.4 nm, 4.2 nm, 6.6 nm and 18.2 nm. The direction of the folds has been shown with arrows, and the FFT-transformation of the fringes has been shown in the inset. Intriguingly, the bead-like projections formed specific geometric arrangement in a square array.

In the same nanosheet assembly, another region exhibiting the bead-like structures was found to align in hexagonal pattern as shown in Figure 6.4 B. The spacing between the folds was found to be ~18 nm, which also was the estimation of the diameter of each bead. The same hexagonal pattern in another region of the same nanosheet assembly revealed the bead diameter to be ~7 nm (6.4 C). Another local region of corrugation revealed the beads to be arranged in square arrays, with multidirectional wrinkles (shown with arrows) running across the surface (6.4 D).

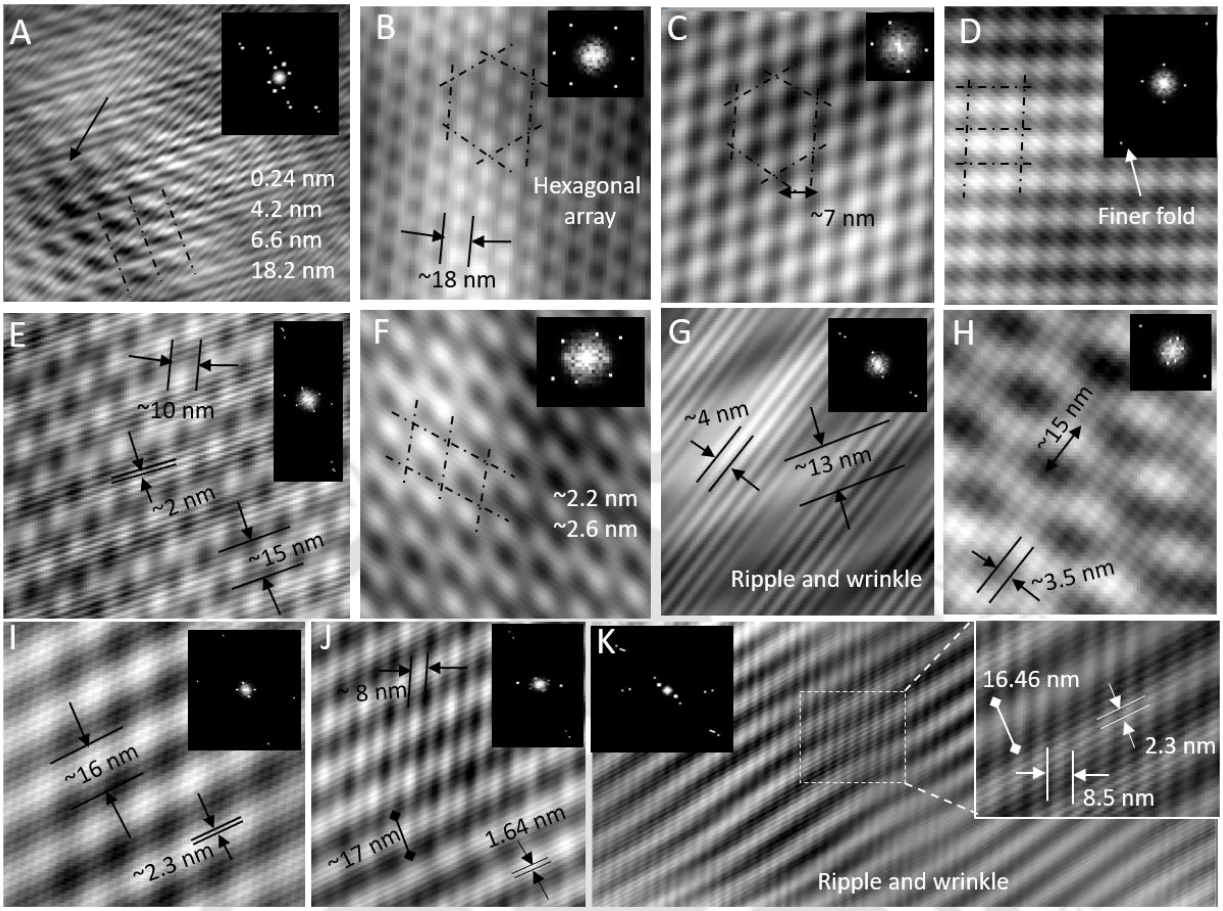


**Figure 6.4.** IFFT images of the surface corrugations of two-dimensional IONP-[$Zn^{2+}$]:[Insulin] nanosheets displaying the superimposition of large-fold and fine-fold wrinkles, and the various geometric arrays of the bead-like projections. All the insets show the FFT transformation of the images displaying the various lattice planes of the surface corrugations.

A complex arrangement of the beads, large-fold and fine-fold wrinkles, arranged in multidirectional pattern has been displayed in 6.4 E, where the large-fold d-spacing was found to be ~10 nm and ~15 nm, and the fine-folds d-spacing to be ~2 nm. The direction of the folds has been shown with arrows. A rhomboid array formation of the beads has been shown in Figure 6.4 F. Figure 6.4 G displays a combination of fine-fold wrinkles (~4 nm) running across a region of a surface ripple of a variable diameter of ~13 nm.

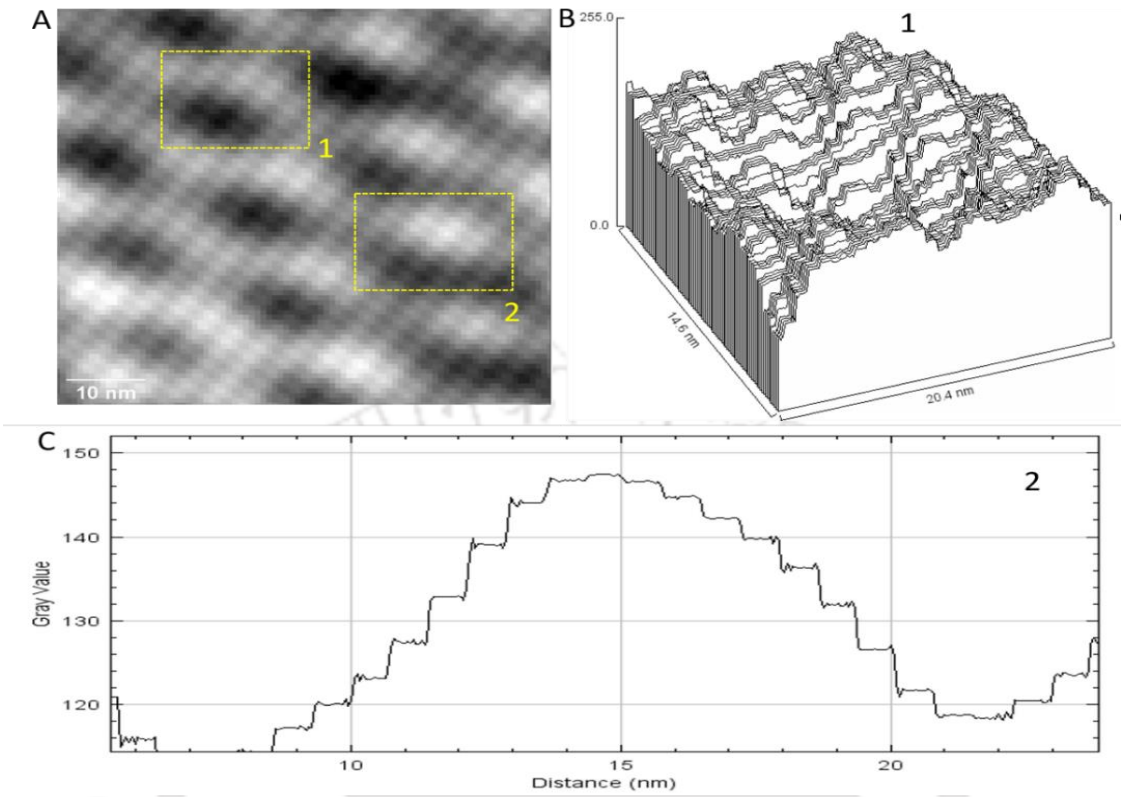


**Figure 6.5.** (A) Bead-like projections formed on the wrinkled surface of IONP-[$Zn^{2+}$]:[Insulin] nanosheet assembly; (B) Surface plot of the selected region shown with dotted rectangle 1; (C) Plot profile of the selected region shown with dotted rectangle 2.

Figure 6.4 H- 6.4 J displays different arrangement of the beads in hexagonal, rhomboid, and square arrays, respectively. The combination of fine-fold wrinkles (~3.5 nm, ~2.3 nm, ~1.64 nm, respectively) and large-fold wrinkles (~15 nm, ~16 nm, ~8 nm and ~17 nm, respectively), can also be seen running across different directions. Figure 6.4 K displays an extended region with multidirectional and multidimensional wrinkle folds. The inset shows the FFT transformation of the crystalline surface indicating multiple lattices of large fold and extremely finer folds of the wrinkles. Enlarged view of the area (shown with a dotted rectangle) displays three wrinkle types with large d-spacings, 16.46 nm and 8.5 nm, and finer wrinkle-folds with 2.3 nm.

The multiple wrinkle-folds running across the nanosheet surface rendered the surface with a highly variable complex architecture. Analysis of the surface plot and the d-spacing profile of beads revealed some interesting features. The surface plot diagram shown in Figure 6.5 B displays the irregularities and symmetries of the same bead surface (highlighted region 1 of 6.5 A) which is an ideal feature of a nanosheet surface intended for cell attachment. Figure 6.5 C shows plot profile of a cross sectional view of the bead which revealed that the ~20 nm diameter of the bead was contributed by the large-folds, whereas, the fine-folds created a regular ~1 nm sized step-wise folded topography on the bead surface.

### 6.2.4 Analysis of the Moiré patterns leading to bead formation

The unique formation of the bead-like projections organized in definite geometric arrays in the two-dimensional nanosheet possibly arose due to the superimposition of the wrinkle lattice fringes of overlapping individual nanosheets. The angular stacking of the local surfaces of two individual nanosheets which contained equidimensional wrinkle lattices might have caused the formation of the bead-like projections. Figure 6.6 shows a comprehensive illustration of two nanosheets with equidimensional wrinkle lattices superimposed at different angles, wherein, it can be observed that Moiré patterns begin to form at an angle of 10º. When the angle between the lattices reaches ~30º, a linear arrangement of bead-like projections was found to develop, which appeared similar to the actual projections displayed at 4A. At 50º-60º, the Moiré pattern displays an arrangement similar to a hexagonal or honeycomb array of bead-like projections, similar to 6.4 B, 6.4 C and 6.4 H.

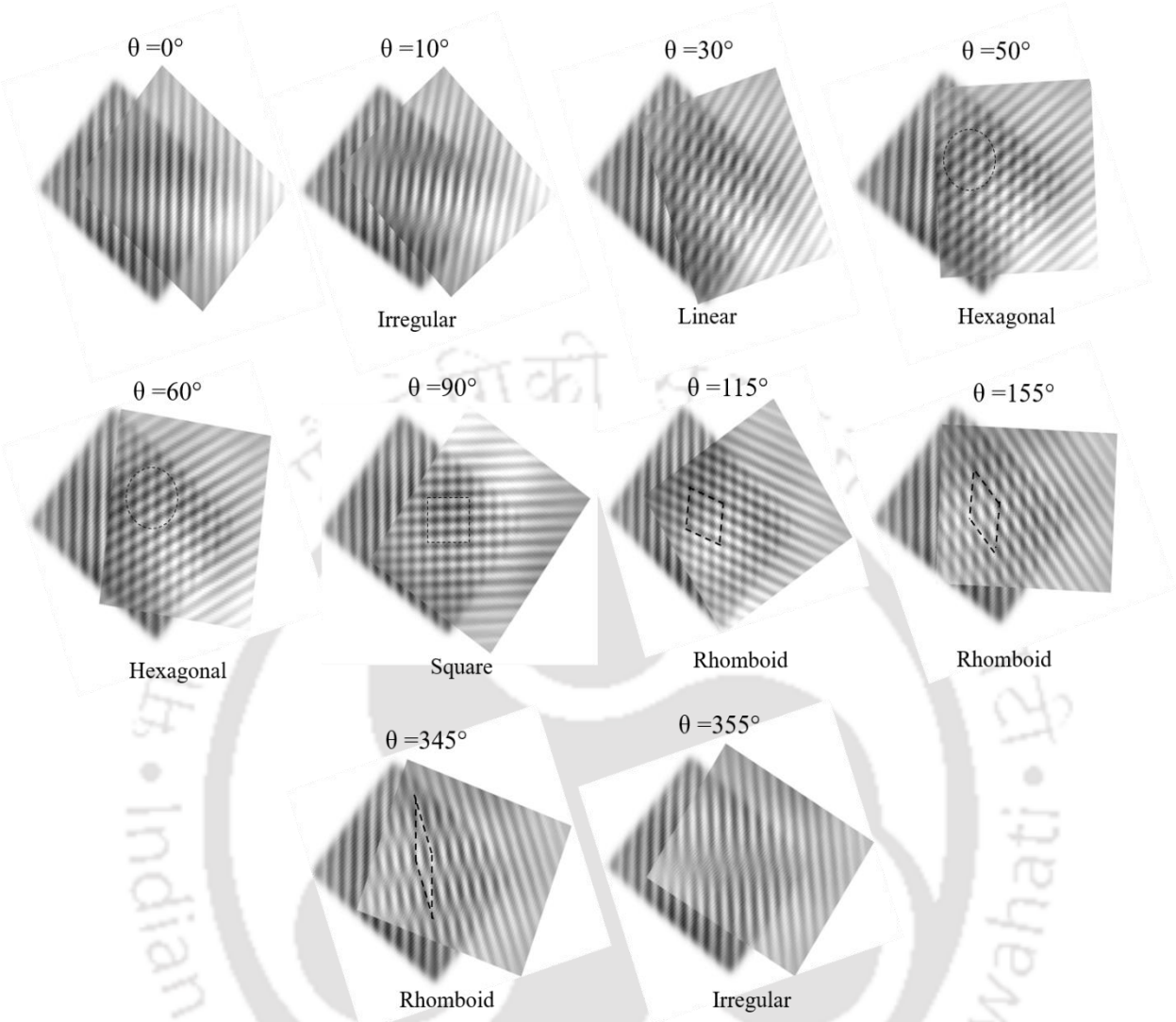


**Figure 6.6.** Comprehensive illustration of the possible Moiré patterns of the equidimensional wrinkle-folds leading to the formation bead-like projections on the nanosheet surface.

A square array of the beads similar to 6.4 D could have arisen due to the superimposition of the wrinkle lattices placed perpendicularly to each other, whereas, a rhomboid arrangement at 6.4 F and 6.4 I might have formed by the superimposition of the nanosheet wrinkles at 115º. The ripple effect in the wrinkles displayed at 6.4 K, most possibly was a Moiré pattern formed at small angular shift of the nanosheets, like the 5º shift of the equidimensional wrinkles shown in Figure 5 with

355º shift. The Moiré patterns arising due to the two-layer stacking of nanosheets at angular rotations has been reported earlier for silica SBA-15 nanosheets where ordered structures at the surface were observed [305–307].

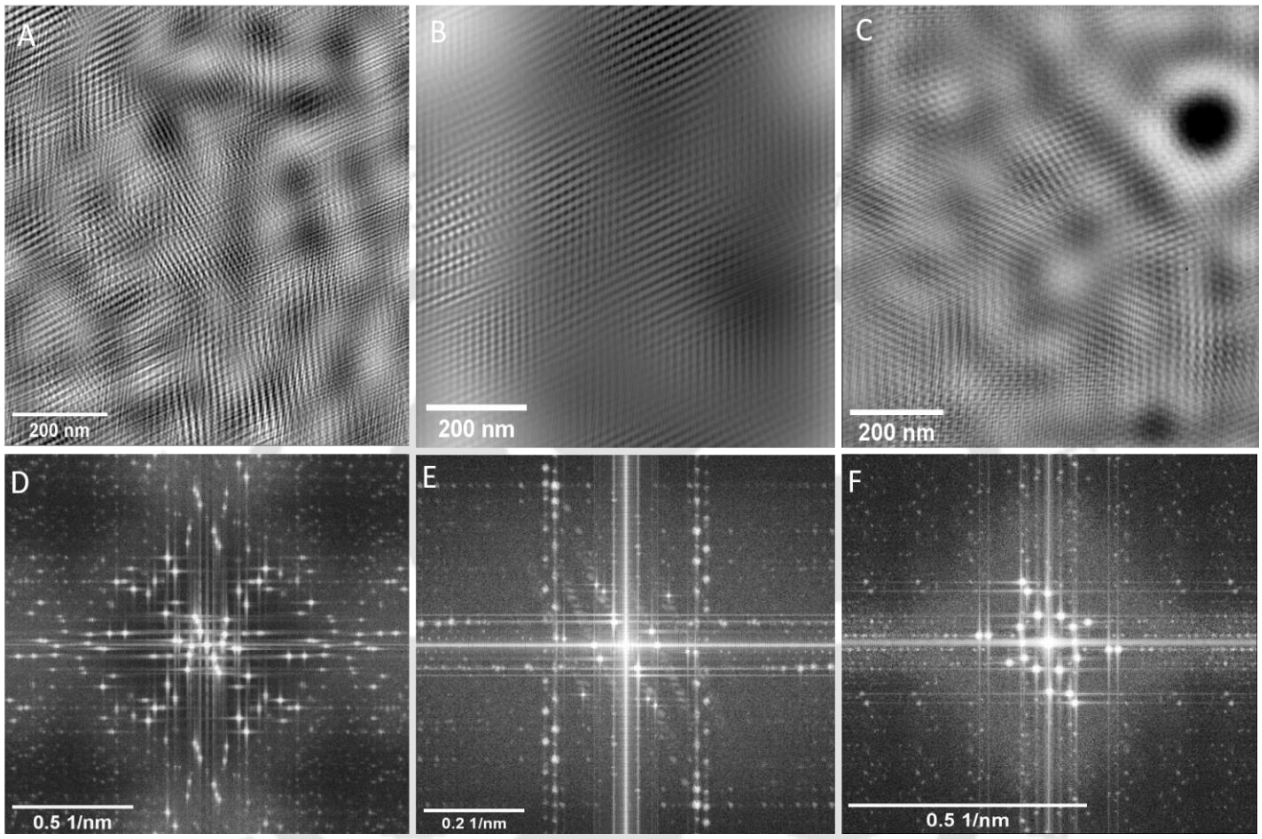


**Figure 6.7**. (A), (B), (C) Representative IFFT images of the surface of the two-dimensional IONP-[$Zn^{2+}$]:[Insulin] nanosheets showing the complex superimposition of various wrinkle folds arisen due to stacking of individual nanosheets; (D), (E), (F) Shows the FFT transformation of the images images displayed at (A), (B), and (C), respectively.

The local corrugations have been shown in Figure 6.4 and their possible stacking angle has been explained in Figure 6.6, however, the nanosheet surface globally comprised of an extremely complex superimposition of multidirectional and multidimensional wrinkles and ripples. Figure 6.7 A to 6.7 C shows the IFFT transformation images of large section of the nanosheet which

displays the complex arrangement of the wrinkle folds leading to the local formation of arrays of bead-like projections and surface channels. The number of lattice planes can be observed in the FFT images as bright dots displayed in 6.7 D to 6.7 F. For a more multidirectional arrangement of the superimposed wrinkles like 6.7 A, the corresponding FFT image (6.7 D) shows randomly arranged bright dots, indicative of the complex network of the surface channels formed by the wrinkles. On the other hand, 6.7 E shows a more geometrically aligned surface channels as the FFT dots mainly align in particular direction. A combination of randomly organized and particularly aligned FFT dots can be seen in 6.7 F, which represents the regions of change in the orientation of the wrinkle lattices.

Therefore, the stacked assembly of two-dimensional IONP-[$Zn^{2+}$]:[Insulin] nanosheet gave rise to extremely variable and complex surface topography comprising of a network of surface channels. The unique creation of surface topography by wrinkled two-dimensional nanosheets superimposed at different angles might open future possibilities of creating definite geometric patterns for varied applications, if a controlled method of construction is developed through further studies. In that light, corrugated surfaces have been observed to enhance cell adhesion and proliferation in tissue engineering scaffolds [308–311].

### 6.2.5 Investigation into the presence and position of IONPs in the two-dimensional nanosheets

After the confirmation that the lattice fringes and crystalline regions of the two-dimensional nanosheet were not created by the IONPs, the obvious question was about the fate of the IONPs. The nanosheets were observed under higher magnification, wherein, it was observed that extremely small particles were distributed across the surface. A representative image of the finding

has been displayed in Figure 6.8 A, which shows ultra-small nanoparticles to be adhered on the surface of the nanosheet (6.2 A). To identify the nature of the ultra-small nanoparticles, HRTEM imaging was performed at 800 K magnification to observe whether these nanoparticles exhibited crystalline nature, and thereby, the characteristic lattice fringes.

A representative HRTEM image of an unidentified ultra-small nanoparticles have been shown in Figure 6.8 B. The particle shown was found to be ~2.74 nm in diameter and exhibited lattice fringes. Upon a reduced-FFT transformation of the HRTEM image, the pattern yielded revealed a singular plane (Figure 6.8 C) and IFFT showed the orientation of the said plane with an interplanar d-spacing of ~0.25 nm (Figure 6.8 D), which corresponded with the (311) plane of typical $Fe_3O_4$ nanoparticles [185]. This confirmed that the ultra-small nanoparticles possibly were the IONPs whose size reduced from 18-22 nm to 2-5 nm. After the HRTEM analysis of an isolated particle, a cluster of these ultra-small IONPs were observed at 600 K magnification to identify other planes.

Figure 6.9 shows the representative HRTEM image of the ultra-small IONPs in a cluster, which has been observed from the region of distributed particles on the surface of the nanosheets shown in Inset 1. The reduced-FFT transformation of the region highlighted with a dashed rectangle revealed two other interplanar d-spacings, ~0.29 nm and 0.36 nm (Inset 2). These values were in agreement with IONP planes (220) and (012), respectively, which has been reported in other studies [185,312].

A hybrid of graphene oxide and IONP has also been reported to have the d-spacing value of 0.36 nm [313]. Hence, it further confirmed that the ultra-small nanoparticles were indeed size-reduced IONPs. IFFT transformation (inset 3) revealed the arrangement of atoms of the selected IONP showing a compact array of atoms in distinct planes.

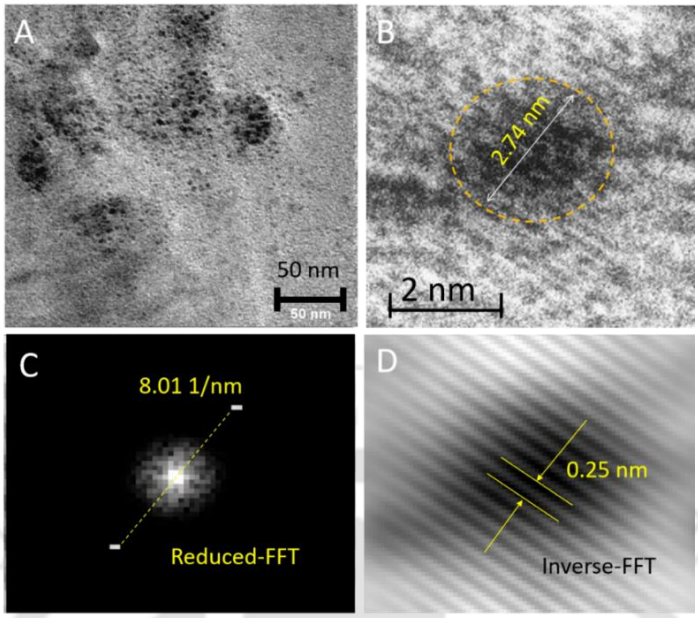


**Figure 6.8.** (A) Ultra-small IONPs decorated on the nanosheet; (B) HRTEM image of a size-reduced ultra-small IONP with 2.74 nm diameter; (C) Reduced-FFT transformation (mask applied); (D) IFFT transformation showing a 0.25 nm d-spacing.

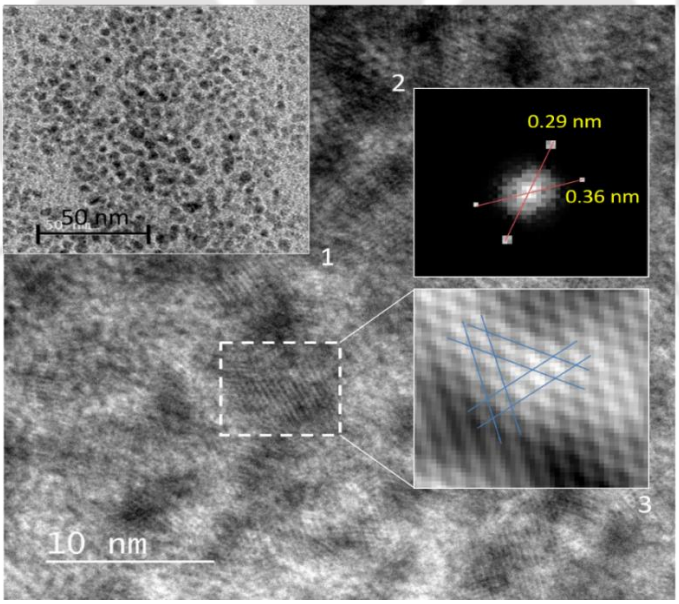


**Figure 6.9.** HRTEM image a cluster of re-organized ultra-small IONPs. Inset 1 shows the dispersed IONPs on the surface. Inset 2 shows the reduced-FFT transformation displaying 0.29

nm and 0.36 nm d-spacing. Inset 3 shows the atomic arrangement of the re-organized ultra-small IONPs.

### 6.2.6 Elemental mapping of the IONP-[$Zn^{2+}$]:[Insulin] nanosheets

The re-affirmation that the surface of the two-dimensional nanosheets was indeed formed by the conjugation of insulin and $Zn^{2+}$, and subsequently assembled into a macromolecular organization with size-reduced IONPs-decorated surface, was crucial to the interpretation of the study. Therefore, an elemental mapping was performed in STEM mode to identify whether N and S atoms (the salient atoms of the protein) constituted the nanosheets. Further, Uranium atoms were also mapped, as uranyl acetate was used for negative staining which specifically binds to proteins. Next, Zn atoms were mapped as its cationic form is known to establish ioninc linkages between insulin molecules to form macromolecular assemblies [265,269]. Fe atoms were mapped to investigate whether the Fe atoms distributed across the nanosheet, which could reaffirm that the surface was decorated by size-reduced IONPs.

Figure 6.10 shows the elemental maps of a IONP-[$Zn^{2+}$]:[Insulin] nanosheet which is shown as a scanned STEM image in 6.10 A. The elemental maps which were detected has have been displayed, which are as follows: carbon map (6.10 B), nitrogen map (6.10 C), sulfur map (6.10 D), uranium map (6.10 E), iron map (6.10 F), zinc map (6.10 G), sodium map 6.10 H), and chlorine map (6.10 I). The borders of the STEM image (6.10 A) have been highlighted with a dashed outline (black), and the borders of the maps containing the highest density of the atoms has been outlined in yellow. The density of the N, S, and U atoms in the maps coincided with the highlighted border outline of the actual STEM image of the nanosheets, which indicated that the nanosheet was constituted by insulin. Next, the macromolecular assembly was found to have Zn atoms distributed across the nanosheet boundaries, which indicated the assembly was driven by [$Zn^{2+}$]:[Insulin]

conjugations. The presence of Fe atoms within the nanosheet boundaries, likewise, confirmed that the ultra-small nanoparticles which decorated the surface of the nanosheet were indeed IONPs. Interestingly, two other elements constituted density maps which coincided with nanosheet boundaries, which were Na and Cl atoms. This indicated that the $Na^+$ and $Cl^-$ ions of the buffer also contributed to the macromolecular organization by binding to the local charged groups of the protein.

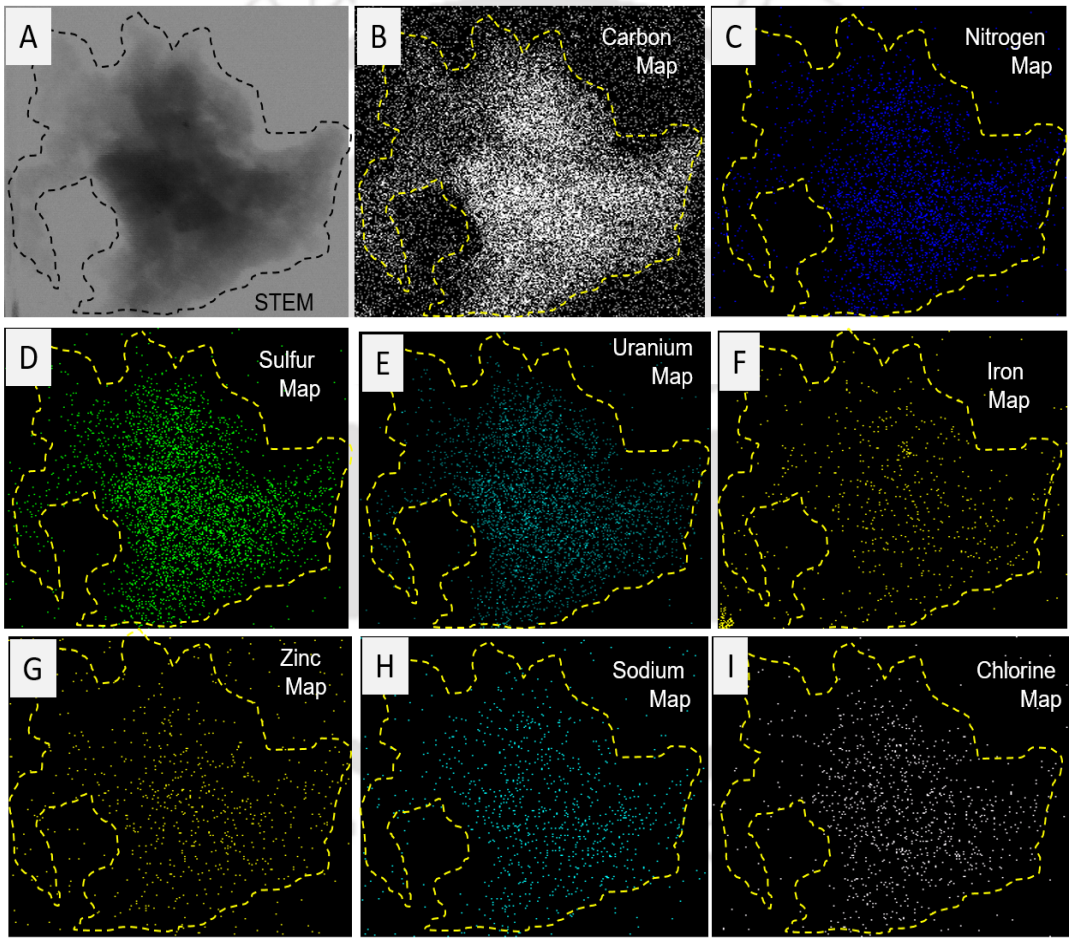


**Figure 6.10.** (A) STEM image of an IONP-[$Zn^{2+}$]:[Insulin] nanosheet; (B) Carbon Map; (C) Nitrogen Map; (D) Sulfur Map; (E) Uranium Map; (F) Iron Map; (G) Zinc map; (H) Sodium Map; (I) Chlorine Map**.**

### 6.2.7 Effect of co-incubation IONP on the morphology of [$Zn^{2+}$]:[Insulin] assembly

After 6 hour incubation of equimolar [$Zn^{2+}$]:[Insulin] with a hydrophobic layer of IONP (in toluene), the reaction mixture with the immiscible phases was kept still at 4°C for 24 hour. After the aging process, the IONP layer dissolved in [$Zn^{2+}$]:[Insulin] solution. The size reduction of the IONPs in the process from ~20 nm to ~2-3 nm has been shown in Figure 6.1 and 6.8, respectively. The formation of the size-reduced IONP-adhered two-dimensional [$Zn^{2+}$]:[Insulin] nanosheet has been shown and discussed in the previous section.

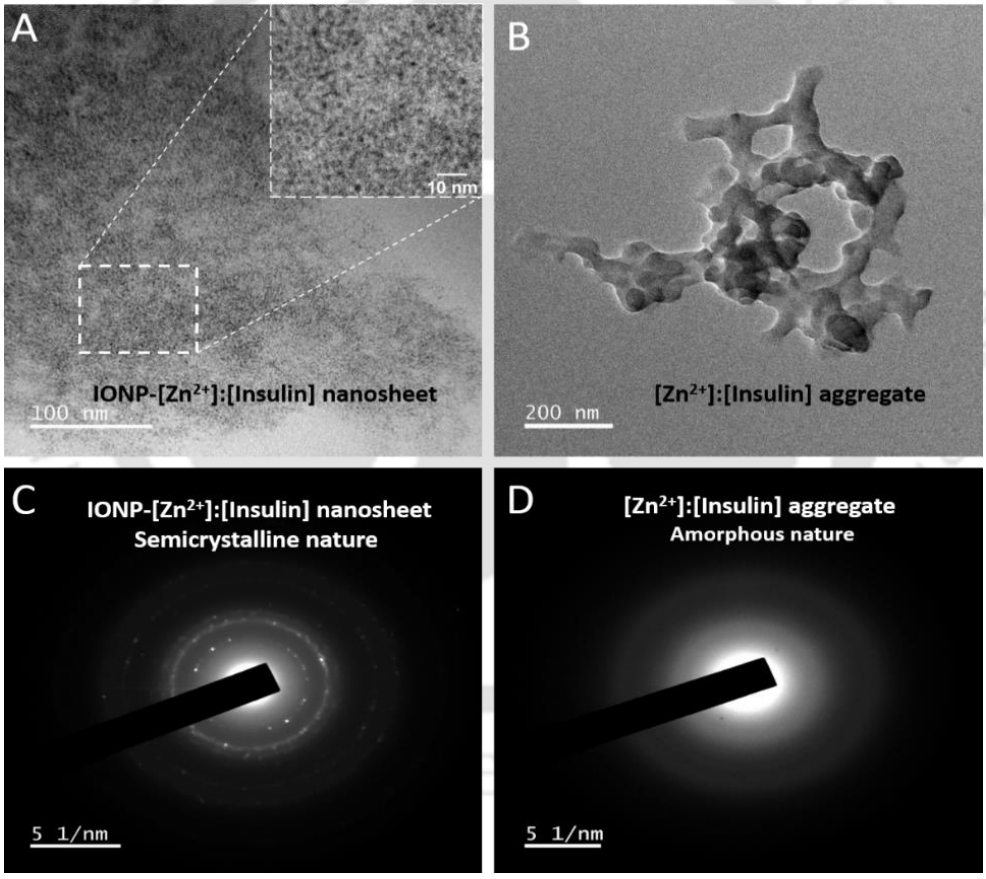


**Figure 6.11.** (A) IONP-decorated [$Zn^{2+}$]:[Insulin] nanosheet surface; (B) [$Zn^{2+}$]:[Insulin] macromolecular organization (control); (C) Semi-crystalline SAED pattern of IONP-[$Zn^{2+}$]:[Insulin] nanosheet surface; (D) Amorphous SAED pattern of [$Zn^{2+}$]:[Insulin] organization.

To understand the effect of the IONP co-incubation on the morphology of [$Zn^{2+}$]:[Insulin] assembly, [$Zn^{2+}$]:[Insulin] was incubated at 60°C and pH 7.4 for a duration of 6 hour. The morphology of the [$Zn^{2+}$]:[Insulin] assembly was found to be prefibrillar aggregate-like (6.11 B) as opposed to the two-dimensional nanosheet formed by IONP-[$Zn^{2+}$]:[Insulin] (6.11 A). Also, the surface of the nanosheet was found to be dispersed with ultra-small IONPs (shown in inset). Due to the presence of the ultra-small IONPs the SAED pattern of the -[$Zn^{2+}$]:[Insulin] nanosheet was found to exhibit a semi-crystalline nature (6.11 C), whereas, the control [$Zn^{2+}$]:[Insulin] assembly/aggregate was found to be amorphous in nature (6.11 D).

The possible cause for the dissolution of the phase-difference between the hydrophobic IONP layer and the bulk solution of [$Zn^{2+}$]:[Insulin] could presumably be $Zn^{2+}$-mediated aggregation of insulin, which in turn, leads to increase in hydrophobicity. The gradual increase of hydrophobicity of the [$Zn^{2+}$]:[Insulin] solution possibly underwent a hydrophobic-hydrophobic interaction with the IONP layer, resulting in dissolution of the two-phase.

### 6.2.8 Investigation into the effect of IONP-[$Zn^{2+}$]:[Insulin] nanosheet in BHK-21 cell growth

The effect of the two-dimensional IONP-[$Zn^{2+}$]:[Insulin] nanosheet on BHK-21 fibroblast was examined by growing the fibroblasts on a solidified layer of the nanosheet. It was observed that the BHK-21 cells exhibited normal adherent morphology when grown on the nanosheet layer (Figure 6.12 A- 6.12 D). Interestingly, the microscopic images of the fibroblasts grown on the nanosheet layer clearly showed patches of the nanosheets adhered on the cell surface, and inside the cellular compartments.

Inset at 6.12 C shows an enlarged view of a possible cellular uptake of the nanosheets by BHK-21 cells. The possible entry of the nanosheets was seen in both adherent and suspended cells, and the

images also indicated the possible path of entry by attaching to the cell surface and subsequently entering the inner compartment of the cells. Cellular uptake of nanosheets by cells has been demonstrated by Mu et al. wherein cellular uptake of protein-coated graphene sheets was observed in mouse mesenchymal progenitor C2C12 cells [314]; but this present study is only limited to the speculation of a possible cellular uptake hinted by the images, and thereby, needs further studies to prove the same.

Figure 6.12 E displays the enhancement of BHK-21 cell growth in presence of the IONP-[$Zn^{2+}$]:[Insulin] nanosheet, reaching up to a maximum growth till 24 hour, showing no cytotoxicity. In presence of the nanosheets, the cell growth was found to increase by 32.152% within 24 hour of the incubation (Figure 6.12 E).

Figure 6.12 F shows the MALDI-TOF/MS of the IONP-[$Zn^{2+}$]:[Insulin] which was recorded to understand whether the nanosheet was formed by insulin multimers or monomeric insulin. A predominant peak of 5815.523 Da was detected corresponding to the monomeric form of insulin, which indicated that the nanosheet was formed by the organization of insulin monomers (Figure 6.12 C). Formation of the nanosheet by monomeric insulin when corroborated with the elemental map of $Zn^{2+}$ (Figure 6.10 G) indicates that the layer of insulin monomers was possibly organized by inter-molecular $Zn^{2+}$-bridges. Such formation of intermolecular cross-links by $Zn^{2+}$ ions has been demonstrated in a number of earlier studies [208,229,268,269,277]. Alongside a predominant presence of monomeric insulin, a slight fraction of dimeric form was also detected at ~11628 Da. The MALDI-TOF/MS results clearly indicated that the two-dimensional layer of IONP-[$Zn^{2+}$]:[Insulin] was composed of monomeric form of insulin which possibly organized through $Zn^{2+}$-linkages, and stacking.

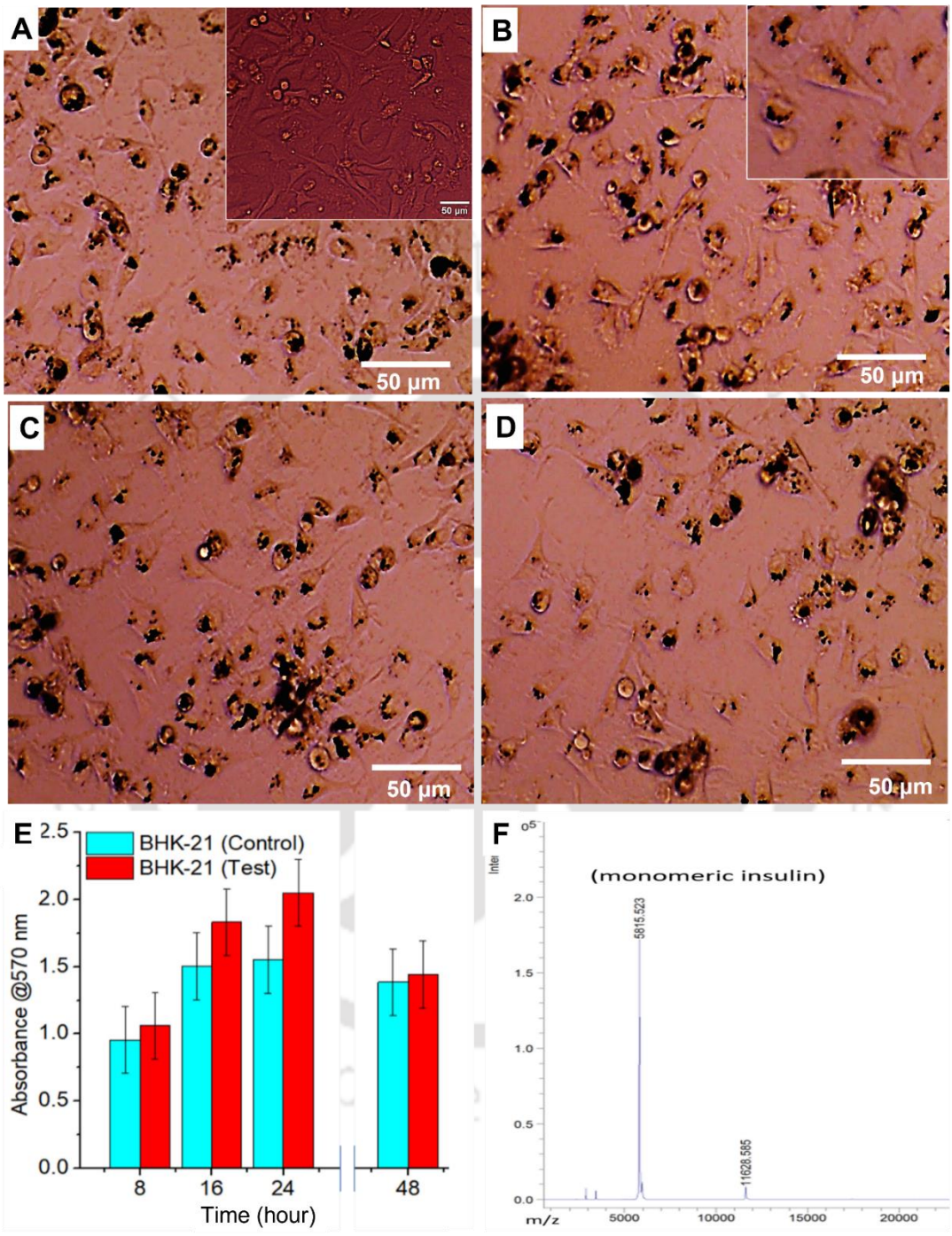


**Figure 6.12.** (A) to (D) BHK-21 fibroblast cells grown on IONP-[$Zn^{2+}$]:[Insulin] nanosheet surface showing a possible cellular uptake of nanosheets by BHK-21 cells. Inset at (C) shows a

possible cellular uptake of the nanosheet by BHK-21 cells. Inset at (A) shows the BHK-21 fibroblasts in the control sample; (E) Growth pattern of BHK-21 fibroblasts grown in presence nanosheet; (D) MALDI-TOF/MS graph of the nanosheet showing the monomeric form of insulin**.**

### 6.3 Conclusion

This study presented the novel architecture and potential function of a two-dimensional nanosheet formed by monomeric insulin interlinked by $Zn^{2+}$ ions in phase difference with 20 nm sized hydrophobic IONPs. The gradual dissolution of the phases into a single hydrophobic phase resulted in the re-organization of the IONPs into ultra-small nanoparticles (2-3 nm) which were found to adhere to the surface of the nanosheets. The amorphous nanosheet interacted and formed overlapped assemblies that gave rise to surface corrugations, mainly wrinkles, which exhibited highly crystalline properties. The lattice fringes of the crystalline wrinkles ranged from large-fold (4-18 nm) to fine-fold wrinkles (1-3 nm). The semi-crystalline and flexible surface of the supported the growth and cell targeting of BHK-21 fibroblasts in a non-cytotoxic manner. Therefore, the novel nanosheet with its unique IONP-decorated ordered surface channels can be a potential platform for cell growth and cell targeting.

# Chapter 7

## Conclusions and suggestions for future works

### 7.1 Conclusions for the present work

This thesis presents simple and facile ways to create multifunctional nanostructures with protein amyloids by modulating their aggregation pathway with intrinsic and extrinsic nanoagents. For the first time, the ability of heme to dissociate from cytochrome C and re-organize into fluorescent quantum dots of 2-3 nm has been reported in Chapter 3. Heme is a ferroprotoporphyrin structurally, which dissociates from the cytochrome C holoform conformation when thermal and pH stress causes self-oxidation of the protein. The oxidation event leads to fragmentation of the protein which self-assemble into a cross-linked amyloid structure, whereas, the ferroprotoporphyrin ring of heme converts into ferriprotoporphyrin. The chloride ions of the buffer then bind to the ferriprotoporphyrin ring, and subsequently reorganize into fluorescent quantum dots, named FeQDs in the study. The FeQDs then adhere on the surface of the amyloid network and creates a FeQD-decorated cytochrome C amyloid network.

These findings about the amyloidogenic events of cytochrome C have never been reported earlier and therefore, contributes to the understanding of protein amyloidogenesis when the functional structure has a prosthetic group. Furthermore, the FeQD-decorated amyloid network can be a potential platform for cell adhesion and growth of BHK-21 fibroblasts.

Multimerization or aggregation of insulin in presence of $Zn^{2+}$ has been reported earlier, however, the novel findings described in Chapter 4 provides an alternate view of the macromolecular organization of insulin- $Zn^{2+}$ as a transient viscous biomolecular condensate and not an irreversible

aggregate. Insulin molecules undergoes a conformational change to attain a slightly different conformational variant form, and self-assemble into amyloid-like state by establishing intermolecular $Zn^{2+}$-bridges. This amyloid-like state was confirmed as a condensate state by the ability of the complex to dissolve back into monomeric insulin solution when pH is lowered. This finding provides an alternate view of the understanding of the behaviour of insulin molecules, and can be of particular interest in the formulation of oral delivery of the hormone.

The condensation of insulin molecules to a reversible amyloid-like state can be further modulated by co-incubating cellulosic nanomaterials, and metallic nanoparticles. With each co-incubatory agent, the condensation behaviour changes and results in the formation of various nanostructures which can be of particular interest to biomaterial design.

The semi-crystalline long fibers of CNF were found to be reduced to highly crystalline nanorods of 20 nm length, which evenly decorated the surface of insulin condensate structure. On the other hand, the rod-shaped small fibers of magnetic CNC were found to be resolved into small ultrathin fibers, which interacted with each other and formed spherical CNCs. Thusthe structural properties of magnetic CNC were found to be transformed completely. The spherical CNCs were then packaged into the insulin condensate to create MagCNC-insulin microspheres. These microspheres were found to adhere on the surface of the BHK-21 cell surface and penetrate inside the cells subsequently. This cellular uptake of the microspheres can be further explored to create cell targeting platform. Insulin condensate modulated by CNF and MagCNC were found to be biocompatible and promoted the growth of BHK-21 fibroblasts.

Chapter 5 explicates another condensate variant of insulin formed by the sorption of insulin molecules on the surface of citrate-capped AuNPs. The amyloidogenic stretch of insulin, which is

responsible for the structural transition of insulin from a helical structure to a β-sheet rich structure, adheres on the surface of the AuNPs resulting in the lowering of degree of freedom of the amyloidogenic stretch. As a result, the insulin molecules remain in their native-like conformation, yet organize into a macromolecular structure. The sequence of events has been described in chapter 5 which explains the surface sorption of insulin molecules on AuNP surface and creation of a protein layer around the AuNPs. Subsequently the layer attracts other insulin molecules and forms nucleating species with dendritic morphology. These nucleating dendrites then assemble and condense into a macromolecular structure with AuNPs displayed on the surface. This AuNP-decorated insulin condensate was found to be biocompatible, and promoted the growth of BHK-21 cells. The condensate variant was also found to dissolve into monomeric solution when pH of the solution was lowered.

The same insulin- $Zn^{2+}$ condensation behaviour shows a completely different pattern when incubated with hydrophobic IONPs. The initial hydrophilic phase of insulin solution creates a phase-difference with the hydrophobic IONPs which forms a thin layer on the protein solution. With progress of thermal stress due to a prolonged time of incubation, the insulin solution transits from a hydrophilic nature to a hydrophobic nature and the IONP layer dissolves into the protein solution. The phase dissolution results in the re-organization of the IONPs (18-20 nm average size) to ultrasmall nanoparticles of 2-3 nm diameter. On the other hand, the macromolecular organization of insulin was found to attain two-dimensional nanosheet structure similar to graphene oxide nanosheets. The two-dimensional nanosheets subsequently stack with each other and results in the appearance of striking patterns of surface corrugation. The superimposition of the equidimensional wrinkles results in the formation of Moire patterns, and ultimately ordered arrays of surface channels. The re-organized IONPs also adhere to the surface of the nanosheets

and decorate its surface in local regions. The two-dimensional IONP-insulin nanosheet was also found to adhere on the surface of BHK-21 fibroblasts, and possibly penetrated inside the cellular compartments. Further studies are required to establish the cellular uptake of the nanosheets by the cells.

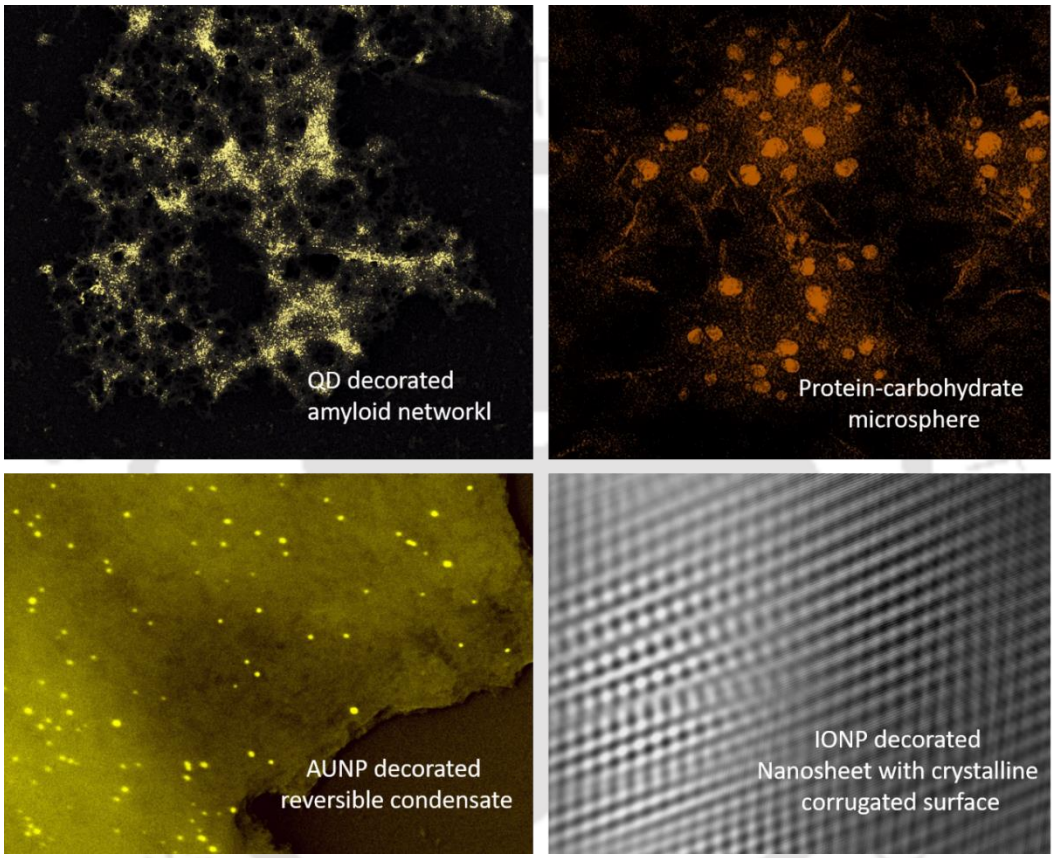


**Figure 7.1.** Various nanostructures designed by modulating the supramolecular organization of protein molecules.

### 7.2 Suggestions for future works

The findings entailed in this thesis might open newer avenues for employing various amyloid structures in designing smart materials, and will contribute to the understanding of protein

amyloidogenic variance, protein interactions and amyloid polymorphism. Figure 7.1 shows some of the novel nanostructures designed in this study.

The FeQDs decorated on the surface of cytochrome C amyloid network were found to simultaneously exhibit both the d-spacings of Fe (II) and Fe (III) forms, which is indicative of the presence of heterojunctions. This is a unique property of the FeQD-decorated cytochrome c amyloid network and can be explored in medicine, sensing systems, and bioelectronic devices as well. The FeQD-decorated network was also found to support cell growth. An extension of the application could be explored in the differentiation of stem cells into neuronal cells through electrical stimulation. Nevertheless, the limitation of the present study is primarily the lack of controlled mechanism of amyloid and FeQD formation, and investigation of cytotoxicity towards other cell types. Therefore, a multitude of investigations intended to further develop the system is essential.

The findings entailed in this thesis also show the highly modulable supramolecular assembly of insulin in presence of organic and inorganic modulatory nanoagents (CNF, MagCNC, AuNP, IONP). With the same protein, formation of four distinctly different nanostructures have been demonstrated. The microspheres of insulin with loaded MagCNC nanoparticles could be explored for drug delivery. It has also been demonstrated that these microspheres were able to adhere to the BHK-21 fibroblast cells, indicating possible cell-targeting potential. In that regard, the limitation of the present study was that investigation whether MagCNC microspheres penetrated the cell membrane was not performed. Therefore, an ample of improvements are necessary in the future for utilizing these microspheres for drug delivery. Similarly, CNR-decorated insulin condensate and AuNP-decorated insulin assembly could be explored for cell proliferating platforms. AuNP-

insulin assembly could be employed in oral formulations of insulin as described in the relevant chapters.

Another interesting nanostructure was the surface channels formed in the IONP-decorated insulin nanosheets. The ordered surface patterns could be explored for the differentiation of stem cells into endothelial or neuronal cells, as patterned platforms are already under investigation for the same. In order to create desired patterns, investigation for further development of these nanosheets to be used for 3D printing is of great interest. Several strategies could be undertaken for the same, such as further hybridization of the nanosheets with polymeric material like polylactic acid (PLA) to create proteinaceous-sculptures for cell proliferation. Further exploration of the practical applications of the nanostructures designed in this study is therefore emphasized to the larger scientific community.

## References


[1] T. Das, V. Kolli, S. Karmakar, N. Sarkar, Functionalisation of polyvinylpyrrolidone on gold nanoparticles enhances its anti-amyloidogenic propensity towards hen egg white lysozyme, Biomedicines. 5 (2017) 19.

[2] R. Chatterjee, V. Kolli, N. Sarkar, Trehalose and Magnesium Chloride Exert a Common Anti-amyloidogenic Effect Towards Hen Egg White Lysozyme, Protein J. 36 (2017) 138–146.

[3] L.M. Pandey, S. Le Denmat, D. Delabouglise, F. Bruckert, S.K. Pattanayek, M. Weidenhaupt, Surface chemistry at the nanometer scale influences insulin aggregation, Colloids Surfaces B Biointerfaces. 100 (2012) 69–76.

[4] A. Singh, A. Hasan, S. Tiwari, L.M. Pandey, Therapeutic Advancement in Alzheimer Disease: New Hopes on the Horizon?, CNS Neurol. Disord. Drug Targets. (2018).

[5] J.C. Bridi, F. Hirth, Mechanisms of α-Synuclein Induced Synaptopathy in Parkinson's Disease, Front. Neurosci. 12 (2018) 80.

[6] K. Hu, X. Chen, W. Chen, L. Zhang, J. Li, J. Ye, Y. Zhang, L. Zhang, C.-H. Li, L. Yin, Neuroprotective effect of gold nanoparticles composites in Parkinson's disease model, Nanomedicine Nanotechnology, Biol. Med. 14 (2018) 1123–1136.

[7] L.S. Kaltenbach, E. Romero, R.R. Becklin, R. Chettier, R. Bell, A. Phansalkar, A. Strand, C. Torcassi, J. Savage, A. Hurlburt, Huntingtin interacting proteins are genetic modifiers of neurodegeneration, PLoS Genet. 3 (2007) e82.

[8] A. Ramos-Miguel, A. Barr, A. Dwork, G. Rosoklija, J. Mann, W. Honer, SA101. Characterization of Presynaptic SNAP-25 Aggregates in Human Postmortem Brain: A Novel Pathologic Index in Schizophrenia?, Schizophr. Bull. 43 (2017) S149–S149.

[9] A. Brinkmalm, J. Dumurgier, G. Brinkmalm, O. Hansson, H. Zetterberg, E. Bouaziz-Amar, J. Hugon, C. Paquet, K. Blennow, The pre-synaptic vesicle protein synaptotagmin is a novel biomarker for Alzheimer's disease, Alzheimers. Res. Ther. 8 (2016).

[10] A. Ramos-Miguel, C.L. Beasley, A.J. Dwork, J.J. Mann, G. Rosoklija, A.M. Barr, W.G. Honer, Increased SNARE protein-protein interactions in orbitofrontal and anterior cingulate cortices in schizophrenia, Biol. Psychiatry. 78 (2015) 361–373.

[11] A. Ramos-Miguel, A.A. Jones, K. Sawada, A.M. Barr, T.A. Bayer, P. Falkai, S.E. Leurgans, J.A. Schneider, D.A. Bennett, W.G. Honer, Frontotemporal dysregulation of the SNARE protein interactome is associated with faster cognitive decline in old age, Neurobiol. Dis. 114 (2018) 31–44.

[12] S. Karmakar, L.G. Sharma, A. Roy, A. Patel, L.M. Pandey, Neuronal SNARE complex: A protein folding system with intricate protein-protein interactions, and its common neuropathological hallmark, SNAP25, Neurochem. Int. 122 (2019) 196–207.

[13] C.M. Dobson, Protein folding and misfolding, Nature. 426 (2003) 884.

[14] L.M. Luheshi, C.M. Dobson, Bridging the gap: from protein misfolding to protein misfolding diseases, FEBS Lett. 583 (2009) 2581–2586.

[15] T.P.J. Knowles, M. Vendruscolo, C.M. Dobson, The amyloid state and its association with protein misfolding diseases, Nat. Rev. Mol. Cell Biol. 15 (2014) 384.

[16] N. Sarkar, A.N. Singh, V.K. Dubey, Effect of curcumin on amyloidogenic property of molten globule-like intermediate state of 2, 5-diketo-D-gluconate reductase A, Biol. Chem. 390 (2009) 1057–1061.

[17] A. Singh, P. Datta, L.M. Pandey, Deciphering the mechanistic insight into the stoichiometric ratio

dependent behavior of Cu (II) on BSA fibrillation, Int. J. Biol. Macromol. 97 (2017) 662–670.

[18] D. Samuel, T.K.S. Kumar, G. Ganesh, G. Jayaraman, P.-W. Yang, M.-M. Chang, V.D. Trivedi, S.-L. Wang, K.-C. Hwang, D.-K. Chang, Proline inhibits aggregation during protein refolding, Protein Sci. 9 (2000) 344–352.

[19] S. Lee, T.H.T. Trinh, M. Yoo, J. Shin, H. Lee, J. Kim, E. Hwang, Y. Lim, C. Ryou, Self-assembling peptides and their application in the treatment of diseases, Int. J. Mol. Sci. 20 (2019) 5850.

[20] K. Matsuurua, Rational design of self-assembled proteins and peptides for nano-and micro-sized architectures, RSC Adv. 4 (2014) 2942–2953.

[21] C. Meier, I. Lifincev, M.E. Welland, Conducting core–shell nanowires by amyloid nanofiber templated polymerization, Biomacromolecules. 16 (2015) 558–563.

[22] M.M. Castellanos, J.A. Pathak, R.H. Colby, Both protein adsorption and aggregation contribute to shear yielding and viscosity increase in protein solutions, Soft Matter. 10 (2014) 122–131.

[23] S.K. Maji, D. Schubert, C. Rivier, S. Lee, J.E. Rivier, R. Riek, Amyloid as a depot for the formulation of long-acting drugs, PLoS Biol. 6 (2008) e17.

[24] A. Altunbas, S.J. Lee, S.A. Rajasekaran, J.P. Schneider, D.J. Pochan, Encapsulation of curcumin in self-assembling peptide hydrogels as injectable drug delivery vehicles, Biomaterials. 32 (2011) 5906–5914.

[25] M.R. Sawaya, S. Sambashivan, R. Nelson, M.I. Ivanova, S.A. Sievers, M.I. Apostol, M.J. Thompson, M. Balbirnie, J.J.W. Wiltzius, H.T. McFarlane, Atomic structures of amyloid cross-β spines reveal varied steric zippers, Nature. 447 (2007) 453.

[26] S. Povilonienė, V. Časaitė, V. Bukauskas, A. Šetkus, J. Staniulis, R. Meškys, Functionalization of α-synuclein fibrils, Beilstein J. Nanotechnol. 6 (2015) 124.

[27] C. Li, J. Adamcik, R. Mezzenga, Biodegradable nanocomposites of amyloid fibrils and graphene with shape-memory and enzyme-sensing properties, Nat. Nanotechnol. 7 (2012) 421.

[28] I. Rivera, R. Capone, D.M. Cauvi, N. Arispe, A. De Maio, Modulation of Alzheimer's amyloid β peptide oligomerization and toxicity by extracellular Hsp70, Cell Stress Chaperones. 23 (2018) 269–279.

[29] T. Söllner, M.K. Bennett, S.W. Whiteheart, R.H. Scheller, J.E. Rothman, A protein assembly-disassembly pathway in vitro that may correspond to sequential steps of synaptic vesicle docking, activation, and fusion, Cell. 75 (1993) 409–418.

[30] C. Andreini, I. Bertini, A bioinformatics view of zinc enzymes, J. Inorg. Biochem. 111 (2012) 150–156.

[31] R. Tycko, Amyloid polymorphism: structural basis and neurobiological relevance, Neuron. 86 (2015) 632–645.

[32] D. Thirumalai, G. Reddy, J.E. Straub, Role of water in protein aggregation and amyloid polymorphism, Acc. Chem. Res. 45 (2012) 83–92.

[33] J.S. Jeong, A. Ansaloni, R. Mezzenga, H.A. Lashuel, G. Dietler, Novel mechanistic insight into the molecular basis of amyloid polymorphism and secondary nucleation during amyloid formation, J. Mol. Biol. 425 (2013) 1765–1781.

[34] N.P. Reynolds, M. Charnley, R. Mezzenga, P.G. Hartley, Engineered lysozyme amyloid fibril networks support cellular growth and spreading, Biomacromolecules. 15 (2014) 599–608.

[35] S.L. Gras, A.K. Tickler, A.M. Squires, G.L. Devlin, M.A. Horton, C.M. Dobson, C.E. MacPhee, Functionalised amyloid fibrils for roles in cell adhesion, Biomaterials. 29 (2008) 1553–1562.

[36] J. Seeliger, K. Estel, N. Erwin, R. Winter, Cosolvent effects on the fibrillation reaction of human

IAPP, Phys. Chem. Chem. Phys. 15 (2013) 8902–8907.

[37] K.-N. Liu, C.-M. Lai, Y.-T. Lee, S.-N. Wang, R.P.-Y. Chen, J.-S. Jan, H.-S. Liu, S.S.-S. Wang, Curcumin's pre-incubation temperature affects its inhibitory potency toward amyloid fibrillation and fibril-induced cytotoxicity of lysozyme, Biochim. Biophys. Acta (BBA)-General Subj. 1820 (2012) 1774–1786.

[38] G. Kramer, D. Boehringer, N. Ban, B. Bukau, The ribosome as a platform for co-translational processing, folding and targeting of newly synthesized proteins, Nat. Struct. Mol. Biol. 16 (2009) 589.

[39] N.J. Bulleid, R.B. Freedman, Defective co-translational formation of disulphide bonds in protein disulphide-isomerase-deficient microsomes, Nature. 335 (1988) 649.

[40] V.A. Kolb, E. V Makeyev, A.S. Spirin, Co-translational folding of an eukaryotic multidomain protein in a prokaryotic translation system, J. Biol. Chem. 275 (2000) 16597–16601.

[41] C.B. Anfinsen, E. Haber, M. Sela, F.H. White, The kinetics of formation of native ribonuclease during oxidation of the reduced polypeptide chain, Proc. Natl. Acad. Sci. 47 (1961) 1309–1314.

[42] R. Zwanzig, A. Szabo, B. Bagchi, Levinthal's paradox, Proc. Natl. Acad. Sci. 89 (1992) 20–22.

[43] C. Levinthal, Are there pathways for protein folding?, J. Chim. Phys. 65 (1968) 44–45.

[44] F. Chiti, C.M. Dobson, Protein misfolding, functional amyloid, and human disease, Annu. Rev. Biochem. 75 (2006) 333–366.

[45] K.K. Turoverov, I.M. Kuznetsova, V.N. Uversky, The protein kingdom extended: ordered and intrinsically disordered proteins, their folding, supramolecular complex formation, and aggregation, Prog. Biophys. Mol. Biol. 102 (2010) 73–84.

[46] S. Karmakar, Studies on Effect of Proline Capped Gold Nanoparticles on Hen Egg White Lysozyme

(HEWL) and Cytochrome C (Cyt C) Amyloidogenesis, 2017.

[47] C. Soto, Unfolding the role of protein misfolding in neurodegenerative diseases, Nat. Rev. Neurosci. 4 (2003) 49.

[48] F.U. Hartl, M. Hayer-Hartl, Converging concepts of protein folding in vitro and in vivo, Nat. Struct. Mol. Biol. 16 (2009) 574.

[49] E. Gazit, A possible role for π-stacking in the self-assembly of amyloid fibrils, FASEB J. 16 (2002) 77–83.

[50] S. Gilead, E. Gazit, Self-organization of short peptide fragments: from amyloid fibrils to nanoscale supramolecular assemblies, Supramol. Chem. 17 (2005) 87–92.

[51] J. Dong, J.E. Shokes, R.A. Scott, D.G. Lynn, Modulating amyloid self-assembly and fibril morphology with Zn (II), J. Am. Chem. Soc. 128 (2006) 3540–3542.

[52] G.G. Glenner, C.W. Wong, Alzheimer's disease: initial report of the purification and characterization of a novel cerebrovascular amyloid protein, Biochem. Biophys. Res. Commun. 120 (1984) 885–890.

[53] J.T. Jarrett, P.T. Lansbury Jr, Seeding "one-dimensional crystallization" of amyloid: a pathogenic mechanism in Alzheimer's disease and scrapie?, Cell. 73 (1993) 1055–1058.

[54] J.D. Sipe, A.S. Cohen, History of the amyloid fibril, J. Struct. Biol. 130 (2000) 88–98.

[55] K. Johnson-Wood, M. Lee, R. Motter, K. Hu, G. Gordon, R. Barbour, K. Khan, M. Gordon, H. Tan, D. Games, Amyloid precursor protein processing and Aβ42 deposition in a transgenic mouse model of Alzheimer disease, Proc. Natl. Acad. Sci. 94 (1997) 1550–1555.

[56] M. Garvey, H. Ecroyd, N.J. Ray, J.A. Gerrard, J.A. Carver, Functional Amyloid Protection in the Eye Lens: Retention of α-Crystallin Molecular Chaperone Activity after Modification into Amyloid

Fibrils, Biomolecules. 7 (2017) 67.

[57] S.K. Maji, M.H. Perrin, M.R. Sawaya, S. Jessberger, K. Vadodaria, R.A. Rissman, P.S. Singru, K.P.R. Nilsson, R. Simon, D. Schubert, Functional amyloids as natural storage of peptide hormones in pituitary secretory granules, Science (80-. ). 325 (2009) 328–332.

[58] L. Rochin, I. Hurbain, L. Serneels, C. Fort, B. Watt, P. Leblanc, M.S. Marks, B. De Strooper, G. Raposo, G. van Niel, BACE2 processes PMEL to form the melanosome amyloid matrix in pigment cells, Proc. Natl. Acad. Sci. 110 (2013) 10658–10663.

[59] A.M. Gravagnuolo, S. Longobardi, A. Luchini, M.-S. Appavou, L. De Stefano, E. Notomista, L. Paduano, P. Giardina, Class I hydrophobin Vmh2 adopts atypical mechanisms to self-assemble into functional amyloid fibrils, Biomacromolecules. 17 (2016) 954–964.

[60] E.B. Sawyer, D. Claessen, M. Haas, B. Hurgobin, S.L. Gras, The assembly of individual chaplin peptides from Streptomyces coelicolor into functional amyloid fibrils, PLoS One. 6 (2011) e18839.

[61] A. Chen, Session 2G: Characterization of Alzheimer's Disease Associated Amyloid Beta Oligomers and Phosphorylated Tau in the Developing Avian CNS, (2018).

[62] J.W. Kelly, Amyloid fibril formation and protein misassembly: a structural quest for insights into amyloid and prion diseases, Structure. 5 (1997) 595–600.

[63] R. Diaz-Avalos, C.-Y. King, J. Wall, M. Simon, D.L.D. Caspar, Strain-specific morphologies of yeast prion amyloid fibrils, Proc. Natl. Acad. Sci. 102 (2005) 10165–10170.

[64] M.G. Spillantini, M.L. Schmidt, V.M.-Y. Lee, J.Q. Trojanowski, R. Jakes, M. Goedert, α-Synuclein in Lewy bodies, Nature. 388 (1997) 839.

[65] K. Markopoulou, Y. Compta, Cerebrospinal fluid levels of alpha-synuclein in PARKINSON'S disease: Another long and winding road, (2018).

[66] D.R. Rosen, T. Siddique, D. Patterson, D.A. Figlewicz, P. Sapp, A. Hentati, D. Donaldson, J. Goto, J.P. O'Regan, H.-X. Deng, Mutations in Cu/Zn superoxide dismutase gene are associated with familial amyotrophic lateral sclerosis, Nature. 362 (1993) 59.

[67] H.D. Durham, J. Roy, L. Dong, D.A. Figlewicz, Aggregation of mutant Cu/Zn superoxide dismutase proteins in a culture model of ALS, J. Neuropathol. Exp. Neurol. 56 (1997) 523–530.

[68] A.K.-H. Chen, R.Y.-Y. Lin, E.Z.-J. Hsieh, P.-H. Tu, R.P.-Y. Chen, T.-Y. Liao, W. Chen, C.-H. Wang, J.J.-T. Huang, Induction of amyloid fibrils by the C-terminal fragments of TDP-43 in amyotrophic lateral sclerosis, J. Am. Chem. Soc. 132 (2010) 1186–1187.

[69] G. Bates, Huntingtin aggregation and toxicity in Huntington's disease, Lancet. 361 (2003) 1642–1644.

[70] A.K. Thakur, M. Jayaraman, R. Mishra, M. Thakur, V.M. Chellgren, I.-J.L. Byeon, D.H. Anjum, R. Kodali, T.P. Creamer, J.F. Conway, Polyglutamine disruption of the huntingtin exon 1 N terminus triggers a complex aggregation mechanism, Nat. Struct. Mol. Biol. 16 (2009) 380.

[71] J.R. Brender, S. Salamekh, A. Ramamoorthy, Membrane disruption and early events in the aggregation of the diabetes related peptide IAPP from a molecular perspective, Acc. Chem. Res. 45 (2012) 454–462.

[72] L. Marzban, K. Park, C.B. Verchere, Islet amyloid polypeptide and type 2 diabetes, Exp. Gerontol. 38 (2003) 347–351.

[73] M.M. Sousa, I. Cardoso, R. Fernandes, A. Guimaraes, M.J. Saraiva, Deposition of transthyretin in early stages of familial amyloidotic polyneuropathy: evidence for toxicity of nonfibrillar aggregates, Am. J. Pathol. 159 (2001) 1993–2000.

[74] E. Scherzinger, A. Sittler, K. Schweiger, V. Heiser, R. Lurz, R. Hasenbank, G.P. Bates, H. Lehrach,

E.E. Wanker, Self-assembly of polyglutamine-containing huntingtin fragments into amyloid-like fibrils: implications for Huntington's disease pathology, Proc. Natl. Acad. Sci. 96 (1999) 4604–4609.

[75] M. Sunde, L.C. Serpell, M. Bartlam, P.E. Fraser, M.B. Pepys, C.C.F. Blake, Common core structure of amyloid fibrils by synchrotron X-ray diffraction, J. Mol. Biol. 273 (1997) 729–739.

[76] E. Frare, P.P. de Laureto, J. Zurdo, C.M. Dobson, A. Fontana, A highly amyloidogenic region of hen lysozyme, J. Mol. Biol. 340 (2004) 1153–1165.

[77] A.C. Badrick, C.E. Jones, The amyloidogenic region of the human prion protein contains a high affinity (Met) 2 (His) 2 Cu (I) binding site, J. Inorg. Biochem. 103 (2009) 1169–1175.

[78] H. Zhou, S. Liu, Q. Shao, D. Ma, Z. Yang, R. Zhou, Mechanism by which DHA inhibits the aggregation of KLVFFA peptides: A molecular dynamics study, J. Chem. Phys. 148 (2018) 115102.

[79] J.P. Zbilut, A. Colosimo, F. Conti, M. Colafranceschi, C. Manetti, M. Valerio, C.L. Webber Jr, A. Giuliani, Protein aggregation/folding: the role of deterministic singularities of sequence hydrophobicity as determined by nonlinear signal analysis of acylphosphatase and Aβ (1–40), Biophys. J. 85 (2003) 3544–3557.

[80] G.G. Tartaglia, A. Cavalli, R. Pellarin, A. Caflisch, The role of aromaticity, exposed surface, and dipole moment in determining protein aggregation rates, Protein Sci. 13 (2004) 1939–1941.

[81] E. Jack, M. Newsome, P.G. Stockley, S.E. Radford, D.A. Middleton, The organization of aromatic side groups in an amyloid fibril probed by solid-state 2H and 19F NMR spectroscopy, J. Am. Chem. Soc. 128 (2006) 8098–8099.

[82] K. Tao, P. Makam, R. Aizen, E. Gazit, Self-assembling peptide semiconductors, Science (80-. ). 358 (2017) eaam9756.

[83] Y. Zhao, W. Yang, C. Chen, J. Wang, L. Zhang, H. Xu, Rational design and self-assembly of short amphiphilic peptides and applications, Curr. Opin. Colloid Interface Sci. (2018).

[84] M. Sunde, C. Blake, The structure of amyloid fibrils by electron microscopy and X-ray diffraction, in: Adv. Protein Chem., Elsevier, 1997: pp. 123–159.

[85] R. Nelson, M.R. Sawaya, M. Balbirnie, A.Ø. Madsen, C. Riekel, R. Grothe, D. Eisenberg, Structure of the cross-β spine of amyloid-like fibrils, Nature. 435 (2005) 773.

[86] J.L. Jimenez, E.J. Nettleton, M. Bouchard, C. V Robinson, C.M. Dobson, H.R. Saibil, The protofilament structure of insulin amyloid fibrils, Proc. Natl. Acad. Sci. 99 (2002) 9196–9201.

[87] E. Gazit, Self-assembled peptide nanostructures: the design of molecular building blocks and their technological utilization, Chem. Soc. Rev. 36 (2007) 1263–1269.

[88] G. Lamour, R. Nassar, P.H.W. Chan, G. Bozkurt, J. Li, J.M. Bui, C.K. Yip, T. Mayor, H. Li, H. Wu, Mapping the broad structural and mechanical properties of amyloid fibrils, Biophys. J. 112 (2017) 584–594.

[89] I. Cherny, E. Gazit, Amyloids: not only pathological agents but also ordered nanomaterials, Angew. Chemie Int. Ed. 47 (2008) 4062–4069.

[90] L. Yang, K.O. Van der Werf, C.F.C. Fitié, M.L. Bennink, P.J. Dijkstra, J. Feijen, Mechanical properties of native and cross-linked type I collagen fibrils, Biophys. J. 94 (2008) 2204–2211.

[91] J.F. Smith, T.P.J. Knowles, C.M. Dobson, C.E. MacPhee, M.E. Welland, Characterization of the nanoscale properties of individual amyloid fibrils, Proc. Natl. Acad. Sci. 103 (2006) 15806–15811.

[92] B. Choi, T. Kim, S.W. Lee, K. Eom, Nanomechanical characterization of amyloid fibrils using single-molecule experiments and computational simulations, J. Nanomater. 2016 (2016).

[93] T.J. Paul, Z. Hoffmann, C. Wang, M. Shanmugasundaram, J. DeJoannis, A. Shekhtman, I.K.

Lednev, V.K. Yadavalli, R. Prabhakar, Structural and mechanical properties of amyloid beta fibrils: a combined experimental and theoretical approach, J. Phys. Chem. Lett. 7 (2016) 2758–2764.

[94] O.M.A. El-Agnaf, S. Nagala, B.P. Patel, B.M. Austen, Non-fibrillar oligomeric species of the amyloid ABri peptide, implicated in familial British dementia, are more potent at inducing apoptotic cell death than protofibrils or mature fibrils, J. Mol. Biol. 310 (2001) 157–168.

[95] J. Bieschke, M. Herbst, T. Wiglenda, R.P. Friedrich, A. Boeddrich, F. Schiele, D. Kleckers, J.M.L. del Amo, B.A. Grüning, Q. Wang, Small-molecule conversion of toxic oligomers to nontoxic β-sheet–rich amyloid fibrils, Nat. Chem. Biol. 8 (2012) 93.

[96] B. Winner, R. Jappelli, S.K. Maji, P.A. Desplats, L. Boyer, S. Aigner, C. Hetzer, T. Loher, M. Vilar, S. Campioni, In vivo demonstration that α-synuclein oligomers are toxic, Proc. Natl. Acad. Sci. 108 (2011) 4194–4199.

[97] R.S. Jacob, S. Sen, S.K. Maji, Adhesion of Human Mesenchymal Stem Cells and Differentiation of SH-SY5Y Cells on Amyloid Fibrils, in: Macromol. Symp., Wiley Online Library, 2016: pp. 35–42.

[98] G. Nyström, W.-K. Fong, R. Mezzenga, Ice-templated and cross-linked amyloid fibril aerogel scaffolds for cell growth, Biomacromolecules. 18 (2017) 2858–2865.

[99] T.A. Pertinhez, M. Bouchard, E.J. Tomlinson, R. Wain, S.J. Ferguson, C.M. Dobson, L.J. Smith, Amyloid fibril formation by a helical cytochrome, FEBS Lett. 495 (2001) 184–186.

[100] S. Shaham-Niv, P. Rehak, L. Vuković, L. Adler-Abramovich, P. Král, E. Gazit, Formation of apoptosis-inducing amyloid fibrils by tryptophan, Isr. J. Chem. 57 (2017) 729–737.

[101] S. Han, M. Kollmer, D. Markx, S. Claus, P. Walther, M. Fändrich, Amyloid plaque structure and cell surface interactions of β-amyloid fibrils revealed by electron tomography, Sci. Rep. 7 (2017) 43577.

[102] D. Ghosh, P. Dutta, C. Chakraborty, P.K. Singh, A. Anoop, N.N. Jha, R.S. Jacob, M. Mondal, S. Mankar, S. Das, Complexation of amyloid fibrils with charged conjugated polymers, Langmuir. 30 (2014) 3775–3786.

[103] R.A. Taheri, Y. Akhtari, T.T. Moghadam, B. Ranjbar, Assembly of Gold Nanorods on HSA Amyloid Fibrils to Develop a Conductive Nanoscaffold for Potential Biomedical and Biosensing Applications, Sci. Rep. 8 (2018) 9333.

[104] P.R. Selvakannan, A. Swami, D. Srisathiyanarayanan, P.S. Shirude, R. Pasricha, A.B. Mandale, M. Sastry, Synthesis of aqueous Au core− Ag shell nanoparticles using tyrosine as a pH-dependent reducing agent and assembling phase-transferred silver nanoparticles at the air− water interface, Langmuir. 20 (2004) 7825–7836.

[105] W. Zhang, J. Xi, Y. Zhang, Z. Su, G. Wei, Green synthesis and fabrication of an electrochemical and colorimetric sensor based on self-assembled peptide-Au nanofibril architecture, Arab. J. Chem. 13 (2020) 1406–1414.

[106] B. Schmuck, M. Gudmundsson, J. Blomqvist, H. Hansson, T. Härd, M. Sandgren, Production of Ready-To-Use Functionalized Sup35 Nanofibrils Secreted by Komagataella pastoris, ACS Nano. 12 (2018) 9363–9371.

[107] S. Rima, M. Lattuada, Protein Amyloid Fibrils as Template for the Synthesis of Silica Nanofibers, and Their Use to Prepare Superhydrophobic, Lotus-Like Surfaces, Small. (2018) 1802854.

[108] J.-M. Jung, G. Savin, M. Pouzot, C. Schmitt, R. Mezzenga, Structure of heat-induced β-lactoglobulin aggregates and their complexes with sodium-dodecyl sulfate, Biomacromolecules. 9 (2008) 2477–2486.

[109] A.J. Patil, J.L. Vickery, T.B. Scott, S. Mann, Aqueous stabilization and self-assembly of graphene sheets into layered bio-nanocomposites using DNA, Adv. Mater. 21 (2009) 3159–3164.

[110] T.P.J. Knowles, M.J. Buehler, Nanomechanics of functional and pathological amyloid materials, Nat. Nanotechnol. 6 (2011) 469.

[111] M. Yolamanova, C. Meier, A.K. Shaytan, V. Vas, C.W. Bertoncini, F. Arnold, O. Zirafi, S.M. Usmani, J.A. Müller, D. Sauter, Peptide nanofibrils boost retroviral gene transfer and provide a rapid means for concentrating viruses, Nat. Nanotechnol. 8 (2013) 130.

[112] Y. Kuang, X. Du, J. Zhou, B. Xu, Supramolecular nanofibrils inhibit cancer progression in vitro and in vivo, Adv. Healthc. Mater. 3 (2014) 1217–1221.

[113] H. Jang, F.T. Arce, M. Mustata, S. Ramachandran, R. Capone, R. Nussinov, R. Lal, Antimicrobial protegrin-1 forms amyloid-like fibrils with rapid kinetics suggesting a functional link, Biophys. J. 100 (2011) 1775–1783.

[114] B. Hu, Y. Shen, J. Adamcik, P. Fischer, M. Schneider, M.J. Loessner, R. Mezzenga, Polyphenol-Binding Amyloid Fibrils Self-Assemble into Reversible Hydrogels with Antibacterial Activity, ACS Nano. 12 (2018) 3385–3396.

[115] S. Das, K. Zhou, D. Ghosh, N.N. Jha, P.K. Singh, R.S. Jacob, C.C. Bernard, D.I. Finkelstein, J.S. Forsythe, S.K. Maji, Implantable amyloid hydrogels for promoting stem cell differentiation to neurons, NPG Asia Mater. 8 (2016) e304.

[116] S. Das, M.K. Kumawat, S. Ranganathan, R. Kumar, J. Adamcik, P. Kadu, R. Padinhateeri, R. Srivastava, R. Mezzenga, S.K. Maji, Cell Alignment on Graphene–Amyloid Composites, Adv. Mater. Interfaces. 5 (2018) 1800621.

[117] S. Kirti, K. Patel, S. Das, P. Shrimali, S. Samanta, R. Kumar, D. Chatterjee, D. Ghosh, A. Kumar, P. Tayalia, Amyloid Fibrils with Positive Charge Enhance Retroviral Transduction in Mammalian Cells, ACS Biomater. Sci. Eng. (2018).

[118] U.O.S. Seker, A.Y. Chen, R.J. Citorik, T.K. Lu, Synthetic biogenesis of bacterial amyloid nanomaterials with tunable inorganic–organic interfaces and electrical conductivity, ACS Synth. Biol. 6 (2017) 266–275.

[119] S. Bolisetty, M. Arcari, J. Adamcik, R. Mezzenga, Hybrid amyloid membranes for continuous flow catalysis, Langmuir. 31 (2015) 13867–13873.

[120] Y. Shen, G. Nyström, R. Mezzenga, Amyloid Fibrils form Hybrid Colloidal Gels and Aerogels with Dispersed CaCO3 Nanoparticles, Adv. Funct. Mater. 27 (2017) 1700897.

[121] J. Lee, J. Lee, B. Yeom, K. Char, Layer-by-Layer Assembly of κ-Casein Amyloid Fibrils for the Preparation of Hollow Microcapsules, Macromol. Chem. Phys. 219 (2018) 1700382.

[122] B. Maleki, F. Tabandeh, Z.-S. Soheili, D. Morshedi, Application of proteinous nanofibrils to culture retinal pigmented epithelium cells: A versatile biomaterial, React. Funct. Polym. 115 (2017) 36–42.

[123] Y. Shen, L. Posavec, S. Bolisetty, F.M. Hilty, G. Nyström, J. Kohlbrecher, M. Hilbe, A. Rossi, J. Baumgartner, M.B. Zimmermann, Amyloid fibril systems reduce, stabilize and deliver bioavailable nanosized iron, Nat. Nanotechnol. 12 (2017) 642.

[124] N.P. Reynolds, M. Charnley, M.N. Bongiovanni, P.G. Hartley, S.L. Gras, Biomimetic topography and chemistry control cell attachment to amyloid fibrils, Biomacromolecules. 16 (2015) 1556–1565.

[125] R.S. Jacob, D. Ghosh, P.K. Singh, S.K. Basu, N.N. Jha, S. Das, P.K. Sukul, S. Patil, S. Sathaye, A. Kumar, Self healing hydrogels composed of amyloid nano fibrils for cell culture and stem cell differentiation, Biomaterials. 54 (2015) 97–105.

[126] X. Wu, M. Li, Z. Li, L. Lv, Y. Zhang, C. Li, Amyloid-graphene oxide as immobilization platform of Au nanocatalysts and enzymes for improved glucose-sensing activity, J. Colloid Interface Sci. 490 (2017) 336–342.

[127] I. Nandi, S. Chall, S. Chowdhury, T. Mitra, S.S. Roy, K. Chattopadhyay, Protein fibril-templated biomimetic synthesis of highly fluorescent gold nanoclusters and their applications in cysteine sensing, ACS Omega. 3 (2018) 7703–7714.

[128] P. Hanczyc, L. Sznitko, C. Zhong, A.J. Heeger, Stimulated emission from rhodamine 6G aggregates self-assembled on amyloid protein fibrils, ACS Photonics. 2 (2015) 1755–1762.

[129] B. Schmuck, M. Sandgren, T. Härd, A fine-tuned composition of protein nanofibrils yields an upgraded functionality of displayed antibody binding domains, Biotechnol. J. 12 (2017) 1600672.

[130] N. Amini, M.B. Gholivand, M. Shamsipur, A.A.M. Movahedi, S. Farahi, M. Habibi-Rezaei, A. Maleki, R. Rezaee, K. Naderi, Fabrication of a glycation induced amyloid nanofibril and polyalizarin yellow R nanobiocomposite: application for electrocatalytic determination of hydrogen peroxide, Int. J. Biol. Macromol. 123 (2019) 1297–1304.

[131] C. Li, A. Born, T. Schweizer, M. Zenobi-Wong, M. Cerruti, R. Mezzenga, Amyloid-hydroxyapatite bone biomimetic composites, Adv. Mater. 26 (2014) 3207–3212.

[132] G. Kabay, A.E. Meydan, G.K. Can, C. Demirci, M. Mutlu, Controlled release of a hydrophilic drug from electrospun amyloid-like protein blend nanofibers, Mater. Sci. Eng. C. 81 (2017) 271–279.

[133] E. Axpe, A. Duraj-Thatte, Y. Chang, D.-M. Kaimaki, A. Sanchez-Sanchez, H.B. Caliskan, N.-M. Dorval Courchesne, N.S. Joshi, Fabrication of amyloid curli fibers–alginate nanocomposite hydrogels with enhanced stiffness, ACS Biomater. Sci. Eng. 4 (2018) 2100–2105.

[134] M. Rashtchian, A. Hivechi, S.H. Bahrami, P.B. Milan, S. Simorgh, Fabricating alginate/poly (caprolactone) nanofibers with enhanced bio-mechanical properties via cellulose nanocrystal incorporation, Carbohydr. Polym. 233 (2020) 115873.

[135] K. Saha, A.J. Keung, E.F. Irwin, Y. Li, L. Little, D. V Schaffer, K.E. Healy, Substrate modulus

directs neural stem cell behavior, Biophys. J. 95 (2008) 4426–4438.

[136] M. Usuelli, T. Germerdonk, Y. Cao, M. Peydayesh, M. Bagnani, S. Handschin, G. Nyström, R. Mezzenga, Polysaccharide-reinforced amyloid fibril hydrogels and aerogels, Nanoscale. 13 (2021) 12534–12545.

[137] N. Duraffourg, M. Leprince, S. Crouzy, O. Hamelin, Y. Usson, L. Signor, C. Cavazza, V. Forge, L. Albertin, Hybrid amyloid-based redox hydrogel for bioelectrocatalytic H2 oxidation, Angew. Chemie. (2021).

[138] B. Hu, S. Yu, C. Shi, J. Gu, Y. Shao, Q. Chen, Y. Li, R. Mezzenga, Amyloid–polyphenol hybrid nanofilaments mitigate colitis and regulate gut microbial dysbiosis, ACS Nano. 14 (2020) 2760–2776.

[139] D. Wang, L. Niu, Z.-Y. Qiao, D.-B. Cheng, J. Wang, Y. Zhong, F. Bai, H. Wang, H. Fan, Synthesis of self-assembled porphyrin nanoparticle photosensitizers, ACS Nano. 12 (2018) 3796–3803.

[140] H. Khalesi, C. Sun, J. He, W. Lu, Y. Fang, The role of amyloid fibrils in the modification of whey protein isolate gels with the form of stranded and particulate microstructures, Food Res. Int. 140 (2021) 109856.

[141] T. Ghosh, K. Nakano, N. Mulchandani, V. Katiyar, Curcumin loaded iron functionalized biopolymeric nanofibre reinforced edible nanocoatings for improved shelf life of cut pineapples, Food Packag. Shelf Life. 28 (2021) 100658.

[142] L. Gao, K. Fan, X. Yan, Iron oxide nanozyme: A multifunctional enzyme mimetics for biomedical application, Nanozymology. (2020) 105–140.

[143] N.S. De Groot, S. Ventura, Amyloid fibril formation by bovine cytochrome c, Spectroscopy. 19 (2005) 199–205.

[144] T.N. Tikhonova, N.R. Rovnyagina, A.Y. Zherebker, N.N. Sluchanko, A.A. Rubekina, A.S. Orekhov, E.N. Nikolaev, V. V Fadeev, V.N. Uversky, E.A. Shirshin, Dissection of the deep-blue autofluorescence changes accompanying amyloid fibrillation, Arch. Biochem. Biophys. 651 (2018) 13–20.

[145] S.E. Rankin, A. Watts, H. Roder, T.J.T. Pinheiro, Folding of apocytochrome c induced by the interaction with negatively charged lipid micelles proceeds via a collapsed intermediate state, Protein Sci. 8 (1999) 381–393.

[146] Y. Chen, M.D. Barkley, Toward understanding tryptophan fluorescence in proteins, Biochemistry. 37 (1998) 9976–9982.

[147] A.B.T. Ghisaidoobe, S.J. Chung, Intrinsic tryptophan fluorescence in the detection and analysis of proteins: a focus on Förster resonance energy transfer techniques, Int. J. Mol. Sci. 15 (2014) 22518–22538.

[148] L. Whitmore, B.A. Wallace, Protein secondary structure analyses from circular dichroism spectroscopy: methods and reference databases, Biopolym. Orig. Res. Biomol. 89 (2008) 392–400.

[149] J. Dong, P.L. Carpinone, G. Pyrgiotakis, P. Demokritou, B.M. Moudgil, Synthesis of precision gold nanoparticles using Turkevich method, KONA Powder Part. J. 37 (2020) 224–232.

[150] Y. Xu, Y. Yan, D. Seeman, L. Sun, P.L. Dubin, Multimerization and aggregation of native-state insulin: effect of zinc, Langmuir. 28 (2012) 579–586.

[151] A.C. Steven, M.A. Navia, Specificity of stain distribution in electron micrographs of protein molecules contrasted with uranyl acetate, J. Microsc. 128 (1982) 145–155.

[152] B. Schaffer, Digital Micrograph, in: Transm. Electron Microsc., Springer, 2016: pp. 167–196.

[153] T.J. Collins, ImageJ for microscopy, Biotechniques. 43 (2007) S25–S30.

[154] S. Karmakar, A. Sankhla, V. Katiyar, Supramolecular organization of Cytochrome-C into quantum-dot decorated macromolecular network under pH and thermal stress, Int. J. Biol. Macromol. (2021).

[155] H. Hoeft, P. Schwaab, Investigations towards optimizing EDS analysis by the Cliff-Lorimer method in scanning transmission electron microscopy, X-Ray Spectrom. 17 (1988) 201–208.

[156] S.O. Garbuzynskiy, M.Y. Lobanov, O. V Galzitskaya, FoldAmyloid: a method of prediction of amyloidogenic regions from protein sequence, Bioinformatics. 26 (2010) 326–332.

[157] O. V Galzitskaya, S.O. Garbuzynskiy, M.Y. Lobanov, FoldUnfold: web server for the prediction of disordered regions in protein chain, Bioinformatics. 22 (2006) 2948–2949.

[158] M.Y. Lobanov, M.Y. Suvorina, N. V Dovidchenko, I. V Sokolovskiy, A.K. Surin, O. V Galzitskaya, A novel web server predicts amino acid residue protection against hydrogen–deuterium exchange, Bioinformatics. 29 (2013) 1375–1381.

[159] M.Y. Lobanov, I. V Sokolovskiy, O. V Galzitskaya, IsUnstruct: prediction of the residue status to be ordered or disordered in the protein chain by a method based on the Ising model, J. Biomol. Struct. Dyn. 31 (2013) 1034–1043.

[160] A.C. Wallace, R.A. Laskowski, J.M. Thornton, LIGPLOT: a program to generate schematic diagrams of protein-ligand interactions, Protein Eng. Des. Sel. 8 (1995) 127–134.

[161] N. Mirkin, J. Jaconcic, V. Stojanoff, A. Moreno, High resolution X-ray crystallographic structure of bovine heart cytochrome c and its application to the design of an electron transfer biosensor, Proteins Struct. Funct. Bioinforma. 70 (2008) 83–92.

[162] V.I. Timofeev, R.N. Chuprov-Netochin, V.R. Samigina, V. V Bezuglov, K.A. Miroshnikov, I.P. Kuranova, X-ray investigation of gene-engineered human insulin crystallized from a solution containing polysialic acid, Acta Crystallogr. Sect. F Struct. Biol. Cryst. Commun. 66 (2010) 259–

263.

[163] D. Schneidman-Duhovny, Y. Inbar, R. Nussinov, H.J. Wolfson, PatchDock and SymmDock: servers for rigid and symmetric docking, Nucleic Acids Res. 33 (2005) W363–W367.

[164] R.A. Laskowski, M.B. Swindells, LigPlot+: multiple ligand–protein interaction diagrams for drug discovery, (2011).

[165] Y. Wang, Y. Shen, G. Qi, Y. Li, X.S. Sun, D. Qiu, Y. Li, Formation and physicochemical properties of amyloid fibrils from soy protein, Int. J. Biol. Macromol. 149 (2020) 609–616.

[166] P. Awasthi, A. Singh, S. Khatun, A.N. Gupta, S. Das, Fibril growth captured by electrical properties of amyloid-β and human islet amyloid polypeptide, Phys. Rev. E. 101 (2020) 62413.

[167] A.M. Garcia, R. Lavendomme, S. Kralj, M. Kurbasic, O. Bellotto, M.C. Cringoli, S. Semeraro, A. Bandiera, R. De Zorzi, S. Marchesan, Self-Assembly of an Amino Acid Derivative into an Antimicrobial Hydrogel Biomaterial, Chem. Eur. J. 26 (2020) 1880–1886.

[168] Y. Han, Y. Cao, S. Bolisetty, T. Tian, S. Handschin, C. Lu, R. Mezzenga, Amyloid Fibril-Templated High-Performance Conductive Aerogels with Sensing Properties, Small. 16 (2020) 2004932.

[169] N. Singh, K. Patel, A. Navalkar, P. Kadu, D. Datta, D. Chatterjee, A. Shaw, S. Jadhav, S.K. Maji, Amyloid fibril-based hydrogels for high-throughput tumor spheroid modeling, BioRxiv. (2020).

[170] J. Liu, M. Tian, L. Shen, Nanopatterned polymer surface modulates twist polymorphism in a single amyloid fibril, Macromol. Rapid Commun. 41 (2020) 1900619.

[171] M. Tunesi, L. Izzo, I. Raimondi, D. Albani, C. Giordano, A miniaturized hydrogel-based in vitro model for dynamic culturing of human cells overexpressing beta-amyloid precursor protein, J. Tissue Eng. 11 (2020) 2041731420945633.

[172] J.T. Lee, J. Lee, Y. Kwon, J.Y. Kim, Y. Lin, Y.-H. Lee, S.R. Paik, Ultra-thin free-floating carbon

nanotube/gold nanoparticle hybrid film prepared with self-assembly protein of α-synuclein, Sensors Actuators B Chem. 305 (2020) 127514.

[173] J. Berndtsson, A. Aufschnaiter, S. Rathore, L. Marin-Buera, H. Dawitz, J. Diessl, V. Kohler, A. Barrientos, S. Büttner, F. Fontanesi, Respiratory supercomplexes enhance electron transport by decreasing cytochrome c diffusion distance, EMBO Rep. 21 (2020) e51015.

[174] J.-M. Alakoskela, A. Jutila, A.C. Simonsen, J. Pirneskoski, S. Pyhäjoki, R. Turunen, S. Marttila, O.G. Mouritsen, E. Goormaghtigh, P.K.J. Kinnunen, Characteristics of fibers formed by cytochrome c and induced by anionic phospholipids, Biochemistry. 45 (2006) 13447–13453.

[175] S.T. Kim, Y.-J. Lee, Y.-S. Hwang, S. Lee, Study on aggregation behavior of Cytochrome C–conjugated silver nanoparticles using asymmetrical flow field-flow fractionation, Talanta. 132 (2015) 939–944.

[176] A. Nucara, M. Carbone, F. Ripanti, R. Manganiello, P. Postorino, M. Carbonaro, Achieving cytochrome c fibril/aggregate control towards micro-platelets and micro-fibers by tuning pH and protein concentration: a combined morphological and spectroscopic analysis, Int. J. Biol. Macromol. 138 (2019) 106–115.

[177] L.R. Menezes, J.C. Araújo-Chaves, D.M. Lopes, J.D. Bronzato, G. Sombrio, D. Criado, A. Zúñiga, A.J.C. Lanfredi, J.A. Souza, I.L. Nantes-Cardoso, Effect of the protein structure and heme iron coordination sphere on the long-range electron transfer from hematite and zinc oxide nanostructures to cytochrome c, Int. J. Nanotechnol. 17 (2020) 42–56.

[178] X. Gong, T. Milic, C. Xu, J.D. Batteas, C.M. Drain, Preparation and characterization of porphyrin nanoparticles, J. Am. Chem. Soc. 124 (2002) 14290–14291.

[179] J. Yang, L. Xiong, M. Li, J. Xiao, X. Geng, B. Wang, Q. Sun, Preparation and characterization of tadpole-and sphere-shaped Hemin nanoparticles for enhanced solubility, Nanoscale Res. Lett. 14

(2019) 1–9.

[180] J. Wan, H.A. Kalpage, A. Vaishnav, J. Liu, I. Lee, G. Mahapatra, A.A. Turner, M.P. Zurek, Q. Ji, C.T. Moraes, Regulation of respiration and apoptosis by cytochrome c threonine 58 phosphorylation, Sci. Rep. 9 (2019) 1–16.

[181] L. Wang, E. Santos, D. Schenk, M. Rabago-Smith, Kinetics and mechanistic studies on the reaction between cytochrome c and tea catechins, Antioxidants. 3 (2014) 559–568.

[182] M. Hulko, I. Hospach, N. Krasteva, G. Nelles, Cytochrome C biosensor—A model for gas sensing, Sensors. 11 (2011) 5968–5980.

[183] M.-T. Hopp, B.F. Schmalohr, T. Kühl, M.S. Detzel, A. Wißbrock, D. Imhof, Heme Determination and Quantification Methods and Their Suitability for Practical Applications and Everyday Use, (2020).

[184] J. Wei, J. Qiu, L. Li, L. Ren, X. Zhang, J. Chaudhuri, S. Wang, A reduced graphene oxide based electrochemical biosensor for tyrosine detection, Nanotechnology. 23 (2012) 335707.

[185] V.E. Noval, J.G. Carriazo, Fe3O4-TiO2 and Fe3O4-SiO2 core-shell powders synthesized from industrially processed magnetite (Fe3O4) microparticles, Mater. Res. 22 (2019).

[186] J. Zhang, A. Byeon, J.W. Lee, Boron-doped carbon–iron nanocomposites as efficient oxygen reduction electrocatalysts derived from carbon dioxide, Chem. Commun. 50 (2014) 6349–6352.

[187] W. Zhang, S. Xiao, D.U. Ahn, Protein oxidation: basic principles and implications for meat quality, Crit. Rev. Food Sci. Nutr. 53 (2013) 1191–1201.

[188] D.M. Arciero, A.B. Hooper, M. Cai, R. Timkovich, Evidence for the structure of the active site heme P460 in hydroxylamine oxidoreductase of Nitrosomonas, Biochemistry. 32 (1993) 9370–9378.

[189] L.R. Hanton, K. Lee, C− S Bond Cleavage by Chloride in a Thioether N2S2 Complex of Platinum, Inorg. Chem. 38 (1999) 1634–1637.

[190] Z. Wang, Y. Ando, A.D. Nugraheni, C. Ren, S. Nagao, S. Hirota, Self-oxidation of cytochrome c at methionine80 with molecular oxygen induced by cleavage of the Met–heme iron bond, Mol. Biosyst. 10 (2014) 3130–3137.

[191] F.I. Rosell, A.G. Mauk, Spectroscopic properties of a mitochondrial cytochrome c with a single thioether bond to the heme prosthetic group, Biochemistry. 41 (2002) 7811–7818.

[192] G.E.D. Mullen, M.J. Went, S. Wocadlo, A.K. Powell, P.J. Blower, Electron Transfer Induced C S Bond Cleavage in Rhenium and Technetium Thioether Complexes: Structural and Chemical Evidence for π Back-Donation to C S σ* Orbitals, Angew. Chemie Int. Ed. English. 36 (1997) 1205–1207.

[193] A. Merlino, X-ray structure of bovine heart cytochrome c at high ionic strength, BioMetals. 31 (2018) 277–284.

[194] S.J. Ferguson, J.M. Stevens, J.W.A. Allen, I.B. Robertson, Cytochrome c assembly: a tale of ever increasing variation and mystery?, Biochim. Biophys. Acta (BBA)-Bioenergetics. 1777 (2008) 980–984.

[195] H. Theorell, Studies on cytochrome c. IV. The magnetic properties of ferric and ferrous cytochrome c, J. Am. Chem. Soc. 63 (1941) 1820–1827.

[196] V.M. Friebe, D. Millo, D.J.K. Swainsbury, M.R. Jones, R.N. Frese, Cytochrome c provides an electron-funneling antenna for efficient photocurrent generation in a reaction center biophotocathode, ACS Appl. Mater. Interfaces. 9 (2017) 23379–23388.

[197] A. Mullard, Biomolecular condensates pique drug discovery curiosity, Nat. Rev. Drug Discov.

(2019) NA-NA.

[198] K. Hong, D. Song, Y. Jung, Behavior control of membrane-less protein liquid condensates with metal ion-induced phase separation, Nat. Commun. 11 (2020) 1–12.

[199] V. Yeong, E.G. Werth, L.M. Brown, A.C. Obermeyer, Formation of biomolecular condensates in bacteria by tuning protein electrostatics, ACS Cent. Sci. 6 (2020) 2301–2310.

[200] C.P. Brangwynne, C.R. Eckmann, D.S. Courson, A. Rybarska, C. Hoege, J. Gharakhani, F. Jülicher, A.A. Hyman, Germline P granules are liquid droplets that localize by controlled dissolution/condensation, Science (80-. ). 324 (2009) 1729–1732.

[201] C.P. Brangwynne, T.J. Mitchison, A.A. Hyman, Active liquid-like behavior of nucleoli determines their size and shape in Xenopus laevis oocytes, Proc. Natl. Acad. Sci. 108 (2011) 4334–4339.

[202] P. Li, S. Banjade, H.-C. Cheng, S. Kim, B. Chen, L. Guo, M. Llaguno, J. V Hollingsworth, D.S. King, S.F. Banani, Phase transitions in the assembly of multivalent signalling proteins, Nature. 483 (2012) 336–340.

[203] S. Wegmann, B. Eftekharzadeh, K. Tepper, K.M. Zoltowska, R.E. Bennett, S. Dujardin, P.R. Laskowski, D. MacKenzie, T. Kamath, C. Commins, Tau protein liquid–liquid phase separation can initiate tau aggregation, EMBO J. 37 (2018) e98049.

[204] M. Du, Z.J. Chen, DNA-induced liquid phase condensation of cGAS activates innate immune signaling, Science (80-. ). 361 (2018) 704–709.

[205] J.J. Bouchard, J.H. Otero, D.C. Scott, E. Szulc, E.W. Martin, N. Sabri, D. Granata, M.R. Marzahn, K. Lindorff-Larsen, X. Salvatella, Cancer mutations of the tumor suppressor SPOP disrupt the formation of active, phase-separated compartments, Mol. Cell. 72 (2018) 19–36.

[206] W. Li, J. Hu, B. Shi, F. Palomba, M.A. Digman, E. Gratton, H. Jiang, Biophysical properties of

AKAP95 protein condensates regulate splicing and tumorigenesis, Nat. Cell Biol. 22 (2020) 960–972.

[207] N.B. Nedelsky, J.P. Taylor, Bridging biophysics and neurology: aberrant phase transitions in neurodegenerative disease, Nat. Rev. Neurol. 15 (2019) 272–286.

[208] J. Kim, D. Choi, S.-Y. Cha, Y.-M. Oh, E. Hwang, C. Park, K.-S. Ryu, Zinc-mediated reversible multimerization of Hsp31 enhances the activity of holding chaperone, J. Mol. Biol. 430 (2018) 1760–1772.

[209] K. Hagner, S. Setayeshgar, M. Lynch, Stochastic protein multimerization, activity, and fitness, Phys. Rev. E. 98 (2018) 62401.

[210] K.S. Christopherson, N.T. Sweeney, S.E. Craven, R. Kang, A.E.-D. El-Husseini, D.S. Bredt, Lipid- and protein-mediated multimerization of PSD-95: implications for receptor clustering and assembly of synaptic protein networks, J. Cell Sci. 116 (2003) 3213–3219.

[211] J. Mohanty, M.N. Shinde, N. Barooah, A.C. Bhasikuttan, Reversible insulin hexamer assembly promoted by ethyl violet: pH-controlled uptake and release, J. Phys. Chem. Lett. 7 (2016) 3978–3983.

[212] A.W.P. Fitzpatrick, H.R. Saibil, Cryo-EM of amyloid fibrils and cellular aggregates, Curr. Opin. Struct. Biol. 58 (2019) 34–42.

[213] D. Li, C. Liu, Structural diversity of amyloid fibrils and advances in their structure determination, Biochemistry. 59 (2020) 639–646.

[214] J. Adamcik, J.-M. Jung, J. Flakowski, P. De Los Rios, G. Dietler, R. Mezzenga, Understanding amyloid aggregation by statistical analysis of atomic force microscopy images, Nat. Nanotechnol. 5 (2010) 423–428.

[215] Y. Sun, A. Kakinen, Y. Xing, P. Faridi, A. Nandakumar, A.W. Purcell, T.P. Davis, P.C. Ke, F. Ding, Amyloid Self-Assembly of hIAPP8-20 via the Accumulation of Helical Oligomers, α-Helix to β-Sheet Transition, and Formation of β-Barrel Intermediates, Small. 15 (2019) 1805166.

[216] M.C. Carpenter, D.E. Wilcox, Thermodynamics of formation of the insulin hexamer: metal-stabilized proton-coupled assembly of quaternary structure, Biochemistry. 53 (2014) 1296–1301.

[217] E. Duboué-Dijon, P. Delcroix, H. Martinez-Seara, J. Hladílková, P. Coufal, T. Křížek, P. Jungwirth, Binding of divalent cations to insulin: capillary electrophoresis and molecular simulations, J. Phys. Chem. B. 122 (2018) 5640–5648.

[218] C.G. Frankær, P. Sønderby, M.B. Bang, R.V. Mateiu, M. Groenning, J. Bukrinski, P. Harris, Insulin fibrillation: the influence and coordination of Zn2+, J. Struct. Biol. 199 (2017) 27–38.

[219] X. Chang, A.M.M. Jørgensen, P. Bardrum, J.J. Led, Solution structures of the R6 human insulin hexamer, Biochemistry. 36 (1997) 9409–9422.

[220] E. Mosekilde, K.S. Jensen, C. Binder, S. Pramming, B. Thorsteinsson, Modeling absorption kinetics of subcutaneous injected soluble insulin, J. Pharmacokinet. Biopharm. 17 (1989) 67–87.

[221] Q. Hua, M. Liu, S.-Q. Hu, W. Jia, P. Arvan, M.A. Weiss, A conserved histidine in insulin is required for the foldability of human proinsulin: structure and function of an ALAB5 analog, J. Biol. Chem. 281 (2006) 24889–24899.

[222] G. Bentley, E. Dodson, G.U.Y. Dodson, D. Hodgkin, D.A.N. Mercola, Structure of insulin in 4-zinc insulin, Nature. 261 (1976) 166–168.

[223] J. Kevin, F. Xu, S. Toufanian, K.J.W. Chan, S. Said, T.C. Stimpson, E. González-Martínez, J.M. Moran-Mirabal, E.D. Cranston, T. Hoare, Multi-scale structuring of cell-instructive cellulose nanocrystal composite hydrogel sheets via sequential electrospinning and thermal wrinkling, Acta

Biomater. (2021).

[224] T. Paulraj, A. V Riazanova, A.J. Svagan, Bioinspired capsules based on nanocellulose, xyloglucan and pectin–The influence of capsule wall composition on permeability properties, Acta Biomater. 69 (2018) 196–205.

[225] L. Xie, C.-L. Tsou, Comparison of secondary structures of insulin and proinsulin by FTIR, J. Protein Chem. 12 (1993) 483–487.

[226] R.I. Litvinov, D.A. Faizullin, Y.F. Zuev, J.W. Weisel, The α-helix to β-sheet transition in stretched and compressed hydrated fibrin clots, Biophys. J. 103 (2012) 1020–1027.

[227] T. Ito, K. Kanazawa, H. Kimura-Suda, Analysis of collagen fiber orientation in bone of different aged rats using FTIR imaging, Mol. Cryst. Liq. Cryst. 622 (2015) 114–119.

[228] J. Kim, K. Park, Y. Cho, H. Shin, S. Kim, K. Char, J.W. Choi, Zn2+–Imidazole Coordination Crosslinks for Elastic Polymeric Binders in High-Capacity Silicon Electrodes, Adv. Sci. (2021) 2004290.

[229] N.S. Raut, P.R. Deshmukh, M.J. Umekar, N.R. Kotagale, Zinc cross-linked hydroxamated alginates for pulsed drug release, Int. J. Pharm. Investig. 3 (2013) 194.

[230] S. Mondal, S. Das, A.K. Nandi, A review on recent advances in polymer and peptide hydrogels, Soft Matter. 16 (2020) 1404–1454.

[231] T.-Y. Chen, W.-J. Cheng, J.-C. Horng, H.-Y. Hsu, Artificial peptide-controlled protein release of Zn2+-triggered, self-assembled histidine-tagged protein microparticle, Colloids Surfaces B Biointerfaces. 187 (2020) 110644.

[232] P. Dhar, D. Tarafder, A. Kumar, V. Katiyar, Effect of cellulose nanocrystal polymorphs on mechanical, barrier and thermal properties of poly (lactic acid) based bionanocomposites, RSC Adv.

5 (2015) 60426–60440.

[233] P. Dhar, U. Bhardwaj, A. Kumar, V. Katiyar, Cellulose nanocrystals: a potential nanofiller for food packaging applications, in: Food Addit. Packag., ACS Publications, 2014: pp. 197–239.

[234] S. Schmidt, K. Uhlig, C. Duschl, D. Volodkin, Stability and cell uptake of calcium carbonate templated insulin microparticles, Acta Biomater. 10 (2014) 1423–1430.

[235] W. Huang, S. Zhou, B. Tang, H. Xu, X. Wu, N. Li, X. Zan, W. Geng, Efficient delivery of cytosolic proteins by protein-hexahistidine-metal co-assemblies, Acta Biomater. (2021).

[236] L.J. de Asua, C. Smith, A.M. Otto, Insulin stimulates some initial events necessary for the initiation of DNA replication in Swiss 3T3 cells, Cell Biol. Int. Rep. 6 (1982) 791–797.

[237] J. Shirakawa, M. Fernandez, T. Takatani, A. El Ouaamari, P. Jungtrakoon, E.R. Okawa, W. Zhang, P. Yi, A. Doria, R.N. Kulkarni, Insulin signaling regulates the FoxM1/PLK1/CENP-A pathway to promote adaptive pancreatic β cell proliferation, Cell Metab. 25 (2017) 868–882.

[238] J. HICKMAN, A. McELDUFF, Insulin promotes growth of the cultured rat osteosarcoma cell line UMR-106-01: an osteoblast-like cell, Endocrinology. 124 (1989) 701–706.

[239] C. Roden, A.S. Gladfelter, RNA contributions to the form and function of biomolecular condensates, Nat. Rev. Mol. Cell Biol. 22 (2021) 183–195.

[240] A. Yamasaki, J.M. Alam, D. Noshiro, E. Hirata, Y. Fujioka, K. Suzuki, Y. Ohsumi, N.N. Noda, Liquidity is a critical determinant for selective autophagy of protein condensates, Mol. Cell. 77 (2020) 1163–1175.

[241] S. Alberti, A.A. Hyman, Biomolecular condensates at the nexus of cellular stress, protein aggregation disease and ageing, Nat. Rev. Mol. Cell Biol. 22 (2021) 196–213.

[242] S. Jiang, J.B. Fagman, C. Chen, S. Alberti, B. Liu, Protein phase separation and its role in

tumorigenesis, Elife. 9 (2020) e60264.

[243] Y.-P. Kim, Y.-H. Oh, H.-S. Kim, Protein kinase assay on peptide-conjugated gold nanoparticles, Biosens. Bioelectron. 23 (2008) 980–986.

[244] S. Karmakar, N. Sarkar, L.M. Pandey, Proline functionalized gold nanoparticles modulates lysozyme fibrillation, Colloids Surfaces B Biointerfaces. 174 (2019) 401–408. https://doi.org/10.1016/j.colsurfb.2018.11.032.

[245] K. Bolaños, M.J. Kogan, E. Araya, Capping gold nanoparticles with albumin to improve their biomedical properties, Int. J. Nanomedicine. 14 (2019) 6387.

[246] W. Xiao, J. Xiong, S. Zhang, Y. Xiong, H. Zhang, H. Gao, Influence of ligands property and particle size of gold nanoparticles on the protein adsorption and corresponding targeting ability, Int. J. Pharm. 538 (2018) 105–111.

[247] Y. Kumari, S.K. Singh, R. Kumar, B. Kumar, G. Kaur, M. Gulati, D. Tewari, K. Gowthamarajan, V.V.S.N.R. Karri, C. Ayinkamiye, Modified apple polysaccharide capped gold nanoparticles for oral delivery of insulin, Int. J. Biol. Macromol. 149 (2020) 976–988.

[248] H.-J. Cho, J. Oh, M.-K. Choo, J.-I. Ha, Y. Park, H.-J. Maeng, Chondroitin sulfate-capped gold nanoparticles for the oral delivery of insulin, Int. J. Biol. Macromol. 63 (2014) 15–20.

[249] K.-C. Lee, W.-J. Chen, Y.-C. Chen, Using Dextran-encapsulated gold nanoparticles as insulin carriers to prolong insulin activity, Nanomedicine. 12 (2017) 1823–1834.

[250] M. Mirsalari, S. Elhami, Colorimetric detection of insulin in human serum using GO/AuNPs/TX-100 nanocomposite, Spectrochim. Acta Part A Mol. Biomol. Spectrosc. 240 (2020) 118617.

[251] Y. Sun, Y. Lin, W. Sun, R. Han, C. Luo, X. Wang, Q. Wei, A highly selective and sensitive detection of insulin with chemiluminescence biosensor based on aptamer and oligonucleotide-AuNPs

functionalized nanosilica@ graphene oxide aerogel, Anal. Chim. Acta. 1089 (2019) 152–164.

[252] T. Li, Z. Liu, L. Wang, Y. Guo, Gold nanoparticles/Orange II functionalized graphene nanohybrid based electrochemical aptasensor for label-free determination of insulin, Rsc Adv. 6 (2016) 30732–30738.

[253] K.P. Prajapati, A. Panigrahi, S. Purohit, M. Ansari, K. Dubey, R.K. Behera, B.G. Anand, K. Kar, Osmoprotectant Coated Thermostable Gold Nanoparticles Efficiently Restrict Temperature-Induced Amyloid Aggregation of Insulin, J. Phys. Chem. Lett. 12 (2021) 1803–1813.

[254] C.P. Hill, Z. Dauter, E.J. Dodson, G.G. Dodson, M.F. Dunn, X-ray structure of an unusual calcium site and the roles of zinc and calcium in the assembly, stability, and storage of the insulin hexamer, Biochemistry. 30 (1991) 917–924.

[255] T. Blundell, G. Dodson, D. Hodgkin, D. Mercola, Insulin: The Structure in the Crystal and its Reflection in Chemistry and Biology by, Adv. Protein Chem. 26 (1972) 279–402.

[256] Y. Dekel, Y. Machluf, T. Gefen, G. Eidelshtein, A. Kotlyar, Y. Bram, E. Shahar, F. Reslane, E. Aizenshtein, J. Pitcovski, Formation of multimeric antibodies for self-delivery of active monomers, Drug Deliv. 24 (2017) 199–208.

[257] K. Huus, S. Havelund, H.B. Olsen, M. van de Weert, S. Frokjaer, Chemical and thermal stability of insulin: Effects of zinc and ligand binding to the insulin zinc-hexamer, Pharm. Res. 23 (2006) 2611–2620.

[258] C.L. Maikawa, A.A.A. Smith, L. Zou, C.M. Meis, J.L. Mann, M.J. Webber, E.A. Appel, Stable monomeric insulin formulations enabled by supramolecular PEGylation of insulin analogues, Adv. Ther. 3 (2020) 1900094.

[259] S.K. Sivaraman, S. Kumar, V. Santhanam, Monodisperse sub-10 nm gold nanoparticles by reversing

the order of addition in Turkevich method–The role of chloroauric acid, J. Colloid Interface Sci. 361 (2011) 543–547.

[260] T. Maruyama, Y. Fujimoto, T. Maekawa, Synthesis of gold nanoparticles using various amino acids, J. Colloid Interface Sci. 447 (2015) 254–257.

[261] Y.-F. Lin, J.-H. Zhao, H.-L. Liu, J.W. Wu, C.-K. Chuang, K.-T. Liu, H.-Y. Lin, W.-B. Tsai, Y. Ho, Insights into the structural stability and possible aggregation pathways of the lyqlen peptides derived from human insulin, J. Taiwan Inst. Chem. Eng. 42 (2011) 394–401.

[262] D. Matthes, V. Daebel, K. Meyenberg, D. Riedel, G. Heim, U. Diederichsen, A. Lange, B.L. de Groot, Spontaneous aggregation of the insulin-derived steric zipper peptide VEALYL results in different aggregation forms with common features, J. Mol. Biol. 426 (2014) 362–376.

[263] S. Damilos, I. Alissandratos, L. Panariello, A.N.P. Radhakrishnan, E. Cao, G. Wu, M.O. Besenhard, A.A. Kulkarni, C. Makatsoris, A. Gavriilidis, Continuous citrate-capped gold nanoparticle synthesis in a two-phase flow reactor, J. Flow Chem. (2021) 1–15.

[264] K. Saeed, S. Ahmad, H. Ahmad, F. Ullah, A. Sadiq, A. Uddin, I. Khan, M. Ahmad, Green Synthesis, Characterization and Cholinesterase Inhibitory Potential of Gold Nanoparticles, J. Mex. Chem. Soc. 65 (2021).

[265] K. Pounot, G.W. Grime, A. Longo, M. Zamponi, D. Noferini, V. Cristiglio, T. Seydel, E.F. Garman, M. Weik, V. Fodera, Zinc determines dynamical properties and aggregation kinetics of human insulin, Biophys. J. 120 (2021) 886–898.

[266] A. Patriati, N. Suparno, S. Soontaranon, E.G.R. Putra, The Influence of Zinc Ions in Insulin Fibrillation by Heat at Acid Solution Revealed Using Small Angle X-Ray Scattering, in: Key Eng. Mater., Trans Tech Publ, 2021: pp. 327–334.

[267] C. Wu, M. Biancalana, S. Koide, J.-E. Shea, Binding modes of thioflavin-T to the single-layer β-sheet of the peptide self-assembly mimics, J. Mol. Biol. 394 (2009) 627–633.

[268] X. Chen, B. Tan, S. Wang, R. Tang, Z. Bao, G. Chen, S. Chen, W. Tang, Z. Wang, C. Long, Rationally designed protein cross-linked hydrogel for bone regeneration via synergistic release of magnesium and zinc ions, Biomaterials. 274 (2021) 120895.

[269] K. Liu, S. Zang, R. Xue, J. Yang, L. Wang, J. Huang, Y. Yan, Coordination-triggered hierarchical folate/zinc supramolecular hydrogels leading to printable biomaterials, ACS Appl. Mater. Interfaces. 10 (2018) 4530–4539.

[270] B.N. Ratha, R.K. Kar, S. Kalita, S. Kalita, S. Raha, A. Singha, K. Garai, B. Mandal, A. Bhunia, Sequence specificity of amylin-insulin interaction: a fragment-based insulin fibrillation inhibition study, Biochim. Biophys. Acta (BBA)-Proteins Proteomics. 1867 (2019) 405–415.

[271] J. Wei, Y.-Z. Lin, J.-M. Zhou, C.-L. Tsou, FTIR studies of secondary structures of bovine insulin and its derivatives, Biochim. Biophys. Acta (BBA)-Protein Struct. Mol. Enzymol. 1080 (1991) 29–33.

[272] B.N. Ratha, R.K. Kar, J.R. Brender, R. Pariary, B. Sahoo, S. Kalita, A. Bhunia, High-resolution structure of a partially folded insulin aggregation intermediate, Proteins Struct. Funct. Bioinforma. 88 (2020) 1648–1659.

[273] B. Vestergaard, M. Groenning, M. Roessle, J.S. Kastrup, M. van de Weert, J.M. Flink, S. Frokjaer, M. Gajhede, D.I. Svergun, A helical structural nucleus is the primary elongating unit of insulin amyloid fibrils, PLoS Biol. 5 (2007) e134.

[274] A.L. Božič, R. Podgornik, pH dependence of charge multipole moments in proteins, Biophys. J. 113 (2017) 1454–1465.

[275] V.R. Lavis, W.J. Thompson, S.J. Strada, Effects of insulin on glycogen metabolism of serum-deprived BHK-21 fibroblasts, J. Cell. Physiol. 103 (1980) 55–62.

[276] C.-L. Lin, C.-H. Lin, H.-C. Chang, M.-C. Su, Protein attachment on nanodiamonds, J. Phys. Chem. A. 119 (2015) 7704–7711.

[277] W. Maret, Protein interface zinc sites: the role of zinc in the supramolecular assembly of proteins and in transient protein–protein interactions, Handb. Met. (2006).

[278] J. Sheng, B.M. Gadella, N.K. Olrichs, D. V Kaloyanova, J.B. Helms, The less conserved metal-binding site in human CRISP1 remains sensitive to zinc ions to permit protein oligomerization, Sci. Rep. 11 (2021) 1–10.

[279] H. Li, J. Zhao, A. Wang, Q. Li, W. Cui, Supramolecular assembly of protein-based nanoparticles based on tumor necrosis factor-related apoptosis-inducing ligand (TRAIL) for cancer therapy, Colloids Surfaces A Physicochem. Eng. Asp. 590 (2020) 124486.

[280] T. Guterman, E. Gazit, Toward peptide-based bioelectronics: reductionist design of conductive pili mimetics, Bioelectron. Med. 1 (2018) 131–137.

[281] X. Dong, Y. Zhang, An insight on egg white: From most common functional food to biomaterial application, J. Biomed. Mater. Res. Part B Appl. Biomater. 109 (2021) 1045–1058.

[282] R. Benavente, D. Lopez-Tejedor, M. del Puerto Morales, C. Perez-Rizquez, J.M. Palomo, The enzyme-induced formation of iron hybrid nanostructures with different morphologies, Nanoscale. 12 (2020) 12917–12927.

[283] X. Su, J. Liu, pH-guided self-assembly of copper nanoclusters with aggregation-induced emission, ACS Appl. Mater. Interfaces. 9 (2017) 3902–3910.

[284] Y.-M. Tu, W. Song, T. Ren, Y. Shen, R. Chowdhury, P. Rajapaksha, T.E. Culp, L. Samineni, C.

Lang, A. Thokkadam, Rapid fabrication of precise high-throughput filters from membrane protein nanosheets, Nat. Mater. 19 (2020) 347–354.

[285] S. Zhang, J. Zhang, W. Fang, Y. Zhang, Q. Wang, J. Jin, Ultralarge single-layer porous protein nanosheet for precise nanosize separation, Nano Lett. 18 (2018) 6563–6569.

[286] X. Jia, K. Minami, K. Uto, A.C. Chang, J.P. Hill, J. Nakanishi, K. Ariga, Adaptive liquid interfacially assembled protein nanosheets for guiding mesenchymal stem cell fate, Adv. Mater. 32 (2020) 1905942.

[287] S. Tufail, M.A. Sherwani, S. Shoaib, S. Azmi, M. Owais, N. Islam, Ovalbumin self-assembles into amyloid nanosheets that elicit immune responses and facilitate sustained drug release, J. Biol. Chem. 293 (2018) 11310–11324.

[288] X. Li, S. Qiao, L. Zhao, S. Liu, F. Li, F. Yang, Q. Luo, C. Hou, J. Xu, J. Liu, Template-free construction of highly ordered monolayered fluorescent protein nanosheets: a bioinspired artificial light-harvesting system, ACS Nano. 13 (2019) 1861–1869.

[289] B. Dai, D. Li, W. Xi, F. Luo, X. Zhang, M. Zou, M. Cao, J. Hu, W. Wang, G. Wei, Tunable assembly of amyloid-forming peptides into nanosheets as a retrovirus carrier, Proc. Natl. Acad. Sci. 112 (2015) 2996–3001.

[290] R.A. Shimkunas, E. Robinson, R. Lam, S. Lu, X. Xu, X.-Q. Zhang, H. Huang, E. Osawa, D. Ho, Nanodiamond–insulin complexes as pH-dependent protein delivery vehicles, Biomaterials. 30 (2009) 5720–5728.

[291] Y. Yordanova, W. Vanderlinden, R. Stoll, D. Rüdiger, A. Tosstorff, W. Zaremba, G. Winter, S. Zahler, W. Friess, Zn 2+-triggered self-assembly of Gonadorelin [6-D-Phe] to produce nanostructures and fibrils, Sci. Rep. 8 (2018) 1–12.

[292] N. Ajinkya, X. Yu, P. Kaithal, H. Luo, P. Somani, S. Ramakrishna, Magnetic iron oxide nanoparticle (IONP) synthesis to applications: present and future, Materials (Basel). 13 (2020) 4644.

[293] A. Hemben, I. Chianella, G.J.T. Leighton, Surface Engineered Iron Oxide Nanoparticles Generated by Inert Gas Condensation for Biomedical Applications, Bioengineering. 8 (2021) 38.

[294] A. Tufani, A. Qureshi, J.H. Niazi, Iron oxide nanoparticles based magnetic luminescent quantum dots (MQDs) synthesis and biomedical/biological applications: A review, Mater. Sci. Eng. C. 118 (2021) 111545.

[295] M. Seifan, A. Ebrahiminezhad, Y. Ghasemi, A.K. Samani, A. Berenjian, Amine-modified magnetic iron oxide nanoparticle as a promising carrier for application in bio self-healing concrete, Appl. Microbiol. Biotechnol. 102 (2018) 175–184.

[296] P. Nehra, R.P. Chauhan, N. Garg, K. Verma, Antibacterial and antifungal activity of chitosan coated iron oxide nanoparticles, Br. J. Biomed. Sci. 75 (2018) 13–18.

[297] S. Ayyanaar, M.P. Kesavan, C. Balachandran, S. Rasala, P. Rameshkumar, S. Aoki, J. Rajesh, T.J. Webster, G. Rajagopal, Iron oxide nanoparticle core-shell magnetic microspheres: Applications toward targeted drug delivery, Nanomedicine Nanotechnology, Biol. Med. 24 (2020) 102134.

[298] Y. Teng, Y. Du, J. Shi, P.W.T. Pong, Magnetic iron oxide nanoparticle-hollow mesoporous silica Spheres: Fabrication and potential application in drug delivery, Curr. Appl. Phys. 20 (2020) 320–325.

[299] Y. Cao, Z. Mao, Y. He, Y. Kuang, M. Liu, Y. Zhou, Y. Zhang, R. Pei, Extremely small iron oxide nanoparticle-encapsulated nanogels as a glutathione-responsive T1 contrast agent for tumor-targeted magnetic resonance imaging, ACS Appl. Mater. Interfaces. 12 (2020) 26973–26981.

[300] D.-W. Jung, S.-W. Han, B.-S. Kong, E.-S. Oh, Crystal modification of iron oxide scale by potassium

addition and its application to lithium-ion battery anodes, J. Power Sources. 242 (2013) 357–364.

[301] H. Shyh-Long, S. Pouyan, Application of anisotropic electron diffraction to determine the displacement vector of stacking fault in pyrite, J. Mater. Sci. Lett. 6 (1987) 1238–1240.

[302] S. Deng, V. Berry, Wrinkled, rippled and crumpled graphene: an overview of formation mechanism, electronic properties, and applications, Mater. Today. 19 (2016) 197–212.

[303] K.-K. Bai, Y. Zhou, H. Zheng, L. Meng, H. Peng, Z. Liu, J.-C. Nie, L. He, Creating one-dimensional nanoscale periodic ripples in a continuous mosaic graphene monolayer, Phys. Rev. Lett. 113 (2014) 86102.

[304] V.A. Drits, E. Silvester, A.I. Gorshkov, A. Manceau, Structure of synthetic monoclinic Na-rich birnessite and hexagonal birnessite: I. Results from X-ray diffraction and selected-area electron diffraction, Am. Mineral. 82 (1997) 946–961.

[305] Y.-Q. Yeh, C.-Y. Tang, C.-Y. Mou, Two-dimensional crystals of mesoporous silica SBA-15 nanosheets with perpendicular and open channels, APL Mater. 2 (2014) 113303.

[306] Y.-Q. Yeh, C.-J. Su, C.-A. Wang, Y.-C. Lai, C.-Y. Tang, Z. Di, H. Frielinghaus, A.-C. Su, U.-S. Jeng, C.-Y. Mou, Diatom-inspired self-assembly for silica thin sheets of perpendicular nanochannels, J. Colloid Interface Sci. 584 (2021) 647–659.

[307] L. Kócs, B. Tegze, E. Albert, C. Major, A. Szalai, B. Fodor, P. Basa, G. Sáfrán, Z. Hórvölgyi, Ammonia-vapour-induced two-layer transformation of mesoporous silica coatings on various substrates, Vacuum. 192 (2021) 110415.

[308] N.M.S. Bettahalli, I.T.M. Arkesteijn, M. Wessling, A.A. Poot, D. Stamatialis, Corrugated round fibers to improve cell adhesion and proliferation in tissue engineering scaffolds, Acta Biomater. 9 (2013) 6928–6935.

[309] F. Gentile, L. Tirinato, E. Battista, F. Causa, C. Liberale, E.M. di Fabrizio, P. Decuzzi, Cells preferentially grow on rough substrates, Biomaterials. 31 (2010) 7205–7212.

[310] C. Birchmeier, T.E. Kreis, H.M. Eppenberger, K.H. Winterhalter, W. Birchmeier, Corrugated attachment membrane in WI-38 fibroblasts: alternating fibronectin fibers and actin-containing focal contacts, Proc. Natl. Acad. Sci. 77 (1980) 4108–4112.

[311] T. Iwamoto, Y. Hieda, Y. Kogai, Effect of hydroxyapatite surface morphology on cell adhesion, Mater. Sci. Eng. C. 69 (2016) 1263–1267.

[312] T. Muthukumaran, J. Philip, Effect of phosphate and oleic acid capping on structure, magnetic properties and thermal stability of iron oxide nanoparticles, J. Alloys Compd. 689 (2016) 959–968.

[313] J.R. Rani, S.-I. Oh, J.M. Woo, J.-H. Jang, Low voltage resistive memory devices based on graphene oxide–iron oxide hybrid, Carbon N. Y. 94 (2015) 362–368.

[314] Q. Mu, G. Su, L. Li, B.O. Gilbertson, L.H. Yu, Q. Zhang, Y.-P. Sun, B. Yan, Size-dependent cell uptake of protein-coated graphene oxide nanosheets, ACS Appl. Mater. Interfaces. 4 (2012) 2259–2266.

# Research Output

**Thesis-related papers:**

1. **Karmakar, Srijeeb**, Arjun Sankhla, and Vimal Katiyar. "Supramolecular organization of Cytochrome-C into quantum-dot decorated macromolecular network under pH and thermal stress." *International Journal of Biological Macromolecules* (2021).

2. **Karmakar, Srijeeb**, Tabli Ghosh, Arjun Sankhla, Sayan Bhattacharjee, and Vimal Katiyar. "Insulin biomolecular condensate formed in ionic microenvironment modulates the structural properties of pristine and magnetic cellulosic nanomaterials." Journal of Molecular Liquids 363 (2022): 119580.

3. **Karmakar, Srijeeb**, Arjun Sankhla, and Vimal Katiyar. "Reversible and biocompatible AuNP-decorated [Zn2+]:[Insulin] condensed assembly for potential therapeutic applications." *European Journal of Pharmaceutical Sciences* (2022): 106168.

4. '**Karmakar, Srijeeb**, Arjun Sankhla, and Vimal Katiyar. "A novel IONP-decorated two-dimensional [Zn2+]:[Insulin] nanosheet with ordered array of surface channels and cellular uptake potential." Colloids and Surfaces A: Physicochemical and Engineering Aspects 648 (2022): 129148.'

5. "Amyloid fibrils: A versatile supramolecular organization for Bionanomaterial synthesis" **(under preparation)**

**Other Publications:**

1. "Spontaneous maturation of oligomeric amyloids on carbon-coated cupper grids" **(under preparation)**

2. **Karmakar, Srijeeb**, Nandini Sarkar, and Lalit M. Pandey. "Proline functionalized gold nanoparticles modulates lysozyme fibrillation." *Colloids and Surfaces B: Biointerfaces* 174 (2019): 401-408.

3. **Karmakar, Srijeeb**, Laipubam Gayatri Sharma, Abhishek Roy, Anjali Patel, and Lalit Mohan Pandey. "Neuronal SNARE complex: A protein folding system with intricate protein-protein interactions, and its common neuropathological hallmark, SNAP25." *Neurochemistry international* 122 (2019): 196-207.

4. **Karmakar, Srijeeb**, Sachin Kumar, and Vimal Katiyar. "Comparative Domain-fold analysis of the SARS-CoV-2 ORF1ab polyprotein: Insight into co-evolution, conservation of folding patterns, potential therapeutic strategies, and the possibility of reemergence." (2020).

5. **Karmakar, Srijeeb,** Varun Saxena, Pranjal Chandra, and L. Pandey. "Novel therapeutics and diagnostics strategies based on engineered nanobiomaterials." *Nanotechnology in Modern Animal Biotechnology: Recent Trends and Future Perspectives; Springer Science and Business Media LLC: Berlin/Heidelberg, Germany* (2019): 1-27.

6. Roy, Abhishek, Shivam Tiwari, **Srijeeb Karmakar**, K. Anki Reddy, and Lalit Mohan Pandey. "The effect of the stoichiometric ratio of zinc towards the fibrillation of Bovine Serum Albumin (BSA): a mechanistic insight." *International journal of biological macromolecules* 123 (2019): 409-419.